

MICROWAVE PL.
FILMS DE

i

**MICROWAVE PLASMA-ASSISTED CVD POLYCRYSTALLINE DIAMOND
FILMS DEPOSITION AT HIGHER PRESSURE CONDITIONS**

By

Stanley Shengxi Zuo

A DISSERTATION

**Submitted to
Michigan State University
in partial fulfillment of the requirements
for the degree of**

DOCTOR OF PHILOSOPHY

Electrical Engineering

2009

ABSTRACT

MICROWAVE PLASMA-ASSISTED CVD POLYCRYSTALLINE DIAMOND FILMS DEPOSITION AT HIGHER PRESSURE CONDITIONS

By

Stanley Shengxi Zuo

This study investigated the growth of polycrystalline diamond films using pressures higher than 100 Torr, which is higher than the pressure nominally used for polycrystalline diamond film deposition. Under these higher pressure operating conditions, high optical quality freestanding films and substrates of polycrystalline diamond with thickness up to 200 microns have been uniformly deposited on 2 inch and 3 inch silicon wafers in a 2.45 GHz microwave plasma-assisted chemical vapor deposition (CVD) system. Several of these films were separated from the silicon substrate and then lapped and polished for window applications. The polycrystalline diamond films are grown in a microwave plasma-assisted CVD reactor using either a hydrogen/methane or a hydrogen/argon/methane chemistry without any other additive gases. The deposition reactor is a microwave cavity applicator with the plasma confined inside a 12 cm diameter fused silica dome. The methane percentage was nominally varied to between 1-2% when reactor deposition pressure varied between 100-180 Torr. The reactor was also modified to improve its performance for higher pressure deposition processing. The substrate temperature was controlled between 900 and 1100°C. The experimentally measured average linear growth rate of the polycrystalline diamond film is as large as 3-4 $\mu\text{m/h}$ at 160 Torr reactor pressure and 2% methane in the feed gas.

The polymer
rate optical quality
is used to identify
The FWHM of the
diamond quality and
The diamond films
completed, the bow
diamond film. It was
film on the silicon wa
from the diamond fil
temperature lower fil

Finally, the di
of film thickness in th
higher pressure condi
radially across a diam
radius of 1.25 inch (or
pressure with argon ad
to $\pm 4.3\%$ radially and \pm
substrate at 160 Torr re
was significantly impro
addition of the argon in

The polycrystalline diamond samples were characterized to determine growth rate, optical quality, film thickness uniformity, and intrinsic stress. Raman spectroscopy is used to identify the spectral width of the sp^3 peak and the ratio of the sp^2 to sp^3 signals. The FWHM of the diamond peak from the Raman spectrum is used as one measure of the diamond quality and the optical transmission measurements was used as another measure. The diamond films were grown on silicon wafers and after the deposition process was completed, the bowing of the wafer and film was used to determine the stress in the diamond film. It was found that stress levels greater than a threshold value in the diamond film on the silicon wafer often result in the film breaking when the silicon is etched away from the diamond film. It was also determined that by controlling the substrate temperature lower film stress could be achieved.

Finally, the diamond film thickness uniformity was evaluated by percent deviation of film thickness in the radial and circumferential directions for samples deposited at higher pressure condition. An example of achieved thickness non-uniformity was $\pm 4.7\%$ radially across a diameter of 2.5 inch (or 6.3 cm) and $\pm 4.0\%$ along the circumference at a radius of 1.25 inch (or 3.15 cm) for a 3-inch diameter deposition area at 120 Torr reactor pressure with argon addition. The achieved thickness non-uniformity was reduced down to $\pm 4.3\%$ radially and $\pm 6.7\%$ along the circumference for a 2-inch diameter silicon substrate at 160 Torr reactor pressure without using argon gas. The thickness uniformity was significantly improved by controlling the substrate temperature to be uniform and the addition of the argon in the feed gas.

Copyright by
Stanley Shengxi Zuo
2009

To my wife

has

To my parents

for

*To my wife, Suzanne, with whose love and patience
has made this all possible.*

*To my parents, Zongshi Zuo and Enhui Chen,
for their endless and selfishnessless support.*

First I would like to thank
advisor, Dr. Timothy C
mental and financial as
making this learning e
is also extended to Dr.
serving as members of

Next, I would like to
giving me the opportu
that I needed to compl
sincere appreciation to
financial support givin
during this study.

I also would like to thank
polishing the diamond
Matthew Swope for th
Dr. Rahul Ramamurti
providing laser cuttin
all my colleagues and

ACKNOWLEDGMENTS

First I would like to take this opportunity to thank my major professor, my adviser, Dr. Timothy Grotjohn, for his constant encouragement, continual support in moral and financial assistance, and guidance through this and other studies. His efforts in making this learning experience worthwhile are deeply appreciated. Sincere appreciation is also extended to Dr. Jes Asmussen, Dr. Donnie Reinhard, and Dr. Greg Swain for serving as members of the Guidance Committee.

Next, I would like to thank Dr. Thomas Schuelke and Fraunhofer USA, Inc. for giving me the opportunity to continue working on this research and the financial support that I needed to complete this dissertation. In addition, I also would like to express my sincere appreciation to Dr. Percy Pierre and Dr. Barbara O'Kelly for the moral and financial support giving when I was awarded as a GANN fellow two years in the past during this study.

I also would like to thank Dr. Donnie Reinhard for providing the lapping and polishing the diamond samples and the optical transmission measurement results, Mr. Matthew Swope for the help he gave setting up and operating the Raman spectrometer, Dr. Rahul Ramamurti for providing the X-ray diffraction results, Mr. Michael Becker for providing laser cutting of diamond film samples. I am appreciated for the friendship with all my colleagues and fellow graduate students.

TABLE OF CONTENTS

LIST OF TABLES.....	x
LIST OF FIGURES.....	xiii
CHAPTER 1 INTRODUCTION	1
1.1 MOTIVATION	1
1.2 RESEARCH OBJECTIVES.....	3
1.3 MY CONTRIBUTIONS	3
1.4 PREVIEW OF CHAPTERS.....	4
CHAPTER 2 REVIEW OF HIGH-PRESSURE DEPOSITION OF CVD DIAMOND FILMS.....	6
2.1 THE SIMPLIFIED PHYSICAL AND CHEMICAL PROCESS OF DIAMOND FORMATION	7
2.2 SIMPLIFIED DIAMOND GROWTH MECHANISM AND SURFACE CHEMISTRY.....	8
2.3 GROWTH ZONE AND BACHMANN C-H-O PHASE DIAGRAM	10
2.4 PLASMA PROPERTIES VERSUS PRESSURE IN CVD DIAMOND DEPOSITION	14
2.4.1 <i>Neutral species concentrations and atomic hydrogen density and their spatial distribution.....</i>	<i>14</i>
2.4.2 <i>Neutral gas temperature.....</i>	<i>22</i>
2.4.3 <i>Electron density and electron temperature</i>	<i>27</i>
2.4.4 <i>Microwave power density.....</i>	<i>28</i>
2.5 KEY RESULTS OF HIGHER PRESSURE RESEARCH STUDIES	30
2.5.1 <i>Comparison of surface texture diamond content and growth rate at high pressures.....</i>	<i>32</i>
2.6 CURVATURE OF FREE STANDING DIAMOND FILMS AND BOWING STRESSES.....	38
2.6.1 <i>Intrinsic stress.....</i>	<i>43</i>
2.6.2 <i>Grain size and disordered diamond crystals.....</i>	<i>43</i>
2.6.3 <i>Defects</i>	<i>47</i>
2.6.4 <i>Impurities.....</i>	<i>48</i>
2.6.5 <i>The stress types and the defects and impurity contents.....</i>	<i>49</i>
2.7 THE EFFECT OF ARGON GAS ADDITION ON MPCVD DIAMOND FILM GROWTH	52
CHAPTER 3 EXPERIMENTAL SETUPS AND PROCEDURES	58
3.1 MPCVD DIAMOND SYSTEM.....	59
3.1.1 <i>2.45 GHz cylindrical cavity mode calculation</i>	<i>63</i>
3.1.2 <i>The experimental process and the details of reactor tuning</i>	<i>70</i>
3.2 MODIFICATIONS OF THE MPCVD REACTOR FOR HIGH-PRESSURE OPERATION	73
3.2.1 <i>Fused silica dome cooling.....</i>	<i>75</i>
3.2.2 <i>Substrate, substrate holder and insert configuration.....</i>	<i>77</i>
3.2.3 <i>High pressure high power operation safety</i>	<i>80</i>
3.3 MEASUREMENT OF SUBSTRATE TEMPERATURE.....	81
3.4 REACTOR TUNING FOR UNIFORM TEMPERATURE ON SUBSTRATE	82

- 3.5 NUCLE
- 3.6 GENER
- 3.7 PROFIL
THICK
- 3.7.1 M
- 3.7.2 C
- 3.7.3 E
- 3.8 X-RAY
SURFA
- 3.8.1 T
- 3.8.2 M
- 3.8.3 F
- 3.8.4 S
- 3.9 DIAMON
INTERC
- 3.10 DIAMON
3.10.1 V
- 3.10.2 R
- 3.10.3 P
- 3.11 DIAMON
3.11.1 S
- 3.11.2 T
- 3.11.3 R
- 3.11.4 T

CHAPTER 4 D

- 4.1 INPUT A
4.1.1 Pr
- 4.1.2 P
- 4.2 OUTPUT
- 4.3 GENERA
- 4.4 DIAMON
- 4.5 DIAMON
- 4.6 GROWTH
CONCEN
- 4.6.1 Gr
- 4.6.2 Gr
- 4.6.3 Gr
- 4.7 THE ARC
4.7.1 The
- 4.7.2 The
- 4.7.3 The

CHAPTER 5 UN FIL

- 5.1 INPUT AN
- 5.2 OUTPUT V

3.5	NUCLEATION, SELECTION OF SUBSTRATE AND ITS PRETREATMENT	88
3.6	GENERAL PROCEDURE OF STARTING UP AND SHUTDOWN A EXPERIMENT.....	93
3.7	PROFILE THE SUBSTRATE FOR GROWTH UNIFORMITY AND DIAMOND FILM THICKNESS MEASUREMENTS.....	96
3.7.1	<i>Measurement of diamond film thickness</i>	96
3.7.2	<i>Calculation of diamond film growth rate</i>	103
3.7.3	<i>Evaluation of diamond film thickness uniformity</i>	103
3.8	X-RAY DIFFRACTION TECHNIQUE, POLE FIGURE, FILM TEXTURE, AND SURFACE MORPHOLOGY	105
3.8.1	<i>The Bragg's law and interpretation of powder X-ray diffraction data</i> ...	105
3.8.2	<i>X-ray diffraction pole figure</i>	115
3.8.3	<i>Film texture</i>	117
3.8.4	<i>Surface morphology</i>	118
3.9	DIAMOND FILM GRAIN SIZE MEASUREMENT, THE METHOD OF LINEAR INTERCEPTS	120
3.10	DIAMOND FILM QUALITY MEASUREMENT	122
3.10.1	<i>Visual inspection</i>	122
3.10.2	<i>Raman spectroscopy for quality evaluation</i>	123
3.10.3	<i>Post processing and optical transmission measurement</i>	126
3.11	DIAMOND FILM STRESS MEASUREMENT	130
3.11.1	<i>Substrate curvature technique and Stoney's equation</i>	131
3.11.2	<i>The thermal stress calculation</i>	146
3.11.3	<i>Raman spectroscopy for stress evaluation</i>	154
3.11.4	<i>The intrinsic stress calculation</i>	159
CHAPTER 4 DIAMOND FILM QUALITY AND GROWTH RATE		161
4.1	INPUT AND REACTOR PARAMETERS.....	161
4.1.1	<i>Pressure and absorbed microwave power density</i>	162
4.1.2	<i>Plasma size and absorbed microwave power</i>	164
4.2	OUTPUT VARIABLES.....	165
4.3	GENERAL OPERATIONAL FIELD MAP AND PERFORMANCE REGION	165
4.4	DIAMOND FILM QUALITY, THE RAMAN SPECTROSCOPY ANALYSIS.....	171
4.5	DIAMOND FILM QUALITY, THE OPTICAL TRANSMISSION ANALYSIS	183
4.6	GROWTH RATE AND QUALITY VERSUS REACTOR PRESSURE, METHANE CONCENTRATION AND SUBSTRATE TEMPERATURE.....	185
4.6.1	<i>Growth rate and quality versus reactor pressure</i>	189
4.6.2	<i>Growth rate and quality versus methane concentration</i>	192
4.6.3	<i>Growth rate and quality versus substrate temperature</i>	199
4.7	THE ARGON EFFECT ON DIAMOND FILM GROWTH RATE AND QUALITY	203
4.7.1	<i>The argon effect on diamond film growth rate and grain size</i>	203
4.7.2	<i>The diamond film quality changes due to the argon addition</i>	208
4.7.3	<i>The secondary nucleation and step bunching with argon addition</i>	213
CHAPTER 5 UNIFORMITY OF THE MICROCRYSTALLINE DIAMOND FILM.....		217
5.1	INPUT AND REACTOR PARAMETERS.....	217
5.2	OUTPUT VARIABLES.....	218

- 5.3 SUBSTRATE TEMPERATURE UNIFORMITY.....
- 5.3.1 *Temperature*.....
- 5.3.2 *Temperature*.....
- 5.3.3 *The argon*.....
- 5.3.4 *Relation of rate*.....
- 5.4 EVALUATION OF SUBSTRATE TEMPERATURE.....

CHAPTER 6 INTRINSIC GROWTH OF DIAMONDS

- 6.1 INPUT AND REACTION.....
- 6.2 OUTPUT VARIABLES.....
- 6.3 THE MEASUREMENT OF GROWTH RATES FOR STRESS CATALYZED GROWTH.....
- 6.4 THE INTRINSIC GROWTH OF DIAMONDS AT TEMPERATURE.....
- 6.5 EVALUATION OF GROWTH RATES AT HIGH PRESSURE AND HIGH TEMPERATURE.....

CHAPTER 7 CONCLUSIONS

- 7.1 CONCLUSION OF THE PRESENT WORK.....
- 7.1.1 *Condition of diamond growth*.....
- 7.1.2 *Improved diamond growth*.....
- 7.1.3 *Measuring diamond growth*.....
- 7.2 SUGGESTIONS FOR FURTHER WORK.....
- 7.2.1 *Alternative diamond growth*.....
- 7.2.2 *Improving diamond growth at higher pressure*.....

- APPENDICES.....
- APPENDIX A ORIGINATION OF DIAMONDS.....
- APPENDIX B MODIFICATION OF DIAMONDS.....
- APPENDIX C ORIGINATION OF DIAMONDS.....

- REFERENCES.....

5.3	SUBSTRATE TEMPERATURE, THICKNESS AND OPTICAL QUALITY UNIFORMITY	218
5.3.1	<i>Temperature uniformity by reactor short and substrate tuning</i>	219
5.3.2	<i>Temperature uniformity by substrate holder and insert design</i>	224
5.3.3	<i>The argon effect on film growth uniformity.....</i>	230
5.3.4	<i>Relation of substrate temperature and thickness uniformity to growth rate.....</i>	236
5.4	EVALUATION OF DIAMOND FILM GROWTH UNIFORMITY – THICKNESS, SUBSTRATE TEMPERATURE, GRAIN SIZE AND SURFACE MORPHOLOGY	240
CHAPTER 6 INTRINSIC STRESSES OF THE POLYCRYSTALLINE DIAMOND FILM.....255		
6.1	INPUT AND REACTOR PARAMETERS.....	258
6.2	OUTPUT VARIABLES.....	258
6.3	THE MEASUREMENTS OF RADIUS OF CURVATURE AND OTHER PARAMETERS FOR STRESS CALCULATION	260
6.4	THE INTRINSIC STRESS CONTROL WITH METHANE CONCENTRATION AND TEMPERATURE VARIATION VERSUS TIME	264
6.5	EVALUATION OF DIAMOND FILM STRESS USING RAMAN DIAMOND PEAK SHIFT AND INTERPRETATION OF STRESS DATA	274
CHAPTER 7 CONCLUSIONS AND FUTURE WORK.....278		
7.1	CONCLUSION OF THIS RESEARCH	279
7.1.1	<i>Conditions of high quality, fast growing polycrystalline CVD diamond films</i>	279
7.1.2	<i>Improved diamond film uniformity.....</i>	280
7.1.3	<i>Measuring and ways of reducing diamond film intrinsic stress.....</i>	281
7.2	SUGGESTIONS FOR FUTURE WORK.....	282
7.2.1	<i>Alternatives of microwave power supply.....</i>	282
7.2.2	<i>Improving cooling deficiency and temperature control of the system at higher pressure.....</i>	283
APPENDICES.....284		
APPENDIX A	ORIGINAL SOURCE CODE FOR THE FITCIRCLE_DEMO.M FILE	284
APPENDIX B	MODIFIED SOURCE CODE FOR THE FITCIRCLE_DEMO.M FILE	286
APPENDIX C	ORIGINAL SOURCE CODE FOR THE FITCIRCLE.M FILE.....	287
REFERENCES		
		293

LIST OF TABLES

Table 2-1: Key result parameters of the current higher pressure CVD diamond research studies.....	31
Table 3-1: Roots X_{np} (when n and $p = 1, 2, 3, 4, 5$) of the Bessel function of the first kind $-J_n(x)$	65
Table 3-2: Roots X'_{np} (when n and $p = 1, 2, 3, 4, 5$) of the derivatives of the Bessel function of the first kind $-J'_n(x)$	65
Table 3-3: Standard deviation calculation of SLE method.....	105
Table 3-4: The theoretical values of the d -spacings, diffraction angles and for diamond crystal materials. All values are based on diamond lattice constant $a = 3.5667 \text{ \AA}$ and X-ray wavelength of $\lambda = 1.540562 \text{ \AA}$	109
Table 3-5: Comparison of the linear thermal expansion coefficients between the best-fit value and original data.	151
Table 4-1: Examples of diamond quality evaluated by Raman FWHM versus their growth conditions. The quality of these as grown diamond films range from near HPHT single crystal (by FWHM value) to close to acceptable (by visual estimation). T_S is the temperature of the substrate at each point averaged from the beginning to the end of the experiment.	180
Table 4-2: Growth rate and quality versus reactor pressure and methane concentration.	187
Table 4-3: A set of samples that cover a range of typical experimental conditions without Ar addition. Substrate temperature is ending temperature if range is not given. The growth rates in parentheses are an average over multiple experiments at the same condition or an adjustment as indicated in the footnotes.	188
Table 4-4: Comparison of the average growth rate by weight gain and the maximum growth rate by linear encoder (LE*). Please note the average of the rows to the left is an average growth rate over a number of samples that were grown under the same growth condition.	193
Table 4-5: A set of samples that shows the argon influences to diamond film growth rate and diamond grain size at different reactor pressure. The absorbed power is nearly controlled to be the same for the two comparing experiments at the same pressure. The film thickness and growth rate	

shows both the
film.....

Table 4-6: The Raman FW
samples deposi
addition. T_S is
from the begin

Table 5-1: A set of data re
sliding short tu
the center and
under the low l

Table 5-2: Sample SZ-2 in
within 24 hour
sccm CH_4

Table 5-3: Sample SZ-2 in
within 24 hour
sccm CH_4 , and

Table 5-4: Diamond film S
encoder and th
deviation form

Table 5-5: Diamond film S
encoder and th
deviation form

Table 5-6: Substrate temp
overview. The
standard devia
percentage dev

Table 5-7: Diamond film
encoder and th
deviation form

Table 5-8: Sample SZ-3i
for first 48 ho

Table 5-9: Diamond film
and the film r
formula, the H

Table 5-10: Sample SZ-2

shows both the average value and the value at the center of the diamond film.....	205
Table 4-6: The Raman FWHM comparison with growth conditions of diamond film samples deposited with argon gas addition to those without the argon addition. T_S is the temperature of the substrate at the point averaged from the beginning to the end of the experiment.....	212
Table 5-1: A set of data recorded on temperature variations for the Test-5 versus sliding short tuning where the minimum temperature difference between the center and the edge of the substrate is shown at 67 °C. UFL indicates under the low limit of the detectable range, which is 600 °C.....	221
Table 5-2: Sample SZ-2inch-1mm-058B temperature variation over time recorded within 24 hours. The growth conditions are 180 Torr, 400 sccm H₂, 4 sccm CH₄.....	232
Table 5-3: Sample SZ-2inch-1mm-059B temperature variation over time recorded within 24 hours. The growth conditions are 180 Torr, 400 sccm H₂, 4 sccm CH₄, and 100 sccm argon.....	232
Table 5-4: Diamond film SZ-2inch-1mm-058B thickness measured by linear encoder and the film non-uniformity calculated using the percentage deviation formula, the Eq. 3-12 provided in section 3.7.3.	233
Table 5-5: Diamond film SZ-2inch-1mm-059B thickness measured by linear encoder and the film non-uniformity calculated using the percentage deviation formula, the Eq. 3-12 provided in section 3.7.3.	234
Table 5-6: Substrate temperature and diamond film thickness uniformity data overview. The substrate temperature uniformity is measured by its standard deviation and the thickness uniformity is measured by its percentage deviation as defined in Eq. 3-12.....	239
Table 5-7: Diamond film SZ-3inch-1mm-022D thickness measured by linear encoder and the film non-uniformity calculated using the percentage deviation formula, the Eq. 3-12 provided in section 3.7.3.	242
Table 5-8: Sample SZ-3inch-1mm-022D temperature variation over time recorded for first 48 hours.	243
Table 5-9: Diamond film SZ-2inch-1mm-053 thickness measured by linear encoder and the film non-uniformity calculated using the percentage deviation formula, the Eq. 3-12 provided in section 3.7.3.	244
Table 5-10: Sample SZ-2inch-1mm-053 temperature variation over time.	245

Table 5-11: Diamond film
encoder and th
deviation form

Table 5-12: Sample SZ-2

Table 5-13: Diamond film
encoder and th
deviation form

Table 5-14: Sample SZ-2

Table 6-1: An example o
the silicon wa
from sample S

Table 6-2: Experiments f
variation vers
constant flow
comparison of
may be influe

Table 6-3: Samples were
appears that s
process when

Table 6-4: This table sho
The growth co
Table 6-3 in t
calculating th
3-59, Eq. 3-6

Table 5-11: Diamond film SZ-2inch-1mm-058A thickness measured by linear encoder and the film non-uniformity calculated using the percentage deviation formula, the Eq. 3-12 provided in section 3.7.3.	248
Table 5-12: Sample SZ-2inch-1mm-058A temperature variation over time.	249
Table 5-13: Diamond film SZ-2inch-1mm-045 thickness measured by linear encoder and the film non-uniformity calculated using the percentage deviation formula, the Eq. 3-12 provided in section 3.7.3.	252
Table 5-14: Sample SZ-2inch-1mm-045 temperature variation over time.	253
Table 6-1: An example of 2-set measured curvature data on the backside surface of the silicon wafer by using Solartron linear encoder. These are real data from sample SZ-2inch-1mm-065A.	262
Table 6-2: Experiments for intrinsic stress control with methane concentration variation versus time. Two groups of reference experiments ran under constant flow of CH ₄ (4 and 6 sccm) are included in this table for comparison of their intrinsic stresses in the film. Other conditions that may be influential to the intrinsic stress are also included.	269
Table 6-3: Samples were not broken during the chemical back etch process. It appears that samples tend to break during the chemical back etch process when the intrinsic stress is greater than 440 Mpa.	273
Table 6-4: This table shows how diamond film stress is calculated for a local point. The growth conditions for these samples can be found in Table 6-2 and Table 6-3 in this chapter. Please note the coefficients of equations for calculating the stress associated with crystal planes are included in Eq. 3-59, Eq. 3-61 and Eq. 3-63.	277

LIST OF FIGURES

Images in this dissert

Figure 2-1: Schematic dia
diamond CVD

Figure 2-2: Illustrated che
carbon atom or
atom is reactiv
the diamond st
they appear in
figures.

Figure 2-3: Illustrated che

Figure 2-4: Illustrated che

Figure 2-5: Bachmann C-
diamond grow

Figure 2-6: Concentration
region as meas
methane in the
oxygen in the

Figure 2-7: Mole fraction
CVD system v
11].....

Figure 2-8: Diamond dep
percentage in
(a) 2 sccm CH
C₂H₂ [9, 12].

Figure 2-9: Atomic hydr

Figure 2-10: Atomic hyc
in part (a) and

Figure 2-11: Radial distr
allowed trans
actinometry a

LIST OF FIGURES

Images in this dissertation are presented in color.

Figure 2-1: Schematic diagram of the physical and chemical processes during diamond CVD.....	8
Figure 2-2: Illustrated chemical reaction: $C_dH + H \rightarrow C_d^* + H_2$. C_d denotes the carbon atom on diamond surface and the symbol asterisk indicates that atom is reactive. This figure is viewed as a 2D plane view, so atoms in the diamond structure and the CH_3 species are not in the same plane as they appear in the figure. This same statement holds for the following figures.	11
Figure 2-3: Illustrated chemical reaction: $C_d^* + CH_3 \rightarrow C_dCH_3$	11
Figure 2-4: Illustrated chemical reaction: $C_dCH_3 + H \rightarrow C_dCH_2 + H_2$	12
Figure 2-5: Bachmann C-H-O diagram (updated version: 1994) indicates where the diamond growth zone located [7, 8].	13
Figure 2-6: Concentration of CH_4 , C_2H_2 , and C_2H_4 in a microwave discharge region as measured by FTIR absorption spectroscopy versus percent methane in the feed gas at an operating pressure of 30 Torr with no oxygen in the feed gas [9, 10].....	15
Figure 2-7: Mole fraction of chemical species measured in a microwave plasma CVD system versus variation in the methane fraction in the feed gas [9, 11].....	16
Figure 2-8: Diamond deposition reactor exhaust gas composition versus oxygen percentage in the feed gas for input gas flows at 97 sccm hydrogen and (a) 2 sccm CH_4 , (b) 1 sccm C_2H_6 , (c) 1 sccm C_2H_4 , and (d) 1 sccm C_2H_2 [9, 12].	17
Figure 2-9: Atomic hydrogen percentage and density versus pressure [9, 17].	19
Figure 2-10: Atomic hydrogen mole fraction versus the microwave power density in part (a) and versus methane concentration in part (b) [9, 18].	20
Figure 2-11: Radial distribution of H-atom mole fraction concluded by two photon allowed transition laser induced fluorescence (TALIF) and by actinometry after Abel inversion of the spectrum from the Optical	

Emission Sp
not a duplica

Figure 2-12: Calculated
above the su
at time mom
is 50 Hz and

Figure 2-13: Atomic hy
density. The
hydrogen O

Figure 2-14: Gas temper
temperatures
photon LIF a

Figure 2-15: Atomic hy
hydrogen ro
percentage i
 9 W-cm^{-3} , 3

Figure 2-16: Molecular
power densi
24].....

Figure 2-17: Molecular
diameter dis
hydrogen di
(453 - 465)
band.

Figure 2-18: Electron d
diamond dep

Figure 2-19: Microwav
methane dis

Figure 2-20 (b): High p
different CH
spectra for th

Figure 2-21 (b): High p
100-150 Torr

Emission Spectroscopy (OES) [19]. This graph is a reproduction and, not a duplicate of the original plot.....	21
Figure 2-12: Calculated density of hydrogen atoms [H] versus radius, r , at a height above the substrate of 0.6 cm ($z = 0.4$ cm) and a pressure of $p = 40$ Torr at time moments 2, 5 and 8 ms from the pulse start. The pulse frequency is 50 Hz and the pulse base duration is 10 ms [21].	21
Figure 2-13: Atomic hydrogen translation temperature versus microwave power density. The temperature was measured using Doppler broadening of hydrogen OES signals [23, 24].....	23
Figure 2-14: Gas temperature versus average microwave power density. Gas temperatures measured include atomic hydrogen temperature by two-photon LIF and hydrogen rotational temperature by CARS [23, 24].....	24
Figure 2-15: Atomic hydrogen temperature (measured by LIF) and molecular hydrogen rotational temperature (measured by CARS) versus methane percentage in the feed gas [23, 24]. Plasma conditions: 600 W, 2500 Pa, $9 \text{ W}\cdot\text{cm}^{-3}$, 300 sccm, $T_s = 900$ °C.....	25
Figure 2-16: Molecular hydrogen rotational temperature versus average microwave power density. Temperature was measured using line-of-sight OES [23, 24].....	26
Figure 2-17: Molecular hydrogen rotational temperature versus pressure for a 5-cm-diameter discharge system [9, 25]. The rotational temperature for hydrogen discharge was determined by OES spectrum around 460 nm (453 – 465) using the R branch of the $\text{H}_2(\text{G}^1\Sigma_g^+)$ to $\text{H}_2(\text{B}^1\Sigma_u^+)$ (0, 0) band.	27
Figure 2-18: Electron density versus pressure for a microwave plasma-assisted diamond deposition discharge [9, 25].....	28
Figure 2-19: Microwave power density versus pressure for 5-cm-diameter hydrogen methane discharge used for diamond deposition [9, 25].	29
Figure 2-20 (b): High power density MPCVD diamond at 900 °C and 150 Torr with different CH_4 concentrations. The figure on the right is the Raman spectra for the corresponding film [34].	34
Figure 2-21 (b): High power density MPCVD diamond using 16 % CH_4/H_2 and 100-150 Torr pressure at different temperature [34].	37

Figure 2-22: Growth rate
in H_2 and (c)
by the author
for High Power
Low Power D

Figure 2-23: Locations for
C-H-O diagram

Figure 2-24: A freestanding
upward after the
diamond film
of a flashlight

Figure 2-25: Comparison of
temperature (T)
length increase

Figure 2-26: The linear thickness
versus the mass

Figure 2-27: Top view SEM
for four diameters
film thickness
morphology of
grains [47]....

Figure 2-28: Cross-sectional

Figure 2-29: Grain size analysis
observed [47]

Figure 2-30: Variation of
source gas. G

Figure 2-31: Stress and growth

Figure 2-32: (a) High resolution
800 °C and C
Arrows in the

Figure 2-33: Micro-Raman
(curve 1) and
1332 cm^{-1} and
attributed to the

Figure 2-22: Growth rate versus substrate temperature in (a) 1 % and (b) 16 % CH ₄ in H ₂ and (c) 16 % CH ₄ +1.6 % O ₂ in H ₂ [34]. Though was not specified by the author (s), the pressure is somewhere in between 100 to 150 Torr for High Power Density (HPD) plasma and a few Torr to tens of Torr for Low Power Density (LPD) plasma defined in the article.....	38
Figure 2-23: Locations for hydrocarbons near the enlarged hydrogen-rich corner in C-H-O diagram [34].	39
Figure 2-24: A freestanding diamond thin film (SZ-2inch-1mm-08) that was bent upward after the silicon substrate was chemically removed. The diamond film is 2 inches in diameter, 46 μm thick, and is sitting on top of a flashlight.	39
Figure 2-25: Comparison of linear thermal expansion with respect to room temperature (293 °K or 20 °C) for diamond and silicon in percentage length increased versus to the temperature of the material [38, 39, 40].....	42
Figure 2-26: The linear thermal expansion coefficients for diamond and silicon versus the material temperature [38, 39, 40].	42
Figure 2-27: Top view scanning electron micrographs, in the same magnification, for four diamond films grown for (a) 1, (b) 3, (c) 6.5 and (d) 10 h. The film thicknesses were 3.0, 8.7, 21 and 42 μm, respectively. The surface morphology of all films exhibited predominantly faceted pyramidal grains [47].....	44
Figure 2-28: Cross-section SEM image of a diamond film on Si substrate [36].....	45
Figure 2-29: Grain size as a function of the film thickness. A linear behavior is observed [47].	46
Figure 2-30: Variation of the average grain size with the methane fraction in the source gas. Grain sizes were calculated from X-ray diffraction data [41].	46
Figure 2-31: Stress and grain size relation [45].....	47
Figure 2-32: (a) High resolution TEM image of grain boundary in material grown at 800 °C and CH ₄ =1% (b) Moire image obtained from CH ₄ =0.1% [45]. Arrows in the figure roughly identify the grain boundary.....	48
Figure 2-33: Micro-Raman spectra of two diamond films with thickness of 3.0 μm (curve 1) and 21 μm (curve 2). Both spectra exhibit the diamond line at 1332 cm ⁻¹ and a broad band centered at around 1550 cm ⁻¹ , which is attributed to the sp ² -bond graphitic carbon phases [47].....	49

Figure 2-34: Luminescence of diamond film induced defects [49].

Figure 2-35: Shift of peak diamond through growth direction lines are drawn.

Figure 2-36: Raman spectra of the film at different temperatures spectra are overlaid.

Figure 2-37: The optical absorption of diamond film under microwave plasma.

Figure 2-38: The optical absorption of diamond film in nitrogen gas [51].

Figure 3-1: Schematic diagram of diamond film deposition on the substrate at the base of the cathode.

Figure 3-2: The overall process of diamond film deposition consisting of 5 essential steps: (1) nucleation, (2) growth, (3) cooling, (4) annealing, and (5) etching. Each of the 5 steps is described in detail in the text. Cooling as well as annealing is performed when the valves are in the closed position.

Figure 3-3: Sketch of TEM image showing intensity distribution of diamond film (left) and the EDS spectrum (right) versus radius r (bottom). The figure depicts the center of the film.

Figure 3-4: Sketch of TEM image showing intensity distribution of diamond film (left) and the EDS spectrum (right) versus its radius r .

Figure 2-34: Luminescence spectra from gem-quality diamond and from CVD diamond films deposited on W and Si substrates. Luminescence from Si induced defect centers in the diamond film grown on Si is clearly shown [49].....	50
Figure 2-35: Shift of peak position and change of width of the Raman peak of diamond through the film thickness. Quality of film improves along the growth direction and strain changes from compressive to tensile. The lines are drawn to guide the eye [49].....	51
Figure 2-36: Raman spectra measured with 514.5 nm laser from the cross section of the film at intervals of 1 μm from the interface to the surface. The spectra are offset vertically for clarity [49].	52
Figure 2-37: The optical emission spectrum of a (4.4% CH₄ + 95.6% H₂) microwave plasma [50].	54
Figure 2-38: The optical emission spectra at different percentage addition of argon gas [51].	55
Figure 3-1: Schematic drawing of the microwave plasma CVD reactor for diamond film deposition [9]. L_s is the Short length, L_p is the Probe length, L₁ is the substrate holder height, L₂ is the depth from bottom of the cavity to base of the cooling stage, and R_{cav} is the cavity radius.	60
Figure 3-2: The overall microwave plasma-assisted CVD reactor system setup. All essential 5 components are depicted in the figure except the cooling for each of the 5 components. The cooling includes both the air and water cooling as which ever is fit. Symbol \otimes represents the mechanical gas valves are installed.....	61
Figure 3-3: Sketch of TM₀₁₃ electromagnetic resonant mode with the electric field intensity distribution along the cavity wall versus its height (upper right, [9]) and the E-field intensity distribution along cavity bottom versus its radius r (bottom, [20]). λ_g is the guide wavelength. Z-axis direction depicts the center axis and the cavity height direction.	67
Figure 3-4: Sketch of TM₀₁₃ electromagnetic resonant mode with the electric field intensity distribution along the cavity center axis versus its height (upper right) and the E-field intensity distribution along the cavity bottom versus its radius r (bottom).	68

Figure 3-5: This figure shows multiple of this wavelength of

Figure 3-6: The cross section of stainless steel metal parts are purpose of showing this reactor design cooling stage.

Figure 3-7: The equivalent

Figure 3-8: Original fused view of the cavity.

Figure 3-9: Modified fused view of the cavity.

Figure 3-10: The cooling

Figure 3-11: An example of the cooling stage flow.

Figure 3-12: Relative position of substrate.

Figure 3-13: Illustration of describes.

Figure 3-14: About 32 seconds

Figure 3-15: About 660 seconds

Figure 3-16: SEM photo showing thickness is maximum value from the tip of

Figure 3-17: With curved slight tilt wafer

Figure 3-18: Solartron line

Figure 3-19: Substrate and Solartron line

Figure 3-5: This figure shows an attached coax structure and its ideal height (can be multiple of this value) with resonant mode TEM ₀₀₁ [74]. λ_0 is the wavelength of this frequency (2.45 GHz) in the air.	72
Figure 3-6: The cross section view of the brass cavity with tuning Short, the stainless steel baseplate and molybdenum substrate holder. The non-metal parts are excluded from this figure (compare to Figure 3-1) for the purpose of showing the components of the actual microwave circuit of this reactor design (include the baseplate). D_{CS} is the diameter of the cooling stage. L_1 and L_2 can be calculated.....	74
Figure 3-7: The equivalent microwave circuit of Figure 3-6.	74
Figure 3-8: Original fused silica dome cooling design: a. Top view and b. side view of the cavity.	76
Figure 3-9: Modified fused silica dome cooling illustration: a. Top view and b. side view of the cavity.	76
Figure 3-10: The cooling stage structure.	78
Figure 3-11: An example of substrate, inserts and the main holder are stacking on the cooling stage. The fused silica tube is acting as a guide to the gas flow.	79
Figure 3-12: Relative position of the fused silica bell jar, the plasma ball and the substrate.	84
Figure 3-13: Illustration of the operational field/road map and parameters the map describes.	86
Figure 3-14: About 32 seeds within 345 μm \times 367 μm silicon surface.	91
Figure 3-15: About 660 seeds within 331 μm \times 269 μm silicon surface.	91
Figure 3-16: SEM photo shows how the diamond film sample (SZ-3inch-1mm-#06) thickness is measured at its cross section. Both local minimum and maximum values are taken to show measurements from the valley and from the tip of the diamond grain to the silicon surface.....	98
Figure 3-17: With curved tip of the point-stage and probe, the deviation due to slight tilt wafer is kept to minimal.....	100
Figure 3-18: Solartron linear encoder and measurement demo with the point-stages. ...	100
Figure 3-19: Substrate and diamond film thickness measurement positions using the Solartron linear encoder. Measured points are labeled in (a) the 2-inch	

substrate and (b)
side. Units are in

Figure 3-20: Comparison of
measurements u
sample diameter
deposition.....

Figure 3-21: Geometry of
direction n indi
plane of the cry

Figure 3-22: 2D illustration
{11}, {21} {31
"cubic" lattice

Figure 3-23: The location
diamond samp

Figure 3-24: The X-ray di
shape of the di
collection of th
negative camer

Figure 3-25: X-ray diffrac
as counts per s
diamond film s
started from 3

Figure 3-26: The spherical
(010). The ori
Textbook of N

Figure 3-27: The surface
Most crystal s
show part of t

Figure 3-28: All possible
{100} and {1
dots and lines

Figure 3-29: A grid of lin
attached to th
diamond grain

Figure 3-30: Logitech LP

substrate and (b) the 3-inch substrate, viewing from facing the polishing side. Units are in inches or specified.	102
Figure 3-20: Comparison of the results of SEM measurements and the measurements using Solartron linear encoder for the thickness across the sample diameter for sample 3-inch-1mm-#06 after 48 hours diamond deposition.....	104
Figure 3-21: Geometry of the Bragg “reflection” analogy and Bragg’s law. The direction n indicates the surface normal of the atomic plane or lattice plane of the crystal grating.	107
Figure 3-22: 2D illustration of the X-ray reflection (diffraction) planes (i.e. $\{10\}$, $\{11\}$, $\{21\}$ $\{31\}$, and $\{41\}$) and their corresponding d -spacing in a “cubic” lattice such as diamond lattice for example [88].....	108
Figure 3-23: The location of the Bragg's angle on camera film for single crystal diamond sample.	110
Figure 3-24: The X-ray diffraction pattern of a powder crystal sample. (a) The cone shape of the diffraction pattern. (b) A strip of camera film setup for collection of the X-ray pattern. (c) The powder X-ray pattern on a negative camera film [88].....	111
Figure 3-25: X-ray diffraction pattern with intensities of each reflection measured as counts per second during the rotation of the MPCVD polycrystalline diamond film sample (SZ-2inch-1mm-035) for the diffraction angle started from 30° to 150°	114
Figure 3-26: The spherical projection of a crystal of plane (100) , $(\bar{1}00)$, (010) , $(0\bar{1}0)$. The original full projection can be found from E. Dana, a Textbook of Mineralogy, 1932, Wiley or reference [99].	116
Figure 3-27: The surface morphology of diamond film sample SZ-2inch-1mm-035. Most crystal surface shows a square shape of facet with a few grains show part of the grain tips look like pyramids or wedges.	119
Figure 3-28: All possible shapes of cubic diamond crystallites. Two stable surfaces $\{100\}$ and $\{111\}$ that normally border diamond crystal are shaded with dots and lines respectively [106, 107].	120
Figure 3-29: A grid of lines are drawn over the photograph taken by the camera attached to the microscope, then the intercepts between the boundary of diamond grains and the line are counted along each line.	122
Figure 3-30: Logitech LP 50 lapping and polishing system.....	127

Figure 3-31: An example of percentage of the wavelength incr

Figure 3-32: A beam with moment $F \cdot L$ is a

Figure 3-33: Schematic dia

Figure 3-34: Schematic dia movement of the moment M

Figure 3-35: The correspond axes δ_1 and δ_2 uniaxial tensile

Figure 3-36: Schematic dia

Figure 3-37: Schematic dia movement of a moment M_r

Figure 3-38: Redraw of the composite beam at reference state external moment

Figure 3-39: Best-Fit function expansion coefficient temperature rate

Figure 3-40: How the differential (differential) coefficient.....

Figure 3-41: XRD spectra samples (SZ-2) the direction (consists of five (331). However no grain that the 45° angle

Figure 3-31: An example of optical transmission spectrum. It is expected that the percentage of the transmission is approaching to near 70% when wavelength increases beyond 800 nm up to 3 μm	129
Figure 3-32: A beam with length L showing the neutral axis - X when an external moment $F \cdot L$ is applied to the beam [145].....	134
Figure 3-33: Schematic diagram showing bending by an external moment M	134
Figure 3-34: Schematic diagrams of a three-step operation for illustrating the movement of the composite two beam neutral axes from an external moment M	135
Figure 3-35: The corresponding stress distributions and the shifting of the neutral axes δ_1 and δ_2 from the central axes of the beams by the applied uniaxial tensile and compressive stresses to the two beams [132].	138
Figure 3-36: Schematic diagram showing bending by an internal moment M_T	139
Figure 3-37: Schematic diagrams of a two-step operation for illustrating the movement of a composite two beam neutral axes from an internal moment M_T	140
Figure 3-38: Redraw of the schematic sketches of the analysis procedure for a composite beam subjected to a differential strain $\Delta\epsilon$: (1) beam geometry at reference state. (2) The final resultant beam configuration with no external moments applied [133].	142
Figure 3-39: Best-Fit functions to the curves in Figure 2-26 for linear thermal expansion coefficient of silicon (above) and diamond (below) for temperature range from 293 $^{\circ}\text{K}$ (or 20 $^{\circ}\text{C}$) to 1400 $^{\circ}\text{K}$ (or 1127 $^{\circ}\text{C}$).	149
Figure 3-40: How the difference of the area is calculated graphically (so is the strain differential) using the best-fit curves of the linear thermal expansion coefficient.	151
Figure 3-41: XRD spectrum from one of the lab grown freestanding diamond film samples (SZ-2inch-043) that shows highly oriented diamond crystals in the direction (111). Diamond is a typical cubic crystal material that consists of five possible lattice planes: (111), (220), (311), (400), and (331). However the (400) plane is missing in the XRD plot. That means no grain that oriented in [400] ($2\theta = 119.5^{\circ}$) direction was found within the 45° angle with the surface normal in this diamond film sample.....	156

Figure 4-1: Operation condition field map of the microwave plasma CVD system for a 3-inch diameter silicon wafer as the substrate. The feed gas composition used for this measurement is 400 sccm H ₂ and 4 sccm CH ₄ . ..	168
Figure 4-2: Operation condition field map of the microwave plasma CVD system for a 2-inch diameter silicon wafer as the substrate. The gases composition used for this measurement is 400 sccm hydrogen and 4 sccm methane.	168
Figure 4-3: Operation condition field map of the microwave plasma CVD system for a 3-inch diameter silicon wafer as the substrate. The gases composition used for this measurement is 400 sccm hydrogen, 200 sccm argon, and 4 sccm methane.....	170
Figure 4-4: Sample SZ-2inch-1mm-31 with thickness of 75 micron is laid on a piece of white paper. Silicon is back etched without any polishing. Label is written on a piece of paper underneath of the diamond film. High degree of transparency clearly can be seen from this sample. From this photograph and the Raman spectra of this sample on next page, high quality polycrystalline diamond film is uniformly deposited. The average growth rate by weight gain was 0.79 μm/h. The substrate temperature was 1083 °C at the beginning, then gradually decreased to 955 °C at the end.	172
Figure 4-5: The Raman spectra for a HPHT single crystal diamond and sample SZ-2inch-1mm-031. The spectra were recorded at four different spots where P1 is about 1 mm to the film edge and P4 is near the center of this 2-inch diameter film. Points P2 and P3 divide the line P1-P4 into three equal distance. (a) Whole view of scanned region. (b) Zoom-in view at the peak wavenumber.	173
Figure 4-6: Sample SZ-2inch-1mm-43 with thickness of 19 micron is laid on a piece of print paper. The transparency of the film is shown from the print underneath. The average growth rate by weight gain was 0.53 μm/h. The substrate temperature was 992 °C at the beginning, then gradually decreased to 954 °C at the end.	174
Figure 4-7: The Raman spectra of sample SZ-2inch-1mm-043 at points P1 through P4 in comparing with a HPHT Single Crystal Diamond (SCD). (a) Whole view. (b) Zoom-in view.	175
Figure 4-8: Sample SZ-2inch-1mm-45 with thickness of 75 micron is laid on a piece of print paper. The transparency of the film is shown from the print underneath. The average growth rate by weight gain was 1.57 μm/h. The substrate temperature was 971 °C at the beginning, then gradually decreased to 952 °C at the end.	176

Figure 4-9: The Raman
P4 in compar
(b) Zoom-

Figure 4-10: Sample S
micron is la
mentioned
weight gain
beginning, a
whiteness (c
the same lig
photographs
whiteness. H
contains 25°
estimating th

Figure 4-11: The Raman
P4 in compar
(b) Zoom-in v

Figure 4-12: Raman spec
peak at 1550
the same mea
crystal.....

Figure 4-13: Raman spec
peaks centerin

Figure 4-14: Sample SZ-
crystal diamon
above a printe
slide that hold

Figure 4-15: Optical tran
Perkin Elmer

Figure 4-16: A plot of th
included in T
parentheses, v
condition, if
that are attac
diamond pea
the average g
Please note t
marked with

Figure 4-9: The Raman spectra of sample SZ-2inch-1mm-045 at points P1 through P4 in comparing with a HPHT Single Crystal Diamond. (a) Whole view. (b) Zoom-in view.....	177
Figure 4-10: Sample SZ-2inch-1mm-53 (lower-right photo) with thickness of 125 micron is laid on a piece of print paper together with other previous mentioned samples (SZ31, SZ43 and SZ45). The average growth rate by weight gain was 2.60 $\mu\text{m}/\text{h}$. The substrate temperature was 977 $^{\circ}\text{C}$ at the beginning, and then was gradually increased to 1017 $^{\circ}\text{C}$ at the end. Their whiteness (or darkness) are significantly different and compared under the same lighting condition. The percentage gray scale below the photographs is a visual reference for the comparison of diamond whiteness. However since the white paper in the photo looks like it contains 25% gray, we should shift the scale down by 25% when estimating the diamond film quality in the photo.....	178
Figure 4-11: The Raman spectra of sample SZ-2inch-1mm-053 at points P1 through P4 in comparing with a HPHT single crystal diamond. (a) Whole view. (b) Zoom-in view.....	179
Figure 4-12: Raman spectrum for a low quality diamond sample. The sp^2 carbon peak at 1550 cm^{-1} is apparent. The FWHM value of the diamond film at the same measured point is about 11.0 cm^{-1} , much broader than single crystal.....	182
Figure 4-13: Raman spectra for the same four samples in Table 4-1. The graphite peaks centering around 1560 cm^{-1} are hardly seen for all samples.....	182
Figure 4-14: Sample SZ-25-3P (left) and a Sumitomo HPHT synthetic single seed crystal diamond (right, yellow) supported on a glass microscope slide above a printed white page. The vertical separation between the glass slide that holds the samples and the underlying page is 15 mm.....	183
Figure 4-15: Optical transmission spectra for different materials measured with Perkin Elmer Lambda 900.....	184
Figure 4-16: A plot of the growth rate versus reactor pressure for all samples included in Table 4-3. Growth rates are taken from the value in the parentheses, which are averaged from samples grown under the same condition, if there are more than one samples were grown. The numbers that are attached to the points are the average FWHM for Raman diamond peak of the sample and the other numbers in parentheses are the average grain size of that sample (same for the following figures). Please note the sample thickness uniformity is very low for the data marked with asterisk.....	190

Figure 4-17: The diamond
diameter. The
thickness was
1mm-#65A. E

Figure 4-18: A plot of the
samples inclu
achievable un

Figure 4-19: Variation of
the feed gas a
at 400 sccm. T

Figure 4-20: Photographs
versus the met
Torr. The met
6 and 8 sccm.

Figure 4-21: The accepta
good optical q
maximum ach
required grow

Figure 4-22: The accepta
for which goo
rate vs. the CH

Figure 4-23: Diamond fil
temperature a
by Solartron I

Figure 4-24: Diamond fil
temperature a

Figure 4-25: Diamond fil
temperature a

Figure 4-26: Diamond fil
temperature.

Figure 4-27: The argon
at different re
Si substrate
temperatures
in Table 4-5.

Figure 4-17: The diamond film thickness (in mm) distribution across the film diameter. The number 1-11 and 12-21 indicates the location where the thickness was measured as introduced in Figure 3-19. Above: SZ-2inch-1mm-#65A. Below: SZ-2inch-1mm-#42.	191
Figure 4-18: A plot of the maximum growth rates versus reactor pressure for samples included in Table 4-4. This plot trend indicates the growth rate achievable under different reactor pressure and methane flow conditions. ..	194
Figure 4-19: Variation of the growth rate with change in methane concentration in the feed gas at different reactor pressures. The hydrogen flow was fixed at 400 sccm. The growth rates were taken from Table 4-4.	195
Figure 4-20: Photographs selected to show diamond film optical quality changes versus the methane concentration in the input gases for at pressure 140 Torr. The methane concentrations for samples #37, #45 and #62 were 4, 6 and 8 sccm, respectively.	195
Figure 4-21: The acceptable quality line on the plot separates the region that the good optical quality diamond grows. This line roughly defines the maximum achievable growth rate for the acceptable film quality with the required growth conditions.	197
Figure 4-22: The acceptable quality line that indicates the growth condition region for which good optical quality diamond can grow on the plot of growth rate vs. the CH ₄ concentration.	198
Figure 4-23: Diamond film linear growth rate relation with respect to the substrate temperature at the reactor pressure of 140 Torr. Thickness is measured by Solartron Linear Encoder (L. E.).	201
Figure 4-24: Diamond film linear growth rate relation with respect to the substrate temperature at the reactor pressure of 160 Torr.	201
Figure 4-25: Diamond film linear growth rate relation with respect to the substrate temperature at the reactor pressure of 180 Torr.	202
Figure 4-26: Diamond film linear growth rate relation with respect to the substrate temperature.	202
Figure 4-27: The argon gas influence on the linear growth rate of the diamond film at different reactor pressure. All diamond films are deposited on 2 inch Si substrate with 1% (or 4 sccm) CH ₄ over 400 sccm H ₂ . Substrate temperatures range are also shown in the plot. Other data can be found in Table 4-5.	206

Figure 4-28: The argon
at different
growth rates

Figure 4-29: The argon
at different
shown in T

Figure 4-30: Samples
4.7.1 are la
scale and tr
4-5. Please
transparenc

Figure 4-31: The Rama
etching of s
single cryst

Figure 4-32: The Rama
etching of s
single cryst

Figure 4-33: Diamond
secondary n
often called

Figure 4-34: Sample SZ
crystal surfac
pressure 140
sccm argon. 7
°C at the cent

Figure 4-35: Sample SZ-
condition exc
than sample S
concentration

Figure 4-36: Sample SZ-
addition in th
Other growth

Figure 5-1: An example
edge of the st
of minimum
holder set is
2.445 inch ar

Figure 4-28: The argon gas influence on the linear growth rate of the diamond film at different reactor pressure. The film thickness used to calculate the growth rate is taken at the diamond film center using the linear encoder.	206
Figure 4-29: The argon gas influence on the diamond crystal grain size of the film at different reactor pressure. Data are from the same set of experiments shown in Table 4-5.	207
Figure 4-30: Samples that were used for growth rate study in last section, section 4.7.1 are laid on a piece of print paper for visual inspection of their grey scale and transparency quality. The growth conditions are listed in Table 4-5. Please note that thicker films may look darker with the same transparency.	209
Figure 4-31: The Raman spectra of sample SZ-2inch-1mm-056 before the back etching of silicon at points P1 through P4 in comparing with a HPHT single crystal diamond (SCD). (a) Whole view. (b) Zoom-in view.	210
Figure 4-32: The Raman spectra of sample SZ-2inch-1mm-059 before the back etching of silicon at points P1 through P4 in comparing with a HPHT single crystal diamond (SCD). (a) Whole view. (b) Zoom-in view.	211
Figure 4-33: Diamond film with high concentration addition of argon causes the secondary nucleation of diamond grains on larger grain surface, which is often called as the twinning effect during the growth.	214
Figure 4-34: Sample SZ-2inch-053 showing typical step bunching on diamond crystal surfaces (upper right inset). The growth conditions list at pressure 140 Torr, 400 sccm hydrogen, 4 sccm CH ₄ with addition of 100 sccm argon. The substrate temperature is measured between 990 to 1015 °C at the center of the substrate.	215
Figure 4-35: Sample SZ-2inch-053 is darker than films grown under the same condition except without argon (SZ-031 and SZ-043). It is even darker than sample SZ-045, which is grown under higher CH ₄ (6 sccm) concentration. The substrate temperature is controlled at the same level.	215
Figure 4-36: Sample SZ-2inch-1mm-056 was deposited with 100 sccm argon addition in the feed gas at average substrate temperature below 900 °C. Other growth condition can be found in Table 4-5.	216
Figure 5-1: An example of plot of the temperature variations for both center and the edge of the substrate when the sliding short is shifted from the position of minimum reflected power. The shim thickness with this particular holder set is at 0.315 inch and the correlated $L_1 = 2.4946$ inch and $L_2 = 2.445$ inch are shown earlier in Figure 3-1.	222

Figure 5-2: Result of the difference between the two surfaces smaller as L_1

Figure 5-3: Insert type 1. Contact with the surface. Bottom view.

Figure 5-4: Insert type 2. Contact with the edge of the surface.

Figure 5-5: Insert type 3. Groove width. Section view.

Figure 5-6: Insert type 4. Above: cross-section.

Figure 5-7: A photograph of a patterned insert at the edge.

Figure 5-8: A photograph of a patterned insert. The surface is cooler than the plasma condition. Absorbed micro-radiation.

Figure 5-9: This figure shows the shape of the cavity and the measured temperature at the places where the temperature is measured.

Figure 5-10: Microscopy of a diamond film. The distribution of the diamond film is shown in Figure 5-10.

Figure 5-11: Calculated distribution of the diamond film to P7 using the sample SZ-2. The calculated standard deviation is 1mm-058B.

Figure 5-2: Result of the substrate temperature optimization. The temperature difference between the center and the edge of the substrate is getting smaller as $L_1 - L_2$ increases.	223
Figure 5-3: Insert type 1, a relatively small area at the center of the insert is in contact with the holder below. Above: cross-section view. Bottom: bottom view.	225
Figure 5-4: Insert type 2, a relatively large contact area is tapered from the center to the edge of the insert. Above: cross-section view. Bottom: bottom view.	226
Figure 5-5: Insert type 3, a groove pattern is cut in the bottom of the insert. The groove width is cut bigger towards the edge of the insert. Above: cross-section view. Bottom: bottom view.	227
Figure 5-6: Insert type 4, a single large groove pattern is cut at the top of the insert. Above: cross-section view. Bottom: top view.	228
Figure 5-7: A photograph of the heated substrate without using any groove-patterned inserts. Usually the center of the substrate is hotter than the edge.	229
Figure 5-8: A photograph of the heated substrate with using type-4 groove-patterned inserts shown in Figure 5-6. The center of the substrate looks cooler than the edge. The holder set condition (L_1 and L_2) and the plasma condition such as reactor pressure, gas composition and the absorbed microwave power are the same as used in Figure 5-7.	229
Figure 5-9: This figure shows how the silicon wafer is aligned with the orientation of the cavity and how and where the temperature on the wafer is measured. The underlined number from point-1 to point-11 are the places where thickness are measured and point P1 to point P7 are the temperature measurement locations.	232
Figure 5-10: Microscopy photographs taken at seven selected points across the diamond film from, (a) sample SZ-2inch-1mm-058B and (b) sample SZ-2inch-1mm-059B, for the study of grains sizes and their size distribution. The seven points P1 to P7 are the same seven points as shown in Figure 5-9.	234
Figure 5-11: Calculated diamond grains sizes at the selected seven points from P1 to P7 using the method of the intercept and their size distributions of, (a) sample SZ-2inch-1mm-058B and (b) sample SZ-2inch-1mm-059B. The calculated standard deviation of the grains sizes for sample SZ-2inch-1mm-058B is 2.14 μm and for sample SZ-2inch-1mm-059B is 1.25 μm	235

Figure 5-12: The uniform thickness of as stands for its s measured by i

Figure 5-13: The relation percentage de higher the ave

Figure 5-14: Diamond fil SZ-3inch-1mr

Figure 5-15: Diamond fil sample SZ-3ir

Figure 5-16: Diamond fil SZ-2inch-1mr

Figure 5-17: Diamond fil sample SZ-2ir

Figure 5-18: (a) Microsc diamond film sizes at points standard dev

Figure 5-19: Diamond fil SZ-2inch-1mr

Figure 5-20: Diamond fil sample SZ-2ir

Figure 5-21: (a) Microsc diamond film sizes at points standard dev

Figure 5-22: Diamond fil SZ-2inch-1mr

Figure 5-23: Diamond fil sample SZ-2ir

Figure 5-24: (a) Microsc diamond film sizes at points standard dev

Figure 5-12: The uniformity relation between substrate temperature and film thickness of as grown diamond. The substrate temperature STD DEV stands for its standard deviation and the thickness non-uniformity is measured by its percentage deviation as defined in Eq. 3-12.....	237
Figure 5-13: The relation between the average linear growth rate and the thickness percentage deviation. The more uniform the diamond film deposited, the higher the average growth rate.	238
Figure 5-14: Diamond film thickness radial distribution and uniformity for sample SZ-3inch-1mm-22D.....	242
Figure 5-15: Diamond film thickness circumferential distribution and uniformity for sample SZ-3inch-1mm-22D.	242
Figure 5-16: Diamond film thickness radial distribution and uniformity for sample SZ-2inch-1mm-053.	244
Figure 5-17: Diamond film thickness circumferential distribution and uniformity for sample SZ-2inch-1mm-053.	245
Figure 5-18: (a) Microscopy photographs from taken at points P1 to P7 across the diamond film of SZ-2inch-1mm-053. (b) Calculated diamond grains sizes at points from P1 to P7 and their size distributions. The calculated standard deviation of the grains sizes is 2.60 μm	246
Figure 5-19: Diamond film thickness radial distribution and uniformity for sample SZ-2inch-1mm-058A.....	248
Figure 5-20: Diamond film thickness circumferential distribution and uniformity for sample SZ-2inch-1mm-058A.	249
Figure 5-21: (a) Microscopy photographs from taken at points P1 to P7 across the diamond film of SZ-2inch-1mm-058A. (b) Calculated diamond grains sizes at points from P1 to P7 and their size distributions. The calculated standard deviation of the grains sizes is 0.50 μm	250
Figure 5-22: Diamond film thickness radial distribution and uniformity for sample SZ-2inch-1mm-045.	252
Figure 5-23: Diamond film thickness circumferential distribution and uniformity for sample SZ-2inch-1mm-045.	253
Figure 5-24: (a) Microscopy photographs from taken at points P1 to P7 across the diamond film of SZ-2inch-1mm-045. (b) Calculated diamond grains sizes at points from P1 to P7 and their size distributions. The calculated standard deviation of the grains sizes is 1.57 μm	254

Figure 6-1: Illustration of
top surface) c
note the diam

Figure 6-2: A simple plot
data points and

Figure 6-3: The Matlab
the partial be

Figure 6-4: The relation
are included in

Figure 6-5: The relation
data from Tab
classified as o

Figure 6-6: The X-ray di
Imm-36. The
the figure.....

Figure 6-7: The X-ray di
Imm-37. The
the figure.....

Figure 6-8: The X-ray di
Imm-43. The
the figure.....

Figure 6-1: Illustration of measuring the distance from the back side surface (the top surface) of the silicon wafer to the top surface of the base. Please note the diamond film is on the bottom side of the measured piece.	261
Figure 6-2: A simple plot to show geometrical relationship between the curvature data points and the distance from the center of the silicon wafer.....	263
Figure 6-3: The Matlab plot of the data points (small circles represented dots) and the partial best geometric fit circle (the line).....	265
Figure 6-4: The relation of intrinsic stress versus the substrate temperature. All data are included in this plot from Table 6-2.	270
Figure 6-5: The relation of intrinsic stress vs. the substrate temperature. Reference data from Table 6-2 under the same experimental condition are classified as one plot.....	271
Figure 6-6: The X-ray diffraction spectrum of diamond film sample SZ-2inch-1mm-36. The intensities of each type diffraction plane are indicated in the figure.....	275
Figure 6-7: The X-ray diffraction spectrum of diamond film sample SZ-2inch-1mm-37. The intensities of each type diffraction plane are indicated in the figure.....	276
Figure 6-8: The X-ray diffraction spectrum of diamond film sample SZ-2inch-1mm-43. The intensities of each type diffraction plane are indicated in the figure.....	276

Chapter 1 Introduction

1.1 Motivation

It has become a common method for depositing (CVD) freestanding films. Low methane concentrations, is used to grow films at pressures less than 100 Torr. The growth rate is typically less than 1 μm per hour. As indicated in Figure 1.1, the growth rate is affected by many interrelated parameters, such as the power density absorbed by the substrate. The increase of methane concentration allows the growth rate of the film to be higher. The quality is lower when the growth rate is higher. The growth of sp² or amorphous carbon has been noticed and it is a common method for growing films. Higher pressure, which is a common method for providing high-quality films. This dissertation discusses the growth of polycrystalline CVD freestanding films.

Chapter 1 Introduction

1.1 Motivation

It has become a common belief that high quality polycrystalline chemical vapor deposition (CVD) freestanding diamond films can be synthesized only at low growth rates. Low methane concentration, which is usually 1% or less of the hydrogen concentration, is used to grow high quality diamond film at the deposition pressures of less than 100 Torr. The growth rate in terms of the thickness gain per hour is less than 1 μm per hour. As indicated by many researchers, the diamond growth rate and quality are affected by many interrelated parameters such as the pressure, substrate temperature, power density absorbed by reactant gases, and finally composition of the reactant gases. The increase of methane concentration in hydrogen during the CVD processing generally allows the growth rate of diamond at higher rates. However, the film turns dark and the quality is lower when the methane concentration is higher due to impurities of graphite, sp^2 or amorphous carbon. The high cost and the low productivity of the low growth rates have been noticed and it does not satisfy the need for some cost-sensitive applications. Higher pressure, which is defined from 100 Torr up to 180 Torr, is considered in this study for providing higher diamond growth rates, as well as, better quality of the as grown films. This dissertation investigates the idea of high quality and high growth rate polycrystalline CVD freestanding diamond film deposition.

This investigation
discs that are uniform. h
most basic level refers to
diamond film also impli
uniform diamond grain s
the intended application o
measurements of the film
diamond films and discs
transparency of the diam
small grains of diamonds
diamond will be used to
windows require the dia
lapping is greatly simpli
control of the intrinsic s
the diamond film is ano
to improve the diamon
deposition rate.

Successful der
economical (at higher
intrinsic stress (good fla
wide array of applicati
wave and microwave w
microscopy. To achie

This investigation looks to simultaneously achieve optical films and plates or discs that are uniform, high quality, flat, and grown at a high rate. The uniformity at the most basic level refers to the thickness of a film, discs or plates. The uniformity of the diamond film also implies uniform quality across the film area, which also indicates that uniform diamond grain size and film texture is desired across the film area. Depending on the intended application of the diamond, this study includes a number of different measurements of the film uniformity. There are many ways to describe the quality of the diamond films and discs or plates. The optical quality usually means the clarity or the transparency of the diamond, as well as the nature of the boundaries between the many small grains of diamonds. The optical properties and Raman spectrum of the deposited diamond will be used to quantify the diamond quality. Applications of diamond for windows require the diamond to be lapped and polished into flat plates or discs. The lapping is greatly simplified when the grown diamond is reasonable flat, which requires control of the intrinsic stress of the deposited diamond. Therefore, the intrinsic stress of the diamond film is another primary investigation of this study. This research is intended to improve the diamond film uniformity, flatness and quality, as well as, increase the deposition rate.

Successful demonstration of polycrystalline diamond deposition that is more economical (at higher growth rate) with good uniformity, high quality, and controlled intrinsic stress (good flatness) will allow the production of diamond plates and discs for a wider array of applications including high power laser windows, high power millimeter wave and microwave windows, and wide transparency diagnostic windows for spectroscopy. To achieve the goals for the deposition of polycrystalline diamond for

these applications the ap
deposition reactor, (2) de
deposition process, (3) ic
quality, film intrinsic str
(4) identification of proc
(growth rate) to be increa
accomplish the goals a n
section.

12 Research objectives

The goal of this r
films at high deposition r
achieve this goal, several
understand the relationsh
deposited by means of m
deposition (MPCVD). T
synthesizes high quality
up to 2 - 3 inches in dia
mechanism of controlli
films.

13 My contribution

In the course of
understanding and techn

these applications the approach to be pursued includes: (1) modification of the diamond deposition reactor, (2) development of an experimental methodology to optimize the deposition process, (3) identification of the relationships between growth rate, diamond quality, film intrinsic stress, and film uniformity versus reactor operation conditions, and (4) identification of process and reactor improvements that allow the deposition pressure (growth rate) to be increased while maintaining uniformity, quality and flatness. To accomplish the goals a number of research objectives are identified and listed in the next section.

1.2 Research objectives

The goal of this research is to synthesize optical quality polycrystalline diamond films at high deposition rates over 2-inch and 3-inch diameter silicon substrate areas. To achieve this goal, several objectives have been identified. The first objective is to understand the relationship of the growth rate versus the diamond quality for films deposited by means of microwave plasma enhanced (or assisted) chemical vapor deposition (MPCVD). The second objective is to develop a reactor design/operation that synthesizes high quality fast growing polycrystalline diamond film uniformly over areas up to 2 – 3 inches in diameter. The third objective is to understand and develop a suitable mechanism of controlling the intrinsic stress in the as grown polycrystalline diamond films.

1.3 My contributions

In the course of this investigation several specific contributions were made to the understanding and technology for deposition of polycrystalline diamond discs and plates.

This investigation looked

maintaining uniformity a

CVD diamond films depo

1. Defining an o

deposition pro

2. Developing a

uniform subst

3. Modifying the

silica bell jar

substrate tem

4. Showing the

pressure inclu

5. Extending ea

intrinsic stres

internal stres

treating the s

the earlier str

6. Determining

diamond fil

14 Preview of chapt

Chapter 2 prese

chemical formation pro

research studies. It cov

This investigation looked at extending the deposition pressure up to 180 Torr while maintaining uniformity and other requirements. My contributions to the polycrystalline CVD diamond films deposition subject area include:

1. Defining an optimum region of diamond growth that gives high quality versus deposition pressure and methane flow in the feed gas.
2. Developing a procedure for characterizing the reactor operation for achieving uniform substrate temperature.
3. Modifying the reactor design to achieve more uniform cooling of the fused silica bell jar and modified the substrate design to achieve more uniform substrate temperature.
4. Showing the impact of the argon addition on diamond film deposition at high pressure including on the deposition uniformity and growth rate.
5. Extending earlier mechanical stress models to understand the diamond film intrinsic stress. This extended stress model distinguishes the difference of internal stress from the external stress of Stoney's original model based on treating the substrate/film as two welded rigid beams or plates. Extension of the earlier stress models are made to suit the stress calculations in this work.
6. Determining an intrinsic stress level that can be used to predict when the diamond film/substrate breaks during the chemical back etching.

1.4 Preview of chapters

Chapter 2 presents a review of high-pressure CVD diamond from its physical and chemical formation process, as well as the most recent key results from higher pressure research studies. It covers the main reasons for high pressure deposition conditions of this

study. This chapter also

factors such as the impu

introduces the MPCVD

for high-pressure operati

processes are operated, n

are done for (1) operation

(2) substrate temperature

film quality analysis. Ch

changes versus the react

This chapter also describ

growth rate. Raman spec

quality analysis. Chapter

special substrate holders

with respect to the temp

gas addition. Chapter

Besides controlling o

by varying the metha

findings and propose

study. This chapter also describes how diamond film quality is affected by a number of factors such as the impurities, defects, grain sizes, and the intrinsic stresses. Chapter 3 introduces the MPCVD system used for this study and the modifications of this system for high-pressure operation. This chapter also gives the general methodology of how processes are operated, measurements are taken, calculations are carried out, and analyses are done for (1) operation of the MPCVD system, (2) diamond film growth preparation, (3) substrate temperature and thickness measurement, (4) film stress calculation, and (5) film quality analysis. Chapter 4 describes the diamond film growth rate and quality changes versus the reactor pressure, methane concentration, and substrate temperature. This chapter also describes how argon gas addition affects the diamond film quality and growth rate. Raman spectroscopy and optical transmission are used for the diamond film quality analysis. Chapter 5 discusses the control of the substrate temperature by designing special substrate holders. The diamond film thickness uniformity results are presented with respect to the temperature uniformity. This chapter also discusses the effect of argon gas addition. Chapter 6 presents a few techniques for reducing the diamond film stresses. Besides controlling of the substrate temperature, the intrinsic stresses can also be reduced by varying the methane concentration over time. Chapter 7 summarizes the major findings and proposes suggestions for further work.

Chapter 2 Review Films

Diamond grows in
element and the rigid and
and physical conditions for
deposition studies were
advantage is the ease to
pressures and input power
eliminates the necessity
the low-pressure (<100
over 1 μm per hour. Some
greater) and high temper
plasma-assisted CVD di
diamond deposition pro
growth rate and diamon
pressure CVD diamond
discharge properties for
conditions. The low pre
similarities and the diff

Chapter 2 Review of High-Pressure Deposition of CVD Diamond Films

Diamond grows in a specific physical and chemical environment. The carbon element and the rigid and specific sp^3 hybrid bonding structure require certain chemical and physical conditions for the growth of diamond. Many current and previous diamond deposition studies were carried out at low pressures, i.e. 100 Torr or less. The obvious advantage is the ease to maintain relatively large and uniform plasmas with lower pressures and input powers. The lower flux to the substrate at the lower pressures eliminates the necessity of designing for substrate cooling. However, it has been shown that low-pressure (<100 Torr) diamond growth results in low growth rates that are seldom over 1 μm per hour. Some studies have indicated that higher pressures (100 Torr or greater) and high temperatures can be used to increase the growth rate significantly in plasma-assisted CVD diamond deposition. This chapter first reviews the basics of the diamond deposition process in order to understand the relationship of deposition pressure, growth rate and diamond quality. This chapter will then cover the background of high pressure CVD diamond synthesis. More specifically this chapter first reviews the plasma discharge properties for plasma-assisted CVD (PACVD) diamond at high pressure conditions. The low pressure condition will also be detailed in order to describe the similarities and the differences between films grown at different pressure conditions. The

second aspect is to review
diamond deposition and
high pressure. The third
films, mostly the intrinsic
in general the important

2.1 The simplified process

The synthesis of
physical process that con
illustrated in Figure 2-1
process, assume only two
typical and minimum gas
which also will be the co
process gasses first are r
the substrate surface. Th
the gases are activated b
reactive atoms, ions and
sources such as hot filar
of the gaseous species a
These reactive fragmen
chemical reactions occu
At this point the specie
the gas phase, or diffus
removed from the surface

second aspect is to review the traditional mechanism of polycrystalline plasma CVD diamond deposition and some past works that have been done both at low pressure and high pressure. The third aspect intends to study the properties of polycrystalline diamond films, mostly the intrinsic stress in deposited diamond films. The last section summarizes in general the important parameters of diamond deposition at high pressure.

2.1 The simplified physical and chemical process of diamond formation

The synthesis of CVD polycrystalline diamond films is a complex chemical and physical process that comprises several different but interrelated features, as illustrated in Figure 2-1. To simplify the complexity of the physical and chemical process, assume only two reactant gases, hydrogen and methane participate. This is a typical and minimum gas composition required for a CVD diamond deposition process, which also will be the composition used in most of studies in this investigation. The process gasses first are mixed before flowing to the reaction chamber and diffused toward the substrate surface. The reaction chamber is located inside a microwave reactor where the gases are activated by the microwave energy and the gaseous molecules fragment into reactive atoms, ions and radicals. The microwave power can be replaced by other energy sources such as hot filament, RF and DC discharge, or laser ablation. At the same time all of the gaseous species are heated up to a few thousand degrees Kelvin of temperature. These reactive fragments continue to mix after the activation region. A complex set of chemical reactions occurs among these fragments until they strike the substrate surface. At this point the species either adsorb and react with the surface, desorb again back into the gas phase, or diffuse around close to the surface until an appropriate reaction site is opened from the surface. One possible process is when the carbon carrying species,

mostly considered to be

reliable, diamond gr

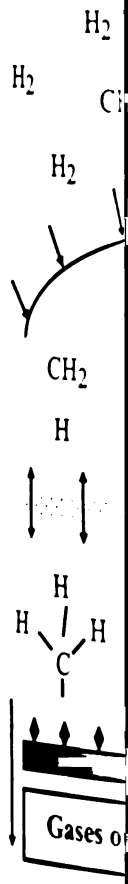


Figure 2-1: Schematic of diamond growth

2.2 Simplified diamond

A relatively common model for diamond growth is accepted by many researchers. The species involved in

mostly considered to be CH_3 radical, have reactions with the surface. If all the conditions are suitable, diamond grows.

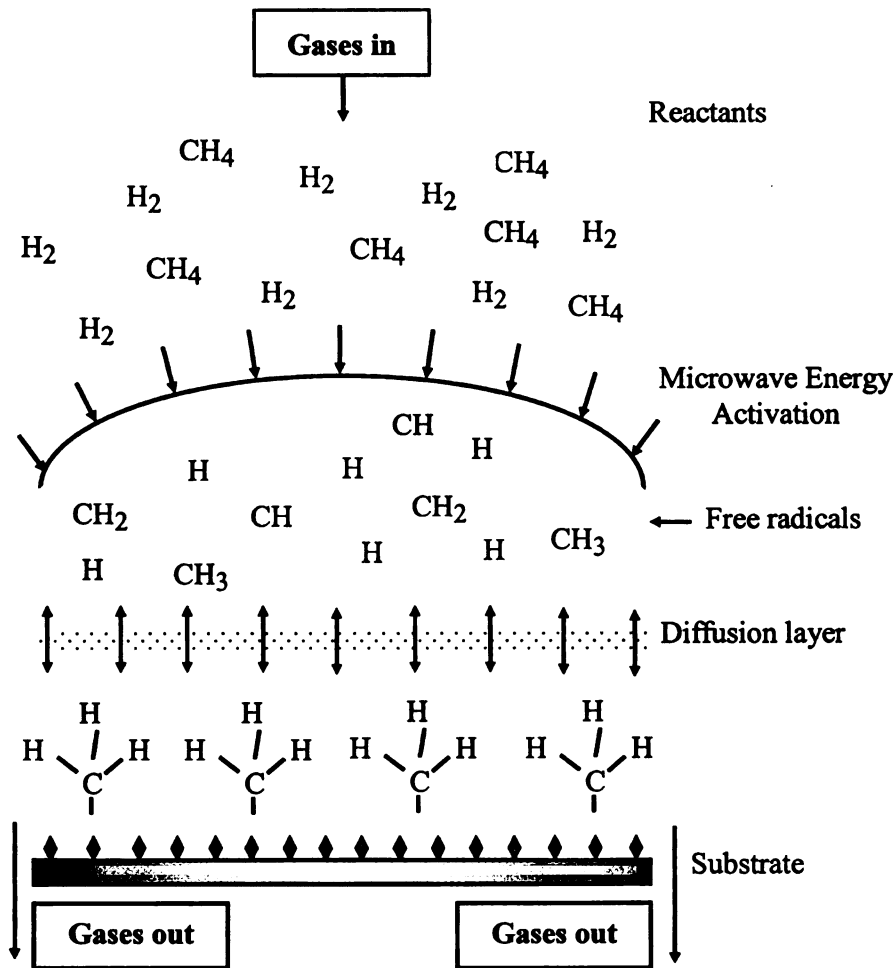


Figure 2-1: Schematic diagram of the physical and chemical processes during diamond CVD.

2.2 Simplified diamond growth mechanism and surface chemistry

A relatively common view of the deposition process for CVD diamond has been accepted by many researchers over the past couple decades. The first question is what are the species involved in diamond growth among the fragments, C , C_2 , CH , C_2H , CH_3 ,

C_2H_2 , CH_3^+ , and diamon

researchers grow CVD d

contains very few ions. T

diamond growth. Among

indicated the irreplaceab

diamond formation.

Diamond grows

condition is that the dia

predominately H_2 plas

placed in hydrogen and

tends can be terminated

polyvalent species depe

replaced by monovalen

environment and becom

hydrogen atoms and hy

leaving behind a reacti

chemistry equation is st

surface site reacts with

situation. However, occ

surface site, eventually

chemical process is illu

ception.

C_2H_2 , CH_3^+ , and diamondoids, such as adamantane. First, one of the facts is that many researchers grow CVD diamond in hot-filament CVD reactors in which the system contains very few ions. This suggests that neutrals are the primary participate reactants in diamond growth. Among the possible neutrals, a number of studies [1, 2, 3, 4, 5, 6] have indicated the irreplaceable importance of the CH_3 species in the growth chemistry of the diamond formation.

Diamond grows best on diamond surfaces or diamond seeded surfaces. The initial condition is that the diamond surface is nearly fully saturated with hydrogen in the predominately H_2 plasma. This statement may not be quite true before the surface is placed in hydrogen and methane, the diamond growth environment. The surface-dangling bonds can be terminated by other monovalent atoms such as nitrogen, or oxygen even polyvalent species depending on the preconditions. However these species will be readily replaced by monovalent hydrogen atoms in the hydrogen and low concentration methane environment and become ideally “fully” saturated with hydrogen. The next step is hydrogen atoms and hydrocarbon species in the discharge abstract a surface H to form H_2 leaving behind a reactive surface site. This is illustrated in Figure 2-2 and the typical chemistry equation is stated in the caption. After the H atom is abstracted, most likely this surface site reacts with another nearby H atom and returns the surface to its previous stable situation. However, occasionally a gas phase CH_3 radical can collide and react with the surface site, eventually adding a carbon to the lattice. This part of the physical and chemical process is illustrated in Figure 2-3 and the chemical reaction is stated in its caption.

Once again the C
the surface due to the th
one of the H atoms from
molecule and the two op
bond locking them into t
24 with the chemical eq
abstraction and methyl
methyl, the CH₃ fragme
surface and form a port
complete.

23 Growth zone and

There have been
since 1991 aimed at
was obtained from
based upon over 70
process gases. Bac
diamond would on
the line. The C-H-O
based on more experi
diamond growth doesn

Once again the CH_3 radical that has reacted with the surface can break apart from the surface due to the thermal desorption leading to an open site on the surface again. Or one of the H atoms from CH_3 abstracts a H-atom from a nearby CH_3 forming a hydrogen molecule and the two open sites left behind from both CH_3 bind together and form C-C bond locking them into the diamond lattice structure. This process is illustrated in Figure 2-4 with the chemical equation shown in the caption. As we know the process of H abstraction and methyl addition may occur any time on any open site. Any attached methyl, the CH_3 fragment, may interact with another adjacent CH_3 fragment on the surface and form a portion of the diamond lattice until the full diamond lattice structure is complete.

2.3 Growth zone and Bachmann C-H-O phase diagram

There have been many studies of the gas phase chemistry in the last 15 years since 1991 aimed at obtaining a clear picture of the principles involved. The first clue was obtained from the “Bachmann diagram” [7], which is a C-H-O composition diagram based upon over 70 deposition experiments in different reactors and using different process gases. Bachmann found that independent of the deposition system or gas mixture, diamond would only grow when the gas composition was close to and just above the CO tie line. The C-H-O diagram was updated in 1994 (Figure 2-5) by Bachmann’s group based on more experiments [8]. One of the findings that enhanced this diagram was that diamond growth doesn’t necessarily need the participation of oxygen.

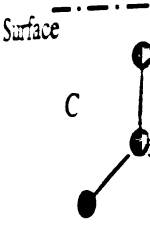


Figure 2-2: Illustration of a carbon atom in diamond. The carbon atom appears to be bonded to two other carbon atoms, one of which is labeled "C". A dashed line above the atom is labeled "Surface".

S

Figure 2-3: Illustration of a surface.

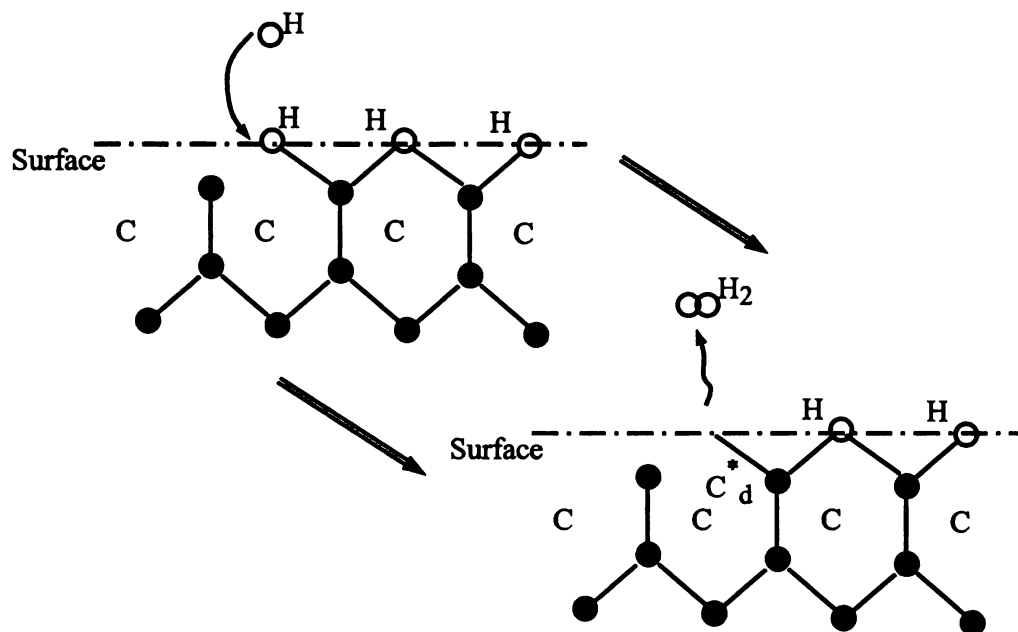


Figure 2-2: Illustrated chemical reaction: $C_dH + H \rightarrow C_d^* + H_2$. C_d denotes the carbon atom on diamond surface and the symbol asterisk indicates that atom is reactive. This figure is viewed as a 2D plane view, so atoms in the diamond structure and the CH_3 species are not in the same plane as they appear in the figure. This same statement holds for the following figures.

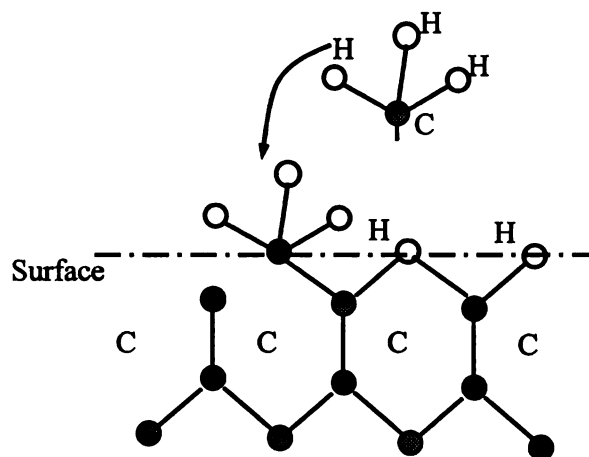


Figure 2-3: Illustrated chemical reaction: $C_d^* + CH_3 \rightarrow C_dCH_3$.

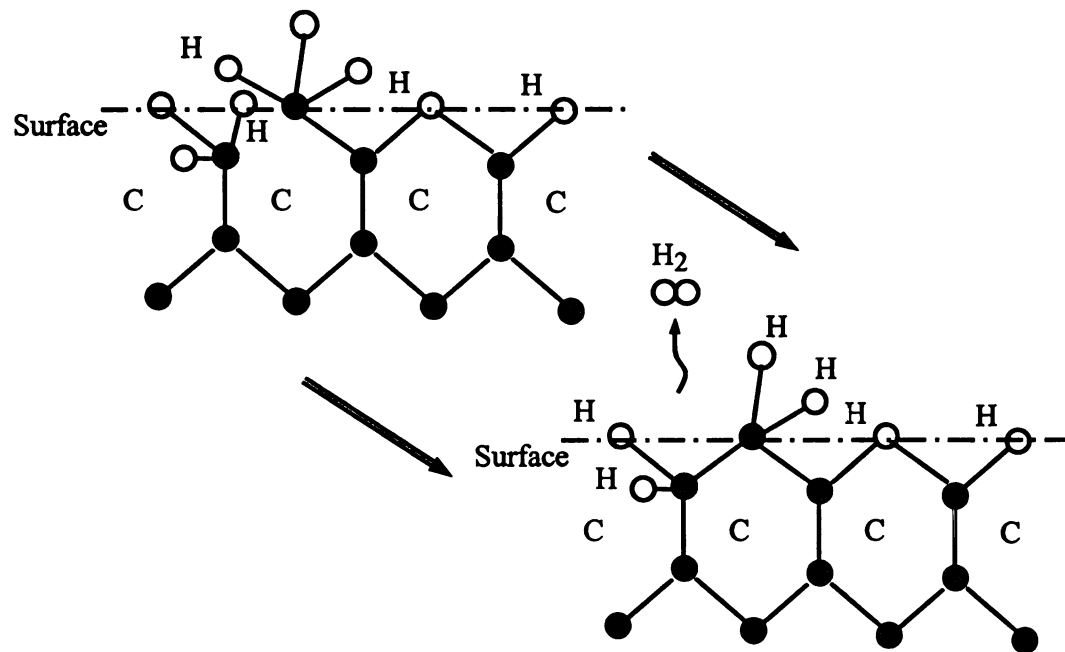


Figure 2-4: Illustrated chemical reaction: $C_dCH_3 + H \rightarrow C_dCH_2 + H_2$.

Diamond
Growth
Region



Figure 2-5: Bach
diam

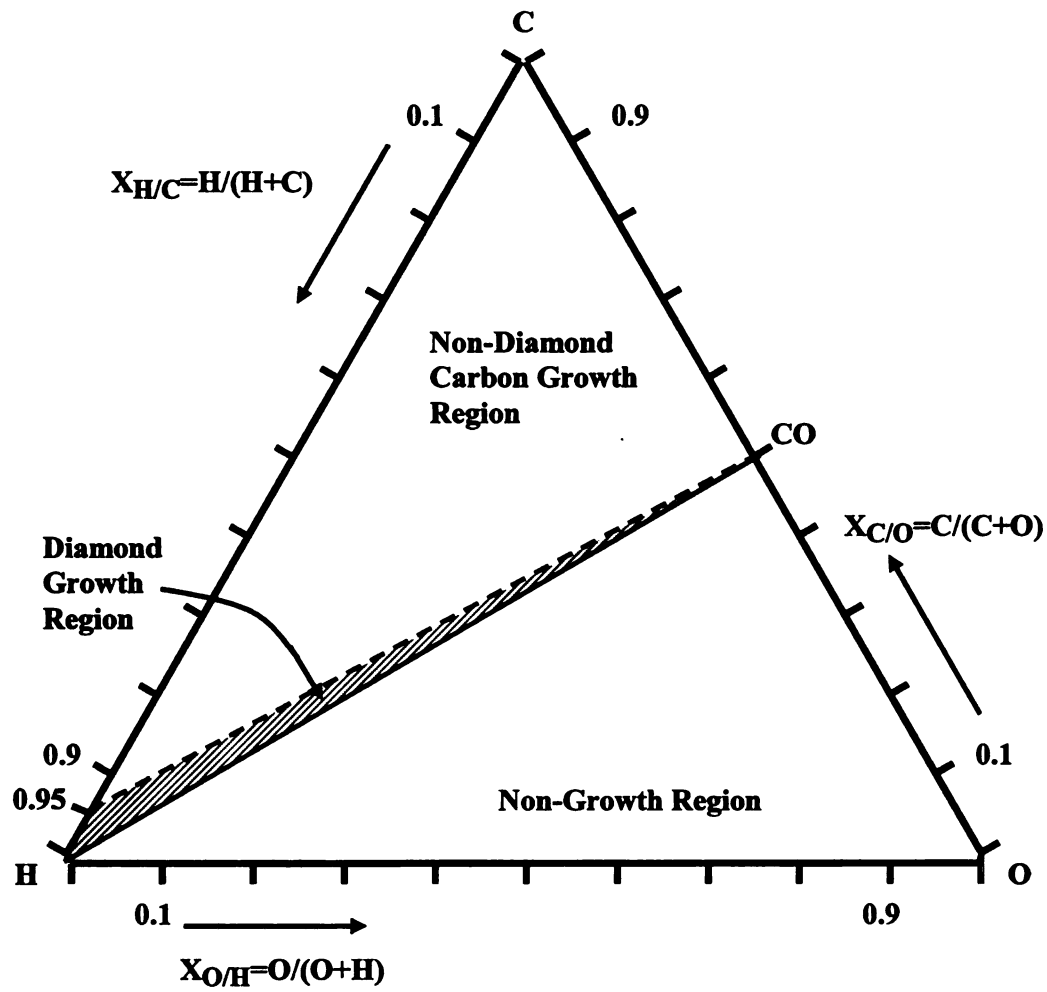


Figure 2-5: Bachmann C-H-O diagram (updated version: 1994) indicates where the diamond growth zone located [7, 8].

24 Plasma

There

plasma is a co

affected by ex

density and tem

include species

temperature and

gas mixture of h

24.1 Neutral distributi

Past studi

discharge using a

summarized. Figu

including CH₄, C

methane in the fee

was used in the fee

under all condition

source gas becomes

The results i

spectrometer. The m

cm. and the methy

2.4 Plasma properties versus pressure in CVD diamond deposition

There are many ways to measure and determine the properties of plasmas. A plasma is a collection of free charged particles moving in random directions as well as affected by external fields. Several general quantities like pressure, microwave power density and temperature are used to characterize plasmas. More specific quantities include species density, mean velocity, energy density, neutral gas temperature, electron temperature and densities. Typical plasma conditions for diamond deposition include a gas mixture of hydrogen with less than 3 % of methane.

2.4.1 Neutral species concentrations and atomic hydrogen density and their spatial distribution

Past studies in the literature have investigated at the species in the plasma discharge using a number of techniques. In this section the results of these studies are summarized. Figure 2-6 shows the concentrations of the three main studied species including CH₄, C₂H₂, and C₂H₄ in a microwave discharge region versus the percentage methane in the feed gas [9, 10]. The operating pressure was at 30 Torr and no oxygen was used in the feed gas. The experiment result shows that the CH₄ and C₂H₂ are found under all condition while C₂H₄ was observed only when the CH₄ percentage in the source gas becomes high [9].

The results in Figure 2-7 were measured using a molecular beam mass spectrometer. The measured plasma discharge species were H₂, argon gas, C₂H₂, CH₄, H atom, and the methyl radical – CH₃. The pressure condition in the plasma was 20 Torr

and the input micro

increase of the radi

the C_2H_2 concentra

Figure 2-8 si

The addition of the

time increases the C

methods that can hel

especially when high

substrate deposition t

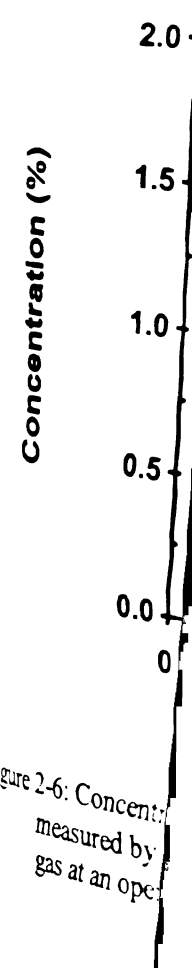


Figure 2-6: Concentration measured by gas at an open

and the input microwave power was 800 W. The experimental result indicated an increase of the radical CH_3 when the fraction of methane increases in the feed gas. Also, the C_2H_2 concentration also increased with CH_3 increases [9, 11].

Figure 2-8 shows the diamond deposition species with the addition of oxygen gas. The addition of the oxygen reduces the concentration of CH_4 and C_2H_2 , but at the same time increases the CO and H_2O level. The addition of oxygen is one of the common methods that can help reduce the graphitization, i.e., the dark film problem, which occurs especially when higher concentrations of CH_4 gas are used in the gas feed or a very high substrate deposition temperature is used [9, 12].

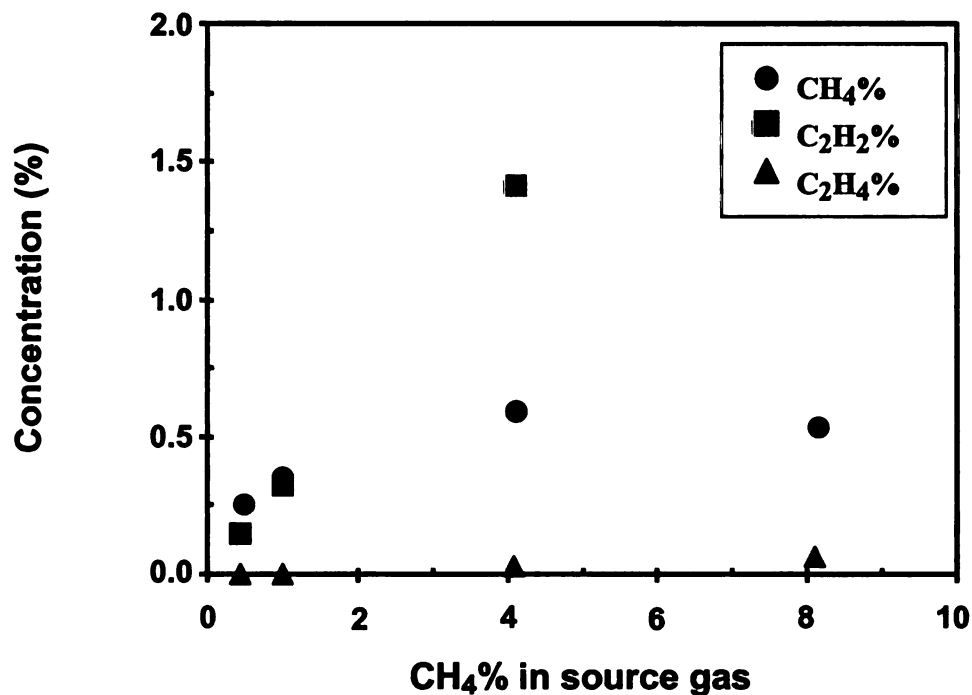


Figure 2-6: Concentration of CH_4 , C_2H_2 , and C_2H_4 in a microwave discharge region as measured by FTIR absorption spectroscopy versus percent methane in the feed gas at an operating pressure of 30 Torr with no oxygen in the feed gas [9, 10].

One of the
density in the plas
in the CVD diamo
independently if th
environment. First
hybridized carbon.
substrate surface. T
carbon about 100 tim

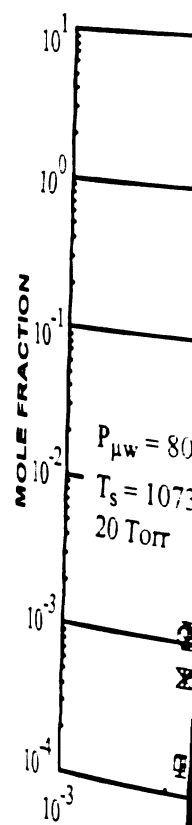


Figure 2-7: Mole fraction
system

One of the many species we are very interested in is the atomic hydrogen and its density in the plasma. It is believed that atomic hydrogen is the most critical component in the CVD diamond synthesis chemistry such that its concentration may determine independently if the final product is diamond or graphite in a hydrocarbon gases mix environment. First of all, the atomic H is known to favor the breaking down of sp^2 -hybridized carbon, such as C_2H_x , over removing the sp^3 -hybridized carbon from the substrate surface. The macroscopic outcome is that the atomic H etches the graphite sp^2 carbon about 100 times faster than diamond-like sp^3 carbon [6, 13, 14, 15, 16].

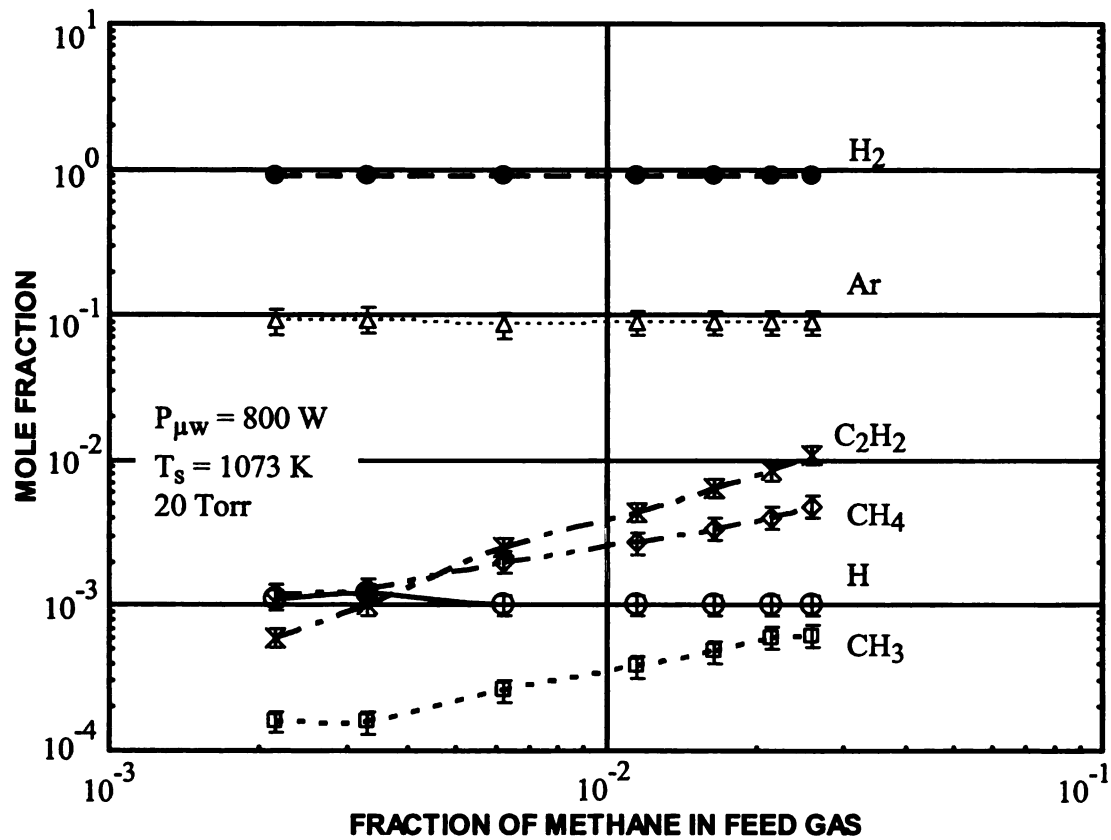


Figure 2-7: Mole fraction of chemical species measured in a microwave plasma CVD system versus variation in the methane fraction in the feed gas [9, 11].

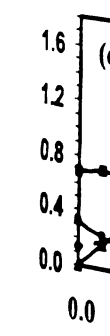
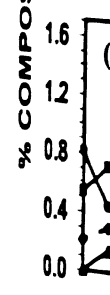
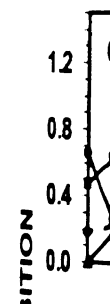


Figure 2-8
per
sec

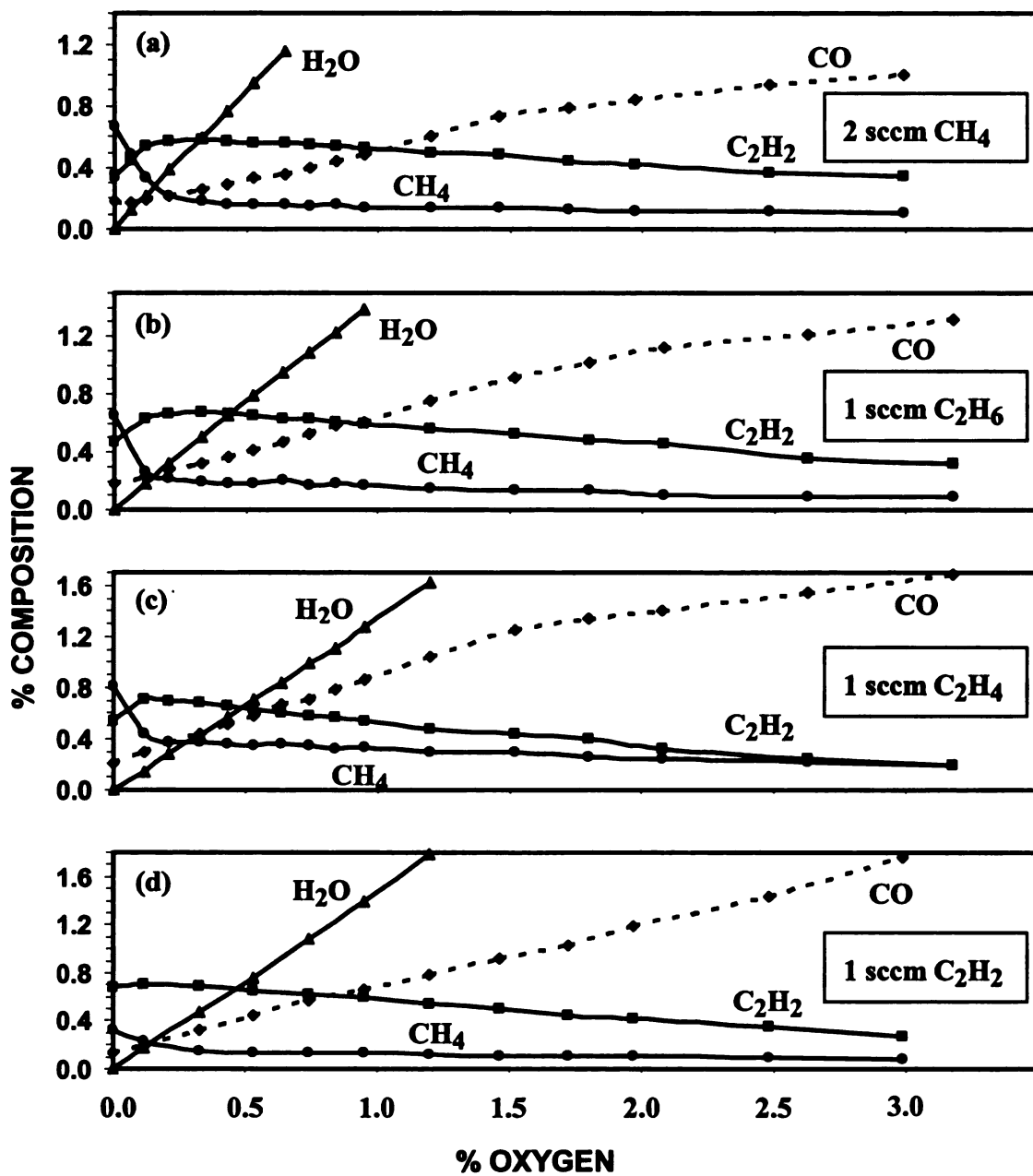


Figure 2-8: Diamond deposition reactor exhaust gas composition versus oxygen percentage in the feed gas for input gas flows at 97 sccm hydrogen and (a) 2 sccm CH₄, (b) 1 sccm C₂H₆, (c) 1 sccm C₂H₄, and (d) 1 sccm C₂H₂ [9, 12].

The net result is

atom and leave

the same time pro

ring structures in

are also the other

diamonds, which n

releasing a H₂ mol

our the steps of form

Since atomic

given to deposition o

the atomic hydrogen

with pressure [9, 17].

discharge.

Figure 2-10 sh

the microwave power

atomic hydrogen conce

gas however, a large in

increase of the power o

density is that the pow

It is also very

uniform across the sub

expanding plasma sph

The net result is that the atomic hydrogen helps greatly to abstract the surface hydrogen atom and leave a site for CH_3 to adsorb on the surface and further to form diamond and at the same time preventing the surface graphitization and the build-up of polymers or large ring structures in the gas phase or on the substrate surface. Second, the excited H atoms are also the other important source for stable CH_3 radicals for the formation of the diamonds, which may be formed from a neutral CH_4 radical reacts with an H atom by releasing a H_2 molecule. As it has been described earlier, these neutral CH_3 radicals carry out the steps of forming diamond on the open sites of a diamond surface.

Since atomic H is so important to diamond synthesis, extensive attention has been given to deposition conditions that increase the neutral H atom species. Figure 2-9 shows the atomic hydrogen concentration and indicates that the atomic hydrogen density increases with pressure [9, 17]. This measurement was done in a microwave powered plasma discharge.

Figure 2-10 shows the atomic hydrogen concentration and how it is influenced by the microwave power density and the percentage methane in the input gas [9, 18]. The atomic hydrogen concentration changes little due to the percentage methane in the input gas however, a large increase is seen in the atomic hydrogen mole fraction due to the increase of the power density in the plasma. The primary factor that influences the power density is that the power density increases strongly with pressure.

It is also very important to note that the atomic hydrogen distribution is not uniform across the substrate for a typical free-expanding plasma sphere. The free-expanding plasma sphere means the visible plasma ball is smaller in size than the space

filled with the feeding

the one shown in Fig

depicted, a symmetric

the highest atomic hy

2-11 uses actinometry

enhanced CVD reacto

field intensity radial d

used in this study is al



Figure 2-9: Ator

filled with the feeding working mixture of gases under the fused silica bell jar, such as the one shown in Figure 3-1. A. Gicquel et al. [19] has indicated, though not directly depicted, a symmetric radial distribution of the H-atoms as shown in Figure 2-11 where the highest atomic hydrogen mole fraction is measured at the center of the plasma. Figure 2-11 uses actinometry for estimating the relative H-atom densities in a microwave plasma enhanced CVD reactor similar to the one utilized in this study. A similar plot of the E-field intensity radial distribution [20] for the microwave plasma-enhanced CVD reactor used in this study is also shown later in Chapter 3.

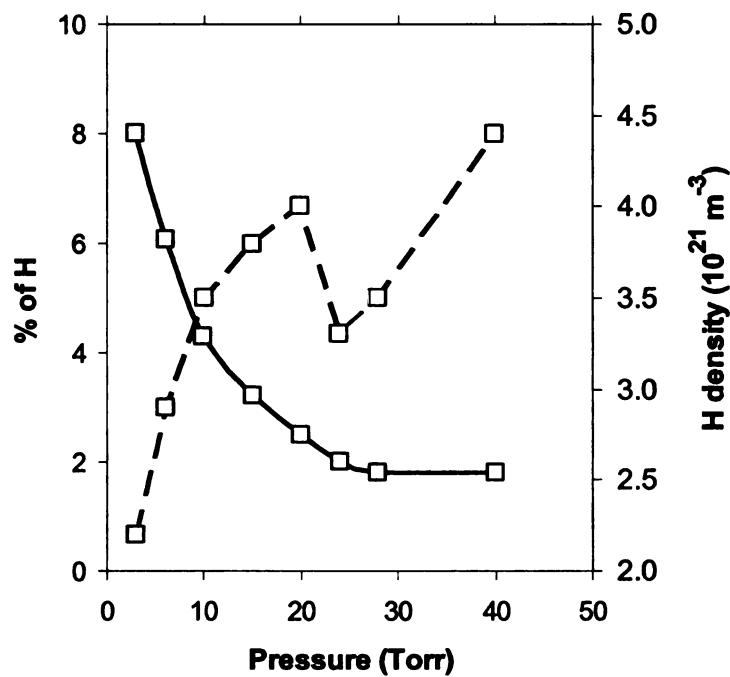


Figure 2-9: Atomic hydrogen percentage and density versus pressure [9, 17].

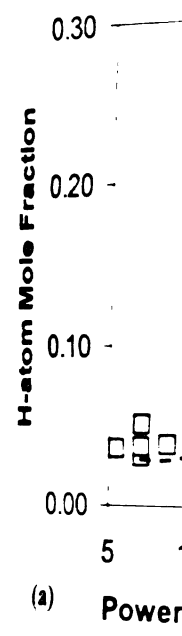


Figure 2-10: Atom
part (a)

R. A. Akhmedzh

radial distribution of the
 studied the pulsed oper
 is similar to the reactor
 literature review is bec
 density may be one of
 microwave (or other po
 atomic hydrogen plays
 radial uniformity are n

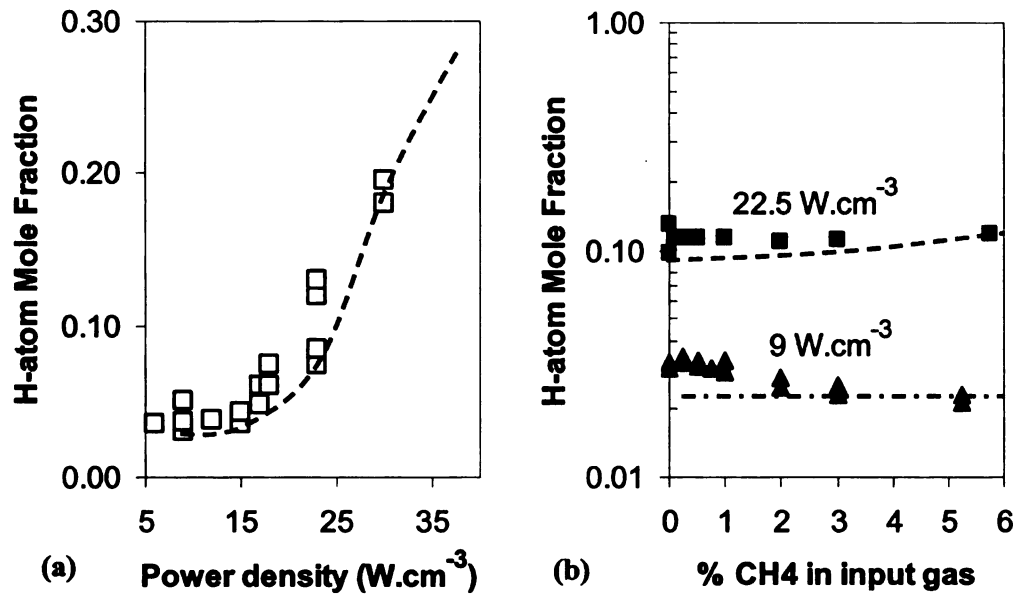


Figure 2-10: Atomic hydrogen mole fraction versus the microwave power density in part (a) and versus methane concentration in part (b) [9, 18].

R. A. Akhmedzhanov et al. [21] also provided a similar graph (Figure 2-12) of the radial distribution of the atomic hydrogen density based on their calculation. They studied the pulsed operation regime of a microwave powered CVD plasma reactor, which is similar to the reactor used for this study. The reason these studies are included in this literature review is because this non-uniform radial distribution of the atomic hydrogen density may be one of the most important factors that contributes to the nonuniform microwave (or other power source) plasma-assisted diamond film deposition. Since the atomic hydrogen plays a crucial role of the deposition process, efforts to increase its radial uniformity are needed.

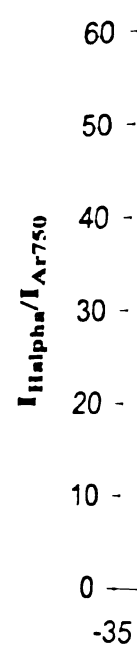


Figure 2-11: Radial allowed tra
 allowed tra
 Abel invers
 [19]. This g

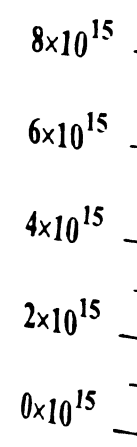


Figure 2-12: Calculated
 the substrate
 moments 2, 3
 the pulse bas

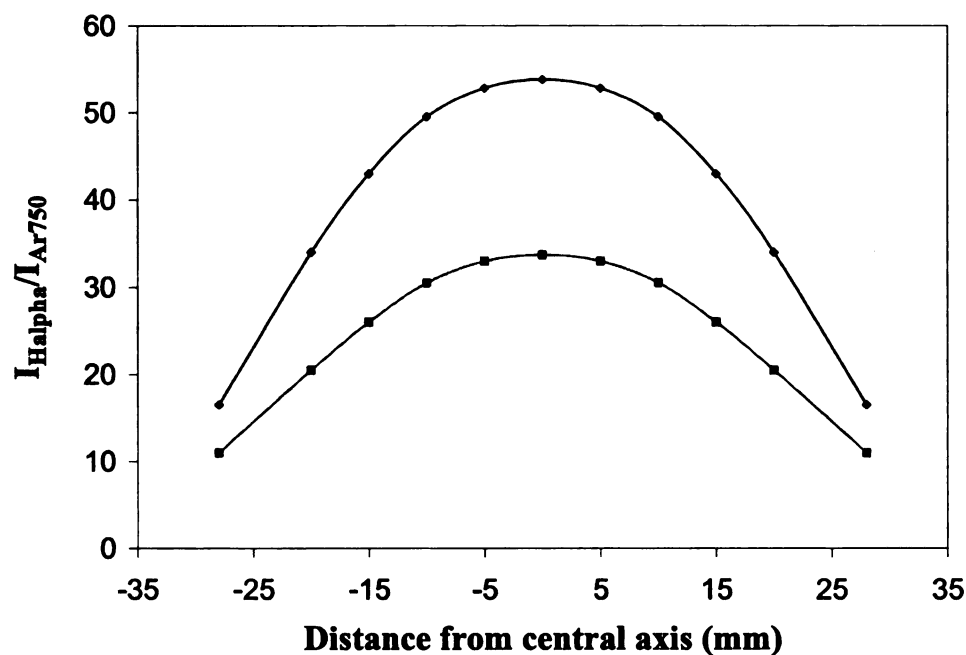


Figure 2-11: Radial distribution of H-atom mole fraction concluded by two photon allowed transition laser induced fluorescence (TALIF) and by actinometry after Abel inversion of the spectrum from the Optical Emission Spectroscopy (OES) [19]. This graph is a reproduction and, not a duplicate of the original plot.

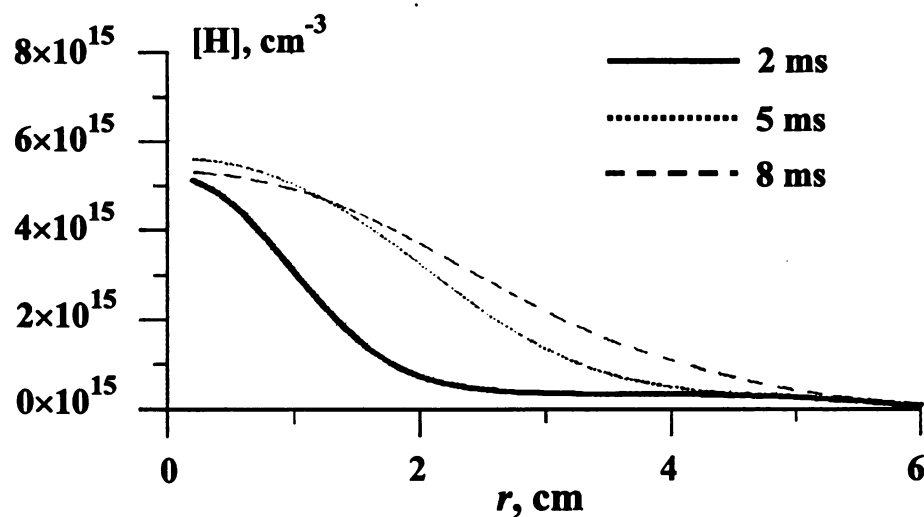


Figure 2-12: Calculated density of hydrogen atoms $[H]$ versus radius, r , at a height above the substrate of 0.6 cm ($z = 0.4\text{ cm}$) and a pressure of $p = 40\text{ Torr}$ at time moments 2, 5 and 8 ms from the pulse start. The pulse frequency is 50 Hz and the pulse base duration is 10 ms [21].

2.4.2 Neutral gas

The neutral gas temperature is a function of the energy of the plasma and the neutral gas temperature include the energy of the plasma. The neutral gas temperature of Laser Induced Fluorescence (LIF) [21], and Coherent Anti-Stokes Raman Spectroscopy (CARS) [22], and the neutral gas temperature is shown in Figure 2-16 presented in this report. The neutral gas temperature covered all four of the neutral gas temperatures: hydrogen, methane, and nitrogen. The neutral gas temperature versus the neutral gas temperature measured by all four methods is shown in Figure 2-16. The neutral gas density and pressure are shown in Figure 2-17. The neutral gas density and pressure of hydrogen by a thermocouple is shown in Figure 2-18. The neutral gas density and pressure of hydrogen by a thermocouple associates with high

2.4.2 Neutral gas temperature

The neutral gas temperature is a measurement that determines the average kinetic energy of the plasma gas discharge. There are a number of ways used to measure the gas temperature include Doppler broadening of optical emission signals, Doppler broadening of Laser Induced Fluorescence (LIF) signals, Coherent Anti-Stokes Raman Spectroscopy (CARS) [22], and rotational temperature of optically emitting molecules [9]. Figure 2-13 to Figure 2-16 present results from a systematic study by Gicquel et al. [23, 24] that has covered all four of the methods of measuring the neutral gas temperature versus power density and methane concentration. Figure 2-17 presents a result of the neutral gas temperature versus the pressure by Grotjohn et al. [25]. The neutral gas temperatures as measured by all four techniques show temperature increases with increases of power density and pressure. At the higher temperature (about 3000 K), the dissociation of the hydrogen by a thermal process increases leading to more atomic hydrogen, which associates with higher quality.

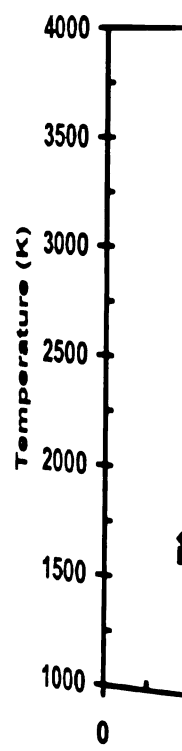


Figure 2-13: Atomic
The temperatu
signals [23, 24

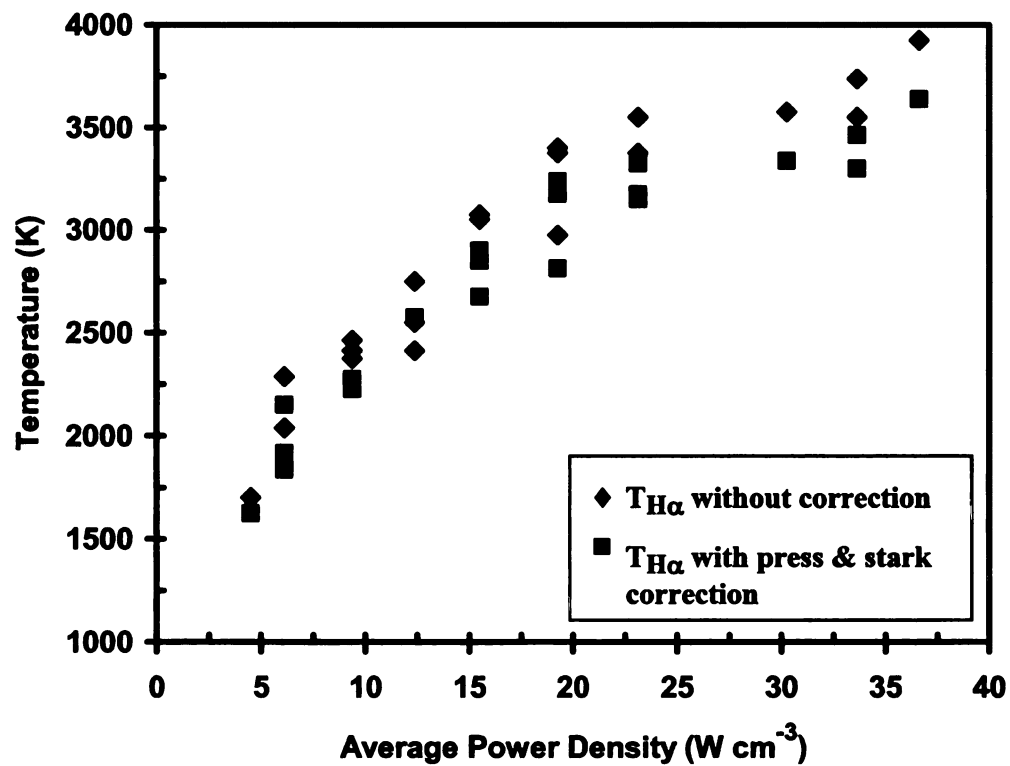


Figure 2-13: Atomic hydrogen translation temperature versus microwave power density. The temperature was measured using Doppler broadening of hydrogen OES signals [23, 24].

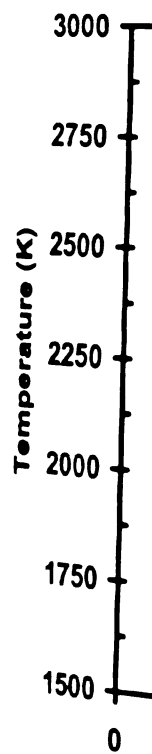


Figure 2-14: Gas to
temperatur
LIF and hy

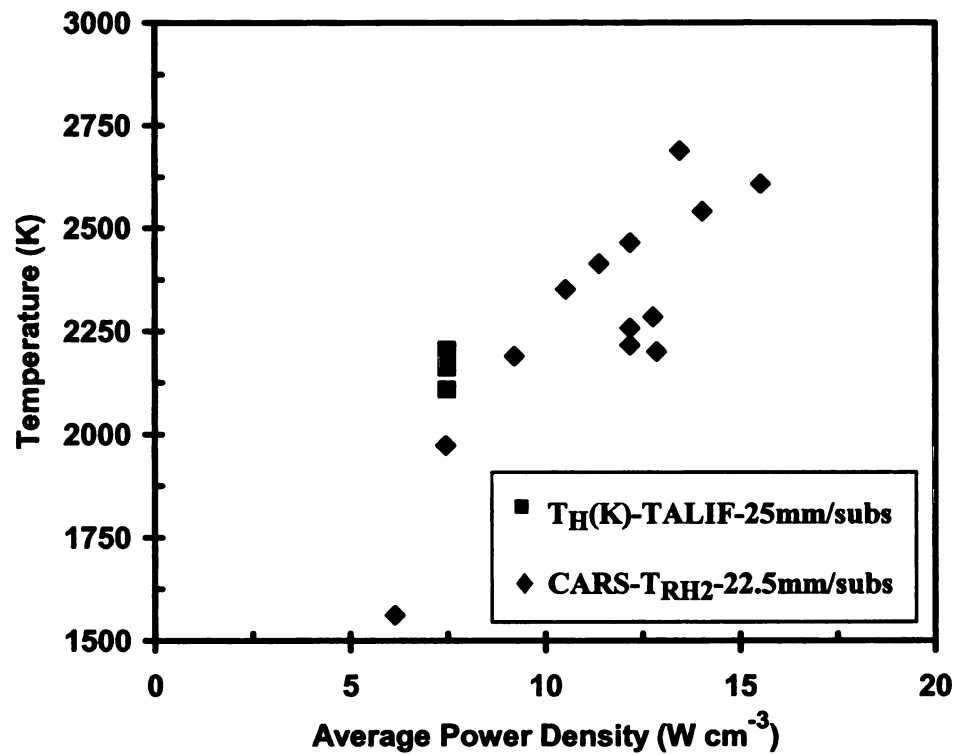


Figure 2-14: Gas temperature versus average microwave power density. Gas temperatures measured include atomic hydrogen temperature by two-photon LIF and hydrogen rotational temperature by CARS [23, 24].



Figure 2-15: Atom
rotational
feed gas [2
900 °C.

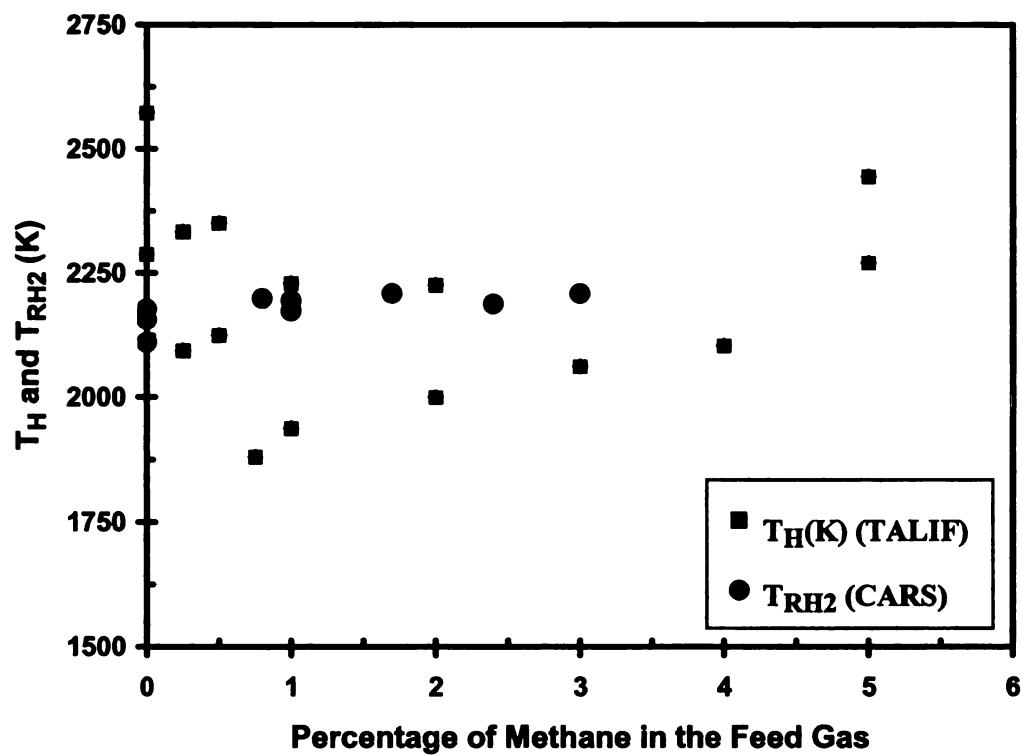


Figure 2-15: Atomic hydrogen temperature (measured by LIF) and molecular hydrogen rotational temperature (measured by CARS) versus methane percentage in the feed gas [23, 24]. Plasma conditions: 600 W, 2500 Pa, $9 \text{ W}\cdot\text{cm}^{-3}$, 300 sccm, $T_s = 900 \text{ }^\circ\text{C}$.



Figure 2-16: N
power

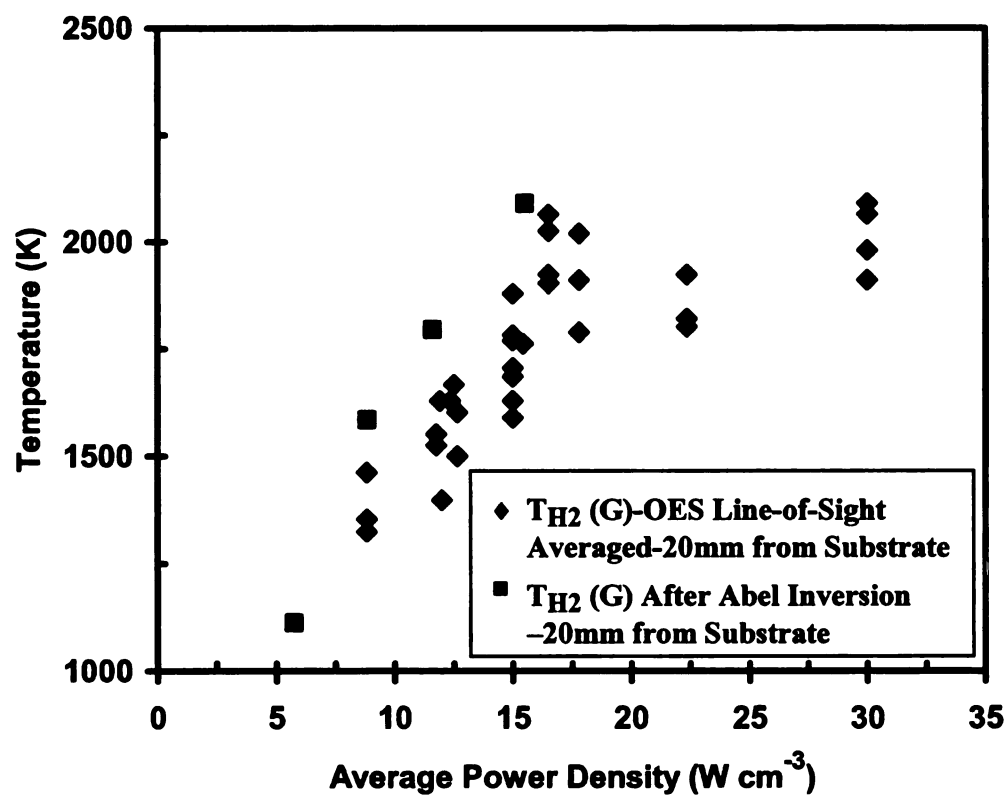


Figure 2-16: Molecular hydrogen rotational temperature versus average microwave power density. Temperature was measured using line-of-sight OES [23, 24].

2000
1800
1600
1400
1200
1000

Gas Temperature (K)

Figure 2-17: Molecular
diameter disch
discharge was
the R branch o

2.4.3 Electron dens

The electron d
volume and the electr
measuring electron te

One result from Grotj

$1.5 \times 10^{11} \text{ cm}^{-3}$ for a p

microwave reactor (F

operating at 30 GHz

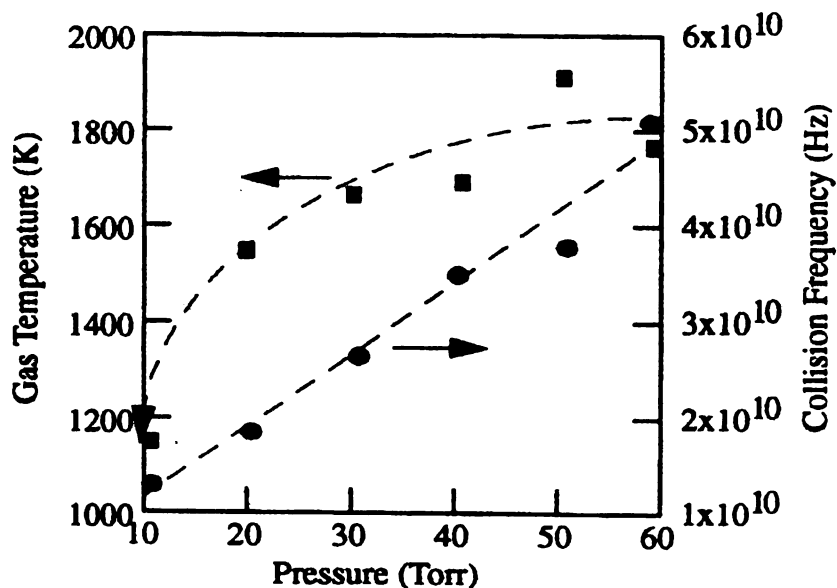


Figure 2-17: Molecular hydrogen rotational temperature versus pressure for a 5-cm-diameter discharge system [9, 25]. The rotational temperature for hydrogen discharge was determined by OES spectrum around 460 nm (453 – 465) using the R branch of the $H_2(G^1\Sigma_g^+)$ to $H_2(B^1\Sigma_u^+)$ (0, 0) band.

2.4.3 Electron density and electron temperature

The electron density is the average number of electrons contained in a unit volume and the electron temperature is the average kinetic energy of the electrons. For measuring electron temperature, one electron volt is also equivalent to 11,606 Kelvin. One result from Grotjohn and coworkers [9, 25] measured the electron density range as $1\text{--}5 \times 10^{11} \text{ cm}^{-3}$ for a pressure range from 10 – 60 Torr plasma discharge and a 2.45-GHz microwave reactor (Figure 2-18). They used a millimeter wave Fabry-Perot resonator operating at 30 GHz to measure the electron density.

Microwave p
volume. The volume
by the discharge. Dr
increases with an inc
2-19.

10
Electron Density ($\times 10^{11} \text{ cm}^{-3}$)
1

Figure 2-18: Elec
diam

2.4.4 Microwave power density

Microwave power density is defined as the plasma absorbed power per unit volume. The volume is estimated from the region of most intense visible light emission by the discharge. Dr. Grotjohn and his group [9, 25] found that the power density increases with an increase in the pressure of the plasma discharges, as shown in Figure 2-19.

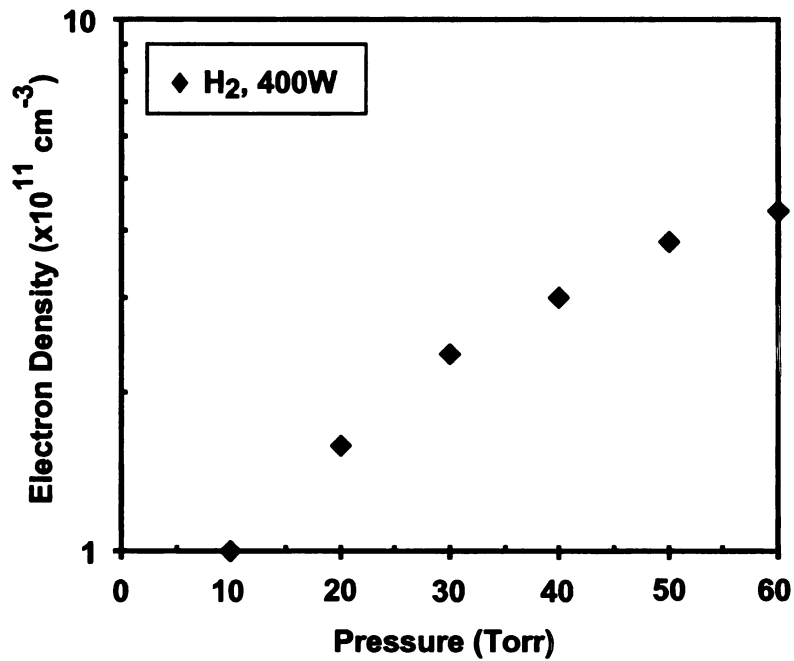


Figure 2-18: Electron density versus pressure for a microwave plasma-assisted diamond deposition discharge [9, 25].

4
30
20
10
0

Power Density (W cm^{-3})

Figure 2-19: Micro
meth

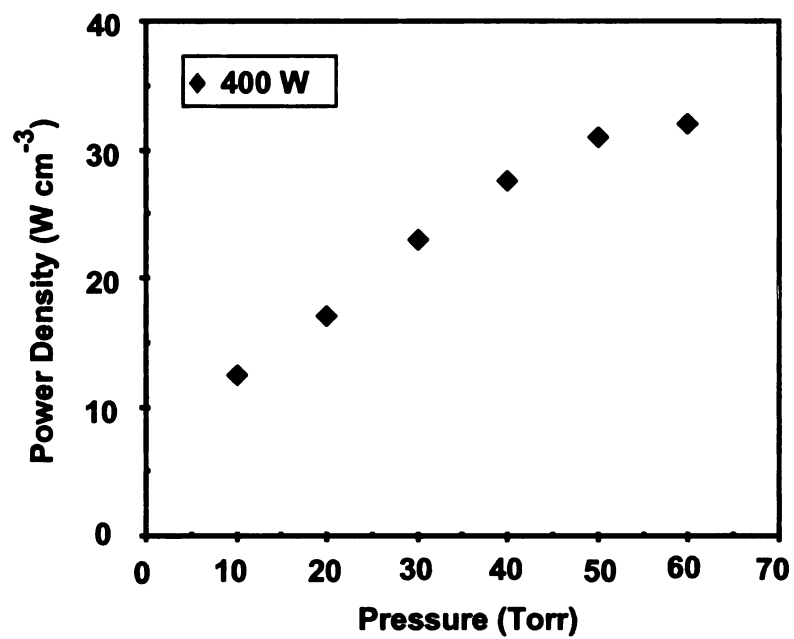


Figure 2-19: Microwave power density versus pressure for 5-cm-diameter hydrogen methane discharge used for diamond deposition [9, 25].

15 Key results of h

The previous s
diagnostic measureme
properties. These diag
regime of less than 10
diamond deposition at
measurements of the p
literature at the higher

Table 1 summ
deposition from eight
important parameters
growth rate, substrate
quality of the diamon

2.5 Key results of higher pressure research studies

The previous section described the diamond deposition process and various diagnostic measurements that are routinely employed to understand the plasma properties. These diagnostic measurements have been made primarily in the low pressure regime of less than 100 Torr. Several research groups have developed and demonstrated diamond deposition at higher pressures of 100 to 200 Torr. However, systematic measurements of the plasma discharge conditions are not readily found in the research literature at the higher pressures.

Table 1 summarizes key results for higher pressure (above 100 Torr) diamond deposition from eight CVD diamond research groups. The table indicates several important parameters including the type of diamond grown, the growth method, the growth rate, substrate temperature, the methane concentrations in hydrogen, and the quality of the diamond, etc.

Diamond Type	Growth Method	Growth Rate ($\mu\text{m}/\text{h}$)	Pressure (Torr)	T_s ($^{\circ}\text{C}$)	$\text{C}/\text{H}_4/\text{H}_2$	Quality	Power (kW)	Additives	Thickness (μm)	Ref.
Poly	MPCVD	6.27	135	1015	3%	NA	4.5	No	NA	Kuo [26, 27]
Single	MPCVD	6.0			4%	Good		No	520	

Diamond Type	Growth Method	Growth Rate ($\mu\text{m/h}$)	Pressure (Torr)	Ts (°C)	CH ₄ /H ₂	Quality	Power (kW)	Additives	Thickness (μm)	Ref.	
Poly	MPCVD	6.27	135	1015	3 %	NA	4.5	No	NA	Kuo [26, 27]	
		6.0			4 %	Good		520			
Single	MPCVD	11-15	165	850	6-7 %	Step Bunching	3.2	No	NA	Tallaire [28]	
		33			4 %	Good		1700			
Poly	MPCVD	4.5	188	1075	2.5 %	Impurities	6.0	N ₂	NA	Morret [29]	
		11			14.5 %	Step Bunching		No	NA		
Single	MPCVD	2.0	120	880	4 %	Good	3.8	No	NA	Teraji [30]	
		150			NA	NA		NA	NA		
Single	MPCVD	58	160	1220	12 %	Color & impurity	2.0	3 % N ₂ /CH ₄	700	Yan [31]	
					10	1-7 %		Good	3 % N ₂ /CH ₄		NA
					800-1000	9 %		Good	0.2-2 % O ₂ /CH ₄		NA
Poly	Hot Filament CVD	16	200	700	5-7 %	Good	2.6	No	NA	Wei [32]	
		16 or NA			9 %	Impurities		No	NA		
Single	MPCVD	50	170	800	7 %	(1) Step Bunching (2) 2 nd nuclel (overheat)	2.5	No	3-hour growth	Williams [33]	
		10			4 %	Good		O ₂	NA		
Poly	MPCVD	30	150	1450	16 %	Fair	6.0	1.6 % O ₂	NA	Chen [34]	
		50			16 %	Impurities		No	NA		

Table 2-1: Key result parameters of the current higher pressure CVD diamond research studies.

diamond growth
concentration (C)
rate increases as
statement is that
function of power
suggests that further
parameters, including
order to understand
some of the studies

2.5.1 Comparison of pressures

Chein [34]

a range of methane
and substrate temperature
Raman spectra for the
Figure 2-20 [34]. The
still grow diamond
in contrast to low pressure
only graphite deposition

Table 2-1 indicates some important trends and differences from lower pressure diamond growth. A general observation is that with a pressure increase, the methane concentration (percentage) in the input feed gas can be increased such that the growth rate increases and good diamond deposition can still be achieved. A further general statement is that the results from different groups have significant variability in terms of function of power density, higher pressure and substrate temperature. This variability suggests that further studies of high pressure diamond deposition versus several parameters, including power density or pressure and substrate temperature, are needed in order to understand high growth rate diamond deposition. The following section details some of the studies that have been done in the high pressure regime.

2.5.1 Comparison of surface texture diamond content and growth rate at high pressures

Chein [34] did a study of diamond deposition at a pressure of up to 150 Torr over a range of methane volume concentrations in the feed gas that varied from 1 to 100 % and substrate temperature that varied from 550 to 1600 °C. The diamond morphology and Raman spectra for the films formed from the different methane concentrations are shown Figure 2-20 [34]. The results indicate that high concentrations of methane up to 100 % still grow diamond though a high fraction of graphite content appears in the films. This is in contrast to low pressure deposition where a higher methane concentration produces only graphite deposition with no diamond.

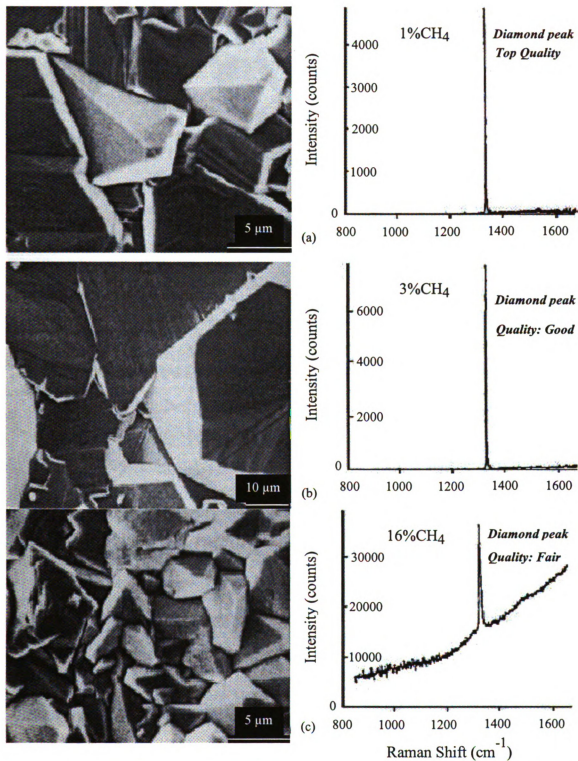


Figure 2-20 (a): Texts with the italic font are added in addition to original graphs labeling the diamond and graphite peaks and indicating the quality roughly defined by Raman spectroscopy in this study. (to be continued on next page)

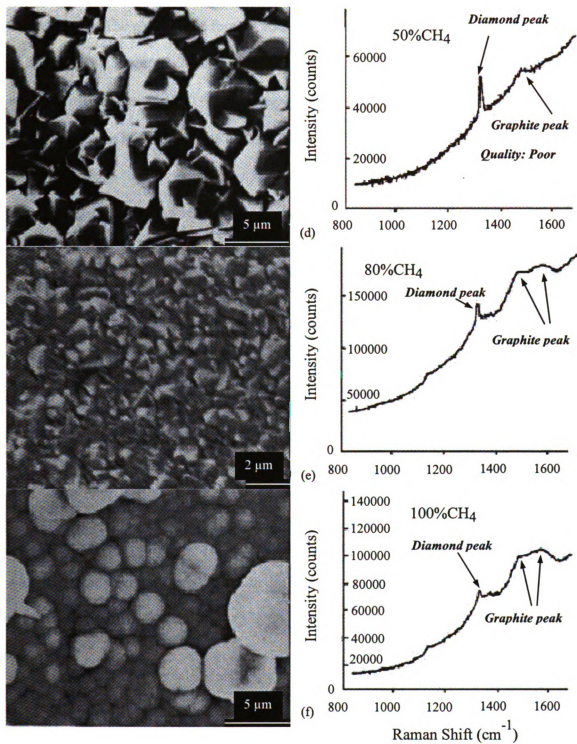


Figure 2-20 (b): High power density MPCVD diamond at 900 °C and 150 Torr with different CH₄ concentrations. The figure on the right is the Raman spectra for the corresponding film [34].

The Figure 2

Chen's study. The p

of 100-150 Torr. Fig

substrate temperature

Raman spectra at the

density condition (hi

higher temperatures t

At substrate t

instead of diamond in

power density plasma

for both curves (b) an

oxygen gas in the fee

1200 °C and started t

However, the growth

high power density p

high power density c

conditions, the diamo

as shown in Figure 2

The Figure 2-21 shows the diamond synthesis at different temperatures from Chein's study. The plasma was formed with 16 % methane in hydrogen and at pressures of 100-150 Torr. Figure 2-21 shows that at least some diamond is synthesized when the substrate temperature is 1500 °C or below. No diamond, but graphite was indicated in the Raman spectra at the temperature of 1600 °C and up. This also means at the high power density condition (high pressure), the MPCVD diamond can be synthesized at much higher temperatures than with the lower power density plasmas (Figure 2-22).

At substrate temperatures of 1200 °C and above, graphite is usually deposited instead of diamond in lower power density microwave plasmas. In Figure 2-22, a low power density plasma was used for curve (a) and a high power density plasma was used for both curves (b) and (c). The only difference for (c) from (b) is the addition of 1.6% oxygen gas in the feed gas. As shown in Figure 2-22, the growth rate increases up to 1200 °C and started to decrease above that temperature for low power density plasma. However, the growth rate increased steadily versus temperature up to 1500 °C for the high power density plasma. The addition of the oxygen lowered the growth rate for the high power density condition. Chein [34] showed that for the high power density plasma conditions, the diamond growth zone in the Bachman diagram was found to be expanded as shown in Figure 2-23.

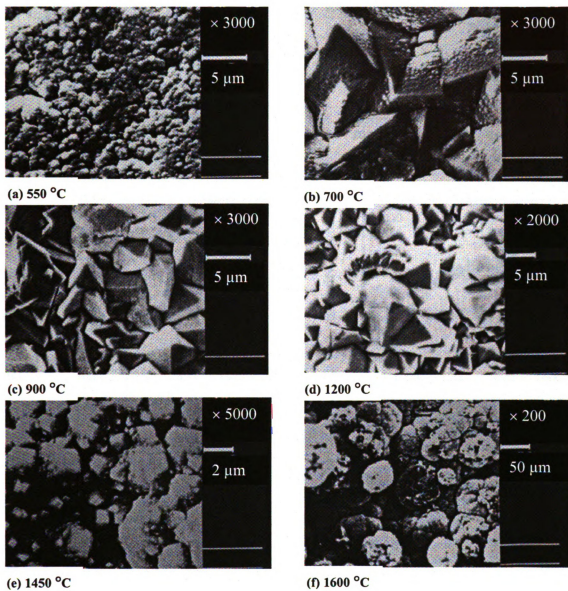
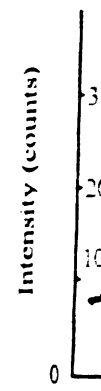
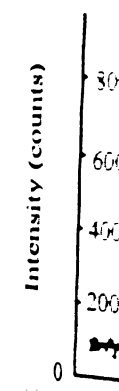


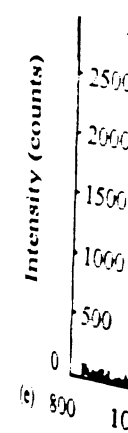
Figure 2-21 (a): Texts with the italic font are added in addition to original graphs labeling the diamond and graphite peaks and indicating the quality roughly defined by Raman spectroscopy in this study. (to be continued on next page)



(a) 800



(c) 800



(e) 800

Figure 2-21 (C)

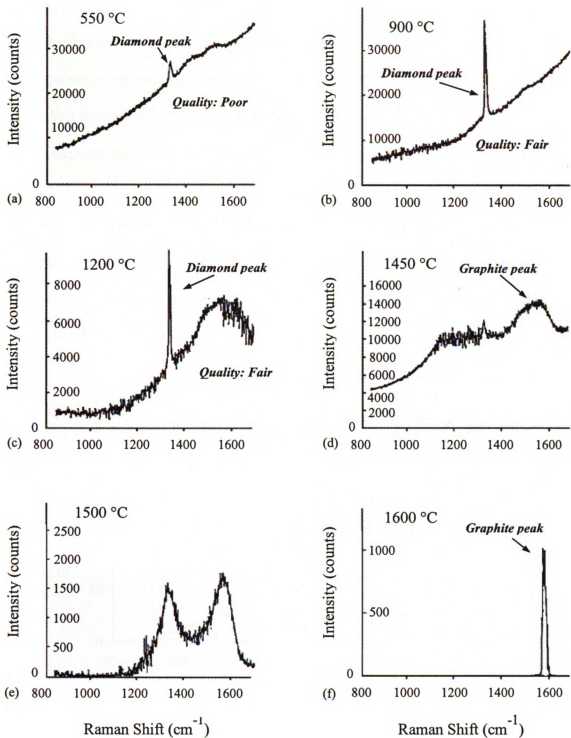


Figure 2-21 (b): High power density MPCVD diamond using 16 % CH_4/H_2 and 100-150 Torr pressure at different temperature [34].

2.6 Curvature of

Bowing stress
very frequently observed
freestanding diamond
Possible explanation
diamond film and im
film bowing and how
applications, such as
surfaces and doped d
so far, it is still an op

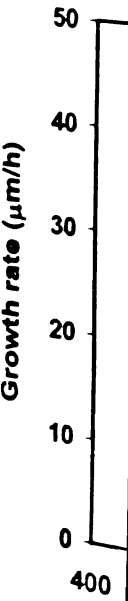


Figure 2-22: Growth
and (c) 16 %
(s), the pressu
Density (HPL
(LPD) plasma

2.6 Curvature of free standing diamond films and bowing stresses

Bowing stress and curvature of the freestanding polycrystalline diamond films are very frequently observed in plasma-assisted CVD deposition. Figure 2-24 shows a freestanding diamond thin film that bends itself upward after the substrate is removed. Possible explanations for the bowing include structural defects in the polycrystalline diamond film and impurities in the diamond film. The study of what causes the diamond film bowing and how to measure the bowing stress become very important in many applications, such as diamond optical windows, diamond coatings on different material surfaces and doped diamond electrodes. Though many research studies have been done so far, it is still an open issue.

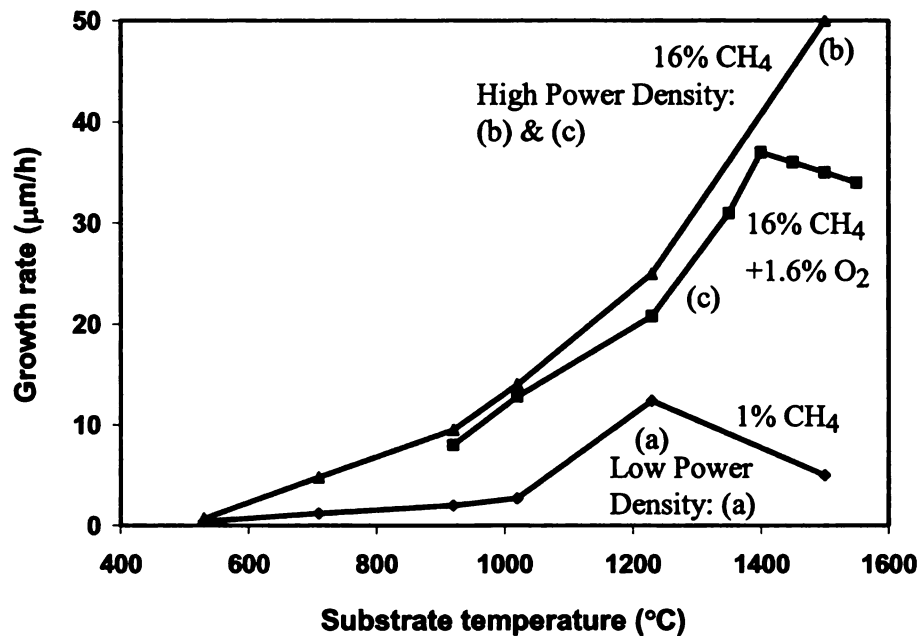


Figure 2-22: Growth rate versus substrate temperature in (a) 1 % and (b) 16 % CH₄ in H₂ and (c) 16 % CH₄+1.6 % O₂ in H₂ [34]. Though was not specified by the author (s), the pressure is somewhere in between 100 to 150 Torr for High Power Density (HPD) plasma and a few Torr to tens of Torr for Low Power Density (LPD) plasma defined in the article.

16% CH



Figure 2-23: Location of
O diagram



Figure 2-24: A free
after the sil:
in diameter.

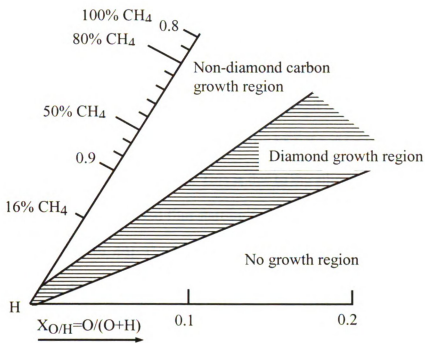


Figure 2-23: Locations for hydrocarbons near the enlarged hydrogen-rich corner in C-H-O diagram [34].

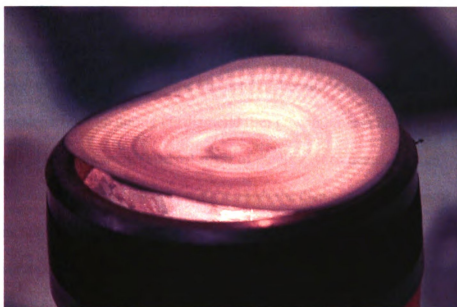


Figure 2-24: A freestanding diamond thin film (SZ-2inch-1mm-08) that was bent upward after the silicon substrate was chemically removed. The diamond film is 2 inches in diameter, 46 μm thick, and is sitting on top of a flashlight.

Stresses

the thermal stress

other is the inter

difference in the

causes the bendi

substrate cool do

thermal expansio

1650 degree Kelv

comparison of lin

the plot were coll

Expansion of Non

temperature, the la

shrinkage when bo

temperature. There

cool down. Howev

another stronger st

is usually called the

substrate), which ca

our applications, the

the silicon substrate

inside the diamond f

section.

Stresses that lead to film bowing are generally of two types [35, 36, 37]. One is the thermal stress between the diamond film and the substrate that supports the film. The other is the internal stress within the diamond film, also called intrinsic stress. The difference in thermal expansion of two materials (silicon and diamond, for example) causes the bending towards the silicon substrate after both the diamond film and silicon substrate cool down to room temperature. This is due to the silicon wafer having a larger thermal expansion than the diamond film starting from room temperature up to about 1650 degree Kelvin [38, 39, 40]. This plot, as shown in Figure 2-25, shows the comparison of linear thermal expansion for diamond and silicon material. Data used for the plot were collected from *Thermophysical Properties of Matter: Volume 13: Thermal Expansion of Nonmetallic Solids*. Below 1650 °K and with respect to the room temperature, the larger linear thermal expansion (Figure 2-25) for silicon leads to a larger shrinkage when both diamond film and silicon wafer are cooled down to room temperature. Therefore, the diamond film will bend towards the silicon substrate upon cool down. However, we usually do not see this bending because of the co-existence of another stronger stress built up during the diamond film growth process itself. This stress is usually called the intrinsic stress (internal stress of the film when detached from substrate), which causes the bending or bowing towards the diamond film. For most of our applications, the thermal stress can be removed from the diamond film by removing the silicon substrate. The diamond film becomes freestanding and the intrinsic stress inside the diamond film becomes our sole concern that leads to the discussion in the next section.

Please note t

expansion of diamon

expansion coefficient

linear thermal expan

thermal expansion v

coefficients are asso

thermal expansion. I

slope of the diamond

2-25 and Figure 2-26

depending on the app

of linear thermal exp

one in Figure 2-26 in

Figure 2-25 and Figu

room temperature an

Please note the same set of data that is used to compare the linear thermal expansion of diamond and silicon can also be used to compare the linear thermal expansion coefficients of diamond and silicon as shown in Figure 2-26. By definition, the linear thermal expansion coefficient is proportional to $\frac{\partial L}{\partial T}$, the derivative of the linear thermal expansion versus temperature. Therefore, the linear thermal expansion coefficients are associated directly with the slope of the curves in the plot of the linear thermal expansion. It is easy to locate the point in Figure 2-25 (about 1000 °K) where the slope of the diamond curve becomes bigger than the slope of the silicon curve. Figure 2-25 and Figure 2-26 are equivalent but one may be more convenient than the other depending on the application. For example, some researchers [41, 42, 43, 44] used a plot of linear thermal expansion coefficients of diamond and silicon materials similar to the one in Figure 2-26 instead of Figure 2-25, for their own applications. The data shown in Figure 2-25 and Figure 2-26 are the most recent for thermal expansion with respect to room temperature and its corresponding coefficient at the given temperature.

Linear Thermal Expansion (%)

0.470

0.370

0.270

0.170

0.070

-0.030 0

Figure 2-25: Compar
(293 °K or 20
the temperatu

Linear Thermal Expansion Coefficients
(10^{-6} K^{-1})

7.00 -

6.00 -

5.00 -

4.00 -

3.00 -

2.00 -

1.00 -

0.00 -

-1.00 -

Figure 2-26: The lin
material term

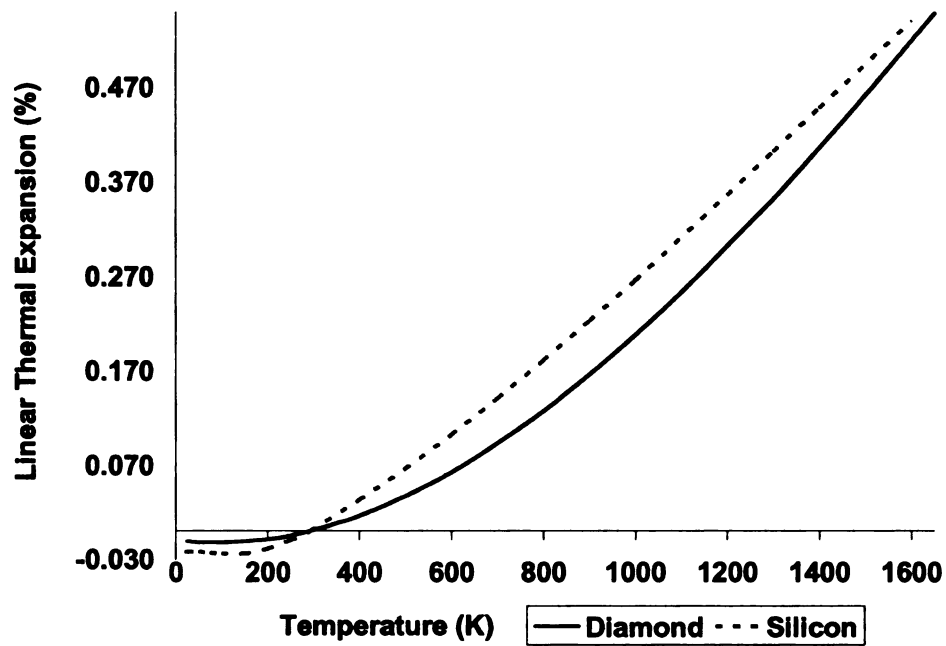


Figure 2-25: Comparison of linear thermal expansion with respect to room temperature (293 °K or 20 °C) for diamond and silicon in percentage length increased versus to the temperature of the material [38, 39, 40].

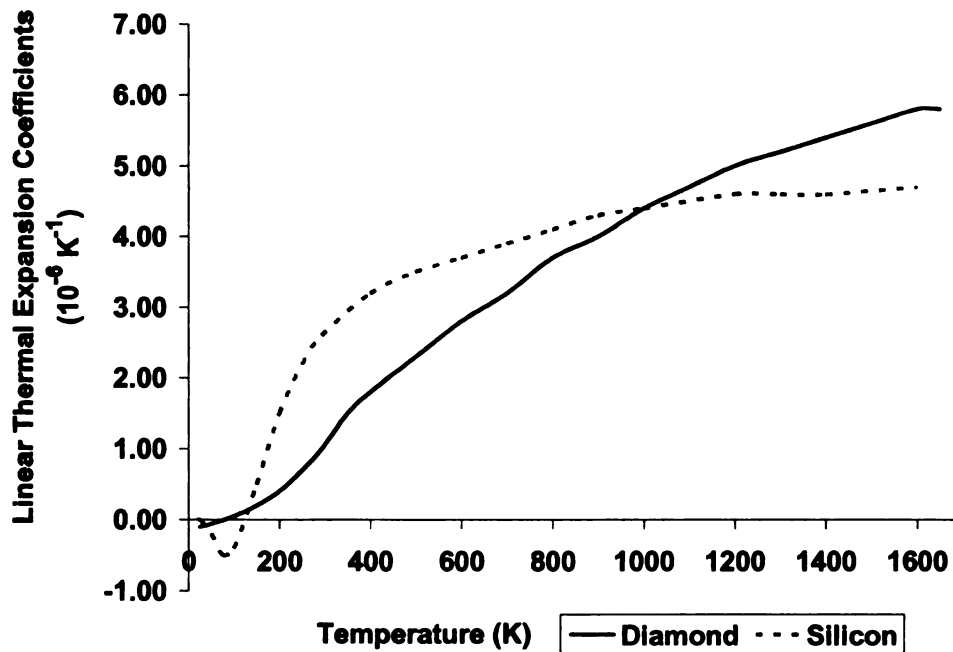


Figure 2-26: The linear thermal expansion coefficients for diamond and silicon versus the material temperature [38, 39, 40].

2.6.1 *Intrinsic*

Freestand

Several paramete

composition of th

of intrinsic stress

caused by the coal

stress changed with

mentioned the crys

general the intrinsi

associated with the

many structural det

2.6.2 *Grain size a*

The crystal s

Figure 2-27 display

after growth for one

clearly see that the d

This increas

SEM micrograph in

crystals can be seen

takes place. The thi

surfaces start to coa

columnar growth, w

polycrystalline diam

2.6.1 *Intrinsic stress*

Freestanding CVD diamond thin films are grown under very complex conditions. Several parameters affect the growth including substrate temperature, pressure, and the composition of the feed gases. Many attempts have been made to understand the cause(s) of intrinsic stress within the diamond film. Some researchers proposed the stress is caused by the coalescence of the diamond crystal boundaries [45]. Others noticed the stress changed with the growth temperature and methane concentration [41]. Some mentioned the crystallographic orientation might induce the intrinsic stress [46]. In general the intrinsic stress is believed to build up during the film growth, and is associated with the non-diamond material at the region of grain boundaries and with many structural defects including impurities, microtwins, and dislocations [47].

2.6.2 *Grain size and disordered diamond crystals*

The crystal size generally increases with the growth time and the film thickness. Figure 2-27 displays four SEM micrographs that reveal the diamond film morphology after growth for one hour, three hours, six and a half hours, and ten hours [47]. One may clearly see that the diamond grain size gets bigger with time.

This increase in crystal size with growth time can also be seen in the cross section SEM micrograph in Figure 2-28. Also in Figure 2-28, a layer of disordered diamond crystals can be seen near the silicon surface. This is the layer where diamond nucleation takes place. The thickness of this layer can be up to about 3 μm before the isolated grain surfaces start to coalesce to form a continuous polycrystalline diamond film. The columnar growth, which can be found in Figure 2-28, starts dominating the polycrystalline diamond growing process once the diamond film covers the entire

surface. The

growth rate

Figure 2-2

dia

we

ext

The

boundary s

considered

product of

tend to be b

to the film t

distance fro

surface. The completion of this nucleation takes about 1 to 3 hours depending upon the growth rate.

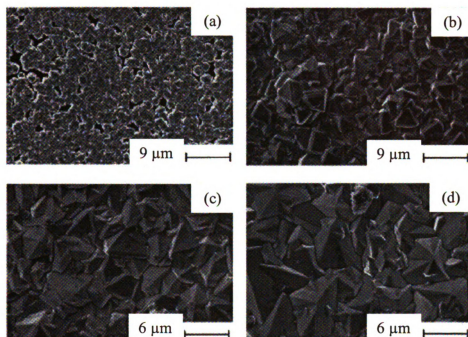


Figure 2-27: Top view scanning electron micrographs, in the same magnification, for four diamond films grown for (a) 1, (b) 3, (c) 6.5 and (d) 10 h. The film thicknesses were 3.0, 8.7, 21 and 42 μm , respectively. The surface morphology of all films exhibited predominantly faceted pyramidal grains [47].

The coalescence of isolated grains pulls the surfaces together to form new grain boundary segments due to the higher energy of free surfaces [45]. This is usually considered a process that induces tensile stress in the adjacent islands and the additional product of the coalescence is that the grain size of new crystals grow from the segments tend to be bigger. Figure 2-29 indicates that the grain size increases linearly with respect to the film thickness along the direction of film growth. The film thickness is the absolute distance from the diamond-silicon interface to the growth surface.

Figure 2-28

One intere
the methane conc
size decreases, the
increased amount
grain sizes are typ
variation in the str
compressively stre

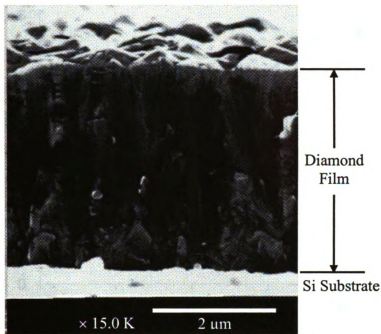


Figure 2-28: Cross-section SEM image of a diamond film on Si substrate [36].

One interesting finding in Figure 2-30 is that the grain size becomes smaller when the methane concentration increases [41]. From Figure 2-31 we can see when the grain size decreases, the intrinsic stress becomes more compressive. This is believed due to the increased amount of graphite and sp^2 carbon in films with smaller grain size. The smaller grain sizes are typically on the nucleation side of the grown diamond film. Hence a variation in the stress can occur in polycrystalline films with the nucleation side more compressively stressed and the growth side more tensile stressed.

Grain size (μm)

Figure 2-2
ob

120

100

GRAIN SIZE, nm

80

60

40

20

0

Figure 2-30
sour

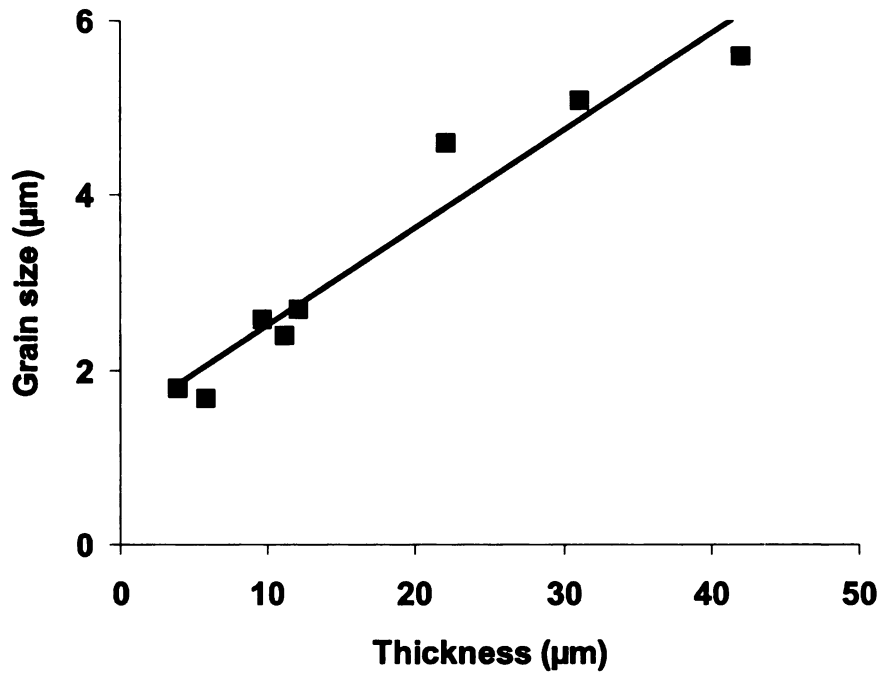


Figure 2-29: Grain size as a function of the film thickness. A linear behavior is observed [47].

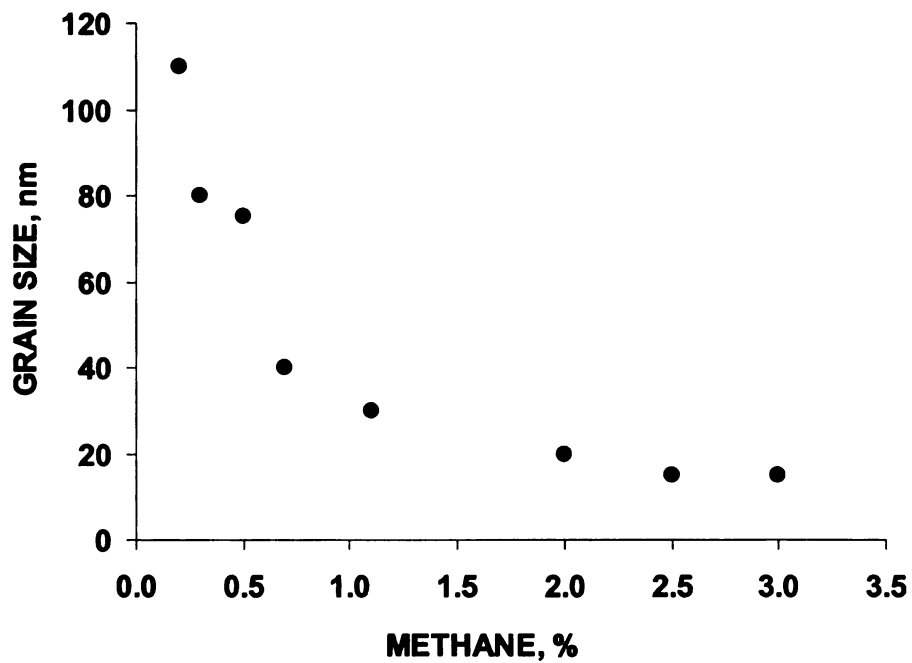


Figure 2-30: Variation of the average grain size with the methane fraction in the source gas. Grain sizes were calculated from X-ray diffraction data [41].

6
5
4
3
2
0

Stress (Gpa)

2.6.3 Defects

Diamond fi
in the diamond latt
observed under hig
interferometer. The
et al. has shown a r
structure in a high
[48].

Figure 2-32
dislocations more d
are local strain vari

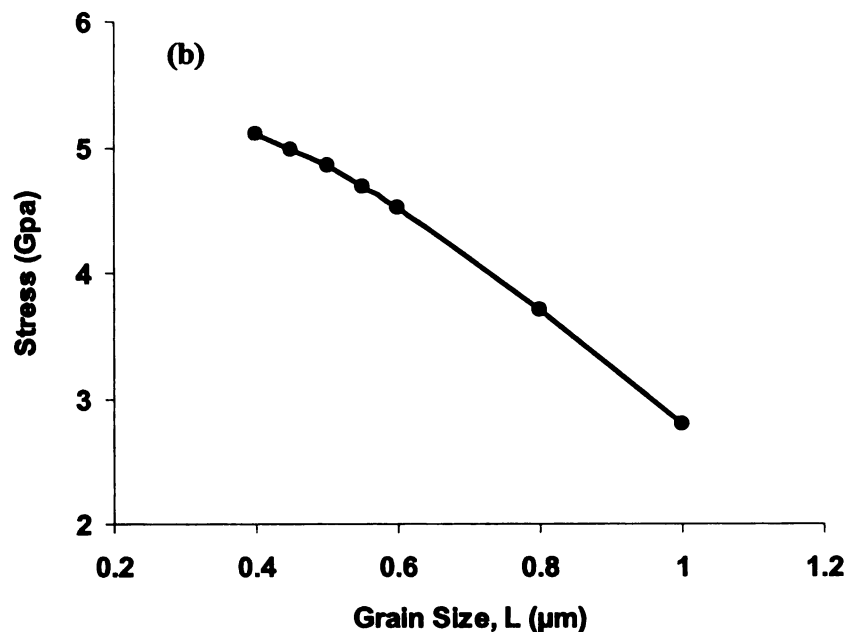


Figure 2-31: Stress and grain size relation [45].

2.6.3 Defects

Diamond film structural defects include vacancies of sp^3 hybridized carbon atoms in the diamond lattice and the dislocation of these atoms. Such defects have been observed under high resolution TEM or from Moire patterns using a Michelson interferometer. The structural defects are one of the main causes of intrinsic stress. Wang et al. has shown a misfit dislocation between the diamond lattice structure and the 'c-BN' structure in a high resolution TEM micrograph of a film deposited on a 'c-BN' substrate [48].

Figure 2-32 is the Moire pattern that shows the position of grain boundary dislocations more clearly. Also, the bending of the Moire lines in (b) indicates that there are local strain variations near the grain boundary [45].

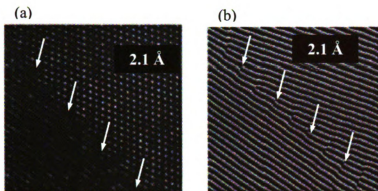


Figure 2-32: (a) High resolution TEM image of grain boundary in material grown at 800 °C and CH₄=1% (b) Moire image obtained from CH₄=0.1% [45]. Arrows in the figure roughly identify the grain boundary.

2.6.4 Impurities

Impurities include the nondiamond sp^3 -bond carbon (DLC) and sp^2 -bond carbon species that are incorporated in the diamond film during growth. Also, non-carbon species can come from the substrate, the deposition reactor walls and the feed gas. The impurities are primarily incorporated into the diamond lattice structure during the CVD growth. Figure 2-33 shows micro-Raman spectra of two diamond films of different thickness. Both spectra exhibit the diamond line at 1332 cm^{-1} plus a broad band centered at 1550 cm^{-1} [47]. This peak is attributed to sp^2 -bond graphite-like carbon. Curve 2 shows much less graphite present in the diamond film, which indicates that the diamond film shows less sp^2 -bonded graphite when the film gets thicker and the growth time becomes longer.

An intense band near 1.68 eV has been observed in the photoluminescence spectrum and has been ascribed to substitutional and/or interstitial Si defects in diamond

[49]. Luminescence

deposited on W and

centers in the Si is

Intensity (a.u.)

Figure 2-33: Micro
1) and 21 μ m
broad band
graphitic ca

2.6.5 The stress t

The data cu
from the Raman sh
axis is the distance
by the Raman peak
upward from the 1
interface. This imp
surface it is tensile

[49]. Luminescence spectra from gem-quality diamond and from CVD diamond films deposited on W and Si substrates are shown in Figure 2-34. Luminescence from Si defect centers in the Si is clear (Figure 2-34). The films were deposited on Si substrates.

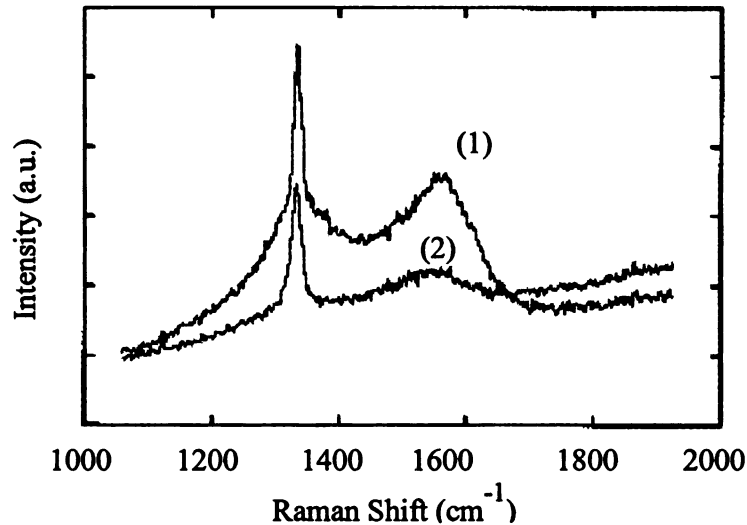


Figure 2-33: Micro-Raman spectra of two diamond films with thickness of 3.0 μm (curve 1) and 21 μm (curve 2). Both spectra exhibit the diamond line at 1332 cm^{-1} and a broad band centered at around 1550 cm^{-1} , which is attributed to the sp^2 -bond graphitic carbon phases [47].

2.6.5 The stress types and the defects and impurity contents

The data curves in Figure 2-35 are the peak width and peak-position extracted from the Raman shift in a diamond film versus depth into the film [49]. The horizontal axis is the distance from the nucleation interface. The stress-free position is determined by the Raman peak position from a diamond powder sample. The band position is shifted upward from the 1333.1 cm^{-1} position, the stress-free position, the closer one gets to the interface. This implies that the strain state at the interface is compressive, whereas at the surface it is tensile. This result is consistent with the observation of the actual sample film

bending. Another

Width Half Max

indicates that the

Luminescence Intensity

Figure 2-34:
diamo
induc

bending. Another fact can be extracted from this plot is that the peak width, the Full Width Half Maximum (FWHM) was found to decrease along the growth direction. This indicates that the diamond quality is getting better along the growth direction.

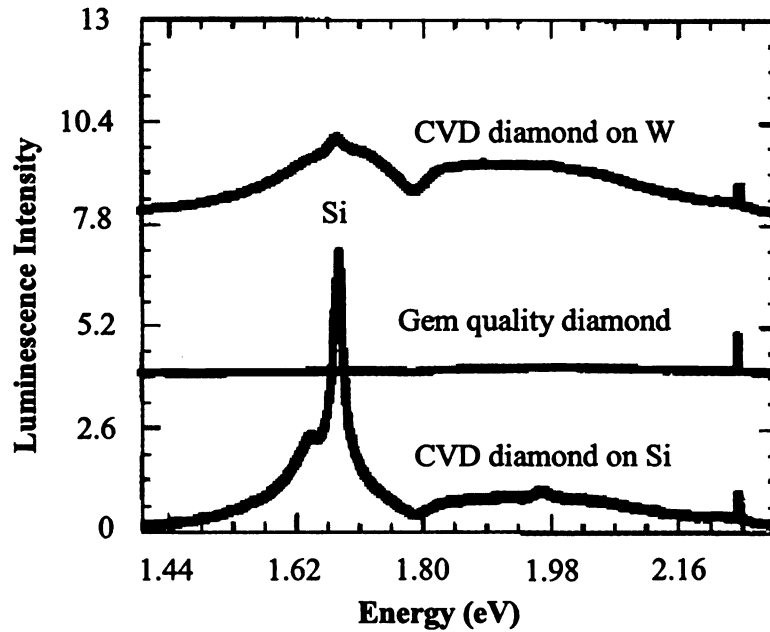


Figure 2-34: Luminescence spectra from gem-quality diamond and from CVD diamond films deposited on W and Si substrates. Luminescence from Si induced defect centers in the diamond film grown on Si is clearly shown [49].

133
133
133
133
133
133

Figure 2-35: Shift of
through
directio
to guid

Figure 2-36

cross section of the
background was su
intensity for each s
the Disorder Induc
 $\sim 1350 \text{ cm}^{-1}$. The
carbon but the wa
and its wave numb
becomes less near

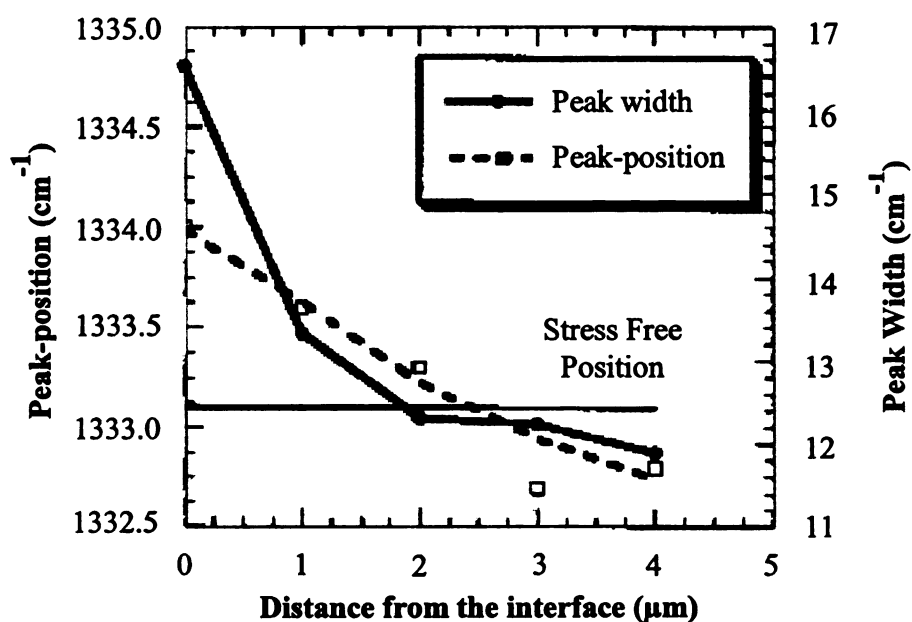


Figure 2-35: Shift of peak position and change of width of the Raman peak of diamond through the film thickness. Quality of film improves along the growth direction and strain changes from compressive to tensile. The lines are drawn to guide the eye [49].

Figure 2-36 shows a series Raman spectra measured at various positions in the cross section of the diamond film from the interface to the growth surface. A linear background was subtracted and then the intensity was normalized with the maximum intensity for each spectrum. There are three major features in the spectra. D band is called the Disorder Induced Band. It comes from the graphite carbon and the wave number is at $\sim 1350 \text{ cm}^{-1}$. The G band is called the Raman Band. It also comes from the graphite carbon but the wave number is at $\sim 1580 \text{ cm}^{-1}$. The last is the Raman peak from diamond and its wave number is at $\sim 1332 \text{ cm}^{-1}$. Figure 2-36 shows that the diamond content becomes less nearer the substrate surface, whereas the disordered sp^2 carbon fraction

increases. C

conditions.

1350 cm^{-1}

planes exp



Figure 2-36

27 The e

Arg

method for

However, it

increases. Clearly the interfacial layer that forms is disordered sp^2 carbon under these conditions. G band at 1580 cm^{-1} is for the lattice phonon for graphite while D band at 1350 cm^{-1} is disorder induced. Ratio of 1350/1580 bands is a measure of fraction of edge planes exposed, i.e., microstructural disorder.

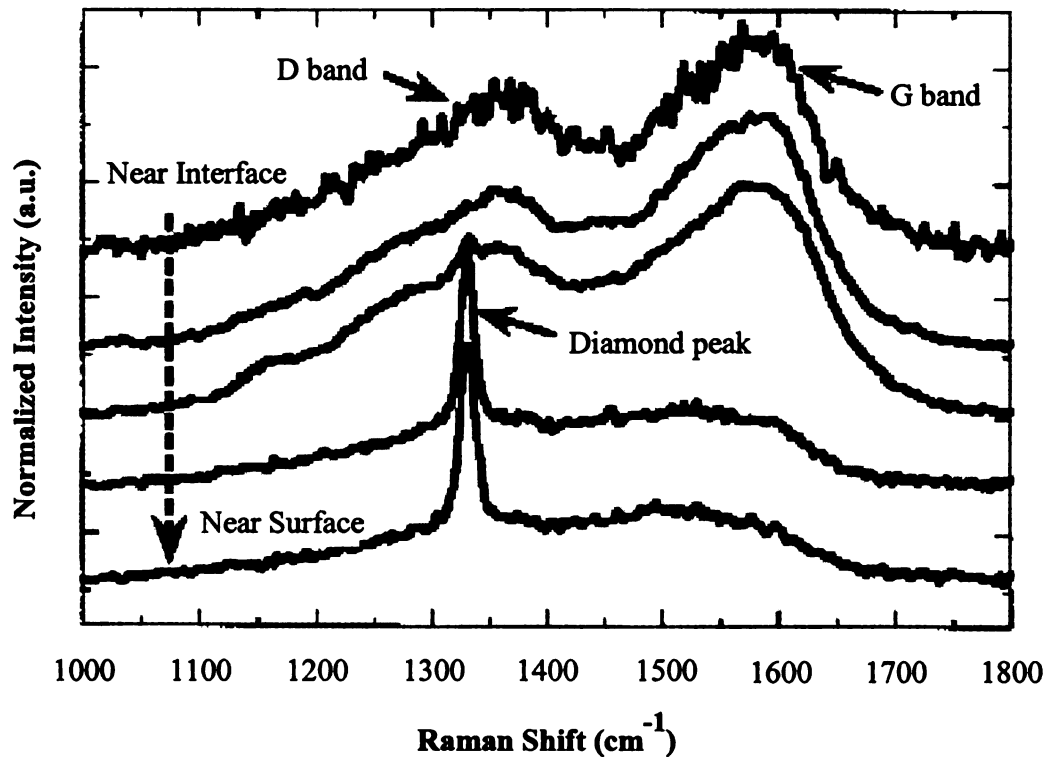


Figure 2-36: Raman spectra measured with 514.5 nm laser from the cross section of the film at intervals of $1\text{ }\mu\text{m}$ from the interface to the surface. The spectra are offset vertically for clarity [49].

2.7 The effect of argon gas addition on MPCVD diamond film growth

Argon and noble gas addition to the plasma discharge has been reported as a method for increasing the diamond growth rate in the CVD process [50, 51, etc].

However, it has not been widely used most likely due to the noticeable changes of the

film microstructu

the plasma. Both

of C_2 intensity in

gas especially wh

also witnessed th

gas. Although Zh

C_2 intensity usin

intensity general

concentration. G

absorption spectr

quantitative abso

increases signific

feed gas by Shog

hydrogen of a ty

spectrum for a p

Figure 2-37. Tw

argon are presen

consistent excep

figure. It is prob

concentration in

hydrocarbons in

film microstructure, texture and surface morphology [51], from the argon addition into the plasma. Both Zhu et al. [50] and Zhou et al. [51] groups identified the drastic increase of C_2 intensity in the CVD plasma with the increase of argon concentration in the feed gas especially when argon concentration reaches 80% and beyond. Ramamurti et al. [52] also witnessed the C_2 dimer intensity increase with an argon content increase in the feed gas. Although Zhu et al., Zhou et al. and Ramamurti et al. only measured the increase of C_2 intensity using the C_2 Swan band in optical emission spectra and the optical emission intensity generally is not an accurate quantitative measurement for gas phase species concentration. Goyette et al. obtained an absolute C_2 concentration using the white-light absorption spectroscopy and confirmed that the C_2 emission is linearly correlated with quantitative absorption measurement [53]. Furthermore the atomic hydrogen level also increases significantly with the increase of argon concentration from 5% to 10% in the feed gas by Shogun et al. during their emission actinometric investigation of atomic hydrogen of a typical plasma-enhanced CVD process [54]. A typical optical emission spectrum for a plasma with no added argon gas is provided by Zhu et al. and is shown in Figure 2-37. Two other OES spectra for plasmas with different percentages of added argon are presented in Figure 2-38 [51]. The measured results for C_2 intensity are consistent except that at the low argon addition the C_2 peak is absent in Zhou et al.'s figure. It is probable that Zhou et al. used higher deposition pressure and lower CH_4 concentration in the feed gas so that the carbon-containing species in plasma are likely hydrocarbons instead of C_2 . This is usually the case of hydrogen rich plasma. High

percentages of arg

nanocrystalline dia

film growth.

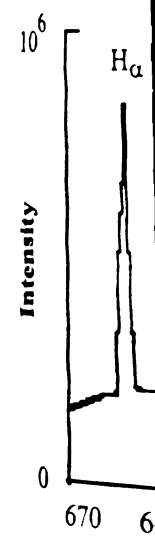


Figure 2-37: T
p!

percentages of argon (>90%) are applicable for growing nanocrystalline or ultra-nanocrystalline diamond films [55, 56, etc] and leads to a different category of diamond film growth.

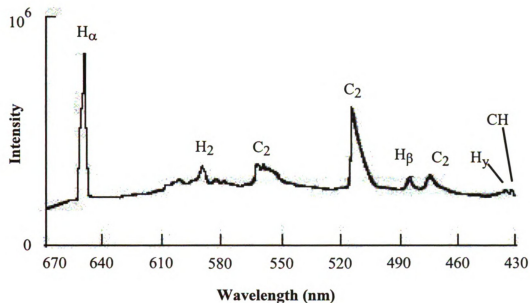


Figure 2-37: The optical emission spectrum of a (4.4% CH_4 + 95.6% H_2) microwave plasma [50].

1.2
Signal (Counts)
8
4

6
Signal (Counts)
4
2

Figure 2

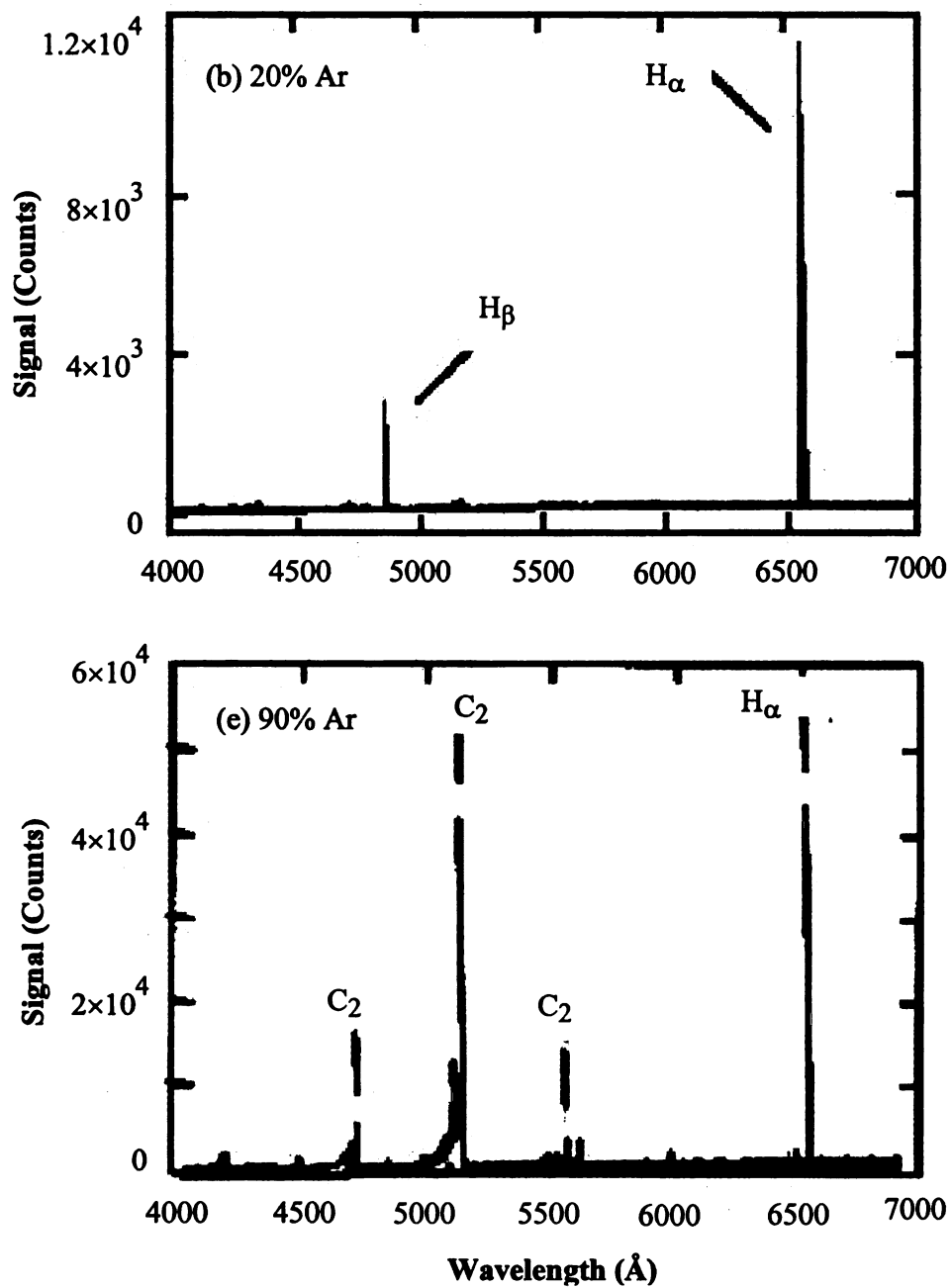


Figure 2-38: The optical emission spectra at different percentage addition of argon gas [51].

A sum
gas on the CV

1.) A

a

p

f

d

2.) C

f

th

3.) C

an

T

op

nu

ha

su

na

ca

di

4.) Lo

po

A summary of the key findings reported in the literature for the effects of argon gas on the CVD diamond growth.

- 1.) Argon strongly enhances the C_2 level in the plasma for all concentrations of argon used and moderately the atomic hydrogen level in plasma for lower percentage concentrations of argon [50, 51]. This opens a way for potentially faster CVD process of polycrystalline and nanocrystalline diamond films deposition.
- 2.) Other noble gases have similar effect, but argon gas appeared to be the most favorable one [50]. It is also the least expensive noble gas normally used in the lab.
- 3.) C_2 is a high energy molecule that can directly insert itself into carbon-carbon and carbon-hydrogen bond without the intervention of atomic hydrogen [52]. This gives opportunity for the fast deposition process. This also gives opportunity for the secondary nucleation [51, 52]. When secondary nucleation rate is high enough, nanocrystallites are produced and they don't have the chance to grow larger. That is why many researchers have suggested that the C_2 dimer seems to be the growth species for nanocrystalline diamond films [51, 52, 57, 58, 59]. Too much C_2 dimer may cause excessive non-diamond phase grow [51, 58] and therefore low quality diamond film deposition.
- 4.) Lower concentration (less than 60% of total) addition of argon may enhance polycrystalline diamond film grow without turning the film into

nanocrystalline film due to the high level of atomic hydrogen excited in the plasma. The low concentration addition of argon may be the key to the faster and better optical quality microcrystalline size diamond film growth [50, 51].

- 5.) Spatial distribution of excited radicals may also change due to the argon addition. The plasma size may be larger due to the addition of the argon gas [60]. Therefore the film thickness uniformity with argon addition is also under investigation of this study.

Chapter 3

The a

thick (usually

to increase th

The higher pr

in nonuniform

of the substra

the substrate t

This increase

pressure. The

the nature of t

in the center t

distribution is

edge. Likewis

that at the edg

requires speci

as compensat

chapter descri

Chapter 3 Experimental Setups and Procedures

The aim for the research is to synthesize high quality large area, uniform, and thick (usually 300 μm and above) fast growing diamond films. The primary approach is to increase the operating pressure of the microwave CVD system to achieve this purpose. The higher pressure leads to a smaller plasma at a fixed input power and therefore results in nonuniform plasma coverage especially at the boundary of the plasma when the edge of the substrate is at or exceeds the boundary of the plasma. To maintain the plasma over the substrate the input microwave power is typically increased, as the pressure increases. This increases the heat load to the substrate which requires substrate cooling at the higher pressure. The plasma tends to heat the center of the substrate more than the edge. Also the nature of the plasma discharge explicitly gives a reactive species density that is higher in the center than at the boundary. The result of the temperature and plasma radicals distribution is that diamond often grows faster at the center of the substrate than at the edge. Likewise the quality of the diamond at the center of the substrate is also higher than that at the edge. For many of these reasons the experimental diamond deposition reactor requires special design consideration to adjust the radical temperature variation, as well as compensate the said uneven distribution of diamond quality and growth rate. This chapter describes the deposition reactor and related experimental procedures.

3.1 MPCV

The

these compon

components

Microwave p

4.) Vacuum p

Cooling. The

State Univers

61, 62, 63, 64

system setup i

microwave po

fed into the mi

coaxial structu

by a dome shap

below where th

bell jar exterior

The wo

channels with fi

diameter stainle

and if the connec

pressure diaphra

before going into

diaphragm-sealed

3.1 MPCVD diamond system

The MPCVD diamond system consists of six major components and each of these components carries out a specific task that ensures the desired final products. These components are: 1.) Microwave plasma CVD reactor and processing chamber; 2.) Microwave power supply and transmission structure; 3.) Feed gas flow control system; 4.) Vacuum pumping and pressure control; 5.) Computer semi-automated control; 6.) Cooling. The microwave plasma-assisted CVD reactor used was designed at Michigan State University (MSU) and it has been used and modified throughout the years [27, 55, 61, 62, 63, 64, 65, 66, 67]. The cross section view [9] is shown in Figure 3-1. The overall system setup is shown in Figure 3-2. The microwave power is a 2.45 GHz, 6kW Cober microwave power supply. The power is transmitted through a rectangular waveguide and fed into the microwave cavity plasma reactor (MCPR) [9] by a MSU self-designed coaxial structure. The process chamber is located at the bottom of the brass cavity. Sealed by a dome shaped fused silica bell jar, the vacuum is maintained inside the bell jar from below where the process chamber becomes a part of the bigger vacuum chamber. The bell jar exterior is cooled by flowing air.

The working gases are supplied from cylinder tanks. There are a total of five channels with five mass flow controllers (MFC) connected to the gas cylinder by ¼ inch diameter stainless steel or plastic tubes (argon gas only) based on if the gas is flammable and if the connection structure is permanent. On each channel there is a high-purity high-pressure diaphragm-sealed valve installed at the input to the MFC. The gases are mixed before going into the processing chamber. There is another high-purity high-pressure diaphragm-sealed valve installed before the processing chamber.

Al
In

Fi
In

Fig

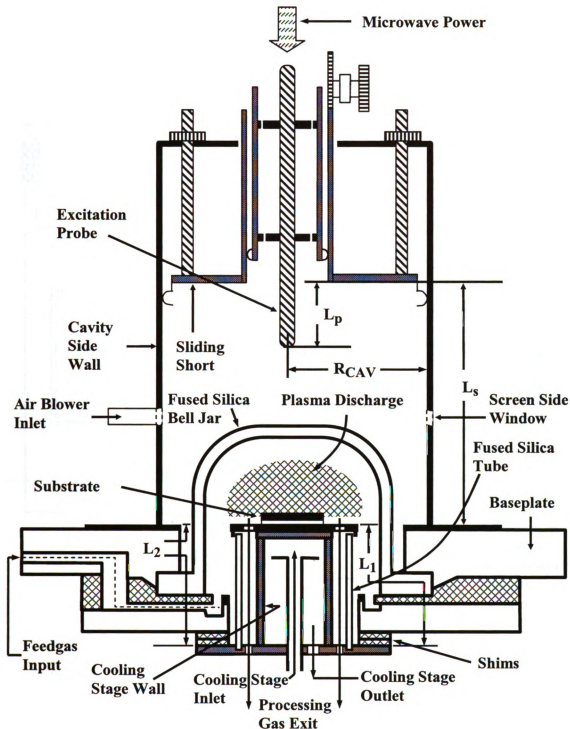


Figure 3-1: Schematic drawing of the microwave plasma CVD reactor for diamond film deposition [9]. L_s is the Short length, L_p is the Probe length, L_1 is the substrate holder height, L_2 is the depth from bottom of the cavity to base of the cooling stage, and R_{CAV} is the cavity radius.

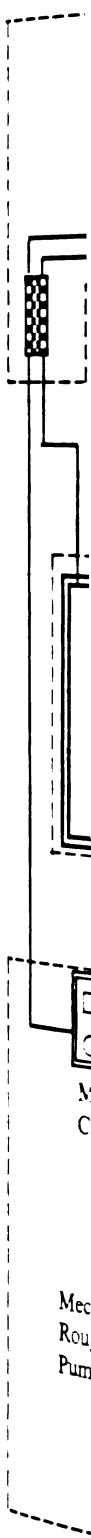


Figure 3-2:
esse
the
ever

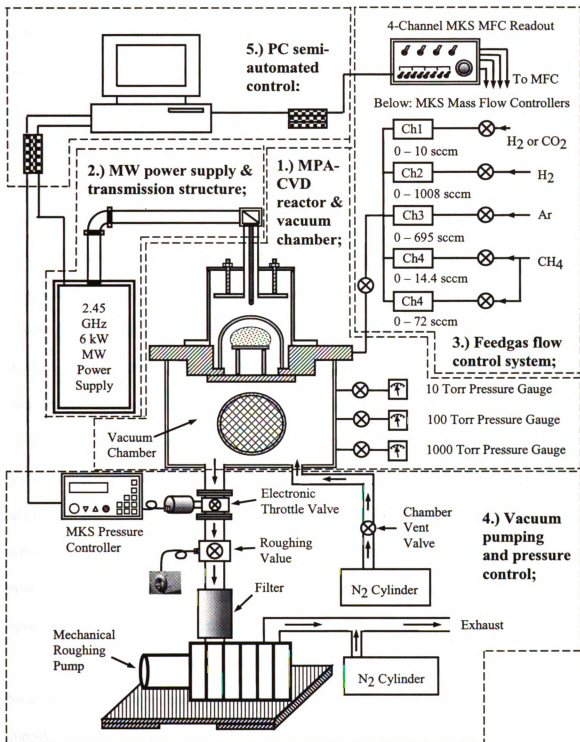


Figure 3-2: The overall microwave plasma-assisted CVD reactor system setup. All essential 5 components are depicted in the figure except the cooling for each of the 5 components. The cooling includes both the air and water cooling as which ever is fit. Symbol ⊗ represents the mechanical gas valves are installed.

The
exhaust. Th
process char
and the roug
pressure dia
nitrogen cyl
flammable c

The
computer. Th
system press
mode if the o
set rate. The
supply and ai
include the pr
adjustment du
automated tas
power, the ope
operations are

Some a
by connecting
supply is given
the manufacture
blower inside th

The pumping system consists of the components of pumping, venting, and the exhaust. The vacuum pump is a mechanical roughing pump and it is located under the process chamber. A throttle valve and a roughing valve are installed between the chamber and the roughing pump. Nitrogen is used for venting purposes and a high-purity high-pressure diaphragm-sealed valve is also installed between the process chamber and the nitrogen cylinder. The exhaust is nitrogen purged to dilute the hydrogen exhaust to non-flammable concentration.

The automated control is implemented both directly and through the control computer. The first priority is the system security and these include the monitoring of the system pressure and cooling wafer flow. The system will go to the emergency shut down mode if the operating pressure goes beyond a set value and if the water flow is below a set rate. The emergency shut down mode includes turning off the microwave power supply and all the gas flows. The other automated controls for processing purposes include the pressure adjustment, the gas flow rate adjustment, and process run time adjustment during a process. The system is also capable of running some general automated tasks such as auto read and record the incident and reflected microwave power, the operating pressure, the gases flow rate, and the time. Other conditions and operations are usually handled manually.

Some air cooling is needed in the reactor. The microwave power supply is cooled by connecting the power supply to the building water. The magnetron inside the power supply is given additional cooling from an air blower installed inside the power supply by the manufacturer. The microwave power transmission waveguide is cooled by this air blower inside the power supply and by fans set around the system. The cavity short, the

baseplate and
Neslab CFT-
that is pipe-c
blowing on th
described in c
electrical and

Inside

the cooling sta
using a set of
fed up along th
around the cool
baseplate and t
and the top slid
sliding structure
where a microw
mounted around
cavity. The tunin
short length - L_s
electromagnetic n

3.1.1 2.45 GHz

The cylin
both ends of a cy

baseplate and the cooling stage, which is used to cool the substrate, is water cooled by a Neslab CFT-300 recirculating chiller. The fused silica bell jar is cooled by an air blower that is pipe-connected to the cavity. The cavity is cooled also by three fans set around blowing on the external surface of the cavity. The overall system setups are also described in detail using flow charts and pictures by a few former MSU students of the electrical and computer department in their thesis and dissertations [27, 68, 69].

Inside the processing chamber, the substrate and substrate holders are sitting on the cooling stage and the height of the substrate is adjusted near the bottom of the cavity using a set of shims as shown in Figure 3-1. The gases are mixed in the feed gas line and fed up along the sidewall of the bell jar, then pumped out (guided by a fused silica tube around the cooling stage) of the processing chamber into the chamber below the baseplate and the cooling stage. The plasma is formed above the substrate. The baseplate and the top sliding structure above the fused silica bell jar are also cooled by water. The sliding structure is an internal microwave circuit tuning structure called a sliding short where a microwave short circuit is realized by pushing a set of finger stock that is mounted around on the top closing brass plate of the cavity against the inner wall of the cavity. The tuning mechanism is provided by moving this plate up and down varying the short length – L_s . The probe is also tunable as indicated by the length L_p and the electromagnetic mode is intended to be fixed at TM_{013} .

3.1.1 2.45 GHz cylindrical cavity mode calculation

The cylindrical cavity resonator can be formed by placing conducting walls at both ends of a cylindrical (or called circular) waveguide. Because of this, the

electromagnetic
cylindrical wave
have the same
functions. Since
the cylindrical
by classifying
cavity resonator

where X_{np} are
the zeros of the
Table 3-2 [71]
convenience of
the length (or
parameter ϵ_0 and
we are already
mode, the position
the radius of the

electromagnetic wave in cylindrical cavity resonator behaves the same as in the cylindrical waveguide except having the end boundary conditions. That is to say they have the same Bessel's differential wave equation and the same general solution – Bessel functions. Since the TEM wave doesn't exist in cylindrical waveguide, neither does it in the cylindrical cavity, the TM or the TE waves are included in Eq. 3-1 and Eq. 3-2 [70] by classifying those waves in varieties of modes. It is important to know what mode the cavity resonator is operating. Here are the mode calculation equations,

$${}^{(f)}TM_{npq} = \frac{1}{2\pi b \sqrt{\mu_0 \epsilon_0}} \sqrt{\left(X_{np}\right)^2 + \left(\frac{q\pi b}{L_s}\right)^2} \quad \text{Eq. 3-1}$$

$${}^{(f)}TE_{npq} = \frac{1}{2\pi b \sqrt{\mu_0 \epsilon_0}} \sqrt{\left(X'_{np}\right)^2 + \left(\frac{q\pi b}{L_s}\right)^2} \quad \text{Eq. 3-2}$$

where X_{np} are the zeros of the Bessel function of the first kind $J_n(x)$ and the X'_{np} are the zeros of the derivatives of the Bessel function of the first kind $J'_n(x)$. Table 3-1 and Table 3-2 [71, 72, 73] has listed roots of X_{np} and X'_{np} respectively for the convenience of calculations. Other parameters such as b is the radius of the cavity, L_s is the length (or height) of the cavity (it is also called Short length in this paper). The parameter ϵ_0 and μ_0 are the permittivity and the permeability in air (same in vacuum). As we are already familiar with the mode that is mostly used in this research, the TM_{013} mode, the position of the cavity length (or the sliding Short) can be easily calculated for the radius of the cavity and the operating frequency of the microwave power supply.

Table 3-1: R

p	k
1	2
2	5
3	8
4	11
5	14

Table 3-2: R

p	J
1	3
2	7
3	10
4	13
5	16

Table 3-1: Roots X_{np} (when n and $p = 1, 2, 3, 4, 5$) of the Bessel function of the first kind – $J_n(x)$.

p	$J_0(x)$	$J_1(x)$	$J_2(x)$	$J_3(x)$	$J_4(x)$	$J_5(x)$
1	2.4048	3.8317	5.1356	6.3802	7.5883	8.7715
2	5.5201	7.0156	8.4172	9.7610	11.0647	12.3386
3	8.6537	10.1735	11.6198	13.0152	14.3725	15.7002
4	11.7915	13.3237	14.7960	16.2235	17.6160	18.9801
5	14.9309	16.4706	17.9598	19.4094	20.8269	22.2178

Table 3-2: Roots X'_{np} (when n and $p = 1, 2, 3, 4, 5$) of the derivatives of the Bessel function of the first kind – $J'_n(x)$.

p	$J'_0(x)$	$J'_1(x)$	$J'_2(x)$	$J'_3(x)$	$J'_4(x)$	$J'_5(x)$
1	3.8317 ¹	1.8412	3.0542	4.2012	5.3175	6.4156
2	7.0156	5.3314	6.7061	8.0152	9.2824	10.5199
3	10.1735	8.5363	9.9695	11.3459	12.6819	13.9872
4	13.3237	11.7060	13.1704	14.5858	15.9641	17.3128
5	16.4706	14.8636	16.3475	17.7887	19.1960	20.5755

¹ *Mathematica* defined the first zero of $J'_0(x)$ to be approximately 3.8317 rather than zero.

For the T
cavity being 8.8
 X_{01} is 2.4048 fr
also called the th
To help v
wavelength (λ_g)
supply is shown
boundary of the
cylindrical cavity
reference [73] an

where f_c is the c
and u is equal to
of the power sur
To calcul
propagation, the

For the TM_{013} ($n = 0, p = 1, q = 3$) mode as an example, with the radius of the cavity being 8.89 cm and the frequency of the microwave power supply being 2.45 GHz, X_{01} is 2.4048 from Table 3-1 and L_s is calculated from Eq. 3-1 to be 21.61 cm. This is also called the theoretical value of the Short length.

To help visualize the fields of the cavity in Figure 3-3 and Figure 3-4, the guide-wavelength (λ_g) instead of the wavelength in air λ_0 from the 2.45 GHz microwave power supply is shown. The guide-wavelength is the wave propagating wavelength inside the boundary of the cylindrical waveguide, and it is also the guide-wavelength of the cylindrical cavity resonator. This guide-wavelength is defined in equation (10-39) from reference [73] and restated in Eq. 3-3,

$$\lambda_g = \frac{\lambda}{\sqrt{1 - (f_c/f)^2}} \quad \text{Eq. 3-3}$$

where f_c is the cut-off frequency of the cylindrical cavity resonator, and

$$\lambda = \frac{u}{f} \quad \text{Eq. 3-4}$$

and u is equal to the light speed in free space and f is equal to the microwave frequency of the power supply, which is 2.45 GHz.

To calculate the cut-off frequency of this cylindrical cavity for EM wave propagation, the appropriate equations are (equation 10-226, [73])

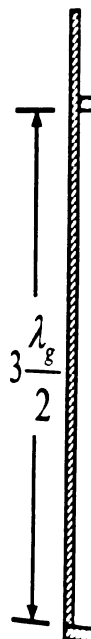


Figure 3-3: Sketch of the electric field intensity $E_z(r)$ in the E-field of the H_{10} mode in a rectangular cavity of length $3\lambda_g/2$.

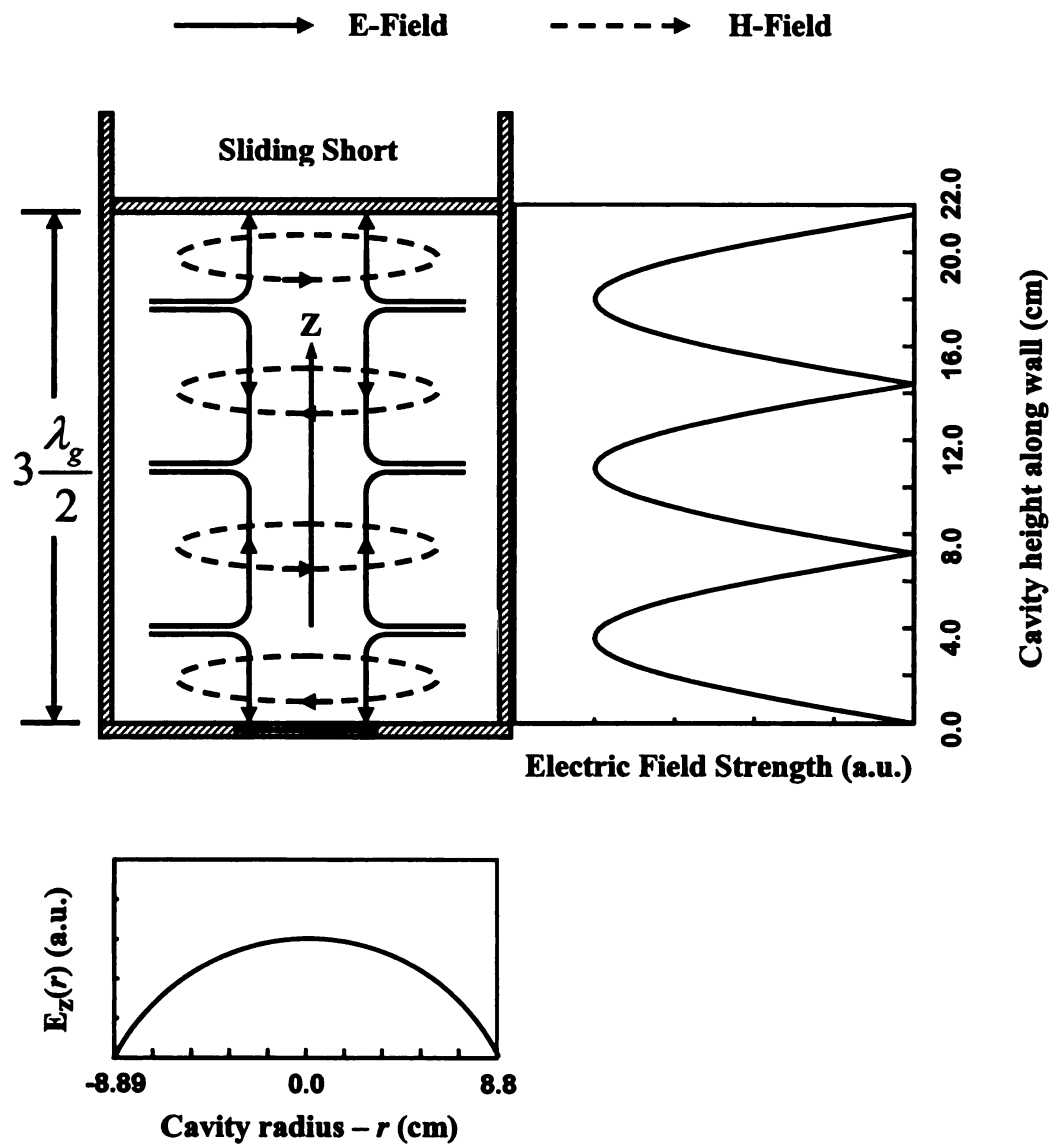


Figure 3-3: Sketch of TM_{013} electromagnetic resonant mode with the electric field intensity distribution along the cavity wall versus its height (upper right, [9]) and the E-field intensity distribution along cavity bottom versus its radius r (bottom, [20]). λ_g is the guide wavelength. Z-axis direction depicts the center axis and the cavity height direction.

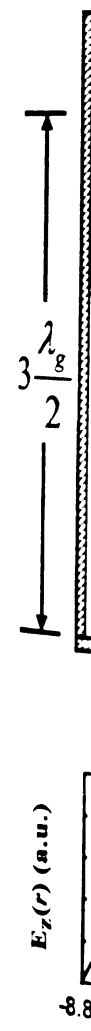


Figure 3-4: St
 int
 rig
 rac

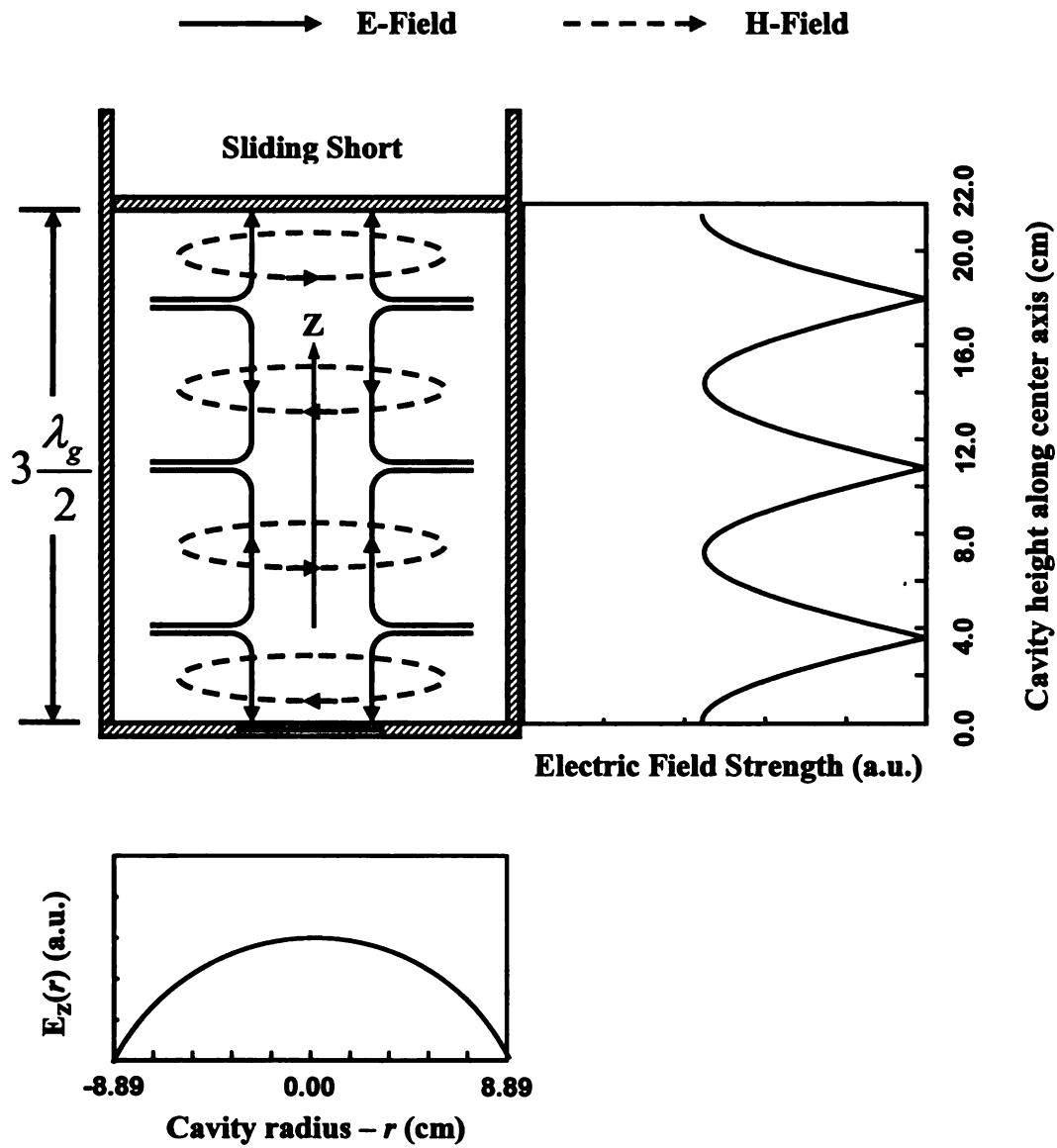


Figure 3-4: Sketch of TM₀₁₃ electromagnetic resonant mode with the electric field intensity distribution along the cavity center axis versus its height (upper right) and the E-field intensity distribution along the cavity bottom versus its radius r (bottom).

TM:

TE:

where b is the
and the wave

Therefore, h a

Then the cut-o

(73),

As an e

cm, then h is ca

and the guide-w

12.25 cm. A qu

length for TM₀,

(7.205 cm). The

TM:

$$J_n(x) \Big|_{x=X_{np}} = J_n(hb) \Big|_{X_{np}} = 0 \quad \text{Eq. 3-5}$$

TE:

$$J'_n(x) \Big|_{x=X'_{np}} = J'_n(h'b) \Big|_{X'_{np}} = 0 \quad \text{Eq. 3-6}$$

where b is the radius of the cylindrical cavity and h is defined by the propagation constant γ and the wavenumber k as shown in Eq. 3-7:

$$h^2 = \gamma^2 + k^2 \quad \text{Eq. 3-7}$$

Therefore, h and h' can be solved from the above two equations, Eq. 3-5 and Eq. 3-6.

Then the cut-off frequency in free space (or in air) can be restated as (equation 10-35, [73]),

$$f_c = \frac{h}{2\pi\sqrt{\mu_0\epsilon_0}} \quad \text{Eq. 3-8}$$

$$f'_c = \frac{h'}{2\pi\sqrt{\mu_0\epsilon_0}} \quad \text{Eq. 3-9}$$

As an example, again use TM_{013} wave as an example, X_{np} is 2.4048, b is 8.89 cm, then h is calculated as 0.2705 cm^{-1} ; the cut-off frequency is then equals to 1.29 GHz and the guide-wavelength is equals to 14.41 cm, longer than the free space wavelength 12.25 cm. A quick check to see if these calculated values are right is to check if the cavity length for TM_{013} mode (21.61 cm) is $q=3$ times of the half of the guide-wavelength (7.205 cm). The result is $21.61/7.205 = 3$.

3.1.2 The experiment

The tunable cavity is designed to operate in the TM_{013} electric mode. The bottom of the cavity is sketched in Figure 3.1. The cavity wall is made of fused silica bell-shaped regions of electric energy is stored in the field, whereas the region of the electric field of the cavity at the bottom of the electric field is $3\lambda_g/4$, which is fused silica bell-shaped regions of electric energy and the other fused silica bell-shaped regions of electric energy on the top surface.

3.1.2 *The experimental process and the details of reactor tuning*

The tuning and optimizing process is quite straight forward as long as we understand the microwave excitation of the discharge in the cavity. This cavity is designed to operate with a 2.45 GHz microwave power source exciting the plasma using the TM_{013} electromagnetic resonant mode (mostly) where the plasma is situated at the bottom of the cavity. The electric and magnetic field distribution for an ideal cylindrical cavity is sketched in Figure 3-3 and Figure 3-4 with the electric field intensity both along the cavity wall and along cavity center axis depicted versus the cavity height. It is the electric energy in the EM field that dissipates energy into the loads and does the heating. So normally we would like to place the load in or near the strongest region of the electric field, whereas the fused silica bell jar (especially the top wall) is placed in the weakest region of the electric field. The region of high electric field strength used is in the bottom of the cavity at the center axis (Figure 3-4). Along the center axis, the weakest two points of the electric field can be at $\lambda_g/4$, which is 3.60 cm above the bottom of the cavity or at $3\lambda_g/4$, which is 10.80 cm above the bottom of the cavity. However, if the top wall of the fused silica bell jar is placed at $3\lambda_g/4$ above the bottom of the cavity, there are two strong regions of electric fields included inside the silica bell jar, i.e. one is at the bottom of the cavity and the other is at $\lambda_g/2$ above the cavity bottom. The severe disadvantage of tall fused silica bell jar design is that the secondary plasma forming inside the bell jar nears the top surface. Therefore if placing the top surface of the bell jar in the weakest E-field

region is the or

above the bott

The act

flange of the fu

height is the su

height of the fu

field is 3.60 cm

for the moment

placing the top

substrate set at

has to go beyon

the top wall of t

the cavity bottom

(measured by in

ideal value of th

depending on th

discharge size. 7

is not in close c

electric field wi

used mostly for

To allow

at the bottom. M

the sample subs

region is the only requirement, the best and the only choice is at $\lambda_g/4$, which is 3.60 cm above the bottom of the cavity.

The actual height of the fused silica bell jar should include the height where the flange of the fused silica bell jar is latched in the baseplate. Refer to Figure 3-6, this height is the sum of 1.4 inch and 0.1 inch, which is 3.80 cm. Therefore, the ideal total height of the fused silica bell jar that placing the top wall in the region of the weakest E-field is $3.60 \text{ cm} + 3.80 \text{ cm} = 7.40 \text{ cm}$. Even though the bell jar height looks determined for the moment, the real plasma discharge size is much larger than the space giving by placing the top wall of the bell jar at the height of 3.60 cm above the cavity bottom while substrate set at the level at the cavity bottom. There are many choices now if the top wall has to go beyond the 3.60 cm above the cavity bottom. However, the limit is obvious that the top wall of the bell jar should not go beyond the second strongest E-field region from the cavity bottom, which is $\lambda_g/2$ above the cavity bottom. The limit of the total height (measured by inner wall) of the fused silica bell jar is $3.80 \text{ cm} + 7.20 \text{ cm} = 11.00 \text{ cm}$. The ideal value of this height should be somewhere in between 7.40 cm to 11.00 cm depending on the designer's choice for reactor pressure, the input power and the plasma discharge size. This height ensures the fused silica bell jar to have a plasma discharge that is not in close contact with the silica walls and further to contain only one region of high electric field with a single plasma discharge at high pressures. The actual dome height used mostly for this study is 9.50 cm, which is 5.7 cm above the cavity bottom.

To allow the sample to be loaded into the cavity, the cavity needs to be cut open at the bottom. Molybdenum holders and the stainless steel cooling stage are used to hold the sample substrates. By attaching the cooling stage to the bottom of the cavity, a

coaxial structure

Figure 3-5. The

substrate cooling

multiple half of

this microwave p

Figure 3-5: This
multiple
this freq

For such

molybdenum su

nearly perfect j

other criteria ar

jar and to have

coaxial structure is formed to the end of the microwave cavity resonator as shown in Figure 3-5. The typical TEM mode for this coax structure resonance formed by the substrate cooling stage is a TEM_{001} mode with the center conductor height set at $\lambda_0/2$ (or multiple half of the wavelength in air for microwave frequency at 2.45 GHz). Therefore this microwave plasma reactor is actually a hybrid microwave cavity plasma source [74].

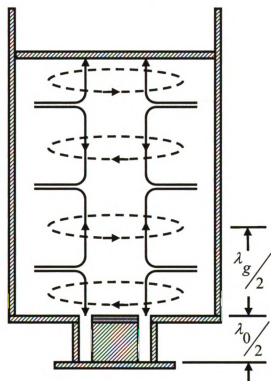


Figure 3-5: This figure shows an attached coax structure and its ideal height (can be multiple of this value) with resonant mode TEM_{001} [74]. λ_0 is the wavelength of this frequency (2.45 GHz) in the air.

For such a hybrid cavity the simplest design is to have the top surface of the molybdenum substrate holder line-up flush with the bottom of the cavity to form two nearly perfect joint cavity and coaxial structures. However in real life situation, there are other criteria and specifications such as to leave space for mounting the fused silica bell jar and to have the capability of adding or subtracting inserts onto or from the cooling

stage for substr
and exact posit
part of the base
shimming of th

is why the actua
of millimeter up

TM₀₁₃. Figure
shimming mech
microwave plas

Figure 3

components are
of inner conduc
inch, another co
diameter of oute
reactor microwa

3.2 Modifica

The resu
substrate temper
in the plasma b
pressures (100-
the plasma size
density and the

stage for substrate temperature control, that influence the shape of the coaxial structure and exact positioning of the cooling stage and substrate holders. These issues become part of the baseplate design. Hence an adjustment of the substrate height is done by shimming of the cooling stage. The cavity Short also needs to be tuned accordingly. This is why the actual cavity length L_s , tuned during the experiment is always off by a fraction of millimeter up to a few millimeters from the theoretical value 21.61 cm for cavity mode TM_{013} . Figure 3-6 shows the space in the baseplate for the fused silica bell jar and the shimming mechanism of the cooling stage with all actual dimensions (not to scale) of this microwave plasma-assisted CVD reactor and its processing chamber.

Figure 3-7 shows the equivalent microwave circuit of Figure 3-6. Three components are characterized as cylindrical cavity circuit, a coaxial circuit with diameter of inner conductor equals to 3.25 inch and diameter of outer conductor equals to 5.54 inch, another coaxial circuit with diameter of inner conductor equals to 3.25 inch and diameter of outer conductor equals to 4.685 inch. All three components are in series in reactor microwave circuit as shown in Figure 3-7.

3.2 Modifications of the MPCVD reactor for high-pressure operation

The result of increasing the reactor's pressure is not only an increase in the substrate temperature so that active substrate cooling becomes critical but also a decrease in the plasma ball size at a fixed input microwave power. The challenge of higher pressures (100-180 Torr) are that, first, higher microwave power is required to maintain the plasma size, and second, the radial gradient of the temperature, the radial plasma density and the radial profile of the active ions and radicals may also be intensified even

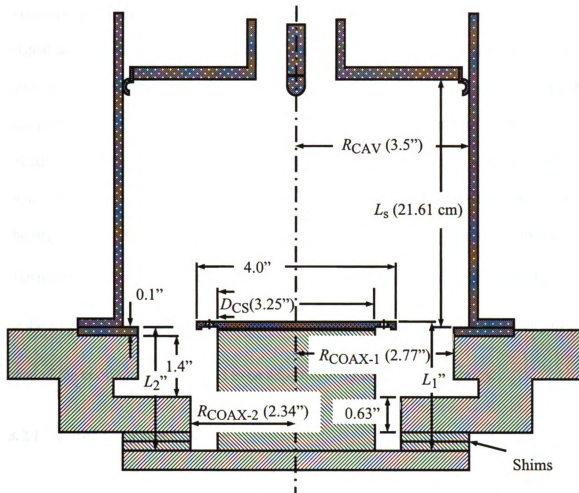


Figure 3-6: The cross section view of the brass cavity with tuning Short, the stainless steel baseplate and molybdenum substrate holder. The non-metal parts are excluded from this figure (compare to Figure 3-1) for the purpose of showing the components of the actual microwave circuit of this reactor design (include the baseplate). D_{CS} is the diameter of the cooling stage. L_1 and L_2 can be calculated.

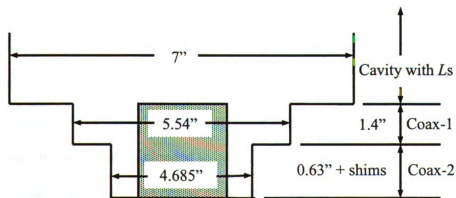


Figure 3-7: The equivalent microwave circuit of Figure 3-6.

when the same
to deal with sin
size, and the in
the temperature
greatly help to
diamond film fi
the deposition s
substrate holder
probe length L_p

base of the cool

3.2.1 Fused s

The fus
from a 70 CFM
window on the
window introd
center line of th
blowing the air
air inlet tube is
along the inner
a). This air inle
the air doesn't
Three outlet wi

when the same plasma discharge size (diameter) is maintained. This is a difficult problem to deal with since all of these may drastically affect the growth rate, the diamond crystal size, and the intrinsic stress in the film. It is believed that maintaining good uniformity of the temperature of the substrate and its surrounding, such as the substrate holder, may greatly help to improve and sometimes even compensate the non-uniform growth of the diamond film from the edge to the center. Two reactor modifications are investigated for the deposition system including improved fused silica dome cooling and an improved substrate holder configuration. Additionally, the reactor tuning (i.e., cavity height L_s , probe length L_p , substrate holder height L_1 , and the depth from bottom of the cavity to base of the cooling stage L_2) need to be adjusted to optimize the uniformity.

3.2.1 Fused silica dome cooling

The fused silica dome (also called bell jar) is cooled by air blowing into the cavity from a 70 CFM flow rate Dayton air blower. In the original design, a 2-inch diameter window on the cavity drilled with 3mm size holes and a brass tube soldered onto the window introduces the cooling air from the blower onto the top portion and along the center line of the dome (Figure 3-8). A modification was implemented where instead of blowing the air along the center line of the cavity as in the old design, the 2-inch diameter air inlet tube is introduced along the side of the cavity wall so that the air is blowing along the inner wall of the cavity creating a swirling motion inside the cavity (Figure 3-9, a). This air inlet window is also intended to be located above the fused silica dome so that the air doesn't blow directly on the dome, which can create an asymmetry in the cooling. Three outlet windows are opened near the bottom of the cavity. Each outlet window is

120° angle in

fused silica dc

a

Top
View

Figure 3-8:

a

Top
View

Figure 3-9:

120°-angle in Φ direction from each other. It is also at a position near the base of the fused silica dome (Figure 3-9, b).

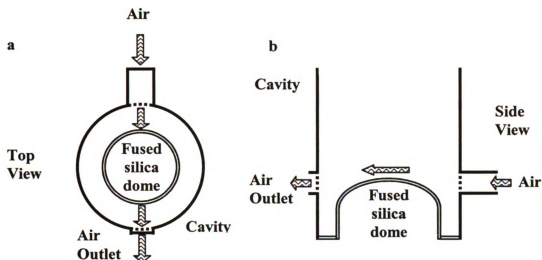


Figure 3-8: Original fused silica dome cooling design: a. Top view and b. side view of the cavity.

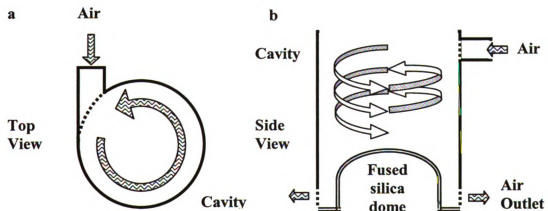


Figure 3-9: Modified fused silica dome cooling illustration: a. Top view and b. side view of the cavity.

3.2.2 *Substrate*

When t

condition, the s

active cooling c

The cooling of

cooling stage. T

flow inside the

conductively vi

MSU design of

plasma from the

Subsequent sub

substrate, can a

subsequent sub

used if a higher

Another

uniformity acro

uniformity of th

the substrate ho

direction. The

a plasma near t

operating frequ

assuming an id

3.2.2 Substrate, substrate holder and insert configuration

When the plasma discharge environment is extended to the high-pressure condition, the substrate is heated to a high temperature often over 1000 °C. This is when active cooling of the substrate is needed to get proper conditions for diamond deposition. The cooling of the substrate is provided by sitting the substrate holder(s) on top of a cooling stage. The cooling stage is a stainless steel cylinder with a flat top and cold water flow inside the cylinder to carry out the task of cooling. The substrate is cooled conductively via contact with the top surface of the cooling stage (Figure 3-10). In the MSU design of Figure 3-1, a main substrate holder base is designed to separate the plasma from the cooling stage and also to guide the gas flow in the process chamber. Subsequent substrate holder pieces, which usually sit in between the main holder and the substrate, can also be designed for the purpose of raising the substrate temperature. These subsequent substrate holders are called ‘inserts’ in this dissertation. More inserts can be used if a higher temperature is needed for the substrate.

Another important design purpose for these inserts is to improve the temperature uniformity across the substrate during diamond deposition thereby improving the uniformity of the deposition rate and diamond quality. In fact, the main consideration for the substrate holder/holders design is the nonuniformity in heating along the radial direction. The 7-inch diameter cylindrical microwave-heating reactor is designed to form a plasma near the bottom of the cavity using a TM_{013} electromagnetic field mode at the operating frequency of 2.45 GHz. The electric field distribution produced in this cavity, assuming an ideal TM_{013} mode, is the strongest at the center and gradually gets weaker

along the direc

Figure 3-4. Th

experience a si

distribution. Th

substrate. In ad

which is air coo

heated. Though

the center to th

inserts should h

achieve temper

the purpose of c

case on the sub

along the direction of the radius up to the wall of the cavity as shown in Figure 3-3 and Figure 3-4. The excited plasma discharge ball, which sits right on the substrate, may experience a similar E-field distribution and therefore may have a similar energy distribution. The center of the substrate usually is then heated hotter than the edge of the substrate. In addition, the edge of the plasma is cooled by the walls of the silica bell jar, which is air cooled from a blower in order to prevent the silica bell jar from getting over heated. Though it is inevitable, this may add a few degrees of temperature gradient from the center to the edge of the plasma. The idea is that the substrate holder/holders or inserts should have the substrate center ($r = 0$) cooled more than the edge in order to achieve temperature uniformity across the substrate. This idea may be carried further for the purpose of compensating the slower growth of the diamond films that is usually the case on the substrate edge. The main control is the temperature.

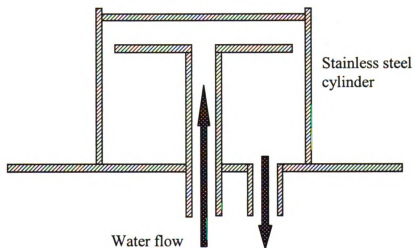


Figure 3-10: The cooling stage structure.

The act
insert is in good
number of grooves
groove width is
edge of the insert
in the heat flow
are discussed in

Figure
stacking on the
replacement in
edge.

M

Figure

The actual design is carried out using the simple conductive cooling method. The insert is in good contact with the main holder in the center portion of the insert with a number of grooves cut on the bottom surface of the insert at the larger "r" location. The groove width is narrower near the center and is gradually widened as it is getting to the edge of the insert. The gap between the insert and the main holder can be used as a break in the heat flow at radiuses some distance from the center. A few actual design samples are discussed in Chapter 5.

Figure 3-11 shows an example of how substrate, inserts and the main holder are stacking on the cooling stage. The quartz tube is acting as a guide to the gas flow. The replacement insert shows the idea of cooling the center of the substrate more than the edge.

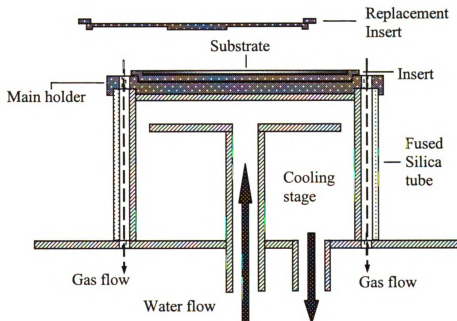


Figure 3-11: An example of substrate, inserts and the main holder are stacking on the cooling stage. The fused silica tube is acting as a guide to the gas flow.

ence

is th

The

sho

start

sho

The

sign

be l

plas

thin

fusi

cou

wit

and

ov

or

wi

co

3.2.3 High pressure high power operation safety

In general, there are three kinds of risk the operators or lab personnel may encounter during the operation of the microwave plasma-assisted CVD system. The first is the high power microwave radiation that could possibly leak from the system.

Therefore, a microwave leak detector is required to be equipped with the system and it should be used to periodically check for leaks during the experiment, especially at the start of the experiment. If microwave leak is detected the microwave power supply should be shutdown immediately either by operator or automatically by the controller.

The second risk is the UV radiation from the plasma discharge. The plasma can radiate significant UV light, especially for some feedgas such as argon. If the UV is bright it can be harmful to human eyes. Blockage of the UV light should be done when an argon plasma or a plasma containing a high percentage of argon in the feed gas is present. The third risk is the thermal run away of the plasma heated substrate or direct overheat of the fused silica bell jar causing possible melting of the fused silica bell jar. An explosion could possibly happen when flammable gases, such as the hydrogen and methane, mix with oxygen in the air. If the fused silica dome or substrate gets too hot the feedgas flow and microwave energy should be shut off immediately.

High pressure and high power microwave plasmas are more susceptible to overheating of the substrate and the fused silica bell jar if cooling is not properly installed or the reactor is not properly tuned. The diamond deposition system should be installed with safety interlocks that shut they system down quickly and safely if unsafe operating conditions are detected. In general, the MPCVD system should be closely watched during

high

not

3.3

opt

sub

opt

pyr

mea

1.0

pyr

mea

obje

since

at λ

then

temp

From

meas

color

from

high pressure, high power operation, especially in parameter regimes that the system has not previously been operated.

3.3 Measurement of substrate temperature

Substrate temperature measurement requires a non-contact measuring device. The optical emission spectroscopy based thermometer is on the top of the list with which the substrate temperature can be easily measured through the view window. Two kinds of optical thermometers currently used in the lab include a handheld portable infrared pyrometer with one fix wavelength (one color) at $0.96\ \mu\text{m}$. The range of the temperature measurement is from 600°C to 3000°C with the emissivity being adjustable from 0.0 to 1.0. The ideal black body radiation is assumed when the emissivity is set at 1.0. This pyrometer gives good measurements and is convenient only when the emissivity of the measured object is known and no blockage except air is in between the pyrometer and the object. Materials, even if they are transparent to the eye, may affect the measurement since they may absorb and reflect the infrared light emitted.

The other infrared thermometer detects two colors within the infrared wavelength at $\lambda_1 = 0.85 - 1.05\ \mu\text{m}$ and $\lambda_2 = 1.05\ \mu\text{m}$. The advantage over the one-color infrared thermometer is that no emissivity needs to be input by the user [75]. The measurable temperature range for the unit used in this investigation is also from 600°C to 3000°C . From experience for the diamond deposition process in the reactor used in this study, the measured temperature from the two-color pyrometer is higher (up to 120°C) than the one-color pyrometer with the emissivity set to 0.6 when the measured substrate temperature is from 800°C to 1200°C . Another issue is the temperature measurement across the

substrate

color uni

It is desi

to repeat

needed to

3.4 Re

T

temperat

probe dep

base of th

the top su

inserts to

surface o

stage (Fi

A

best posi

CVD dia

substrate

particular

to another

adjustmen

addition to

substrate appears to be problematic. The pyrometer, no matter the one-color or the two-color unit, needs to be focused on the substrate in order to give an accurate measurement. It is desired that the pyrometer can focus on a few points across the substrate and be able to repeat the measurement at exactly the same points. A stable pyrometer mounting is needed to get repeatable temperature measurements.

3.4 Reactor tuning for uniform temperature on substrate

The reactor tuning consists of adjusting four parameters to get uniform temperature distribution across the substrate. The four parameters are cavity height L_s , probe depth L_p , substrate holder height L_1 , and the depth from bottom of the cavity to base of the cooling stage L_2 . The substrate holder height L_1 is defined as the height from the top surface of the molybdenum substrate holders including the thickness of all the inserts to the top surface of the base of the cooling stage. L_2 is measured from the upper surface of the brass piece bottom of the cavity to the top surface of the base of the cooling stage (Figure 3-1).

After the substrate holder set is chosen, it is important to optimize it to be at the best position for the most uniform temperature of the substrate inside the plasma-assisted CVD diamond deposition reactor. Because the different shapes and heights of the substrate holders they can vary the microwave field distribution, the system operation, in particular the plasma absorbed power, may be significantly different from one holder set to another. So obtaining a good plasma discharge for diamond deposition may need adjustments of the vertical position of the substrate holder along with the cooling stage in addition to the sliding Short plate adjustments. A useful indicator of a “good” plasma

discharge is that the reflected microwave power is at or near its minimum as the vertical position of the sliding Short is adjusted [76, 77, 78].

The reason for tuning to the minimum reflected power is that the plasma size in the fused silica bell jar is directly related to the reactor pressure and the absorbed microwave power for a given composition of gasses. When the incident microwave power and reactor pressure is fixed, the plasma size can be adjusted only by tuning the reflected microwave power, i.e. by tuning the substrate holder position, the sliding short position and/or the probe position. Tuning the reflected microwave power to the minimum ensures that the system has the largest size of the plasma ball for a given setting, therefore to have the possibility of the most uniform temperature distribution on the substrate.

Also it is desirable to have the discharge position in contact with the substrate as shown in Figure 3-12. The plasma is like a soft ball sitting on the substrate with the lower half of the sphere in contact with the substrate. It is obvious that one should push the substrate higher in order for it to be fully covered by the plasma. The temperature uniformity should also be expected to be better. However, the plasma ball also changes its shape (smaller and may be flatter, and sometimes even donut shape) accordingly and it is difficult for the substrate to be actually at the center of the plasma sphere before the fused silica bell jar gets too hot. The rule of thumb for this tuning and optimizing process is always tune the system to minimum reflected power while trying to push the substrate more into the plasma sphere. A consistent observation is that the reflected microwave power gradually becomes smaller during the system reactor pressure-increasing period at the beginning of each experiment. This means that the reflected microwave power gets

smaller when the plasma ball size gets smaller and vice versa. As we know the plasma size becomes smaller when the reactor pressure is higher. So pushing up the substrate and its holder set is a physically “squeezing” of the plasma ball in between the substrate and the quartz bell jar, and it tends to reduce the system reflected microwave power.

For the current system this substrate position is adjusted by adding or reducing the shims where they are inserted in between the bottom plate of the cooling stage and the baseplate that sustains the cavity. So the vertical position of the substrate and holder set is lowered if shims are added and lifted if shims are reduced (see Figure 3-1).

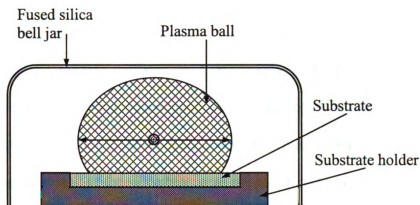


Figure 3-12: Relative position of the fused silica bell jar, the plasma ball and the substrate.

The second variable that may be used to determine the optimal position of the substrate and the holder set is the radial temperature uniformity of the substrate. The initial and also the necessity condition for uniform temperature across the entire wafer is that the plasma fully covers the substrate. The bigger the ratio of the plasma size over the substrate size, the more uniform of the substrate temperature will be. This means a certain minimum microwave power output is desired from the microwave power supply or the temperature uniformity will be impossible. The radial temperature distribution should be

systematically measured over the changes of the thickness of the shims while tuning the sliding short and the probe to the position where the reflected microwave power is the minimum. The best result should be used for the formal diamond growth run.

The temperature uniformity can be well presented in the operational field/road map as shown in Figure 3-13. The operational road map defines the substrate temperature range for a range of chamber processing pressures and the absorbed microwave powers by plasma. This road map is usually used to characterize the working range (condition) of a microwave plasma cavity reactor for a particular substrate loading configuration (cooled or floating substrate holder configuration, holders and inserts configuration, shims configuration) and reactor tuning and cooling configurations. For example, in the parallelogram enclosed working region of the diamond deposition, the left line of the parallelogram draws the line where the plasma is big enough to cover the substrate and the right line of the parallelogram shows the line where the plasma may be too large such that it touches the inner wall of the silica bell jar as indicated in the picture. The upper and lower line of the parallelogram indicates the substrate temperature limits for deposition of good quality diamond.

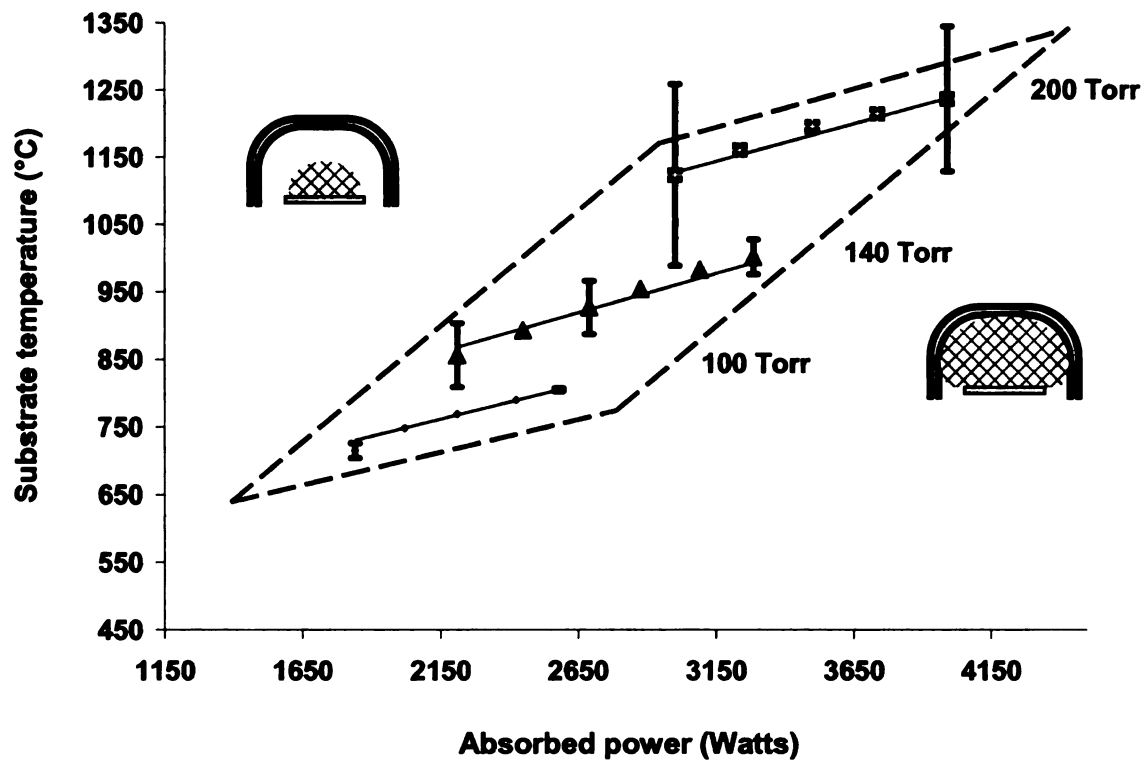


Figure 3-13: Illustration of the operational field/road map and parameters the map describes.

Finally, the temperature error bars in Figure 3-13 can be used to describe the spatial temperature variations across the substrate. The temperature error bar is defined as the maximum-minimum temperature of the substrate and usually the maximum (highest) temperature is at the center of the substrate and the minimum (lowest) temperature is at the edge of the substrate. The temperature uniformity is represented by the temperature error bar. The smaller the error bar, the more uniform the substrate temperature. Usually the most uniform temperature is obtained at the lowest processing pressure and the worst temperature uniformity is obtained at the highest processing pressure. The road map is meaningful and helpful only when the substrate loading configuration is or near optimal along with the reactor tuning and cooling.

The third variable is a limitation that the substrate position and other tuning position should not push the discharge too high that it touches the fused silica bell jar. The top wall of the fused silica bell jar is designed to be near the zero electric field interaction position at $\lambda_g/4$ from the cavity bottom in Figure 3-4. The purpose of this design is to avoid the electric field directly heating the discharge near the fused silica bell jar or directly heating the bell jar which may occur due to some unwanted deposition on the inner wall during long experiments. The other reason for this top wall of the fused silica bell jar to be at the current position instead of being made higher is to avoid the secondary plasma forming inside the bell jar. The fused silica bell jar acts as a separator that holds down the excited plasma onto the substrate instead of floating to the other parts of the cavity. So during this optimization, the surface position of the substrate must not be pushed up so high that the induced microwave plasma gets too close to the quartz bell jar and directly heats the bell jar. This is a risky situation that should be avoided.

3.5 Nucleation, selection of substrate and its pretreatment

This research project has an objective to grow polycrystalline CVD diamond films on silicon substrates and then remove the thick diamond films from these substrates. Silicon wafers are chosen as the substrate not only because of the tremendous success using it as the substrate by many researchers in the past, but also to extend and advance the research of Dr. Kuo-Ping Kuo who was a former MSU student [27]. Technically, diamond does not usually nucleate directly on a non-diamond substrate surface under the typical CVD conditions, except when the composite gases are given additional degrees of ionization and extra energies, such as when a negative substrate potential is applied in bias enhanced nucleation [79]. This treatment is generally called bias enhanced nucleation (BEN) and the heteroepitaxially oriented diamond grains which exhibit a defined orientation relationship to the substrate lattice were found directly on the clean silicon surface by Jia et al. using a high-resolution electron microscope (HREM) [80, 81]. This means that diamonds can be formed directly onto the silicon crystal despite a large lattice mismatch. However, more often an intermediate carbide layer is formed before the subsequent diamond growth. Evidence indicates that the intermediate carbide layer formation may strongly affect the subsequent diamond film growth for various substrate materials including silicon [6, 82]. Though limited quantitative data is available for the carbide layer formation under the working conditions of diamond nucleation, diamond films have been successfully deposited directly on β -SiC via microwave plasma assisted chemical vapor deposition by B.R. Stoner et al. [83]. In this dissertation work the diamond is nucleated using a wafer polishing/scratching

technique that uses diamond powder. The diamond crystal orientation is random using this polishing/scratching technique.

The current microwave plasma-assisted CVD reactor for diamond film deposition was originally designed for 3-inch and 4-inch substrates at low reactor pressures. Under higher pressure conditions the substrate is usually selected to be 2 inch in diameter [26, 27]. In this project the substrate size for deposition at higher pressures are 2 and 3 inch diameters. The thickness of the silicon substrate that has proven to be most useful is 1mm when growing relatively thick diamond films. This thickness has proven to be rigid without allowing too much bending of the silicon wafer with the diamond film but flexible enough to avoid the diamond film peeling off from the silicon wafer due to the residual stresses formation during the diamond film growth. The silicon wafers used are standard single crystal wafers with orientation at $\langle 100 \rangle$, either P-type or N-type doped.

Other considerations for substrate selection are factors such as (1) the melting point of the substrate needs to be higher than the temperature range required for diamond deposition and, (2) little or no carbon solubility or reaction. All the above reasons ensure silicon remains one of the few popular and widely used substrate materials for the deposition of diamond films.

Substrates need some kind of seeding with diamond in order to achieve diamond nucleation at the beginning stage of the diamond formation on the substrate. The seeding procedure varies depending on the diamond film specifications. One of the important specifications is the diamond crystal size that determines the seed size which may be used for seeding process. The other very important specification is the thickness of the diamond film that needs to be produced. Thinner films usually require denser seeding

with smaller size of seeds such as nanocrystalline films. They usually require better uniformity of seeding in order to cover the entire substrate with uniform sized diamond crystals and minimal pin holes.

On the other hand, microcrystalline films are often grown for thicker films. They can be initiated with lower nucleation rate and uniformity in contrast to nanocrystalline films. A continuous layer of microcrystalline diamond film can be formed within the first couple of hours of the CVD process by using the right chemistry and usually the moderately dense and uniform seeding. For this reason, the silicon substrate can simply be seeded by polishing the polished surface of the wafer using 0 to 0.25-micrometer size natural diamond powder for about 5 to 15 minutes. Then the silicon surface is gently wiped after the diamond polishing to eliminate some clusters of diamond powders off the silicon wafer. Very often it is worthwhile to check the seeded surface under the optical microscope for the seeding density and uniformity. For reference, the seeding density used in this research is from a minimum of 25,000 seeds per square centimeter (Figure 3-14) to a moderately high seeding density of 741,000 seeds per square centimeter (Figure 3-15). The two numbers obtained above are approximated based on visually counting the dots in the figures. The pictures are taken by a camera that is attached to the top of an optical microscope. The magnifications of the ocular and objective lenses used is 10×10 . It needs to be noted that many fine diamond particles are too small on the picture to be viewed so that they are not counted. The scratches on the silicon surface also serve as seeds for the diamond nucleation. So they should also be included as seeding. These two seeded surfaces are two typical examples selected from among the

samples that

satisfactory g

Fig

Fig

samples that show the near minimum and maximum seeding densities used that give satisfactory growth results.

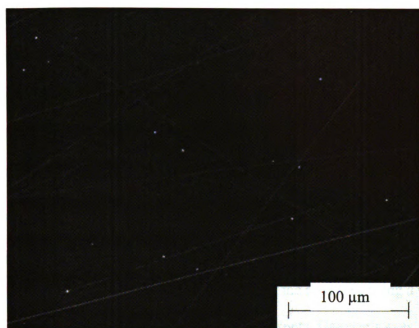


Figure 3-14: About 32 seeds within $345\ \mu\text{m} \times 367\ \mu\text{m}$ silicon surface.

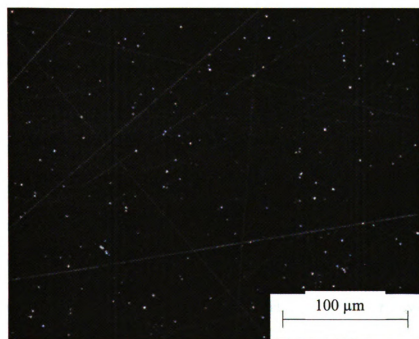


Figure 3-15: About 660 seeds within $331\ \mu\text{m} \times 269\ \mu\text{m}$ silicon surface.

The detailed

1. Place

polish

2. Scoop

(about

subst

profe

seedi

repea

3. Gentl

the K

judgr

of the

4. Chec

For m

our lab and u

thesis from t

matter of fac

1. Place

vacu

wafers

to rub

The detailed nucleation procedure consists of 4 steps:

1. Place the silicon wafer face down and rub the seeding side on a piece 8” diameter polishing microcloth for a couple of minutes. Flip it over when it is finished;
2. Scoop a small amount of 0 to 0.25 micrometer size natural diamond powder (about 30 mg for a 2-inch diameter substrate, 60 mg for a 3-inch diameter substrate) onto the wafer surface, then wrap the index finger with the delicate professional task wipers – Kimwipes[®] EX-L and rub the diamond powder on the seeding surface, usually the polished side of the wafer. Use more powder and repeat this step if not all area of the wafer is fully polished;
3. Gently wipe the excessive diamond powder off the seed area using a clean part of the Kimwipes. Clean off the obvious clustered spots. Use one’s eyes for the best judgment of the uniformity. Don’t wipe too hard. Clean the edge and the backside of the wafer;
4. Check the result under the optical microscope.

For more strict requirements, the original seeding process that was developed in our lab and used for some years is suggested. Though the procedure can be found in the thesis from the former graduate student [68], it is repeated here as a reference. As a matter of fact the previous simplified procedure above is modified from this procedure.

1. Place the silicon wafer on the wafer holder and connect the holder to a small vacuum pump. Take a small amount of diamond powder and put them on the wafer (1/8 tea-spoon). Use a delicate professional task wiper – Kimwipes[®] EX-L to rub the wafer surface (with the diamond powder) for 5 to 7 minutes;

2. Place wafer polished side face down in a watch glass dish and set the dish in a bigger cylindrical glass container filled with methanol just about enough to cover the wafer and the watch glass;
3. Fill de-ionized (DI) water in an ultrasound cleaner;
4. Place the glass container in the ultrasound cleaner and run ultrasound for 30 minutes;
5. Take out the wafer and rinse it in acetone. Rub with the Q-tips if necessary. Rinse the wafer in methanol;
6. Rinse wafer in DI water for 5 minutes;
7. Blow dry with nitrogen gun.

This procedure was developed as the standard procedure for nanocrystalline diamond film seeding by Dr. Wen-Shin Huang who was a former MSU student and it is presented in her dissertation [68].

3.6 General procedure of starting up and shutdown a experiment

The detailed procedure of start up and shutdown is described below. There may be a few differences with the details from former students who used the system based on the changes of the system or personal preference, but overall the whole process should be the same in general.

1. Load the seeded silicon substrate with a selected set of substrate holders and pump down the chamber till about 4 mTorr. This value usually indicates that the system doesn't have a vacuum leak and good enough to start a deposition process. However, the pump down can take up to several hours depends on the power of the roughing pump, the chamber size and the humidity in the air when the system was loaded with

a substrate. Flushing with 3 to 5-sccm argon gas during pump-down can significantly shorten the pumping time to about 30 to 40 minutes.

2. Turn on all the cooling water systems including the microwave power supply, the baseplate and reactor cavity, and the cooling stage; Turn on all the cooling air including the bell jar, microwave coax feeding structure air and all the blowers and fans; Open the exhaust purging nitrogen valve; Then switch on the microwave power supply to be warmed up.
3. Preset the sliding short and the probe position to the position for electromagnetic (EM) wave mode TM_{013} with the calibrated offset (if any). For the current cavity sliding-short, the short is set to 21.6 cm with calibration of -1.14 cm, and the probe is set to 3.5 cm. The position of the previous experiment is also a good reference position.
4. On the computer, open a new process (if it does not exist), select the gases and flow rate, set the system reactor pressure and run time for each step. The process usually should include a final step for the hydrogen termination of the diamond surface (see shutdown procedure). The on screen instructions are self-explanatory. Finally, start this process in auto mode. The grade for hydrogen and argon gases is Grade 5.5, research grade gases with 99.9995% purity. The grade for methane is Grade 5.0, ultrahigh grade gas with 99.999% purity. The hydrogen has less than 1 part per million (ppm) of oxygen, water and nitrogen impurities and less than 0.5 ppm of hydrocarbons and carbon dioxide. Argon has less than 0.5 ppm oxygen and hydrocarbons and less than 1.5 ppm water. The 99.999% purity methane has less than

5 ppm ethane and nitrogen, less than 2 ppm oxygen, other hydrocarbons and water, and total impurities are less than 10 ppm.

5. The plasma should be started when the system reactor pressure is around 5 to 10 Torr. If 5 Torr is preset in the computer process, the microwave power indicator on the computer screen is on when the reactor pressure reaches 5 Torr. The microwave power should be enabled by pushing the red button on the power supply panel. Turn the power knob up slowly until the plasma starts.
6. Gradually increase the microwave power as the reactor pressure increases so that the plasma ball is big enough to cover the substrate since the plasma ball is getting smaller as the reactor pressure is getting higher. After the system reaches the designated pressure, 120 Torr for example, carefully tune the sliding short and the probe till the reflected microwave power is minimum. It is very important to check the substrate temperature is not too high or thermal run away may occur. Adjust the plasma size properly by adjusting the microwave power from the knob on the power supply panel.

The shutdown procedure can also be partly automated, controlled by the computer except the microwave power adjustment. The detailed steps include,

1. Automatically close the methane and argon channel if argon is used.
2. While the hydrogen plasma is still on, gradually decrease the pressure every two minutes for each decrement of 20 Torr pressure. If it is necessary, turn down the microwave power to avoid the plasma ball getting too big.
3. The microwave power and plasma shuts off after 2 minutes duration at the last step of 20 Torr.

4. Turn off the water flow for the cooling stage after the microwave power is off for about 5 minutes to avoid the silicon-diamond wafer being over cooled. Other steps are omitted here.

3.7 Profile the substrate for growth uniformity and diamond film thickness measurements

3.7.1 Measurement of diamond film thickness

Diamond film thickness uniformity involves taking a series of measurements of the thickness of the diamond film at a series of points. The diamond film thickness is measured a number of ways in this study. The most common and easiest way is by the weight gain. The detailed calculation equation is stated in Eq. 3-10,

$$FilmThickness = \frac{Weightgain}{DensityofMass \times Area} \quad Eq. 3-10$$

where the density of mass for diamond is 3.51g/cm^3 and the area depends on the substrate used. This method however only gives the average thickness of the film and also we need to know the exact surface area of the substrate. Many industrial silicon wafers are cut with flats to indicate the wafer orientation. The surface area is usually approximated as a perfect circle without the flat. Sometimes the diamond film over grows on the edge of the substrate. This is also a source of error for the calculation.

The second method uses Scanning Electron Microscope (SEM) cross section profiling to get very high precision measurements. This requires cutting laser or scribing to create the cross section. Figure 3-16 shows how the thickness of the diamond film for a 3-inch sample is determined from the cross section of its SEM photo. Due to the nature of

the SEM photo, the precision is usually very high. However, the SEM sample is limited in size so large films need to be cut into smaller pieces in order to fit to the SEM sample stage. The sample also needs to be prepared by gold sputtering. In addition to that, the measurement takes experienced personnel to identify the clear edge of the diamond from the silicon even though the silicon-diamond wafer is under the high resolution SEM. It is a time consuming and expensive process.

The third method uses a 50 nm precision linear scanning tip encoder. By measuring the substrate thickness before deposition and the substrate + film thickness after deposition, the film thickness is determined. Two measurements at one point are performed, before and after the diamond growth.

The linear encoder is a very simple, but high in precision, device that measures the linear depth in vertical direction as shown in Figure 3-17 and Figure 3-18. It has a built-in smooth and flat stage, which is good for objects with a flat bottom surface. As known, due to the residual stress (the thermal and the intrinsic) the silicon-diamond film bends significantly and the wafer is no longer flat. Therefore the linear encoder becomes useless with the flat stage when the diamond film thickness is only about a few microns or even tens of microns. The point-stage shown in Figure 3-17 is made from a metal rod about the same diameter as the vertical probe on the linear encoder. The top end of the rod is made like a small spherical tip, i.e. the same as the probe on the linear encoder. Finally the rod is attached to a heavy metal base, so it can not be moved easily on the flat stage by small disturbances. The wafer is purposely drawn tilted to emphasize that this point-stage can keep the deviation to the minimal even when the wafer is laid slightly tilted due to the curvature of the wafer, however the wafer should be laid as flat as

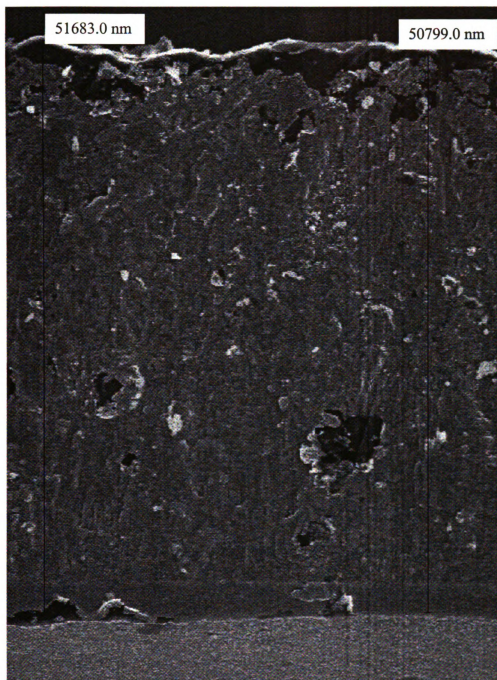


Figure 3-16: SEM photo shows how the diamond film sample (SZ-3inch-1mm-#06) thickness is measured at its cross section. Both local minimum and maximum values are taken to show measurements from the valley and from the tip of the diamond grain to the silicon surface.

possible at the contact point.

Two additional point-stages of the same height but without the heavy base are also made for the purpose of keeping the wafer in a level position as shown in Figure 3-18. The height is adjustable in case whenever it is needed. It is important to align the tip of the point-stage with the tip of the probe before starting the measurement.

In practice, the linear encoder with the point-stage can measure any point of the wafer. For the film thickness uniformity, both the radial and circumferential uniformities are measured. Figure 3-19 shows the radial uniformity is measured on two lines that are perpendicular to each other on the wafer and pass through the center point. The marked points on 2-inch wafer are a little bit different from the 3-inch wafer. This is because the 3-inch wafer was used first when this method was created and all points on the same line of the 3-inch wafer are 9 mm apart except a few points that are on a 2.5-inch diameter circle (from 18 to 29) for the circumferential thickness uniformity analysis. The diamond film thickness uniformity on 3-inch wafer is evaluated only from 2.5 inch diameter instead of 3 inch. All points on the 2-inch wafer at the same line are 5 mm apart and other points used to evaluate the circumferential uniformity of the thickness are on the edge of the wafer. The circumferential uniformity points are 30° angles from each other. Of course, more points and more lines can be chosen if one prefers a description of the uniformity in more detail.

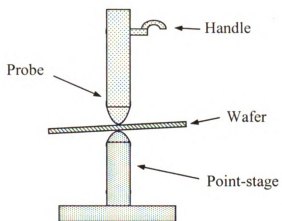


Figure 3-17: With curved tip of the point-stage and probe, the deviation due to slight tilt wafer is kept to minimal.

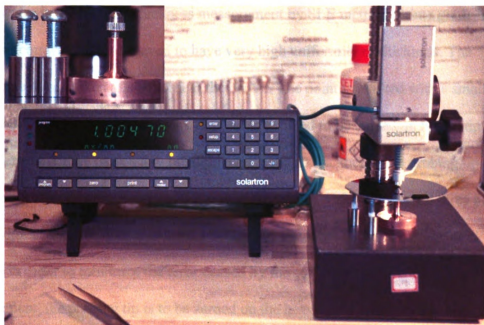
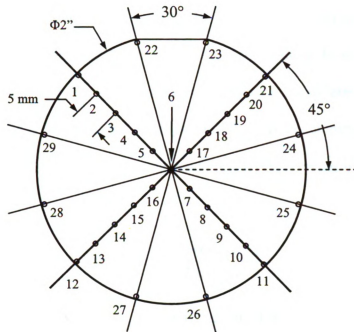


Figure 3-18: Solartron linear encoder and measurement demo with the point-stages.

Figure 3-20 plots out the thickness measurements using both the SEM photos and the measurements using the Solartron linear encoder (SLE). Diamond-shaped and square-shaped symbols represent the SEM local maximum values (upper) and the SEM minimum values (lower) of the diamond film thickness. The triangle-shaped symbol represents the thickness measurements obtained from the Solartron linear encoder. As it has been indicated before, measurements from the tip of the diamond crystal are the local maximum values of the thickness and are labeled as SEM-Max. The measurements from the valley of the surface nearby are the local minimum values of the thickness, are labeled as SEM-Min. The SLE data results appear to match the SEM-Max line.

Another piece of evidence provided to support the Solartron linear encoder method is shown as in Table 3-3. A prime grade new 3 inch in diameter and 1 mm thick silicon wafer is used for the thickness measurement by SLE method. Prime grade, single crystal silicon wafers are believed to have very high uniformity of thickness. The measurements are taken at a point near the center. The point is marked with a small ink dot, however, during measurements this point is avoided to be landed on by the tip since the hardened ink may have a few hundred nanometer in thickness. The probing tip is zeroed on the heavy point stage first, and then the silicon wafer is set on all three point stages without disturbing or moving the first stage. All three stages should be as close as possible in order to minimize the error caused by the curved wafers. After the measurement, the probing tip is to be zeroed on the heavy point-stage again. The measurements are repeated for twelve times. Then the standard deviation is calculated. From Table 3-3, the calculated standard deviation is 3.26×10^{-5} mm or 32.6 nm.

(a)



(b)

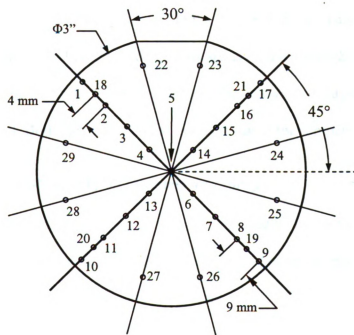


Figure 3-19: Substrate and diamond film thickness measurement positions using the Solartron linear encoder. Measured points are labeled in (a) the 2-inch substrate and (b) the 3-inch substrate, viewing from facing the polishing side. Units are in inches or specified.

3.7.2 Calculation of diamond film growth rate

The growth rate can be measured either by the weight gain per unit hour or by the thickness increased per unit hour. By measuring the weight before the growth of the diamond and then after the growth of film, the weight gain is the difference of the two. Then the growth rate is presented by g(rams)/h(our) or mg/h. In comparison, the diamond film thickness is given in Eq. 3-10. The obtained growth rate becomes $\mu\text{m/h}$, as stated in Eq. 3-11:

$$\text{GrowthRate} = \frac{\text{FilmThickness}}{\text{RunTime}} \quad \text{Eq. 3-11}$$

where the runtime is usually in hours. The diamond film thickness can also be obtained by the Solartron linear encoder with a set of special designed point stage as we have stated before in section 3.7.1. The results from the Solartron linear encoder are usually higher. This is because the linear encoder mostly scans on the tips of the diamond crystals that grow on the silicon substrate. The tip of the probe is obviously larger than the size of the diamond crystal. Both methods are used in this research for comparison.

3.7.3 Evaluation of diamond film thickness uniformity

The diamond film thickness uniformity is evaluated by its thickness percent deviation. The more the film thickness is uniform, the less of its percent deviation. The diamond film thickness percent deviation is defined as:

$$\pm \left[\frac{1}{2} \frac{t_{\max} - t_{\min}}{\frac{1}{N} \sum_{i=1}^N t_i} \right] \times 100\% \quad \text{Eq. 3-12}$$

where t_i is the thickness of the film at a point i and N is the total number of points measured along one of the two perpendicular lines shown in Figure 3-19. Across the film diameter, eleven points are along one line for the measurements of both the 2-inch and 3-inch wafers. In determining the uniformity, two sets of points along two diameters that are perpendicular to each other are measured. The circumferential uniformity is also evaluated by the additional points along the circumference on the substrate. Figure 3-19 shows the details about how these points are labeled for the measurements.

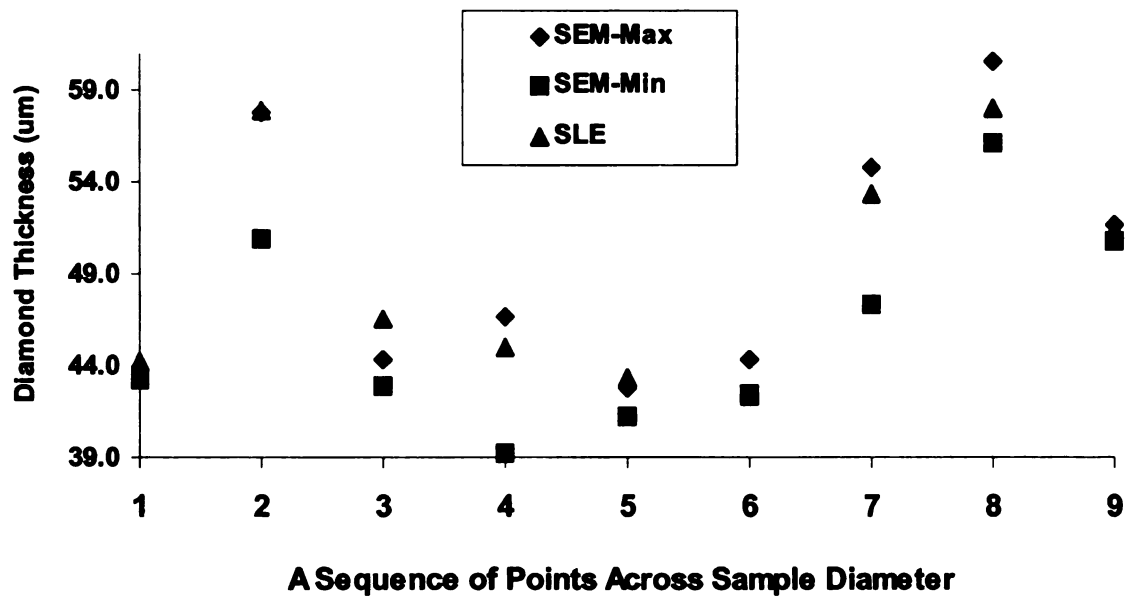


Figure 3-20: Comparison of the results of SEM measurements and the measurements using Solartron linear encoder for the thickness across the sample diameter for sample 3-inch-1mm-#06 after 48 hours diamond deposition.

Table 3-3: Standard deviation calculation of SLE method.

Repetition Times	1st	2nd	3rd	4th	5th	6th		Standard Deviation (mm)
Measuring Result (mm)	1.00555	1.00550	1.00555	1.00550	1.00550	1.00545		3.2567E-05
Repetition Times	7th	8th	9th	10th	11th	12th		Standard Deviation (nm)
Measuring Result (mm)	1.00555	1.00550	1.00550	1.00555	1.00555	1.00550		32.6

3.8 X-ray diffraction technique, pole figure, film texture, and surface morphology

As part of the polycrystalline diamond film properties, film texture and surface morphology are included in this study. Most of the diamond films deposited at higher pressures have CVD polycrystalline diamond grain sizes that are much larger than Nanocrystalline Diamond (NCD) grains. Generally the film surface morphology can be readily observed under optical microscope observation and may not require the assistance of SEM technology. The X-ray diffraction measurements in Bragg-Brentano geometry (2θ scans) are frequently used as a quick check for preferential crystal orientation [84, 85]. Furthermore the film texture and the film microstructure influence the growth rate and the optical quality by allowing different levels of impurities or even vacancies into the film during the deposition process. This study examined the relationships the film texture and surface morphology have to the diamond growth conditions, such as the growth rate, gas composition, substrate temperature, or even intrinsic film stresses.

3.8.1 *The Bragg's law and interpretation of powder X-ray diffraction data*

One of the techniques used in this research is the X-ray diffraction technology. The technique was used to extract the statistical data of micro size diamond crystal

orientation in the polycrystalline diamond film from the X-ray diffraction pattern. The investigation of the crystal orientation in a bulk film is usually termed as the film texture study. However, a complete description of a film texture should be investigated using the pole figure technique, of which some basic concepts will be introduced in section 3.8.2. The X-ray diffraction pole figure is a complex task, though simple in concept, the data taking and processing is laborious. A simple one-time large range in angle X-ray diffraction scan that is usually used for unknown powdered sample material studies is proposed for this purpose. The intensities of each crystal orientation shown in the diffraction pattern relate to X-ray diffraction peaks are taken as the measurement of the statistical quantity of the local crystals oriented in that direction between the scanning angle from beginning to the end of the scan.

The fundamental principle of X-ray diffraction is based on Bragg's law [86, 87]. Bragg's law describes a beam of X-rays incident onto a crystal grating and then describes the reflected X-ray by the crystal (Figure 3-21). The crystal grating is like a set parallel mirrors, of which the reflecting surface – the diffraction plane turns out to be the atomic planes or the lattice planes that have the same interplanar distance or spacing from one to the next in the crystal. This distance or spacing that is marked as d in Figure 3-21 is usually called the d -spacing. If the incident X-ray wavelength is λ , the incident angle is θ versus the lattice plane and n is the order of the reflection, then the “reflected” (diffracted) beams are governed by following relation,

$$n\lambda = 2d \sin \theta \quad (n \text{ is an integer}) \quad \text{Eq. 3-13}$$

Eq. 3-13 is the Bragg's law or Bragg's equation.

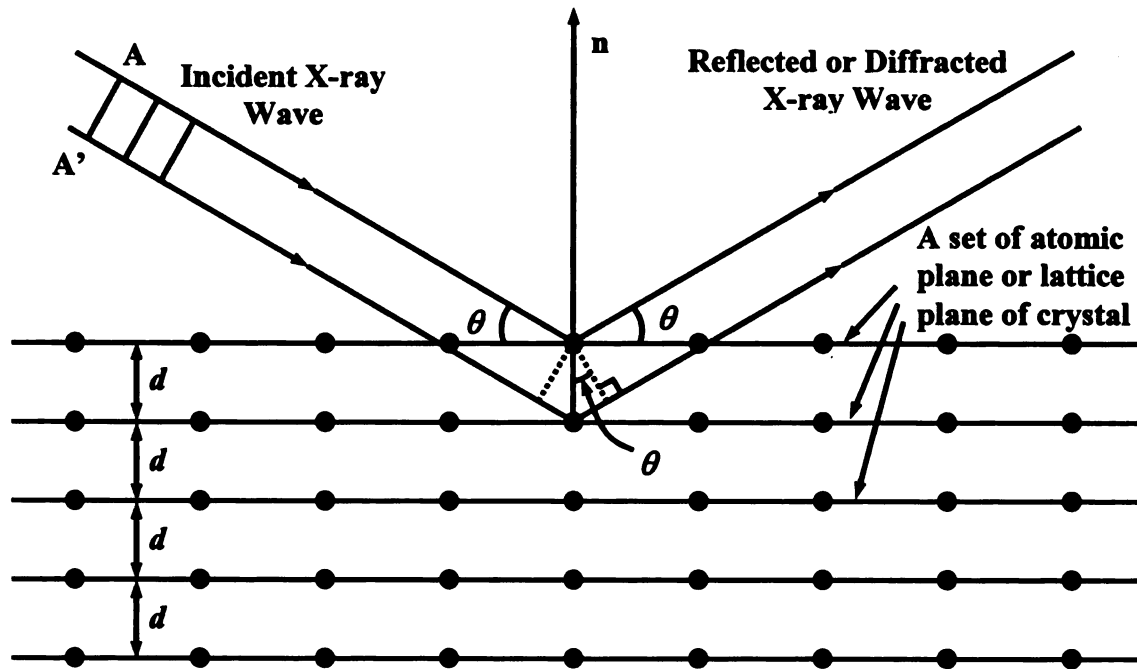


Figure 3-21: Geometry of the Bragg “reflection” analogy and Bragg’s law. The direction n indicates the surface normal of the atomic plane or lattice plane of the crystal grating.

There are many X-ray reflection (diffraction) planes in a single crystal. Take the diamond crystal, i.e. a face center cubic lattice crystal as an example (Figure 3-22, [88]), there are a total of five reflection planes with different values of d -spacing. These d -spacings usually can be theoretically expressed in terms of the Miller indices and the lattice constant of that given lattice. Formulas of the expression for various lattice systems can also be found in textbooks [89]. For the convenience of the studies for diamond crystals, the formula of the d -spacing for cubic lattice is restated as the following,

$$d(hkl) = \frac{a}{\sqrt{h^2 + k^2 + l^2}} \quad \text{Eq. 3-14}$$

where letter a is the lattice constant, which is 3.56670 Å [90, 91, 92] for diamond and (hkl) are the Miller indices.

Though with multiple lattice planes in the crystal lattice, diffraction peak can only be observed while X-ray entering onto the lattice plane with the particular angle based on the Bragg's equation, or no diffraction peaks will be observed. This problem can be overcome by (1) using a range of X-ray wavelength (called white radiation) for the single crystal sample, or (2) rotating the single crystal sample or (3) using a power sample. The angles that satisfy the Bragg's equation with the maximum intensities are called the Bragg's angle. In considering the X-ray source is used for this study, the X-ray wavelength is $\lambda = 1.540562 \text{ \AA}$. The five Bragg's angles with the first-order diffraction fringes for cubic lattice system can also be calculated using the Bragg's equation (Eq. 3-13) by letting $n = 1$. Table 3-4 contains a set of values of d -spacing and diffraction angles using diamond as the example.

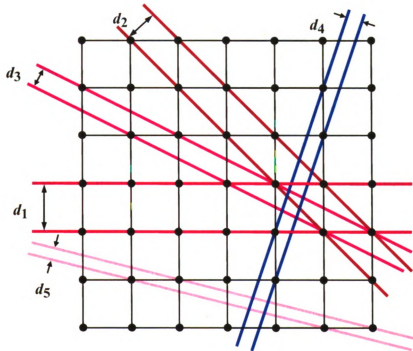


Figure 3-22: 2D illustration of the X-ray reflection (diffraction) planes (i.e. $\{10\}$, $\{11\}$, $\{21\}$ $\{31\}$, and $\{41\}$) and their corresponding d -spacing in a “cubic” lattice such as diamond lattice for example [88].

Table 3-4: The theoretical values of the d -spacings, diffraction angles and f for diamond crystal materials. All values are based on diamond lattice constant $a = 3.5667 \text{ \AA}$ and X-ray wavelength of $\lambda = 1.540562 \text{ \AA}$

Lattice Plane	(111)	(220)	(311)	(400)	(331)
d -spacing (Å)	2.0592	1.2610	1.0754	0.8917	0.8183
Diffraction angle (2θ)	43.9°	75.3°	91.5°	119.5°	140.6°
Multiplicity factor ² [93]	8	12	24	6	24

Based on the results in Table 3-4, it is expected that the diffraction fringes can be seen at the diffraction angles (conventionally it is the angle between the reflected beam and the undeviated incident beam) of 43.9°, 75.3°, 91.5°, 119.5°, and 140.6° in X-ray diffraction pattern on the camera film for diamond crystal (Figure 3-23). The fringes (marked with oval dots) and angles (not to scale in the figure) on bottom half of the circle are symmetric with those on top half of the circle but are not shown in the figure. Figure 3-23 is assuming a monochromatic X-ray source is used so that the single crystal diamond sample is rotated in order to observe all five diffraction peaks in the diffraction pattern. Usually the large diffraction angle is expected, a strip of camera film is technically placed to surround the sample in a circle and sample is placed at the center of that circle.

² The multiplicity factor will be introduced later in this section.

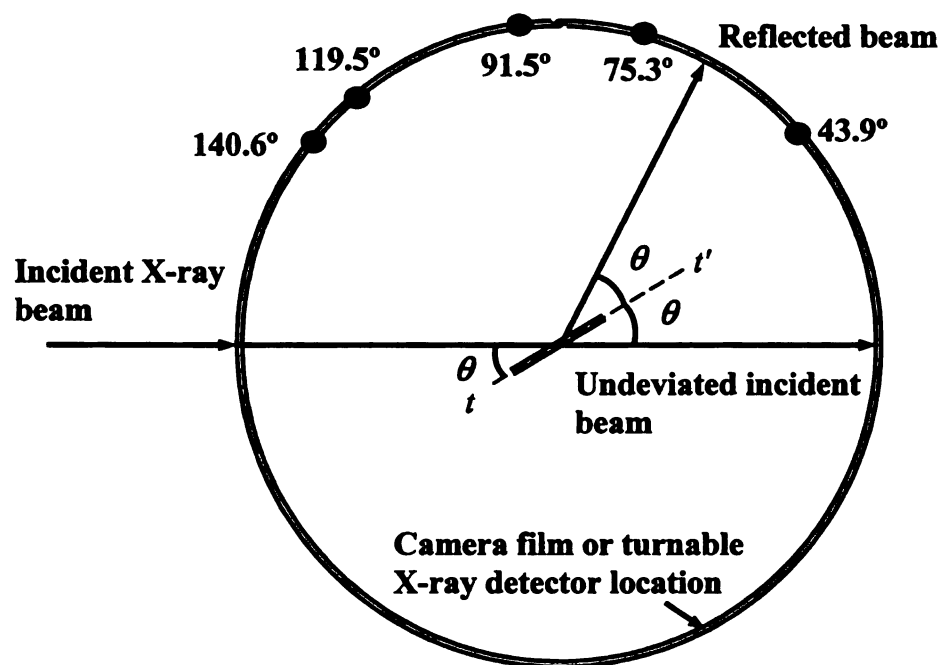
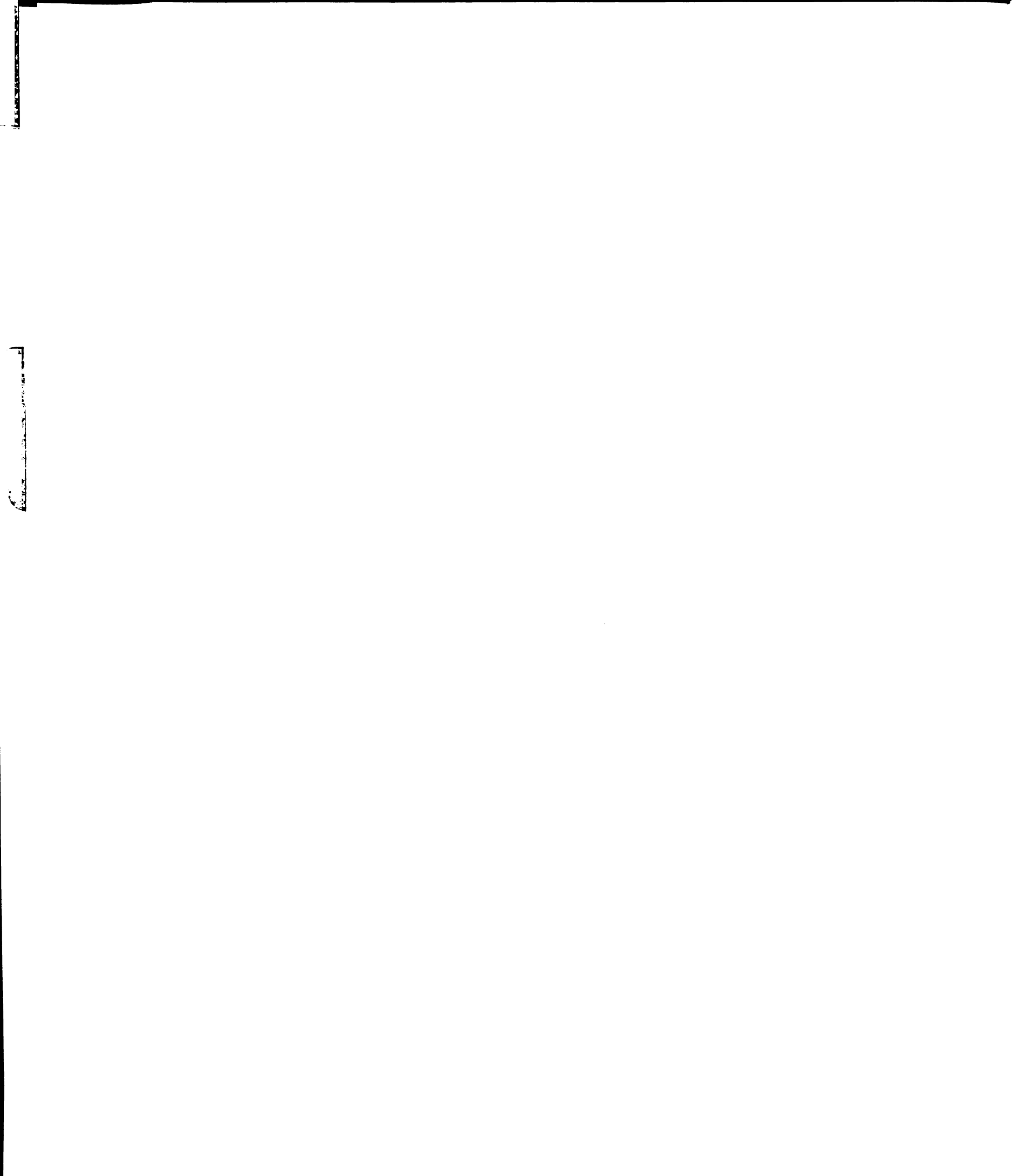


Figure 3-23: The location of the Bragg's angle on camera film for single crystal diamond sample.

The powder sample contains millions of micro size single crystals and these crystals usually randomly align themselves, so the X-ray diffraction pattern may contain all the diffraction peaks for a particular crystal with a monochromatic X-ray source and an arbitrary incident angle. Because of this, millions of these tiny little reflections form a solid line circle that is symmetrical to the incident beam for each Bragg's angle, so that the overall diffraction pattern looks like a series of cones from three dimensions. Figure 3-24 (a) shows the cone shape of the diffraction pattern. Figure 3-24 (b) shows how a strip of camera film is placed for collection of the X-ray pattern. Figure 3-24 (c) shows the actual powder X-ray pattern on a negative camera film.



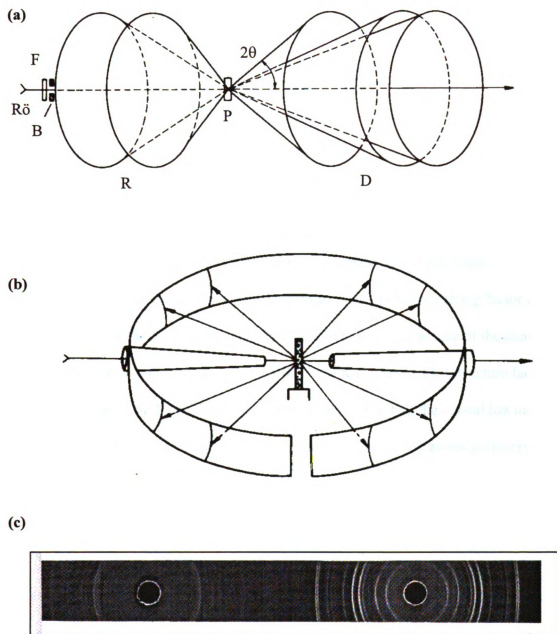


Figure 3-24: The X-ray diffraction pattern of a powder crystal sample. (a) The cone shape of the diffraction pattern. (b) A strip of camera film setup for collection of the X-ray pattern. (c) The powder X-ray pattern on a negative camera film [88].

The absolute intensity data of X-ray diffraction is extremely desirable, but usually difficult to obtain. There are many factors that influence the absolute intensity data, to make it brief, they are the polarization factor, the Lorentz and “velocity” factor, the temperature factor, the atomic scattering factor, the structure factor, the multiplicity factor, and the absorption factor [94]. The polarization factor states the change of the intensity of the X-ray beam after it is diffracted. The Lorentz and “velocity” factor explains the intensity loss if a polychromatic X-ray source is used to produce primary beam or the primary beam produced is not strictly parallel but more or less divergent. The temperature factor describes the diffraction intensity decrease due to the atomic vibrations that associated with the sample temperature. The Atomic scattering factor is about the influence of the diffraction intensity from the finite physical size of the atom or the electrons that cause the phase shift of the diffracted X-ray beam. The structure factor indicates the variations of the X-ray diffraction intensity due to that the crystal has more than one kind of atoms in the crystal. Since diamond only has carbon atoms in the crystal, we may leave this factor out from this study. The multiplicity factor discovers that one plane may reflect multiple times for a particular diffraction angle (Bragg’s angle). The diffraction intensity becomes multiple times stronger than the intensity reflected by a single plane in one crystal or grain. The multiplicity is determined by the lattice planes structure from the type of crystal lattice for single crystal therefore the multiplicity is different for each different type of plane [95]. The multiplicity is usually only applied to oscillating or rotating crystal method. Since the sample is also rotated for the powder method, the multiplicity should also apply. The values of multiplicity of each plane for diamond crystal are extracted from Table 3-1 in the reference book by Klug et al. [96]



and included in Table 3-4. The absorption factor is to say that the diffraction is less intense due to the partial absorption of the incident and diffracted X-ray beam. All factors are indistinguishable to influence the diffraction intensity for all the different diffraction planes in the crystal with the different d -spacing except the multiplicity factor. The conclusion of this discussion is that the multiplicity factor should be taken into account for the value of the **relative intensity** of each diffraction plane (with different d -spacing) that is to be extracted from the X-ray diffraction pattern.

In real powder method X-ray diffraction measurement, the geometrical relation of the X-ray beams and angles shown Figure 3-23 can be converted into a 2D plot when diffraction intensity of the diffracted (reflected) beams can also be measured. This is also the X-ray diffraction pattern, or sometimes called X-ray diffraction spectrum. Figure 3-25 is the typical plot of the X-ray diffraction pattern that shows all the diamond peaks in Table 3-4. Though the diamond sample is not a single crystal, the geometrical locations of the Bragg's angles are the same as the single crystal with the reflection intensities varying from peak to peak.

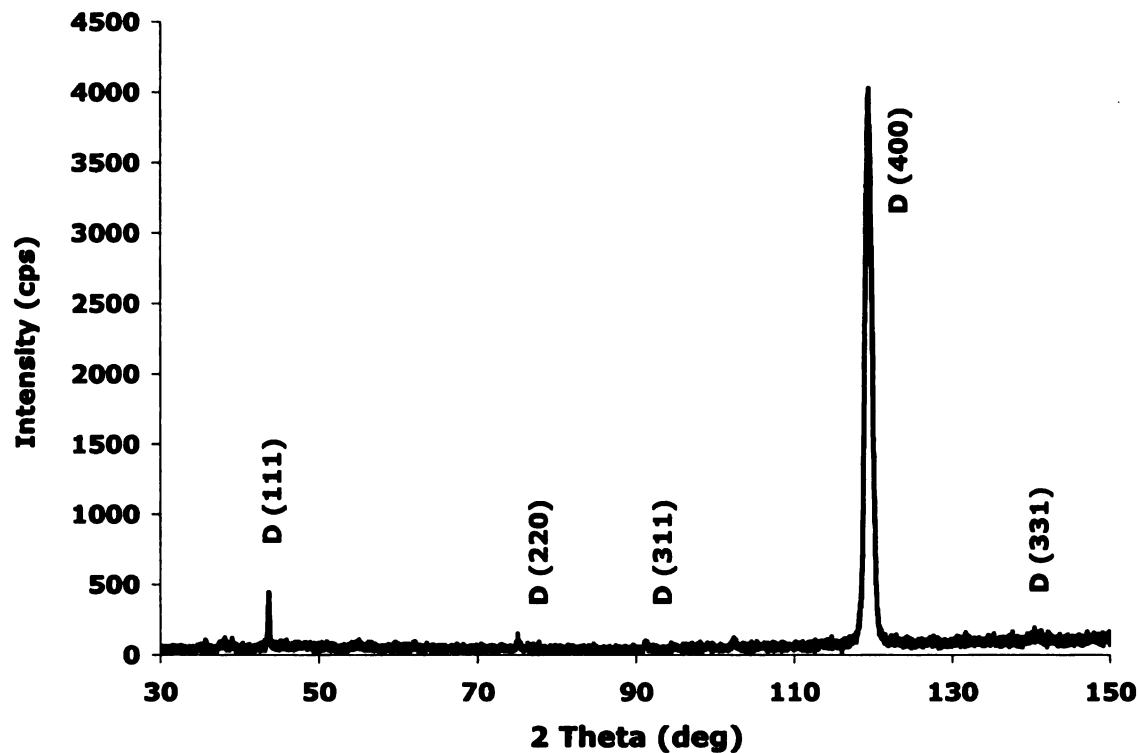


Figure 3-25: X-ray diffraction pattern with intensities of each reflection measured as counts per second during the rotation of the MPCVD polycrystalline diamond film sample (SZ-2inch-1mm-035) for the diffraction angle started from 30° to 150°.

X-ray diffraction powder technique is used to study polycrystalline diamond film due to the closeness of the polycrystalline diamond sample to the powder sample. It has been discussed that the powder sample contains millions of micro size single crystals. The randomly packed powder crystal samples would exhibit a diffraction pattern with the same intensity for each Bragg's angle because the distribution of diffraction planes in space are statistically the same (with in considering multiplicity). This can also be understood as there are statistically equal numbers of diffraction planes (with different d -spacing and from different crystal grain) being detected in the sample. Polycrystalline diamond film grown under the MPCVD condition may also contain some degrees of

randomness of its diffraction planes orientations from one sample to another, however, may usually prefer growth at one direction to others and the film form some sort of texture. Based on previous discussion, the relative intensity data from the diffraction pattern (such as the one in Figure 3-25) gives us the statistical information of how many diffraction planes (or grains) the sample may have in certain orientation relatively. This discussion will be used for stress evaluation from Raman spectroscopy in section 3.11.3. Please note Figure 3-25 shows a highly aligned polycrystalline diamond film in the direction of $\langle 400 \rangle$. Though Figure 3-25 itself does not indicate the diamond film surface normal is also $\langle 400 \rangle$, the angle between the (400) oriented planes (grains) and film surface normal should not be greater than 90° . Since the diffraction angle is set starting at 30° and stopping at 150° , the incident angle of the X-ray beam is then from 15° to 75° . Therefore the detected angle between the (400) oriented planes (grains) and film surface normal should be smaller than 45° .

3.8.2 X-ray diffraction pole figure

A pole figure is a graphical representation of the orientation of objects in space [97]. It is a map of statistical distribution of the normals to given $\{hkl\}$ planes of a polycrystalline sample and provides a very complete picture of the texture of a metal or a polymer, the polycrystalline materials [98]. As it has been mentioned before, the X-ray diffraction pole figure is a complex task, the data taking and processing is rather a tedious and heavy labor work and will not be used for this research. However some fundamental basics are mentioned at several places in this study therefore is introduced. More information about this technology can usually be found from textbooks, such as one of

the references heavily quoted for this technology in this research by Klug et al. [98], and the Internet.

The pole figure is a stereographic description (projection) of plane normals of a crystal and derived from another widely used stereographic description and analysis in geometrical crystallography, called spherical projection. Figure 3-26 only shows the spherical projection of a crystal of plane (100), $(\bar{1}00)$, (010), $(0\bar{1}0)$ to illustrate the idea. The full projection can be found from the references [99]. The crystal plane normals

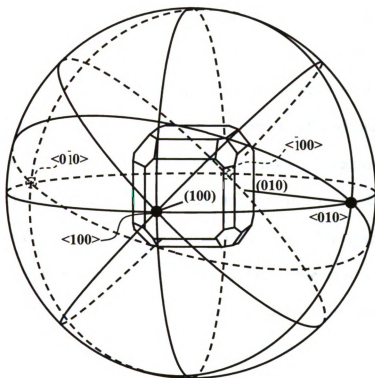


Figure 3-26: The spherical projection of a crystal of plane (100), $(\bar{1}00)$, (010), $(0\bar{1}0)$. The original full projection can be found from E. Dana, a Textbook of Mineralogy, 1932, Wiley or reference [99].

that intersect (project) with the spherical surface are known as the **poles** of the plane surface. The spherical projection is a fine stereographic description of crystal planes

except with one problem, which is the difficulty to put down on 2D viewing media, as humans are used to without overlapping. Though various kinds of schemes for mapping the spherical projection have been developed, one most important of these is the stereographic project – **the pole figure**.

3.8.3 *Film texture*

Three types of textures are usually distinguished for polycrystalline films including random texture, fiber texture and epitaxial aligned texture (or in-plane texture) on single-crystal substrates. The random texture has diamond grains with no preferred alignment orientation. Feng et al. [100] have studied such a randomization in CVD polycrystalline diamond film grown at the temperature range of 850 – 1050 °C. Fiber texture has one crystallographic axis of the film that is parallel to the substrate normal, while there is a rotational freedom around the fiber axis. This is also frequently observed in CVD polycrystalline diamond films. The third texture is usually for single-crystal diamond growth where an in-plane alignment fixes all three axes of the grain with respect to the substrate. A fourth texture type was reported by C. Detavernier et al. in 2003 from IBM T. J. Watson Research Center in New York and it is claimed to be a dominant type of texture for CVD polycrystalline films that grow on the single crystalline material substrate such as the silicon [101]. Though there might be some possibility that our as grown polycrystalline diamond films being like the fourth texture, two reasons kept us from classifying our samples to be the fourth texture. One reason is that the diamond powder is used as the seeding, i.e. the nucleation layer for the diamond crystal growth. So diamond crystals can not be considered as grown on the silicon substrate directly. The second reason is that most of our diamond film samples are grown very thick to tens of

microns or hundreds of microns thickness. The film texture may change due to some planes overgrow others (the columnar growth) and most likely no longer the same as the texture nearby the interface between the diamond film and silicon substrate. In addition, the detailed pole figure analysis is required in order to fully characterize the texture of a polycrystalline material [85]. Since the X-ray pole figure technique is not included in this study, we can not verify if this assumption is right. Therefore all diamond samples textures in this study are considered as the fiber texture and the orientation is primary determined by the XRD 2θ scan in Bragg-Brentano geometry.

3.8.4 *Surface morphology*

Most polycrystalline diamond samples are photographed with a microscope to show their surface morphology and may be assisted by X-ray diffraction spectroscopy without the pole figure. Samples can be viewed clearly under the optical microscope with high resolution because of the large diamond crystals that were grown in the film, but a few samples are photographed with SEM if it is necessary. It is believed that the surface morphology shows in part how the diamond grains are orient at the diamond film surface. However since many of the crystal grains are not with one plane strictly aligned parallel to the film surface normal, the surface morphology can not strictly define the grain orientation by current definition. A few particular shapes of grain surface though are commonly used to describe the plane of a grain that shows on the film surface. As it is known, a triangular shape of facet shows the $\{111\}$ plane surface of the grain [102, 103] and the square or rectangular shape of facet show the $\{100\}$ plane surfaces of the grain [103, 104, 105] in the deposited film.

Figure 3-27 is the photograph of the surface of sample SZ-2inch-1mm-035 where the square shaped facets dominant over others. The pyramid or wedge shaped grains may show two or three joint planes that are not strictly parallel to the film surface normal. Normally, a diamond crystallite is only bordered by stable {100} and {111} surfaces [106, 107]. The 3D shape can be any of these shown in Figure 3-28. Figure 3-28 also shows how the shapes of diamond crystallites change due to the uneven growth rates of plane surfaces between {100} and {111} during the deposition depend on different growth conditions. Therefore, the pyramid or wedge shaped diamond grains may be a combination of any of these two family planes. The photograph in Figure 3-27 shows square and rectangular facets dominate over any other facets on the film surface.



Figure 3-27: The surface morphology of diamond film sample SZ-2inch-1mm-035. Most crystal surface shows a square shape of facet with a few grains show part of the grain tips look like pyramids or wedges.

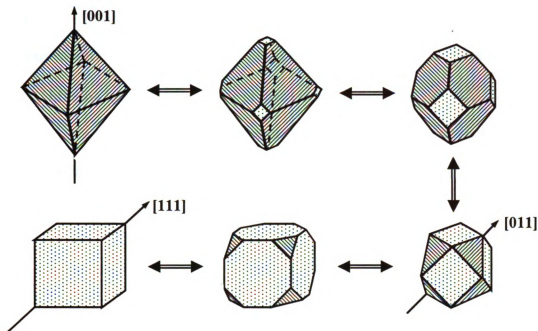


Figure 3-28: All possible shapes of cubic diamond crystallites. Two stable surfaces $\{100\}$ and $\{111\}$ that normally border diamond crystal are shaded with dots and lines respectively [106, 107].

3.9 Diamond film grain size measurement, the method of linear intercepts

The grain size of polycrystalline diamond films is measured using the method of linear intercepts. This method was developed by Mendelson under the assumption of contiguous grown tetrakaidecahedral (truncated octahedral) grains on the film with a log-normal distribution, given by Eq. 3-15, of the grains sizes throughout the film surface [108].

$$g_{LN}(D) = \frac{1}{\sqrt{2\pi}D \ln \sigma} \exp \left\{ -\frac{1}{2} \left[\frac{\ln(D/D_0)}{\ln \sigma} \right]^2 \right\} \quad \text{Eq. 3-15}$$

where \bar{D} is the median value of the grain size and σ is the width of the distribution. A simple expression is derived between the average grain size, \bar{D} , to the average intercept length, \bar{L} , differing by a factor called the proportionality constant, C : $\bar{D} = C\bar{L}$. The parameter C was taken to be 1.56, as determined by Mendelson for contiguous polyhedral grains with approximately equiaxial dimensions in general [108, 109]. This model is considered suitable for diamond poly-microcrystal films grown under the conditions of this research [60].

In terms of measuring the length of intercepts, first the sample is photographed under an optical microscope. The viewed image of the sample is measured using software for the microscope which uses a fixed size at $(249.6 \mu\text{m}) \times (187.1 \mu\text{m})$ when the ocular lens is $10\times$ magnification and objective lens is $50\times$ magnification. Three horizontal and four vertical straight lines are drawn equally spaced on the photograph as shown in Figure 3-29. The number of intercepts of the diamond grain boundaries with the straight lines is counted along the line (i.e. the line with the length of $249.6 \mu\text{m}$ is used). The intercept length of this line is the total length of the line (i.e. $249.6 \mu\text{m}$) divided by the number of the intercepts. A final average of the intercept length is taken for all seven lines. Figure 3-29 shows how the grid lines are drawn on the microscope photograph and length of the lines are used for the calculation.

X-ray diffraction line broadening can also be used to estimate the diamond grain size in the film. However it is more suitable for nanosize bulk crystallites or films contains very small sizes of crystals less than 100 nm as defined by Klug and Alexander [110], and Jiang et al. [111], or less than 150 nm as defined by Keijsers et al. [112]. As it was mentioned before, diamond crystallite sizes grown under the higher pressure

condition are usually tens of microns and hence are bigger than the upper limit of the X-ray diffraction technique. This may produce significant errors. This is also to say that the line broadening caused by large grain sizes in the X-ray diffraction is very small and can be ignored in the case of this study.

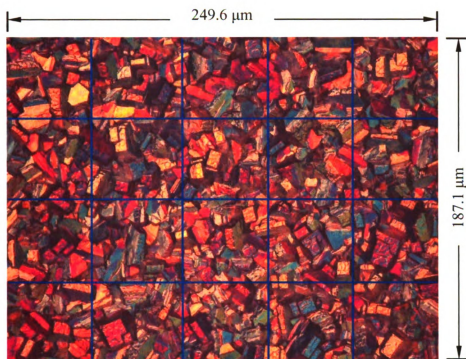
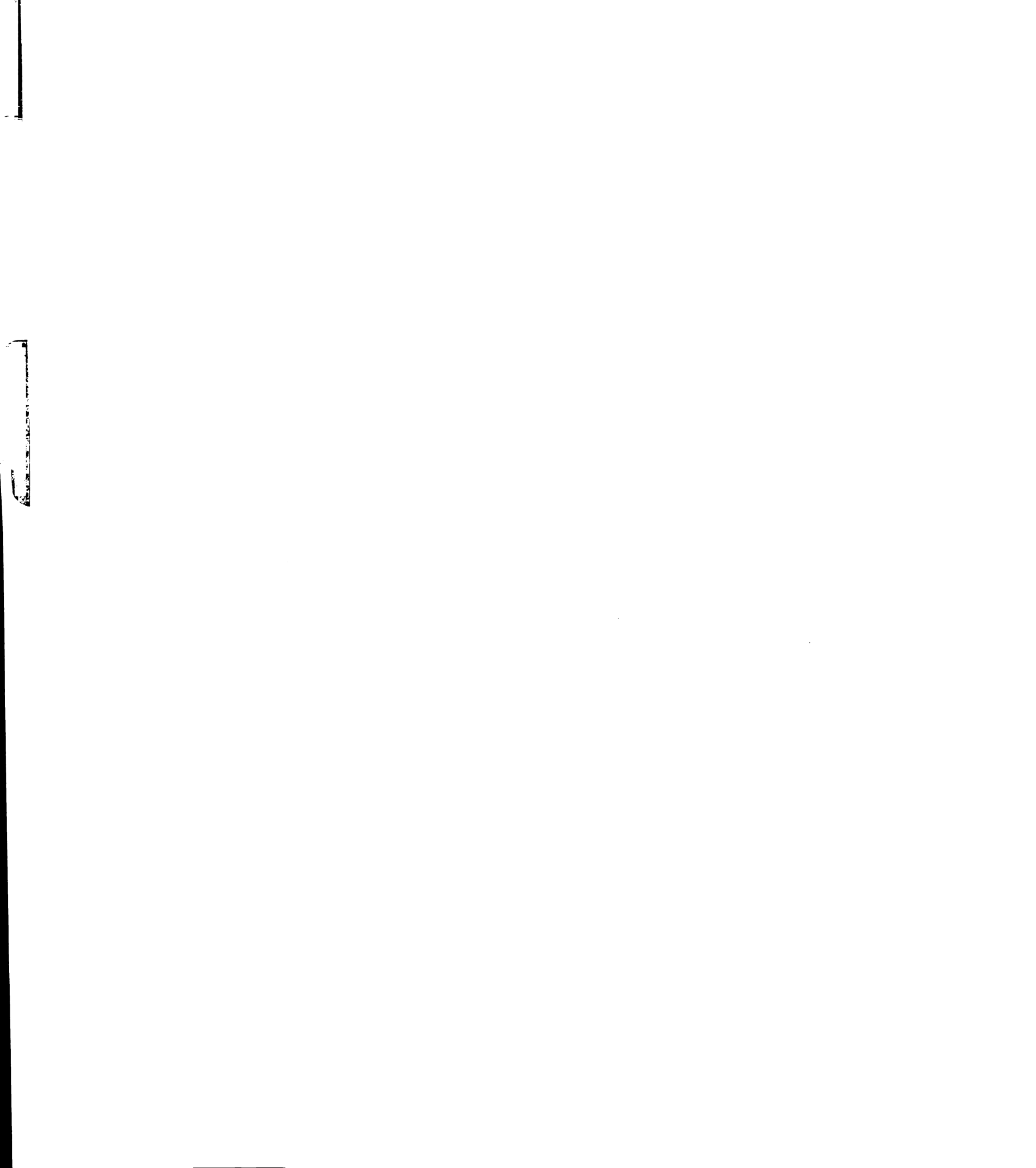


Figure 3-29: A grid of lines are drawn over the photograph taken by the camera attached to the microscope, then the intercepts between the boundary of diamond grains and the line are counted along each line.

3.10 Diamond film quality measurement

3.10.1 Visual inspection

The optical quality of the diamond film can be roughly estimated by visual inspection with the human eye. Since the impurities and defects in the films cause film discoloration and most of the time the impurities and the defects are the major issue, the



optical transparency, which is how well the film lets through the visible light, can be determined qualitatively by the human eye. Basically the optical quality is indicated by its whiteness when a film is not polished. The whiter the film is, the better the quality. The visual estimation is a time-saving and reliable qualitative method of estimating the film quality. As described in the following section, other more quantitative methods are also employed.

3.10.2 Raman spectroscopy for quality evaluation

Raman spectroscopy is a well-known method to investigate the diamond film quality. Good quality diamond shows a sharp, narrow and high intensity peak at 1332 cm^{-1} in the Raman scan with a very small Full Width Half Maximum (FWHM) value. Additionally all other signals from materials such as graphite are absent or small. The FWHM value reflects the crystalline quality of the diamond grain and a smaller FWHM value indicates a higher crystalline order in the diamond lattice of a bulk diamond grains [113, 114]. It is also known that the FWHM value gets larger for polycrystalline diamond with smaller grain sizes [115]. A typical FWHM value of a nature single crystal diamond is less than or equal to 2.0 cm^{-1} . A sample Sumitomo HPHT single crystal diamond that is used for the calibration of the Raman system in the lab has a FWHM value measured around 1.9 cm^{-1} . Most of the high quality polycrystalline diamond film samples reported should have a FWHM value less than or equal to 5.0 cm^{-1} . Raman spectroscopy is a very reliable quantitative measurement for diamond film quality used by many researchers, however, only the local diamond crystals quality information is revealed when a small laser spot size is used. A number of scans (more or less depend on the level of evaluation

one needs) at different location on the diamond film are needed if the overall diamond film quality is to be measured.

For high quality diamond films, the Raman peak shift is as small as a fraction of one cm^{-1} wavenumber. The Raman system used requires high accuracy and resolution in order to obtain the peak location during the scan. The Raman system used for this research is equipped with a 514.5 nm Ar ion laser with a spot size of 20 – 30 μm and resolution of 0.2 cm^{-1} between each acquired data. The end to end length of the Spex 1250 spectrograph assembly is 1.25 meters and is attached to an Olympus BH-2 microscope with the magnification usually set to 10 \times 80. To achieve this high precision goal, a high resolution holographic grating of 1800 grooves/mm is used with a snapshot window fixed from 1134 cm^{-1} to 1508 cm^{-1} . A spectrometer slit width of 50 μm is chosen to achieve a relatively high signal to noise ratio and to sufficiently reduce the laser light that passes through the slit. To increase the signal/noise ratio, an integration time is chosen to obtain a diamond peak intensity around 8000 – 10,000 counts. Other techniques to increase the signal/noise ratio and precision were also done including decreasing the CCD image binning from 5 to 1 and decreasing the data acquisition step to the minimum, which is 1 before starting the scan and, using baseline correction and software tools to fit peaks to the Gaussian/Lorentzian curve for locating the peak position and evaluating the FWHM.

Raman spectroscopy can also be used to show graphite and amorphous carbon, i.e., the sp^2 contents in the diamond film, as part of the diamond film quality measurement.

The sp^2 content is typically the primary impurity in the film for samples grown under the typical condition as in this research. From the information collected from the literature

research, the sp^2 content consists of the disorder induced carbon band (D-band) with bandwidth range from 1330 cm^{-1} to 1392 cm^{-1} and the graphite band (G-band) with bandwidth range from 1500 cm^{-1} to 1605 cm^{-1} . The D-band is typically absent and the G-band observed ranges from 1500 cm^{-1} to 1600 cm^{-1} from the samples obtained in this study. The ratio of intensities for the diamond peak compared to the sp^2 peak can be obtained and can be used to evaluate the diamond film quality.

It is important that the Raman spectrum include the sp^2 band in the scanning range. In order to do so with the system used in this study, the software tool is used to configure the scanning range for multiple scans since one single scan only covers a frequency window from 1134 cm^{-1} to 1508 cm^{-1} as mentioned above. For this study, the scanning range is chosen to be from 1100 cm^{-1} to 1700 cm^{-1} , just enough to cover the diamond peak and graphite band. The Raman system will properly shift the gratings to scan the sample across the frequency range from 1100 cm^{-1} to 1400 cm^{-1} and from 1400 cm^{-1} to 1700 cm^{-1} . The software then combines the two scanning results into one. Because of this, an error is introduced to the Raman spectrum at the juncture where two spectra from two separate scans are joined, which spreads about 140 cm^{-1} wide start from 1400 cm^{-1} . This error can be easily identified as a valley in the spectrum at the place of $1400 - 1540\text{ cm}^{-1}$. Despite the limitation by the Raman system in general, the diamond films have good Raman

signals (with very small FWHM value and a minimal sp^2 band) indicating high quality diamond is being deposited.

3.10.3 Post processing and optical transmission measurement

The optical transmission of the CVD polycrystalline diamond films grown for this research is measured using the Perkin Elmer Lambda 900 UV/Vis/NIR spectrophotometer. The spectrophotometer result directly gives the percentage of the light transmission for a range of wavelengths chosen by the user, which in our case is almost the full range of the machine from UV light to Infrared – 180 nm to 3 μ m is usually the range used. Though the optical transmission scanning process is simple, the diamond films require a series of post processing steps before they can be scanned by the spectrophotometer due to the surface roughness and sometimes the curvature of the film. These main post processing steps include (1) the laser cutting, lapping and polishing of the growth side of the diamond, (2) removal of the silicon substrate, and (3) plasma etching to remove a thin layer on the nucleation side of the diamond film. Laser cutting is performed with a pulsed Nd-YAG laser operating with the third harmonic and removal of the silicon substrate is accomplished with wet etching using a combination of hydrofluoric and nitric acid. Plasma etching of the nucleation surface is performed using an electron-cyclotron-resonant plasma with O₂, Ar, and SF₆ gases mixture as reported by R. N. Chakraborty [116, 117], a former MSU student. Lapping and polishing is performed with a Logitech LP 50 system (Figure 3-30) using procedures recommended by the system provider [118]. Then the surface roughness is measured with the surface profilometer Dektak D6M.



Figure 3-30: Logitech LP 50 lapping and polishing system.

The initial lapping step utilizes a $50\text{-}\mu\text{m}$ diamond slurry and the second lapping step utilizes a $12\text{-}\mu\text{m}$ to $17\text{-}\mu\text{m}$ diamond slurry. In both cases, the sample is placed against a rotating metal plate. After lapping, the samples are polished. For the polishing step, the sample is placed against a rotating felt surface wetted with solutions of the type provided by the industry for chemical mechanical polishing of silicon and other semiconductors. Although the precise compositions of such commercial solutions are proprietary, their generic description is that of an alkaline slurry of colloidal silica. The surface R_a roughness values (the arithmetic average deviation of the surface valleys and peaks) are reduced from hundreds of nm for as-grown films, to several tens of nm after lapping, to a few nm after polishing [60].

Surface roughness causes loss in transmission, even if all scattered light is collected. This is because of phase cancellation of light rays leaving or entering an uneven surface. For a Gaussian distribution of surface roughness with a standard

deviation of R_a , the light transmission into diamond from air is reduced by a factor of S_R as shown in Eq. 3-16,

$$S_R = \exp \left[- \left(\frac{2\pi R_a (n_D - 1)}{\lambda} \right)^2 \right] \quad \text{Eq. 3-16}$$

where n_D is the wavelength dependent refractive index of diamond and λ is the free-space wavelength of light [119]. The refractive index may be calculated using Sellmeir's equation using reported parameters for diamond [120]. Accounting for reflection from the front and back surfaces, the expected transmission may be calculated as in Eq. 3-17,

$$T = \left[\frac{(1-R)^2}{1-R^4} \right] S_{RP} S_{RN} \quad \text{Eq. 3-17}$$

where the term in the square bracket is the average power transmission considering the series of front and back surface reflections [121]. S_{RP} and S_{RN} refer to the scattering term for the polished surface and the surface of nucleation side respectively. R is the Fresnel reflective coefficient and can be calculated from the refractive index of diamond n_D as shown in Eq. 3-18:

$$R = \left(\frac{n_D - 1}{n_D + 1} \right)^2 \quad \text{Eq. 3-18}$$

The transmission rate can be predicted for the sample from the given roughness using Eq. 3-17.

It is worthwhile to mention that the light path in the Lambda 900 is not adjustable, and is such that there are several tens of centimeters between the light source and sample, and between the sample and photomultiplier detector. There may be some significant light loss through the path.

Figure 3-31 shows a typical optical transmission spectrum obtained from the Perkin Elmer Lambda 900 UV/Vis/NIR spectrophotometer for a sample deposited and post-processed in the lab. More optical transmission spectra and detailed discussion are given in Chapter 4 when optical quality of diamond film is discussed.

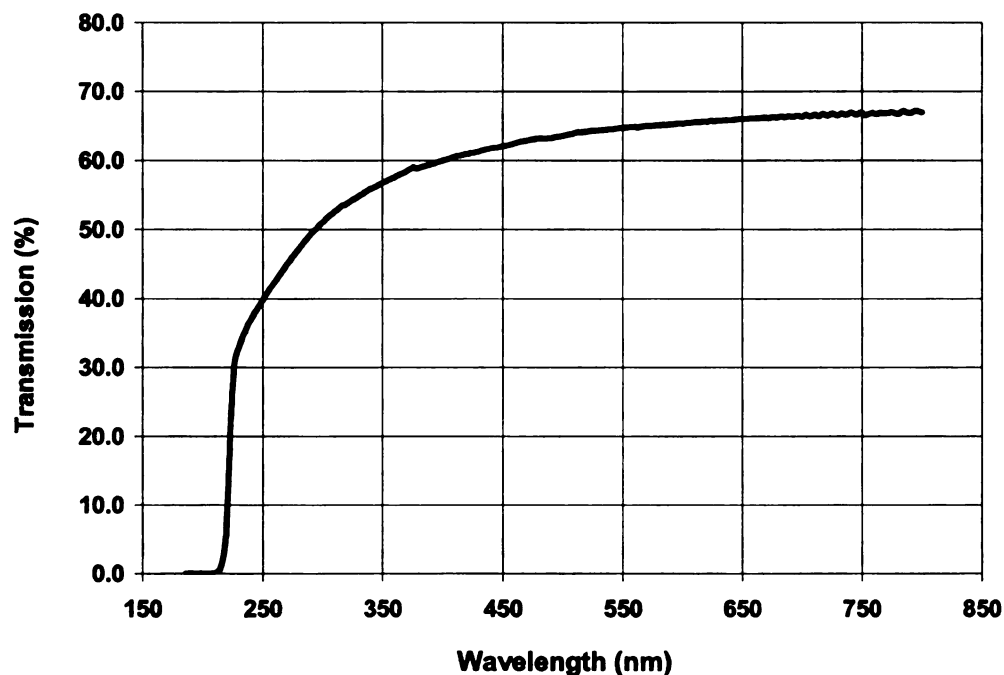


Figure 3-31: An example of optical transmission spectrum. It is expected that the percentage of the transmission is approaching to near 70% when wavelength increases beyond 800 nm up to 3 μm .

3.11 Diamond film stress measurement

This section establishes the way to calculate or measure polycrystalline diamond film stresses based on the most recent literature on polycrystalline diamond film and on composite beams/films/plates mechanical property studies. There are a number of ways to calculate or measure diamond film stresses in the CVD polycrystalline diamond film research community. Due to the complex nature of this task, it is difficult to say that one technique is better than the other, though each may have its own advantages or disadvantages. However, the results from different techniques are converging over time as some researchers have pointed out [47].

Among these most popular methods, one is a traditional method using Stoney's equation [122] from which the curvature of the investigated film and substrate is converted to the stress. It is often referred to as the substrate curvature technique and modifications of the original Stoney's equation have been made by many researchers based on different assumptions [123, 124, 125, 126, 127, 128, 129, 130, 131, 132, 133, 134]. However in general, the stresses calculated from the Stoney's equation or other similar theory are the overall average in-plane stress between the film and the substrate or the in-plane stress field along the normal axis to the film (or multiple beams) and the substrate. Another method is based on the empirical relation between the film stress and the diamond Raman spectroscopy peak shift from the unstressed diamond peak location at 1332 cm^{-1} . The amount of shifting in wave numbers is then calculated as the amount of the film stress present at the measurement location. Though the calculated stress is a local stress and hence will vary at different spots on the film, a relatively large number of scans at different spots on the film and a numerical approach of averaging may be used to

evaluate the overall stress of the film [47]. The third popular method of evaluating the polycrystalline diamond film is the $\text{Sin}^2\Psi$ technique with the X-ray Diffraction scan, often abbreviated as XRD. Though similar in principle to Raman, the X-ray Diffraction technique allows determination of the residual stress averaged over a larger sample area in addition to the transparency of diamond to the X-ray through the whole film depth [47]. X-ray Diffraction can be applied to polycrystals stress estimation [46, 135] while Raman is considered more suitable for single crystals or point to point stress studies [46, 136]. Other variations of film stress measurements are not included in the discussion in this paper.

3.11.1 Substrate curvature technique and Stoney's equation

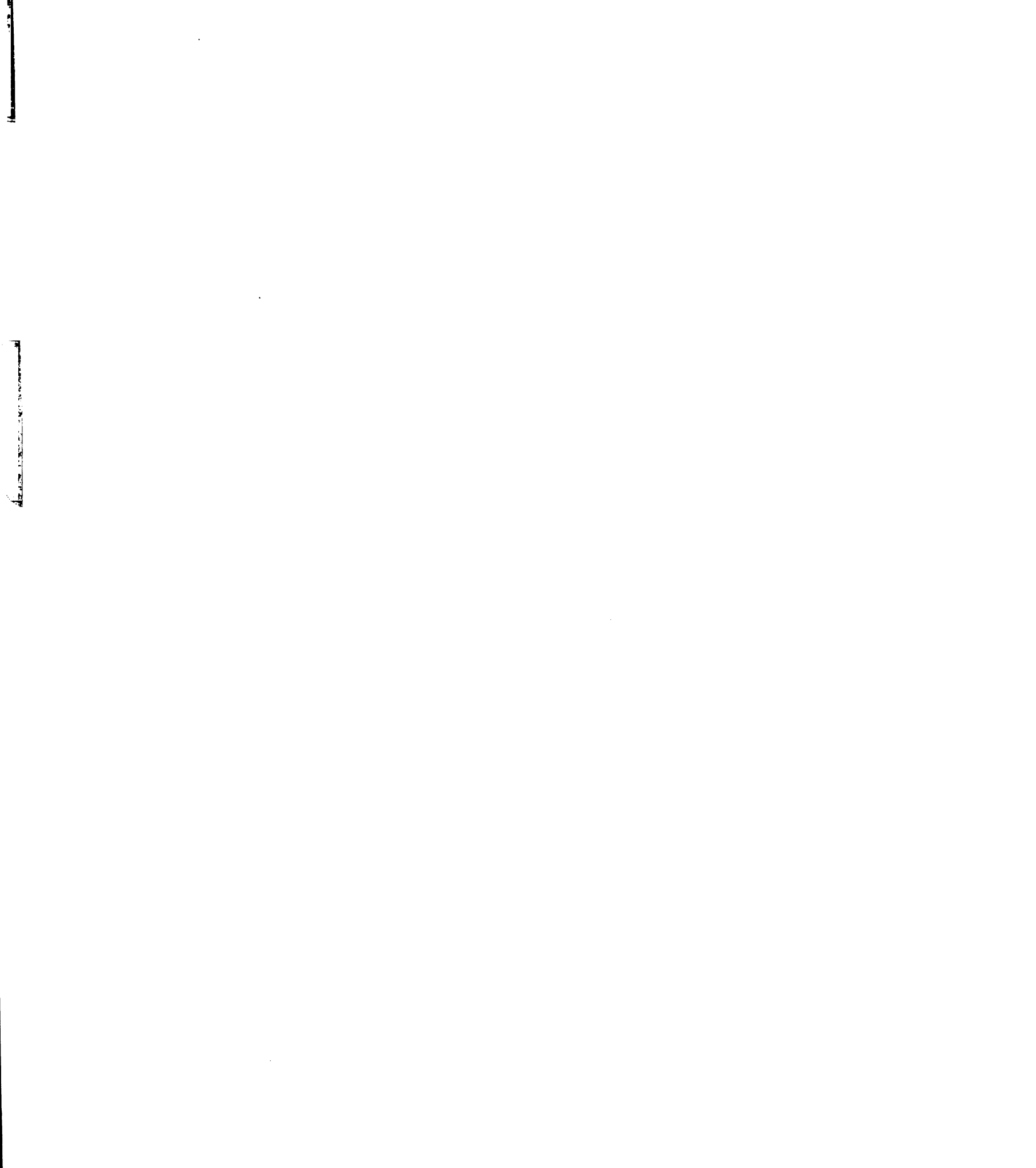
This section discusses Stoney's equation and the stress-curvature relationship so as to determine the formulas or equations to be used to calculate the stresses in polycrystalline diamond films deposited on silicon wafer substrates. Stoney's equation has been around for almost a century since it was first derived in 1909. This equation has been widely used in the area of thin film deposition to calculate the stresses of films grown on a substrate due to its simplicity and reasonable accuracy based on the assumption for ultrathin film deposited on a thick substrate. However since then, many questions have been raised and attempts of improving this equation were made. The reasons for these attempts are simple. First a major error source of Stoney's equation is that the ultrathin film grown on the thick substrate assumption is a rather extreme case in considering the film bending and the stress calculation [122]. Many modifications were developed trying to extend the Stoney's equation to the case of thick films grown on a comparable thickness substrates.

There are four major variations of the development of the stress-curvature relation with pros and cons for each variation described below. In chronological order, 1) Timoshenko published the analytical classic solution from pure mechanics methodology for a two-layer strip model problem with various end conditions in 1925, however the final formula limits its applications only to the bending situation due to the thermal expansion [123]; Blech et al. [137] and Zhang et al. [138] modified Timoshenko's approach to treat round substrates; 2) Brenner and Senderoff extended the Stoney's equation to the case for thick films with various boundary conditions in 1949 [124]; Brenner-Senderoff's approximation of Stoney's equation to thick films was adopted by many researchers in polycrystalline diamond film area [40, 139, 140, 141], this formula also received criticism for rather large errors compare to some other methods [142, 143]; 3) Townsend developed a general theory for the elastic interactions in a composite plate of layers with different relaxed planar dimensions in 1987 [130]; The initial model of the multilayer plates is more complicated than needed for our work and, in addition to that, the proposed solution is difficult to apply in the practical use in this study; However, Klein's modification of Townsend's equations not only relaxed the rigidity of the original solution for multilayered plates [144], but also simplified it to suit the bi-layer that is similar to Stoney's situation with a correction factor [142]; 4) Chu discovered the existence of dual neutral axes in the situation of bending due to the internal stresses, such as the lattice mismatch or thermal expansion differential in 1998 [132] and verified by Chuang et al. [133]; His bi-layer internal stress model extended Stoney's equation to thick films and is quite suitable to be used in this study for the polycrystalline diamond film deposited on the silicon wafer; However, the reactive bending strains was incorrectly

included in the interfacial strain expression in Chu's paper [133]; Chuang et al. corrected this error and therefore Chuang's equation is finally used in this research. It is worth noting that others have followed this scheme and established stress relation with the curvature for more general solutions on the multilayered or composite beams [134, 143]. However, they are beyond the scope of this research.

Another major error source of the Stoney's equation is that the internal bending stresses caused by the lattice mismatch or thermal expansion differentials are omitted [133]. This means for this study, that the diamond thin film would be assumed to have no bending stress acting on the silicon substrate in the model of Stoney's equation. Substantial error is expected when the curvature of the film-substrate or the thickness ratio of the film/substrate gets bigger.

When a beam or shaft or the like is bended by external moments, a neutral axis is defined *in the cross section of the beam or shaft along which there are no longitudinal stresses/strains. If the section is symmetric and is not curved before the bend occurs then the neutral axis is at the geometric centroid* [145] as shown in Figure 3-32. *All fibers on one side of the neutral axis are in a state of tension, while those on the opposite side are in compression.* However, a single neutral axis does not exist when a beam or shaft or the like is bended by internal stresses [132], such as the stresses caused by different linear thermal expansion between two different materials, lattice or structure mismatch for two different materials that adhere or grow together or for the same material that adhere or grow together. The bending stresses caused by CVD diamond film grown on silicon substrate and the subsequent growth of diamond film on diamond is example of the later kind. Since it is very important to construct the neutral axis for the analysis of the stress



field and further more to understand why a single neutral axis does not exist when a beam is bended by internal stresses, Chu's ideas of analysis is provided in this section [132].

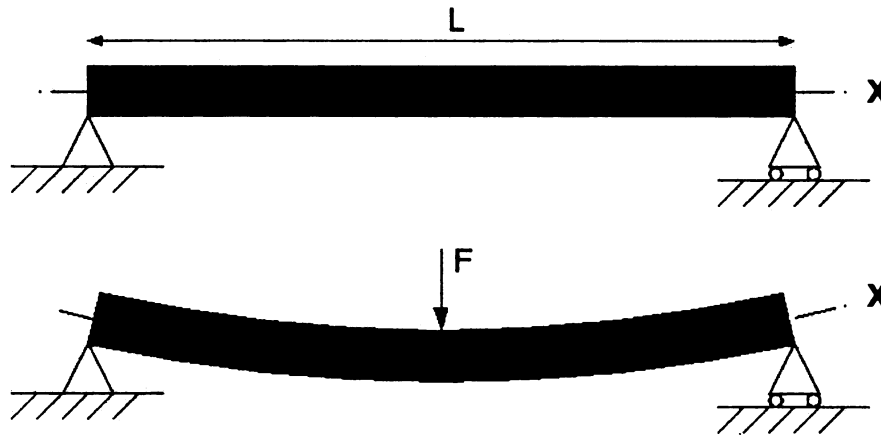


Figure 3-32: A beam with length L showing the neutral axis - X when an external moment $F \cdot L$ is applied to the beam [145].

Consider the case of a composite beam bent by an external moment M at the end of the beam as shown in Figure 3-33. The neutral axis of this composite beam can be constructed by following a three-step operation starting from the two equal length, separate beams before they are bent by external force and welded together.

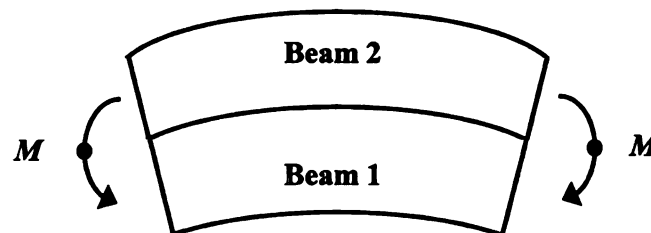
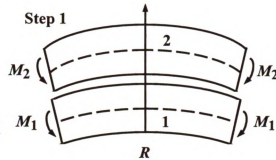
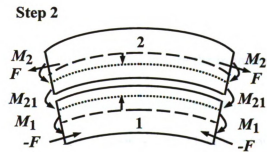


Figure 3-33: Schematic diagram showing bending by an external moment M .

Step 1: The positions of neutral axes indicated by the dotted lines is located at the geometric centroid of the beams with respect to the final radius of the curvature when pure external bending moments M_1 and M_2 are applied to the two separated beams;



Step 2: Compressing beam 1 and stretching beam 2 by external forces $-F$ and F to match the interface, the neutral axes are shifted; the directions of shifting are indicated by the arrow; M_{12} is the moment acting as the weld condition;



Step 3: Beam 1 and beam 2 is welded back at the interface; the total external moment is the sum of the moments M_1 , M_2 , and M_{21} ; the neutral axes from two beams are merged into one as the dash line indicated; the location of the neutral axis is associated with the Young's moduli and the thickness of both beams;

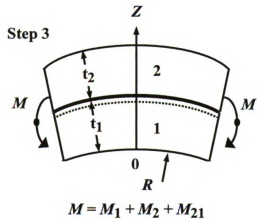


Figure 3-34: Schematic diagrams of a three-step operation for illustrating the movement of the composite two beam neutral axes from an external moment M .

To prove that the two neutral axes of beam 1 and beam 2 are merged into one, a expression of the distance between two neutral axes is derived. The scenario is if the distance of separation between these two neutral axes is zero, they are actually merged into one.

Assume the thermoelastic properties are E_1, ν_1, α_1 and E_2, ν_2, α_2 for beam 1 and beam 2 respectively, where E is Young's modulus, ν the Poisson's ratio, and α the thermal expansion coefficient. The beam geometry such as the length and width are set to be $l = w = 1$ for both beam 1 and beam 2, and the thickness to be t_1 and t_2 . The total thickness is t and t is equal to the sum of t_1 and t_2 . Both beams are flat before the moment M is applied to beams, the radius of curvature are turned into R after the moment M is applied to beams and both beams bends and becomes curved. Please note this bending (or curvature) is a two-dimensional bending and the radius of bending (curvature) is a simple single number measurement and the curvature itself of the bending can also be simply expressed as $1/R$.

Strictly speaking for beam 1 and beam 2 to fit perfectly in one composite beam the radius of beam 2 should be larger than beam 1. We assume that $R_1 = R_2 = R$ due to the radius of curvature R is much bigger than thickness of the beams t . The stress fields in each beam can be expressed for beam 1:

$$\sigma^1_{xx} = E_1 \left(\frac{z - \frac{t_1}{2}}{R} - \varepsilon_1 \right) \quad \text{Eq. 3-19}$$

and for beam 2:

$$\sigma_{xx}^2 = E_2 \left(\frac{z - \frac{t_2}{2} - t_1}{R} + \varepsilon_2 \right) \quad \text{Eq. 3-20}$$

where the first term on the right is due to pure bending strain (δ_1 or δ_2) and the second term is due to uniaxial compression with a strain of $-\varepsilon_1$ for beam 1 and uniaxial tension with a strain of ε_2 for beam 2 based on a general 1D expression (right hand side of both Eq. 3-19 and Eq. 3-20) between the stress and the strain:

$$\text{Stress} = \text{Stiffness} \times \text{Strain} \quad (\text{or } \sigma = E \cdot \varepsilon) \quad \text{Eq. 3-21}$$

The stiffness is usually defined by Young's modulus and the strain is defined as the relative displacement with respect to the original length (if in one dimension) by Eq. 3-22:

$$\varepsilon = \frac{\delta \cdot l}{l_o} = \frac{l - l_o}{l_o} \quad \text{Eq. 3-22}$$

where l_o is the original length of the material and l is the current length of the material.

The positive direction is the direction of the measurement. All parameters associated with above equations are labeled in Figure 3-35.

The shifting of the neutral axes δ_1 for beam 1 and δ_2 for beam 2 can be found from Eq. 3-19 and Eq. 3-20 by setting both σ_{xx}^1 and σ_{xx}^2 to be zero:

$$\delta_1 = \varepsilon_1 R \quad \text{and} \quad \delta_2 = \varepsilon_2 R \quad \text{Eq. 3-23}$$

We obtain the expression for the distance between the two neutral axes:

100

100

$$s = \frac{t_1 + t_2}{2} - (\delta_1 + \delta_2) = \frac{t_1 + t_2}{2} - R(\varepsilon_1 + \varepsilon_2) \quad \text{Eq. 3-24}$$

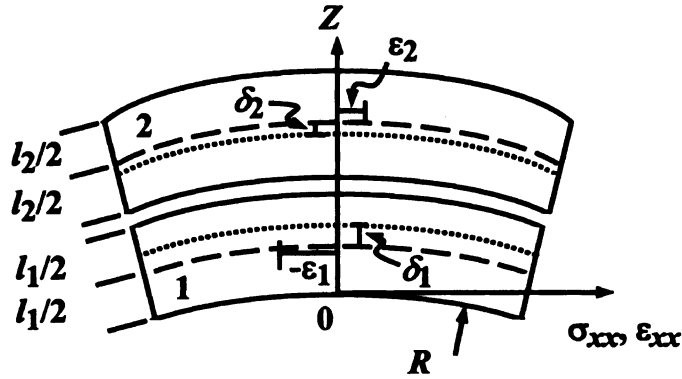


Figure 3-35: The corresponding stress distributions and the shifting of the neutral axes δ_1 and δ_2 from the central axes of the beams by the applied uniaxial tensile and compressive stresses to the two beams [132].

From the strain matching condition at the interface (considered as the boundary condition),

$$\varepsilon^1_{xx}(t_1) = \varepsilon^2_{xx}(t_2) \quad \text{Eq. 3-25}$$

Eq. 3-26 is obtained:

$$\frac{t_1}{2R} - \varepsilon_1 = -\frac{t_2}{2R} + \varepsilon_2 \quad \text{Eq. 3-26}$$

Substituting Eq. 3-26 into Eq. 3-24, the distance between the two neutral axes is proved to be zero under the external applied bending moment:

$$s = 0 \quad \text{Eq. 3-27}$$

Now consider the case of a composite beam is bent by an internal moment M_r , that is the same value as the external example given previously to create the same effect of bending as shown in Figure 3-36. This internal moment can be created as coupled internal reactive forces by applying coupled external forces in two opposite directions on two beams as showing for Step 1 in Figure 3-37, then glue them as one composite beam. Please note that the moment M_r is from the reactive force F_r from inside the material, the movement of the neutral axes is opposite to when the same external force is applied. The location of the neutral axes of this composite beam can also be readily illustrated qualitatively by following the two-step operation shown in Figure 3-37. We leave out the derivations of the equations for the stress field from Chu's work.

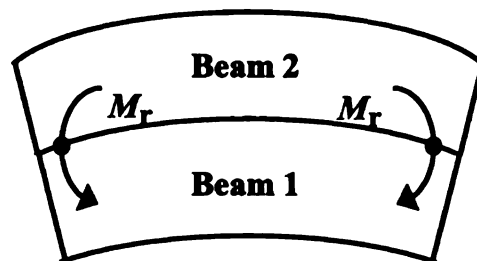


Figure 3-36: Schematic diagram showing bending by an internal moment M_r .

Step 1: Stretching and compressing of

beam 1 and beam 2 respectively to match their lengths before welding;

Step 2: Weld beam 1 and beam 2; due to the expansion of beam 2 and contraction of beam 1 upon removal of the external forces

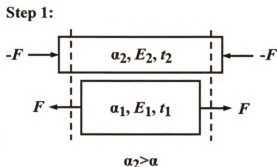
$-F$ and F , the composite beam bend

downwards; since F_r and $-F_r$ are the

reactive forces of the external forces $-F$ and

F from inside the beam, the neutral axis of beam 2 moves upwards and the axis of

beam 1 moves downwards;



Step 2:

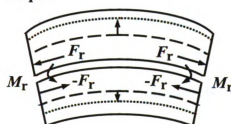


Figure 3-37: Schematic diagrams of a two-step operation for illustrating the movement of a composite two beam neutral axes from an internal moment M_r .

From the above illustration, there are two neutral axes that exist in the composite beam if it is subject to the internal stress. However, because of this omission from the Stoney's equation, the single neutral axis based on zero bending moment causes the error and does not exist in a two-layer system bent by the internal stresses [132].

A hybrid analytical method for the general case of bi-layer composite beam or plate curving problem with the stress field subjected to a strain differential (the difference of the strain) was developed by Chuang and Lee [133]. Their solution and a partial

derivation are restated here with a slight modification to fit into the applications in this study. In order to include internal stresses as we discussed previously in Figure 3-37, the same two-step operation is followed in order to construct the stress field and then solve for the stresses.

In the situation of diamond films deposited on silicon wafers, the strain differential is the linear difference of the length between the film and substrate when both the film and the substrate are thought of as not welded together, i.e. completely relaxed. So they are two separate flat pieces of plates in this situation. Based on the fact from all the samples collected in this study, the diamond film is always bend away from the position of the silicon substrate, therefore the diamond film can be assumed to be shorter at the reference state. This can also be understood as the lattice spacing of diamond is smaller than that of silicon. This strain differential is defined as $\Delta\varepsilon$ in Figure 3-38 (1). Then the diamond film is stretched and the silicon substrate is compressed by external forces F and $-F$ to match the length of the interface of these two separate beams. This completes step 1. The film and the substrate are then welded together. Upon the removal of the external forces the film contracts and the substrate expands causing both the film and the substrate bent towards the film. Step 2 is completed and the final state is shown in Figure 3-38 (2).

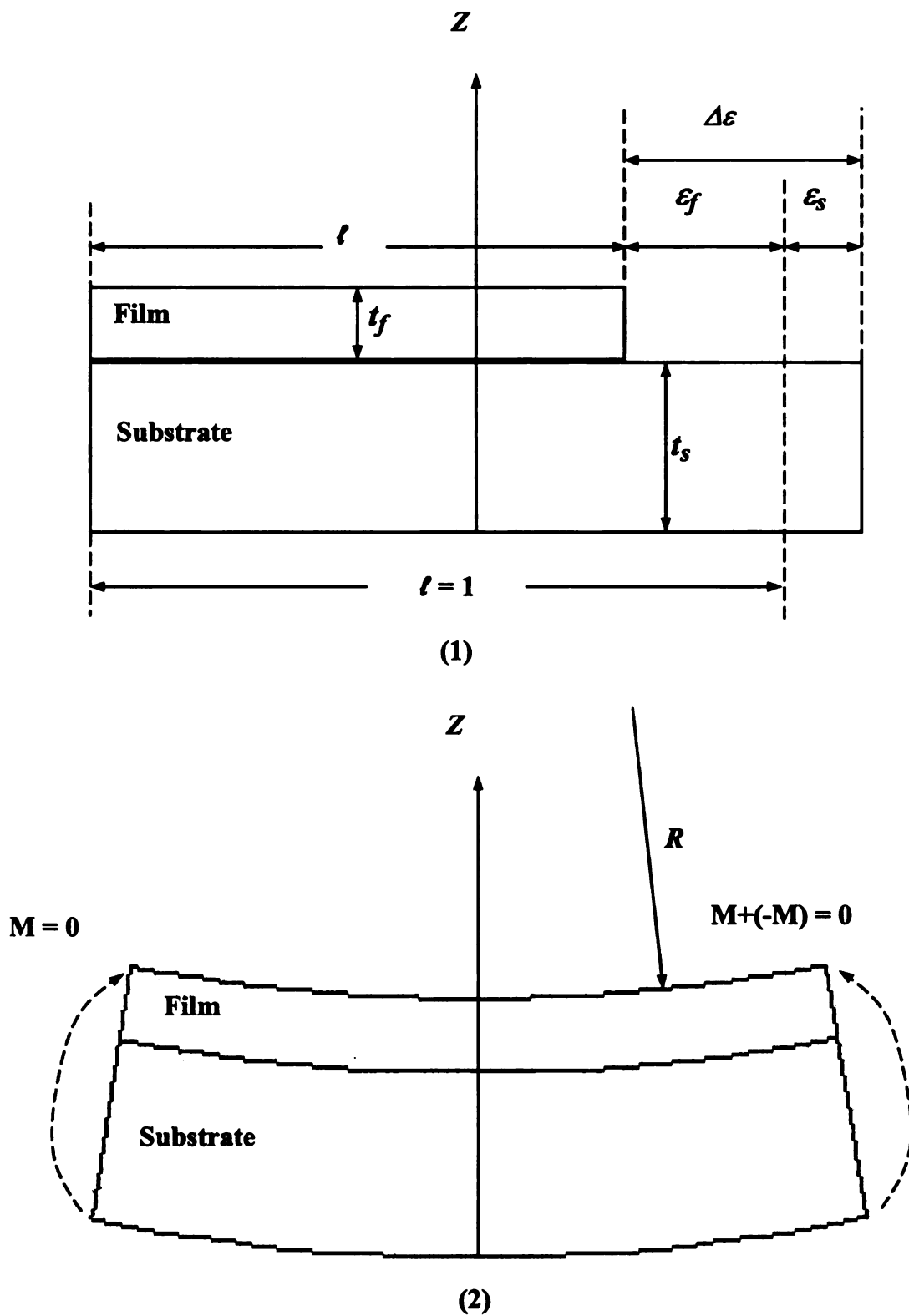


Figure 3-38: Redraw of the schematic sketches of the analysis procedure for a composite beam subjected to a differential strain $\Delta\epsilon$: (1) beam geometry at reference state. (2) The final resultant beam configuration with no external moments applied [133].

Follow Chuang's procedure, two scalar parameters α and β were defined. The α is the ratio of the Young's moduli of the elastic film and the substrate and the β is the ratio of the thickness of the film and the substrate:

$$\alpha \equiv \frac{E_f}{E_s} \quad \text{Eq. 3-28}$$

$$\beta \equiv \frac{t_f}{t_s} \quad (t \equiv t_f + t_s) \quad \text{Eq. 3-29}$$

There are various sources of the strain differential in real situations. In Figure 3-38, $\Delta\varepsilon$ is simply stated as the length differential:

$$\Delta\varepsilon = |\varepsilon_s| + \varepsilon_f, \quad (\varepsilon_s \text{ is negative}) \quad \text{Eq. 3-30}$$

Also the strain differential can be caused by the lattice mismatch:

$$\Delta\varepsilon = \frac{|a_f - a_s|}{a_s} \quad \text{Eq. 3-31}$$

where a_s and a_f are the lattice spacing parameters of the substrate and the film, or by

the linear thermal expansion:

$$\Delta\varepsilon = \Delta\alpha \cdot \Delta T \quad \left(\Delta\alpha = |\alpha_f - \alpha_s| \right) \quad \text{Eq. 3-32}$$

where $\Delta\alpha$ is the difference of the linear thermal expansion coefficient between the diamond film and the silicon substrate. ΔT is the temperature difference between the processing temperature and the temperature of the final state that the silicon wafer-

diamond film is cooled to after the wafer-film is taken out of the processing chamber, which is the room temperature.

In the general case for a strain differential $\Delta\varepsilon$ presented as the linear length differential as expressed in Eq. 3-30 and plotted in Figure 3-38-(1), the relation between the radius of curvature due to the bending shown in Figure 3-38-(2) and the strain differential can be expressed as:

$$\frac{1}{R} = F(\alpha, \beta) \cdot \left(\frac{6 \cdot \Delta\varepsilon}{t_s} \right) \quad \text{Eq. 3-33}^3$$

where

$$F(\alpha, \beta) \equiv \frac{\alpha\beta(1+\beta)}{(1+\alpha\beta^3)(1+\alpha\beta) + 3\alpha\beta(1+\beta)^2} \quad \text{Eq. 3-34}^4$$

This means if the radius of curvature R is measured, the strain differential can be calculated from the above two equations. Then the stress field in the film and the substrate can also be calculated from the calculated strain differential $\Delta\varepsilon$. The equations are provided by Chuang and Lee and shown as Eq. 3-35 and Eq. 3-36.

For stress field in the **film** ($t_s < z < t$):

$$\sigma_f(z) = \frac{\alpha E_s \cdot \Delta\varepsilon}{1 + \alpha\beta} - F(\alpha, \beta) \left(\frac{6\alpha E_s \cdot \Delta\varepsilon}{t_s} \right) \cdot \left[\left(z - t_s - \frac{t_f}{2} \right) + \frac{t}{2(1 + \alpha\beta)} \right] \quad \text{Eq. 3-35}^5$$

For stress field in the **substrate** ($0 < z < t_s$):

³ Equation (Eq. 3-33) is from reference [133]. The derivation is omitted.

⁴ Equation (Eq. 3-34) is from reference [133]. The derivation is omitted.

⁵ Equation (Eq. 3-35) is from reference [133]. The derivation is omitted.

$$\sigma_s(z) = -\frac{E_s \alpha \beta \cdot \Delta \varepsilon}{1 + \alpha \beta} + F(\alpha, \beta) \left(\frac{6E_s \cdot \Delta \varepsilon}{t_s} \right) \cdot \left[\frac{\alpha \beta \cdot t}{2(1 + \alpha \beta)} - \left(z - \frac{t_s}{2} \right) \right] \quad \text{Eq. 3-36}^6$$

where $t = t_s + t_f$, is the total thickness of the substrate and the film. The stress at the **interface** between the diamond film and the silicon substrate when $z = t_s$ should be taken as the **total stress** the substrate exerts on the film. In this study, the stress in the diamond film is of interest. Therefore Eq. 3-35 is used. From Eq. 3-33, the strain $\Delta \varepsilon$ can be expressed as:

$$\Delta \varepsilon = \frac{t_s}{6R \cdot F(\alpha, \beta)} \quad \text{Eq. 3-37}$$

Substitute the $\Delta \varepsilon$ in Eq. 3-35 by Eq. 3-37 and the variable z by t_s , Eq. 3-35 becomes:

$$\sigma_f(z = t_s) = \frac{E_f \cdot t_s}{R(1 + \alpha \beta)} \cdot \left[\frac{1}{6F(\alpha, \beta)} + \frac{\alpha \beta^2}{2} - \frac{1}{2} \right] \quad \text{Eq. 3-38}$$

This is the **total residual stress** include the thermal stress induced by the different thermal expansion between diamond film and silicon wafer after their temperatures are cooled down from the operating temperature (i.e. from 800 °C to 1200 °C) to the room temperature. In real implementation, the initial curvature (defined by $\frac{1}{R}$) of the substrate without the stress can not be ignored because the film-substrate curvature under the stress is also usually small. It has been measured that a new freestanding silicon wafers has some curvature with the radius between 50 to 80 meters. Though this curvature is small

⁶ Equation (Eq. 3-36) is from reference [133]. The derivation is omitted.

with $\frac{1}{R}$ value from 0.0125 to 0.02 m⁻¹, it is not negligible to the total film and substrate

curvature. Therefore Eq. 3-38 becomes,

$$\sigma_{tot} = \sigma_f(z=t_s) = \frac{E_f \cdot t_s}{(1 + \alpha\beta)} \cdot \left[\frac{1}{6F(\alpha, \beta)} + \frac{\alpha\beta^2}{2} - \frac{1}{2} \left[\frac{1}{R} - \frac{1}{R_0} \right] \right] \quad \text{Eq. 3-39}$$

where R_0 is the initial radius of curvature of the silicon substrate without any diamond deposited and R is the final radius of curvature of the composite diamond/silicon plate.

3.11.2 The thermal stress calculation

The thermal stress field can also be calculated using the same set of equations Eq. 3-35 and Eq. 3-36 but with the strain differential $\Delta\varepsilon$ replaced by Eq. 3-32. However, the high optical quality diamond films are deposited at high temperatures over 1000 °C and the linear thermal expansion coefficients of both diamond film and silicon wafer as the substrate vary significantly versus temperature. As Figure 2-26 indicated, the linear thermal expansion coefficient of diamond varies from $1.0 \times 10^{-6} \text{ }^\circ\text{K}^{-1}$ to $5.4 \times 10^{-6} \text{ }^\circ\text{K}^{-1}$ when the temperature changes from room temperature (293 °K or 20 °C) to 1400 °K (or 1127 °C) while of silicon varies from $2.6 \times 10^{-6} \text{ }^\circ\text{K}^{-1}$ to $4.6 \times 10^{-6} \text{ }^\circ\text{K}^{-1}$. Therefore the strain differential $\Delta\varepsilon$ expressed by Eq. 3-32 becomes complicated to calculate due to the fact that both linear thermal expansion coefficient of diamond and silicon are a function of the temperature. However if we assume that these two functions can be expressed as $\alpha_f(T)$ and $\alpha_s(T)$ for diamond and silicon respectively, then graphically the area under

these two curves from temperature point T_1 to point T_2 for silicon wafer can be expressed as,

$$A_s = \int_{T_1}^{T_2} \alpha_s(T) \cdot dT \quad \text{Eq. 3-40}$$

and the diamond as the film growing on the substrate can be expressed as,

$$A_f = \int_{T_1}^{T_2} \alpha_f(T) \cdot dT \quad \text{Eq. 3-41}$$

respectively. Then the difference of these two areas for the same temperature interval from point T_1 to point T_2 is:

$$\Delta A = A_s - A_f = \int_{T_1}^{T_2} [\alpha_s(T)] \cdot dT - \int_{T_1}^{T_2} [\alpha_f(T)] \cdot dT \quad \text{Eq. 3-42}$$

The right hand side of Eq. 3-42 is the definite integral form of Eq. 3-32. This means if we can graphically calculate the difference of the area between the two curves of the linear thermal expansion coefficient of diamond and silicon, the value of the strain differential $\Delta \varepsilon$ is obtained.

The next question is how to find the mathematical expression of the two curves of the linear thermal expansion coefficient of diamond and silicon from Figure 2-26? The numerical curve fitting method is used to determine the function that will be used for the calculation. First the temperature range is defined from room temperature 293 °K (or 20 °C) to 1400 °K (or 1127 °C). Only part of the curve within this range in Figure 2-26 needs to be fitted during the process. This can help us by narrowing down the focus to only the current diamond growth temperature condition (instead of the whole curve) and it will be

easier then to find a math function that best fits to the curve. Figure 3-39 shows the final result of the best-fit of the linear thermal expansion coefficient of silicon (above) and diamond (below) for temperature range from 293 °K (or 20 °C) to 1400 °K (or 1127 °C). The best-fit function for silicon is a logarithm function with the base equal to 2.4 and a down shift constant of minus 3.4:

$$\alpha_s(T) = \log_{2.4}(T - 93) - 3.4 \quad \text{Eq. 3-43}$$

and the best-fit function for diamond is a partial circle with its radius equals to 253660.

$$\alpha_f(T) = \sqrt{253660^2 - (T - 1860)^2} - 253654.15 \quad \text{Eq. 3-44}$$

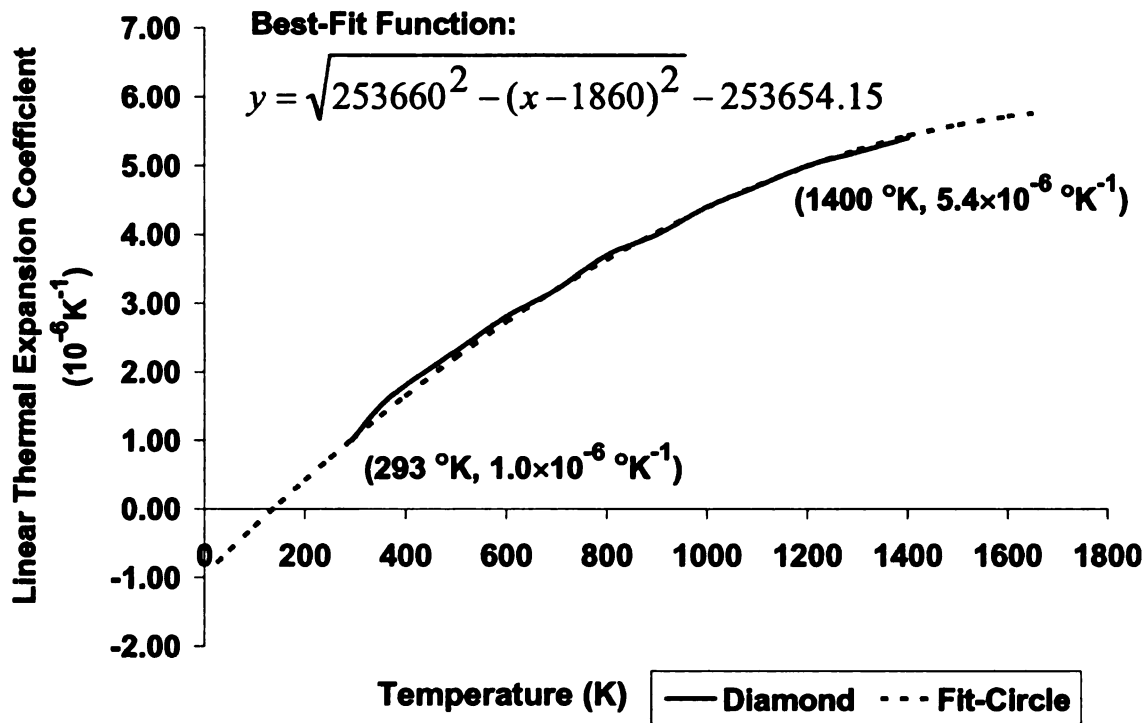
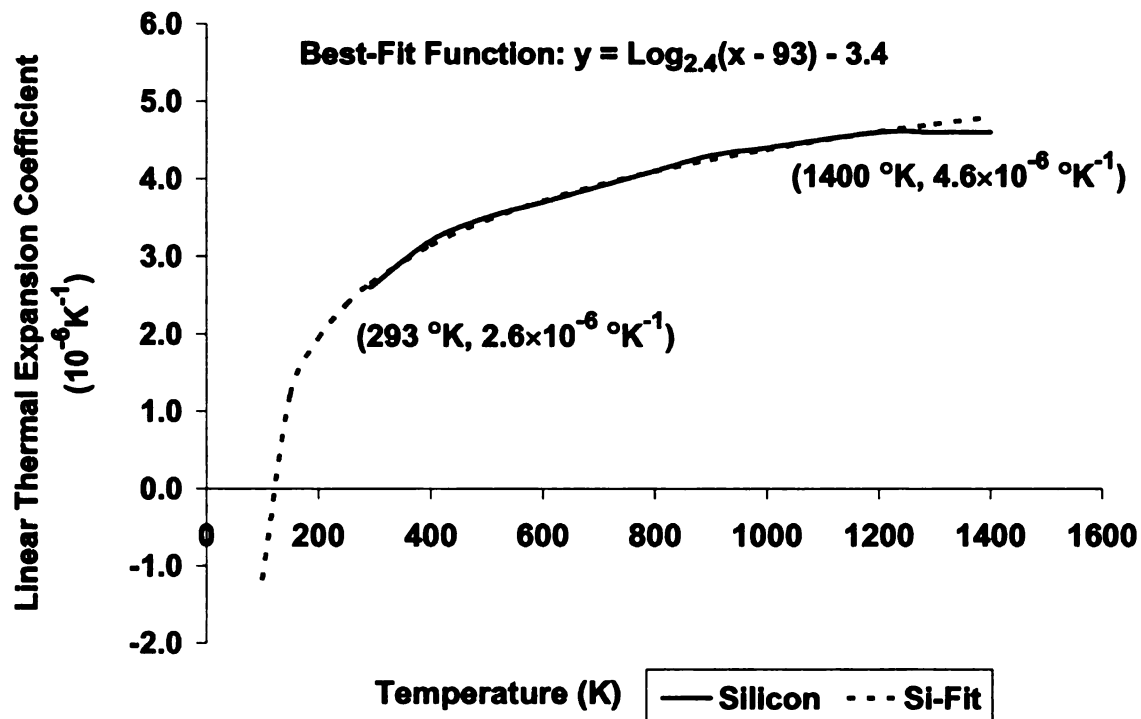


Figure 3-39: Best-Fit functions to the curves in Figure 2-26 for linear thermal expansion coefficient of silicon (above) and diamond (below) for temperature range from 293 °K (or 20 °C) to 1400 °K (or 1127 °C).

Table 3-5 gives an idea of how precise the values are of the best-fit functions to its original data. The precision is quite acceptable for the fit function. The next step is to use these two functions to calculate the difference of the areas under the two different curves and therefore to obtain the strain differentials from the given set of temperatures (T_1 , T_2). The temperature T_1 is the lower limit of the integral, which is always the room temperature to which the substrate and film cool down. For this calculation, $T_1 = 20\text{ }^\circ\text{C}$ (or $293\text{ }^\circ\text{K}$) is always the value used for room temperature. The temperature T_2 is the upper limit of the integral and it is the substrate temperature at which the diamond film is deposited. In considering that the substrate temperature is usually difficult to control plus the deposition temperature varies radially across the substrate diameter and temporally, it is reasonable to divide the deposition temperature into $50\text{ }^\circ\text{K}$ interval from $1050\text{ }^\circ\text{K}$ to $1400\text{ }^\circ\text{K}$ (equivalent to temperature interval from $777\text{ }^\circ\text{C}$ to $1127\text{ }^\circ\text{C}$, between which most deposition temperatures fall). There are seven intervals between $1050\text{ }^\circ\text{K}$ to $1400\text{ }^\circ\text{K}$, therefore the deposition temperature can be chosen from any of these seven intervals.

Figure 3-40 is an example how these best-fit curves of linear thermal expansion coefficient and their areas under the curves look like assuming that the deposition temperature equals to $1400\text{ }^\circ\text{K}$.

Table 3-5: Comparison of the linear thermal expansion coefficients between the best-fit value and original data.

Silicon			Diamond		
Temperature, T, (K)	α , (10^{-6} K^{-1})	Best-fit, logarithm	Temperature, T, (K)	α , (10^{-6} K^{-1})	Best-fit, circle
293	2.6	2.7	293	1.00	1.01
400	3.2	3.1	350	1.50	1.36
500	3.5	3.5	400	1.80	1.65
600	3.7	3.7	500	2.30	2.20
700	3.9	3.9	600	2.80	2.72
800	4.1	4.1	700	3.20	3.20
900	4.3	4.2	800	3.70	3.64
1000	4.4	4.4	900	4.00	4.03
1200	4.6	4.6	1000	4.40	4.39
1300	4.6	4.7	1100	4.70	4.71
1400	4.6	4.8	1200	5.00	4.99
			1300	5.20	5.23
			1400	5.40	5.43

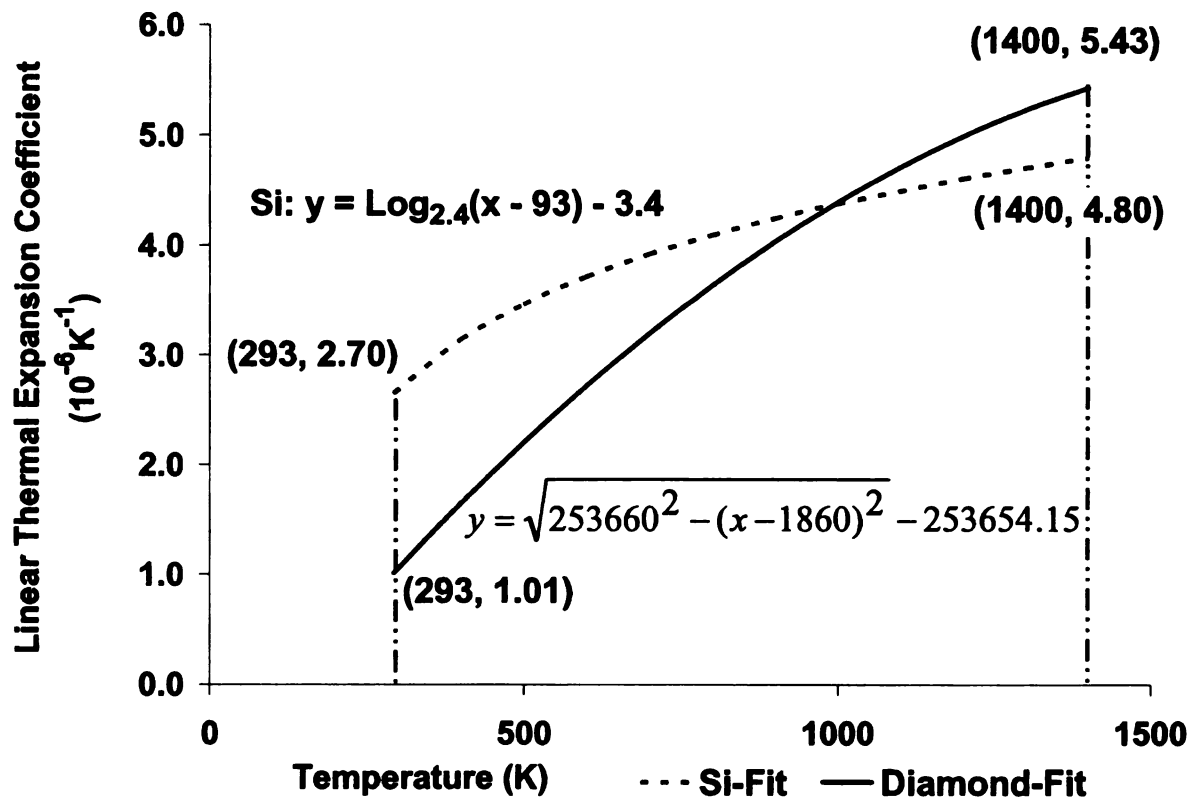


Figure 3-40: How the difference of the area is calculated graphically (so is the strain differential) using the best-fit curves of the linear thermal expansion coefficient.

From Eq. 3-42, the strain differential can be expressed as:

$$\Delta\varepsilon = \Delta A = \int_{T_1}^{T_2} [\alpha_s(T)] \cdot dT - \int_{T_1}^{T_2} [\alpha_f(T)] \cdot dT \quad \text{Eq. 3-45}$$

where $\alpha_s(T)$ and $\alpha_f(T)$ are given by Eq. 3-43 and Eq. 3-44. After using the technique of integration by parts, the final result of the integrals of Eq. 3-43 or the area under the thermal expansion coefficient curve of silicon – A_s , can be expressed as:

$$A_s = \left[(T - 93) \cdot \log_{2.4}(T - 93) \right]_{T_1}^{T_2} - \left(\frac{1}{\ln 2.4} + 3.4 \right) \cdot [T]_{T_1}^{T_2} \quad \text{Eq. 3-46}$$

and the integral of the function in Eq. 3-44 can also be found readily from the integral table. Therefore the area under the thermal expansion coefficient curve of diamond, A_f , can be expressed as:

$$A_f = \left[\frac{(T - a)}{2} \cdot \sqrt{R^2 - (T - a)^2} + \frac{R^2}{2} \cdot \sin^{-1} \left(\frac{T - a}{R} \right) \right]_{T_1}^{T_2} + b \cdot [T - a]_{T_1}^{T_2} \quad \text{Eq. 3-47}$$

where (a, b) is the center of the arc curve coordinates on the temperature-coefficient plane and the “ R ” is the radius of this arc curve. Their values are stated in Eq. 3-48.

$$\left\{ \begin{array}{l} a = 1860 \\ b = -253654.15 \\ R = 253660 \end{array} \right\} \quad \text{Eq. 3-48}$$

Finally the value of the thermal stress due to the strain differential $\Delta\varepsilon$, which is caused by the difference of the linear thermal expansion between the two different

materials silicon and diamond can be solved by using Eq. 3-35 letting $z = t_s$. However, the sign of the thermal stresses need to be discussed and determined.

From the process of calculating the strain differentials between silicon and diamond previously, the overall linear thermal expansion of silicon is larger than diamond for the given range of the temperature variation. This means the silicon wafer expands more than diamond when temperature increases and also shrinks more than diamond when temperature decreases. If we assume the diamond growth direction as the positive direction, then when the temperature drops from the deposition temperature to the lower room temperature the stress direction is opposite to the diamond growth direction since the silicon wafer is under the diamond film. On the other hand, the intrinsic stress direction is the same as the diamond growth direction based on previous observation on freestanding diamond films. The freestanding diamond films are always seen bent towards the diamond growth direction. Therefore the thermal stress is negative to the overall diamond film stress direction, the intrinsic stress direction.

Observations are also consistent with the above analysis. The diamond-silicon wafers all bend toward the diamond growth direction due to the residual stress formed after the diamond film is deposited. All diamond film samples are found to bend more toward the growth direction after the silicon wafer is back etched from the diamond films. That means that the silicon wafer is actually holding back the diamond film from bending more. Therefore the thermal stresses of the silicon wafer that act on the diamond film should be negative to its bending direction, which is already defined as the positive direction.

3.11.3 Raman spectroscopy for stress evaluation

The most popular equation for quantitative measurement of residual stress in CVD grown polycrystalline diamond films by Raman spectroscopy is J. W. Ager's formula published in 1993 [136]. This formula uses a biaxial stress model, which is a more realistic thin-film stress model than the uniaxial stress model of previous studies. The final set of equations is actually quite simple and they are restated as follow.

For the singlet phonon [146]:

$$\tau = -1.08 \frac{\text{GPa}}{\text{cm}^{-1}} (\nu_s - \nu_o) \quad \text{Eq. 3-49}$$

For the doublet phonon [146]:

$$\tau = -0.384 \frac{\text{GPa}}{\text{cm}^{-1}} (\nu_d - \nu_o) \quad \text{Eq. 3-50}$$

where τ is the in-plane residual stress at the point on the film where the Raman is taken, ν_o is the wavenumber when film is at zero stress, which is 1332.0 cm^{-1} for diamond material (this value may vary a few number in the first decimal place in real measurement when system calibrates with a reference single crystal diamond), and ν , the observed wavenumber in the spectrum from the sample. The negative result indicates the stress in the film is compressive and the positive indicates the film stress is tensile. It should be noted that, Eq. 3-49 and Eq. 3-50 are an averaged result obtained from a more complicated set of equations based on crystal orientation. The crystal orientation of each individual crystal must be known for polycrystalline film stress investigation [147]. It should further be noted that the (100) doublet value is not used for the averaging *since Raman scattering from the phonon is forbidden in backscattering* [136].

For the more complicated case, four possible orientations were listed for the CVD diamond crystals in the film as a cubic crystal material by Ager et al. and they are in (100), (111), (110), and $(11\bar{2})$ directions. The residual stresses in the film for these four different oriented crystals are expressed as follow.

Biaxial stress in the (100) plane,

$$\text{Singlet: } \tau = -0.610 \frac{\text{GPa}}{\text{cm}^{-1}} (\nu_s - \nu_o) \quad \text{Eq. 3-51}$$

$$\text{Doublet: } \tau = -0.422 \frac{\text{GPa}}{\text{cm}^{-1}} (\nu_d - \nu_o) \quad \text{Eq. 3-52}$$

Biaxial stress in the (111) plane,

$$\text{Singlet: } \tau = -1.49 \frac{\text{GPa}}{\text{cm}^{-1}} (\nu_s - \nu_o) \quad \text{Eq. 3-53}$$

$$\text{Doublet: } \tau = -0.350 \frac{\text{GPa}}{\text{cm}^{-1}} (\nu_d - \nu_o) \quad \text{Eq. 3-54}$$

Biaxial stress in the (110) plane,

$$\text{Singlet: } \tau = -1.11 \frac{\text{GPa}}{\text{cm}^{-1}} (\nu_s - \nu_o) \quad \text{Eq. 3-55}$$

$$\text{Doublet: } \tau = -0.444 \frac{\text{GPa}}{\text{cm}^{-1}} (\nu_d - \nu_o) \quad \text{Eq. 3-56}$$

Biaxial stress in the $(11\bar{2})$ plane,

$$\text{Singlet: } \tau = -1.11 \frac{\text{GPa}}{\text{cm}^{-1}} (\nu_s - \nu_o) \quad \text{Eq. 3-57}$$

$$\text{Doublet: } \tau = -0.357 \frac{\text{GPa}}{\text{cm}^{-1}} (\nu_d - \nu_o) \quad \text{Eq. 3-58}$$

where the doublets in above equations are averaged from the split doublet values of the spectrum [136].

The average that Ager et al. took is based on assuming that diamond crystals in the diamond film are equally orientated in above four directions, which is considered untrue and impossible in almost all cases. Figure 3-41 provides a typical X-ray diffraction spectrum for a CVD polycrystalline diamond film. The different intensities of different direction oriented diamond crystals that XRD spectrum has shown indicate different amounts of diamond crystals detected at different orientations.

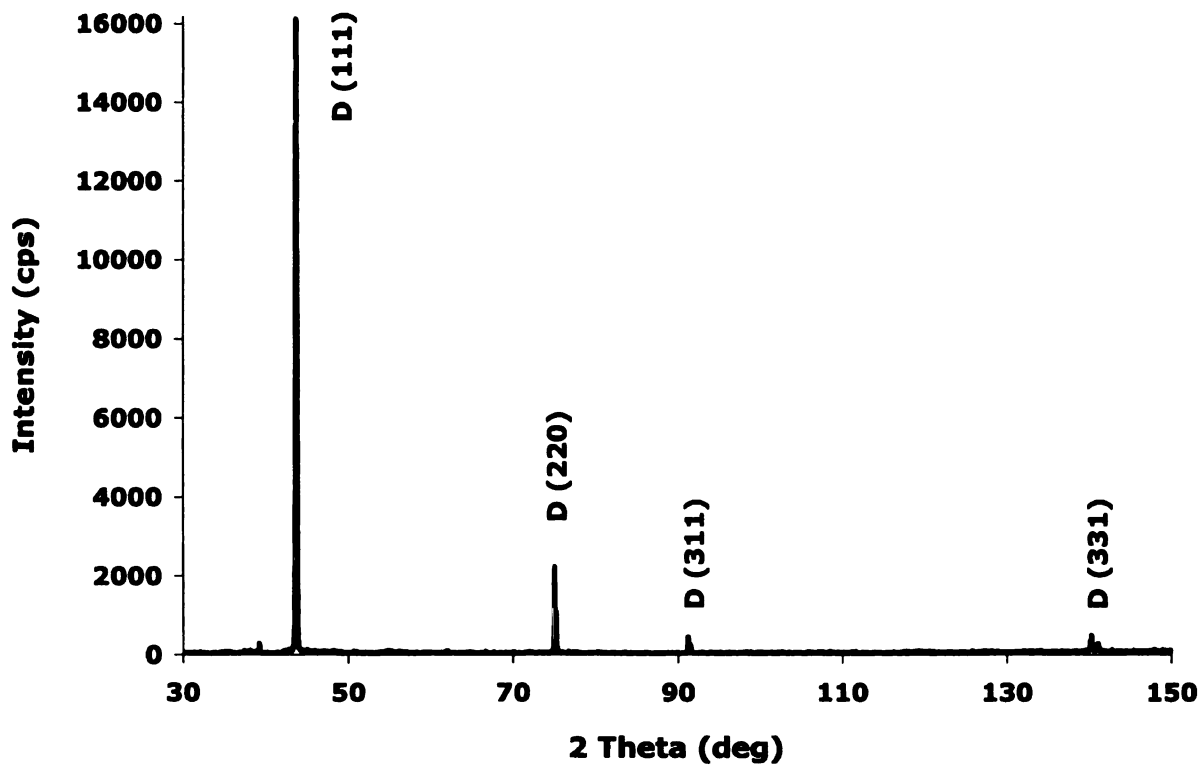


Figure 3-41: XRD spectrum from one of the lab grown freestanding diamond film samples (SZ-2inch-043) that shows highly oriented diamond crystals in the direction (111). Diamond is a typical cubic crystal material that consists of five possible lattice planes: (111), (220), (311), (400), and (331). However the (400) plane is missing in the XRD plot. That means no grain that oriented in [400] ($2\theta = 119.5^\circ$) direction was found within the 45° angle with the surface normal in this diamond film sample.

Theoretically, the possible planes that exhibit Bragg diffraction and can be detected by XRD for a cubic material, such as CVD polycrystalline diamond film are (111), (220), (311), (400), and (331) directions. Even though (220) is a repeat of (110) in the extended lattice space and (400) is a repeat of (100), the plane $(11\bar{2})$ is never found in our diamond samples. Therefore, it is suggested that the residual stress measurement and calculation of the CVD polycrystalline diamond film should be based on the plane information provided by the X-ray diffraction and statistically average the stresses base on the relative intensities of each plane direction. Fang et al. provided another four sets of equations in 2002 in replacing Ager's four sets of equations based on this idea [148].

Biaxial stress in the (111) plane [136, 148],

$$\text{Singlet: } \tau'_{(111)} = -1.49 \frac{\text{GPa}}{\text{cm}^{-1}} (\nu_s - \nu_o) \quad \text{Eq. 3-59}$$

$$\text{Doublet: } \tau''_{(111)} = -0.350 \frac{\text{GPa}}{\text{cm}^{-1}} (\nu_d - \nu_o) \quad \text{Eq. 3-60}$$

Biaxial stress in the (220) plane [148],

$$\text{Singlet: } \tau'_{(220)} = -1.09 \frac{\text{GPa}}{\text{cm}^{-1}} (\nu_s - \nu_o) \quad \text{Eq. 3-61}$$

$$\text{Doublet: } \tau''_{(220)} = -0.370 \frac{\text{GPa}}{\text{cm}^{-1}} (\nu_d - \nu_o) \quad \text{Eq. 3-62}$$

Biaxial stress in the (311) plane [148],

$$\text{Singlet: } \tau'_{(311)} = -1.02 \frac{\text{GPa}}{\text{cm}^{-1}} (\nu_s - \nu_o) \quad \text{Eq. 3-63}$$

$$\text{Doublet: } \tau''_{(311)} = -0.410 \frac{\text{GPa}}{\text{cm}^{-1}} (\nu_d - \nu_o) \quad \text{Eq. 3-64}$$

Biaxial stress in the (400) plane [148],

$$\text{Singlet: } \tau'_{(400)} = -0.610 \frac{\text{GPa}}{\text{cm}^{-1}} (\nu_s - \nu_o) \quad \text{Eq. 3-65}$$

$$\text{Doublet: } \tau''_{(400)} = -0.420 \frac{\text{GPa}}{\text{cm}^{-1}} (\nu_d - \nu_o) \quad \text{Eq. 3-66}$$

However the equations for biaxial stress in the (331) plane is not given. By using the technique similar to what Ager et al. provided in the appendix of the publication [136], this set of equations can also be derived. Please note that the signal strength of (331) plane in XRD spectrum appeared to be always very small. So one option is to assume that the (331) plane oriented diamond crystals are statistically zero in all as grown diamond films for this study without having to derive the last set of equation.

Then equation Eq. 3-59 to Eq. 3-65 (*excluding the (400) doublet value since Raman scattering from the phonon is forbidden in backscattering*) can be statistically averaged by their respective contents provided in XRD spectrum. If it is assumed that the strongest peak intensity in the XRD is 1 and τ_i is the biaxial stress in plane- i , the total averaged residual stress can be expressed as [148]:

$$\tau' = \sum_i I_{ri} \tau'_i \quad (\text{For the singlet phonon}) \quad \text{Eq. 3-67}$$

$$\tau'' = \sum_i I_{ri} \tau''_i \quad (\text{For the doublet phonon}) \quad \text{Eq. 3-68}$$

where I_{ri} is the normalized relative intensity of the XRD pattern in plane- i .

As it has been detailed discussed in section 3.8.1, the multiplicity factor j should be taken into consideration when using the relative intensity of the XRD pattern “reflected” from a particular plane. The multiplicity factors of five different planes for diamond material are included in Table 3-4. If j_i is the multiplicity factor for plane- i and

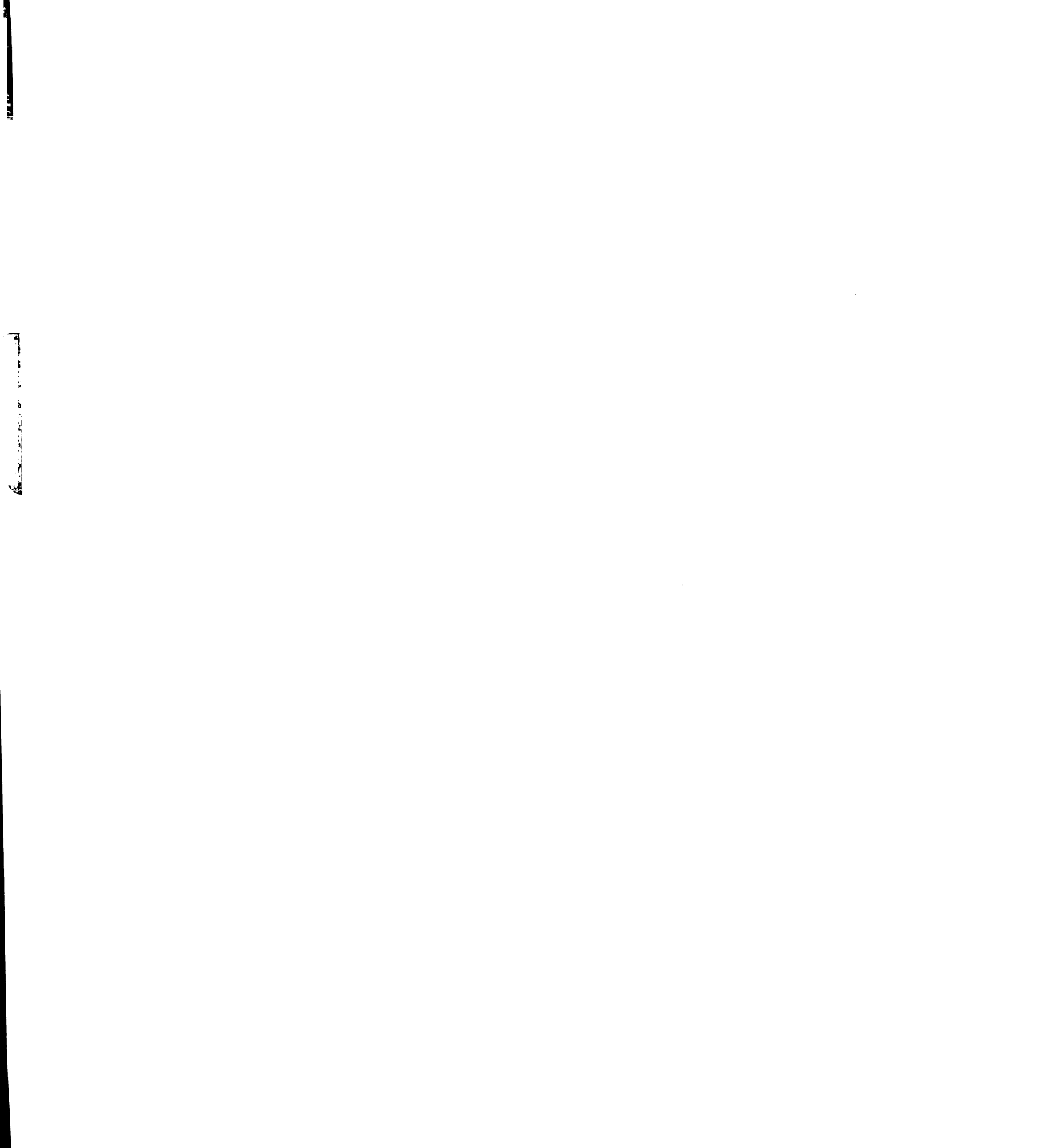
I_{oi} is the original intensity value from the XRD pattern for plane- i , then $\frac{I_{oi}}{j_i}$ should be the value taken to normalize. The relative intensity should also be calculated from the modified intensities. That means I_{ri} is still the same normalized relative intensity of the XRD pattern in plane- i but includes the multiplicity factor j_i in value.

According to Fang et al., the stresses average calculated by the individual contents of different oriented grains using Eq. 3-67 for singlet phonon converge with the result from using Eq. 3-68 for doublet phonon. This means that these two equations work out for calculating residual stress independently and they should come to the same answer ideally. Since the singlet or the doublet spectrum peak(s) are not always shown in Raman spectrum, a better result should be the average of these two if both singlet and doublet peaks are shown in Raman spectrum. Otherwise either Eq. 3-67 or Eq. 3-68 should be enough to determine the stress calculation depending on the peaks shown in the spectrum. Therefore the total residual stress for polycrystalline diamond film by the Raman spectroscopy is

$$\tau = \frac{\tau' + \tau''}{2} \quad \text{Eq. 3-69}$$

3.11.4 The intrinsic stress calculation

For situation of a diamond film deposited on a silicon wafer, the total net stresses at the interface in between the silicon wafer and the diamond film is the sum of the thermal stress between these two materials and the intrinsic stresses exerted from the diamond film. It is also a net stress averaged at the diamond-silicon interface between



two planes, the diamond film and the silicon wafer. This relationship among these stresses can be expressed as the following mathematical form:

$$\textit{Residual or net total stress} = \textit{Intrinsic stress} + \textit{Thermal stress}$$

or

$$\sigma_{tot} = \sigma_{Int} + \sigma_{thermal} \quad \text{Eq. 3-70}$$

Since the net total residual stresses and the thermal stresses are solved previously by using Eq. 3-39 and Eq. 3-35 respectively, the intrinsic stresses can also be easily found and expressed as:

$$\sigma_{Int} = \sigma_{tot} - \sigma_{thermal} \quad \text{Eq. 3-71}$$

Chapter 4 Diamond Film Quality and Growth Rate

The diamond film quality and growth rate can be evaluated in many different ways. They are so tightly related that one should not measure the growth rate without determining or at least estimating the quality. However, it was found that many research papers view the diamond film growth rate without simultaneously and explicitly considering its quality. This may mislead other researcher's attention and focus, and lose its significance for comparing research results. Our concern at the current overall research stage is no longer high growth rate low quality (or high impurity and high defect) dark diamond films. Rather, our intention is to synthesize high growth rate and high quality white polycrystalline diamond film. This requires us to measure both the growth rate and the quality. This chapter presents the relationship of the growth rate versus the diamond quality for films deposited by means of microwave plasma-enhanced chemical vapor deposition. To be more specific, the quality of the diamond films that are used for our data analysis is visually the same (they are white) or they will be specified otherwise.

4.1 Input and reactor parameters

To understand the growth rate and quality relationship the research methodology involves establishing the relationship between the input or reactor parameters and the result of the deposition process. Since the number of input and reactor parameters is

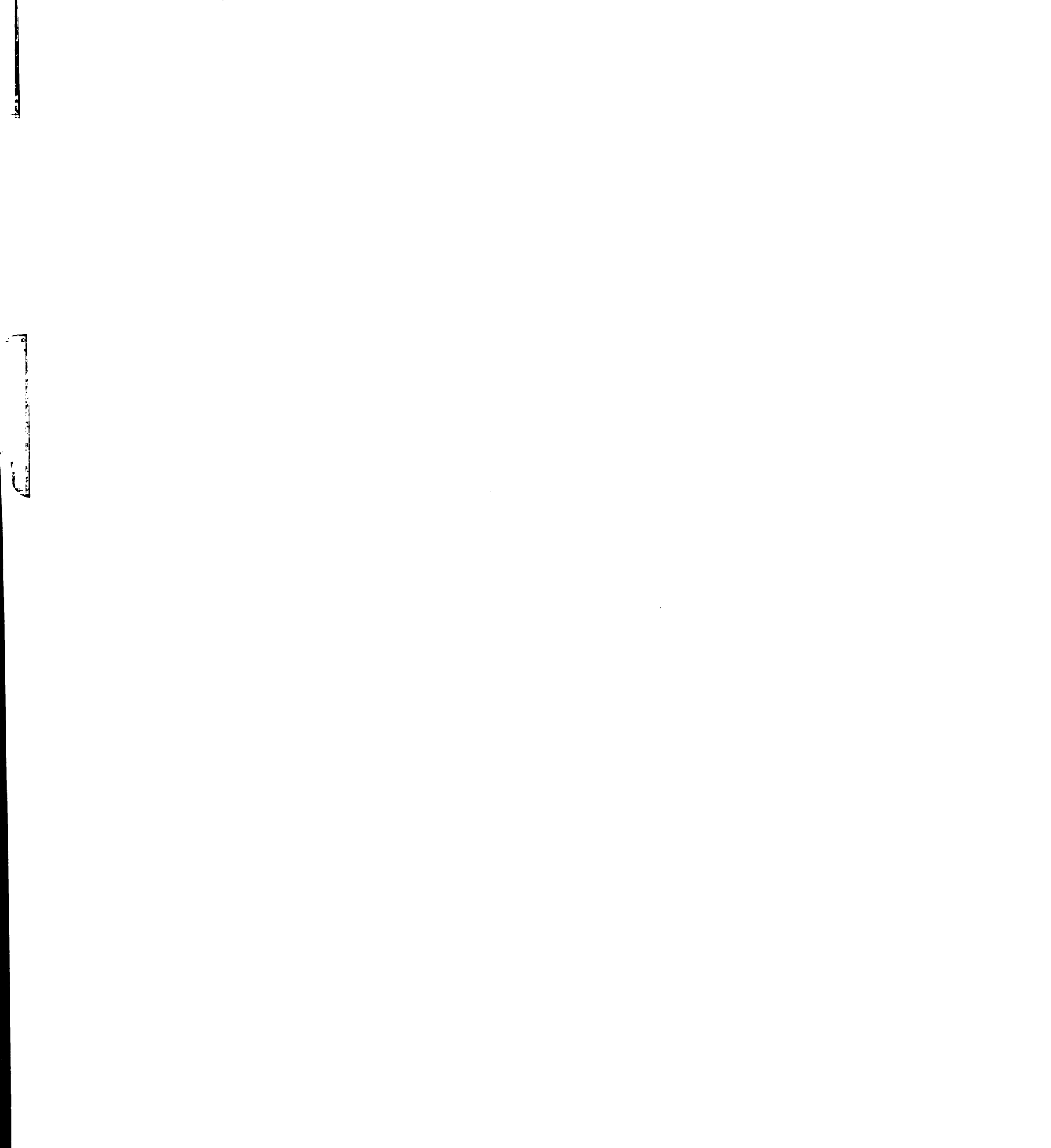
numerous, an important part of the research methodology is the intelligent selection of the key or critical input/reactor parameters. Another part of the methodology is to introduce new reactor improvements and process techniques to meet the objectives.

For the first objective of this study the growth rate and quality of the diamond films are measured versus the input variables such as the reactant gas pressure, the absorbed microwave power, the substrate temperature, the total gas flow, and the methane concentration. All these variables are traditionally considered as the key parameters that can significantly change the growth rate and the quality of the diamond film. **For this objective, three variables are selected as the key input parameters including pressure, methane concentration and substrate temperature.**

The reduction of the many input variables to a limited number (three variables) is based on the understanding of the diamond deposition process as described in Chapter 2 and on previous work at MSU [27, 68, 55]. In this work the pressure, absorbed microwave power and microwave power density is reduced to one variable under the constraint that the plasma size is held constant. To understand this reduction it is useful to examine the relationship of these three variables.

4.1.1 Pressure and absorbed microwave power density

The pair of variables consisting of the gas pressure inside the reactor and the absorbed microwave power density of the plasma in general maintains a linear relationship [149] if the absorbed microwave power is held constant and the plasma discharge is boundless. Here “boundless” means the plasma discharge doesn’t reach the physical boundary of the plasma container and it can expand and shrink freely without having to “touch” the plasma chamber wall. For an example, if the reactor pressure is



doubled, the absorbed microwave power density is also scaled up by a constant numerical factor plus or minus another constant. They may be expressed as an equation such as $y = ax + b$, where x and y are the pressure and the power density, and a , b are the constants. This relationship holds assuming that the plasma has the same feed gas composition. There should be a similar relationship at different absorbed microwave power, but the relationship may have different constants.

It is observed that the plasma ball size naturally decreases when the reactor pressure increases when the input microwave power remains the same. By definition the power density also naturally increases due to the volume of the plasma shrinking and vice versa when the reactor pressure decreases. In the past, studies have been done for microwave plasma CVD diamond deposition looking at the diamond growth related parameters versus either the pressure changes [25, 26, 29, etc] or the absorbed plasma power density changes [34, 150]. However, the pressure and the absorbed microwave power density can be treated as interrelated and equivalent variables for this study. The plasma properties may remain the same as long as the pressure or the power density remains the same for the same reactor and the same feed gas composition. Furthermore, the suggestion to increase the diamond film growth rate by increasing the absorbed microwave power density mentioned in a few past MPCVD diamond film deposition papers [34] is equivalent to the idea of increasing the reactor pressure in this study. There is no need to deal with the absorbed power density separately as an independent variable for the diamond growth except for the purpose of the qualitative or conceptual description of plasma properties.

4.1.2 Plasma size and absorbed microwave power

The second pair of the interrelated variables is the plasma discharge size and absorbed microwave power. The linear relationship between these two quantities is also easy to see when the reactor pressure remains constant. Specifically, increasing the microwave power makes the plasma discharge bigger and decreasing the power makes the plasma discharge get smaller. Under the same pressure, the additional energy absorbed by the plasma goes into the surrounding neutral gases molecules outside the visible plasma and excites them into plasma. The absorbed power density remains approximately the same.

In this study, the plasma size needs to be maintained large enough to fully cover the substrate and be consistent for all experiments. For an example, when hydrogen and methane plasma pressure changes from 100 Torr to 140 Torr, the plasma size may become too small to cover a 2-inch diameter silicon wafer when the absorbed microwave power is smaller than 2.0 kW. When this happens, the diamond film may not fully cover the silicon wafer. This uncovered area can even easily be seen by the naked eye. The absorbed power needs to be increased to above 2.5 kW in order to deposit a fully coated 2-inch diameter silicon wafer. In this situation the plasma size can be maintained as a constant over the 2-inch diameter silicon wafer while the absorbed microwave power varies. If the volume of the plasma is held constant, the pressure change becomes a sole variable among the starting variables of pressure, absorbed power density and absorbed power.

4.2 Output variables

The output variables for objective 1 include the growth rate and diamond quality. One measure of the diamond quality for this study is the film quality for optical transmission. It is measured by the percentage of light transmitted through the diamond film for a range of different wavelengths in the UV/visible/IR regions of the spectrum. The optical transmission of the diamond grown is compared to the ideal transmission versus wavelength for high purity (ideal) diamond. High quality single crystal diamond transmits 70% of the incident light due to the change in the index of refraction between the air and the diamond. This light transmission occurs in the wavelengths that extend into the UV until the photon energy exceeds the band gap energy of the diamond. Because of (1) scattering on the diamond surface or within the films, (2) roughness of the surface and (3) wavelength dependent light absorption in the diamond film, polycrystalline diamond films are expected to have similar transmission behavior as ideal diamond but with a slightly lower percentage of transmission. A measure of the diamond quality is the optical absorption coefficient.

SEM, Raman spectroscopy and X-ray diffraction can be used to assess the diamond film quality.

4.3 General operational field map and performance region

The “field map” shown in Figure 4-1 is used to illustrate the operating conditions of the CVD reactor. The field map gives the substrate temperature as a function of the absorbed microwave power and pressure. The temperature is highly dependent on the cooling stage design and the substrate holder configuration. The field map of a stable substrate holder set usually can be confined in a parallelogram box. The temperature

linearly increases as the absorbed power increases for a fixed reactor pressure. The data lines for different pressures are typically parallel or near parallel. Otherwise, the substrate holders may have contact problem and may need to be resurfaced to improve the thermal conductivity in between the holders (or inserts) and with the substrate. The top and bottom line of the parallelogram usually shows the temperature increases per unit absorbed microwave power. The left side dashed line of the parallelogram indicates the minimum microwave power that forms a plasma discharge large enough to cover the substrate. The right side dash line of the parallelogram indicates the maximum microwave power permitted so that the edge of plasma discharge does not get too close to the fused silica bell jar wall. The field map is how the CVD reactor runs. All points on the field map are not necessarily conditions to produce good diamond.

Note that the left dash line may actually be shifted to the right slightly when pressures become higher than 100 Torr. Though the line is not shown in Figure 4-1, the reader can form this line by connecting the left end of the three shorter lines at pressures of 120 Torr, 140 Torr, and 160 Torr. This shows that higher absorbed power is required in order to have the plasma fully cover the substrate surface due to the decrease of the plasma size when the pressure is increased as described previously. The vertical error bars represent the variation of minimum/maximum temperature for the same pressure across the substrate. As Figure 4-1 indicates, the average minimum/maximum temperature variation at 140 Torr is about $-70/+70$ °C, which is 140 °C difference between the lowest and the highest temperature on the substrate, and the variation of minimum/maximum temperature gets larger on this 3-inch diameter silicon substrate when the pressure gets higher. For such a large temperature variation the quality and the

uniform growth of the diamond film on this substrate becomes problematic. One solution is that a smaller substrate is needed at higher pressure in order to obtain a certain quality and uniformity of the diamond film.

The 2-inch diameter silicon substrate “field map” is similar but the reactor pressure can be pushed higher due to the smaller plasma coverage required. This allows the reactor pressure to be increased higher than for the 3-inch diameter silicon substrate. The temperature variation across the substrate is also more uniform than for the 3-inch diameter silicon substrate. Figure 4-2 shows the field map of a 2-inch diameter silicon wafer as the substrate for its normal operating region and the temperature range of the minimum/maximum variation at its respective operating pressure. Typically the highest temperature is obtained at the center of the substrate. From Figure 4-2, the average temperature variations for 140 Torr are about 80 °C (instead of 140 °C) across the 2-inch diameter silicon substrate. Please note the substrate holder(s) set used for the 2-inch substrate is not necessary the same as the one used for the 3-inch substrate. However, the holder(s) set configurations are the optimal choice for each size of the substrates.

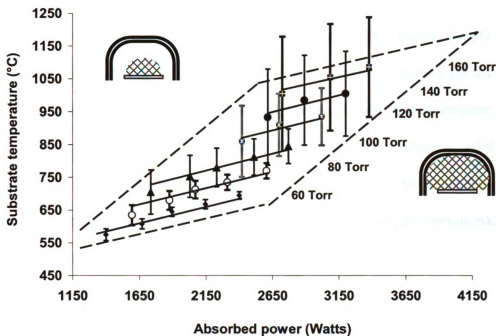


Figure 4-1: Operation condition field map of the microwave plasma CVD system for a 3-inch diameter silicon wafer as the substrate. The feed gas composition used for this measurement is 400 sccm H_2 and 4 sccm CH_4 .

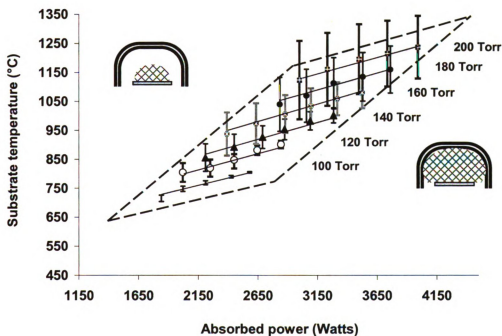


Figure 4-2: Operation condition field map of the microwave plasma CVD system for a 2-inch diameter silicon wafer as the substrate. The gases composition used for this measurement is 400 sccm hydrogen and 4 sccm methane.

Argon gas affects the microwave plasma and the diamond deposition conditions. Argon gas was added to the plasma discharge for the purpose of increasing the plasma size and radial substrate temperature uniformity. Since argon is an additive gas used in this research, a field map is plotted to indicate the shifts of the deposition temperature conditions due to the argon gas. Using a 3-inch silicon wafer as the substrate and the same holder set configuration as Figure 4-1 as an example, the field map with the argon addition is shown in Figure 4-3. With the same substrate holder set, the operational region is shifted towards the upper left. This means that less microwave power is required to maintain the same substrate temperature or the substrate temperature increases at the same given microwave power and pressure. The temperature variations across the substrate are smaller than those without using the argon gas as the additive gas. More uniform temperature is obtained across the silicon wafer. From Figure 4-3, the temperature variations with argon are only about ± 50 °C (or 100 °C difference between minimum and maximum temperature), which is a 40 °C less than (compare to 140 °C) on this 3-inch diameter silicon substrate with no argon at a pressure of 140 Torr with the same substrate holder set. Another feature that is not shown but worth mentioning, is the temperature across the substrate is more uniform when the absorbed microwave power increases at the same pressure. This can be seen from the field maps that the minimum/maximum temperature error bars become smaller as the absorbed power increases for substrate (center) temperatures at the same pressure. This can be explained by higher power producing a bigger plasma, and this is one of the approaches to get more uniform temperature across the substrate. There will be more discussion about this field map in Chapter 5 where diamond film uniformity is investigated.

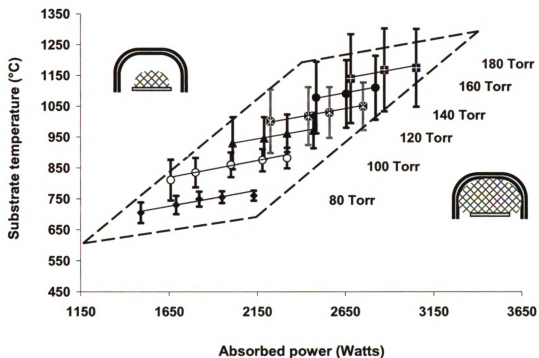


Figure 4-3: Operation condition field map of the microwave plasma CVD system for a 3-inch diameter silicon wafer as the substrate. The gases composition used for this measurement is 400 sccm hydrogen, 200 sccm argon, and 4 sccm methane.

4.4 Diamond film quality, the Raman spectroscopy analysis

In the following figures, photographs of a few as-grown diamond samples are presented along with their Raman spectra. For comparison, the Raman spectrum of a HPHT synthetic single crystal diamond was also presented. The growth conditions of these samples and the FWHM value of each sample from the Raman spectrum indicates the quality of the sample in Table 4-1. The qualities of these as grown diamond films range from near HPHT single crystal quality (by FWHM value) to close to acceptable (by visual inspection). The acceptable optical quality usually shows the visible transparency after the silicon wafer is back-etched and before it is polished. One should be able to see words through, not necessary clearly enough to read them, lying underneath the freestanding diamond film such as the sample SZ-2inch-1mm-053 shown in Figure 4-10. Some of the diamond films may show that the quality at the edge differs from the center with different FWHM value and different level of discoloration. This is an example of non-uniform quality diamond film deposition. All photographs here are taken with freestanding diamond film, that means after the silicon wafers are dissolved away (back etched) in order to show the whiteness or the darkness of the diamond film.

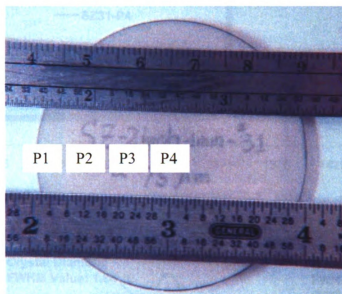


Figure 4-4: Sample SZ-2inch-1mm-31 with thickness of 75 micron is laid on a piece of white paper. Silicon is back etched without any polishing. Label is written on a piece of paper underneath of the diamond film. High degree of transparency clearly can be seen from this sample. From this photograph and the Raman spectra of this sample on next page, high quality polycrystalline diamond film is uniformly deposited. The average growth rate by weight gain was $0.79 \mu\text{m/h}$. The substrate temperature was $1083 \text{ }^\circ\text{C}$ at the beginning, then gradually decreased to $955 \text{ }^\circ\text{C}$ at the end.

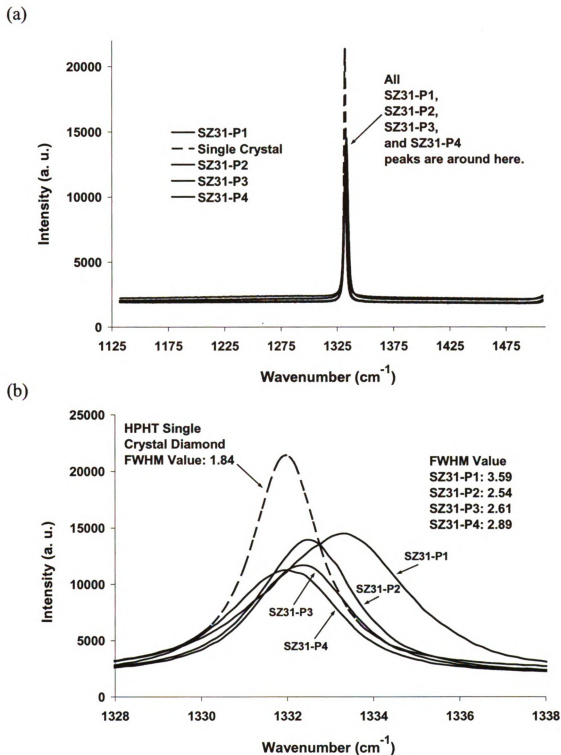


Figure 4-5: The Raman spectra for a HPHT single crystal diamond and sample SZ-2inch-Imm-031. The spectra were recorded at four different spots where P1 is about 1 mm to the film edge and P4 is near the center of this 2-inch diameter film. Points P2 and P3 divide the line P1-P4 into three equal distance. (a) Whole view of scanned region. (b) Zoom-in view at the peak wavenumber.

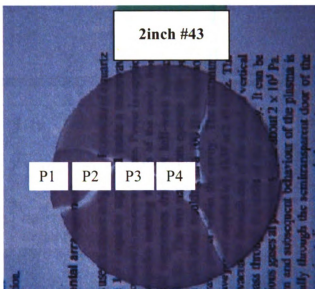


Figure 4-6: Sample SZ-2inch-1mm-43 with thickness of 19 micron is laid on a piece of print paper. The transparency of the film is shown from the print underneath. The average growth rate by weight gain was $0.53 \mu\text{m/h}$. The substrate temperature was 992°C at the beginning, then gradually decreased to 954°C at the end.

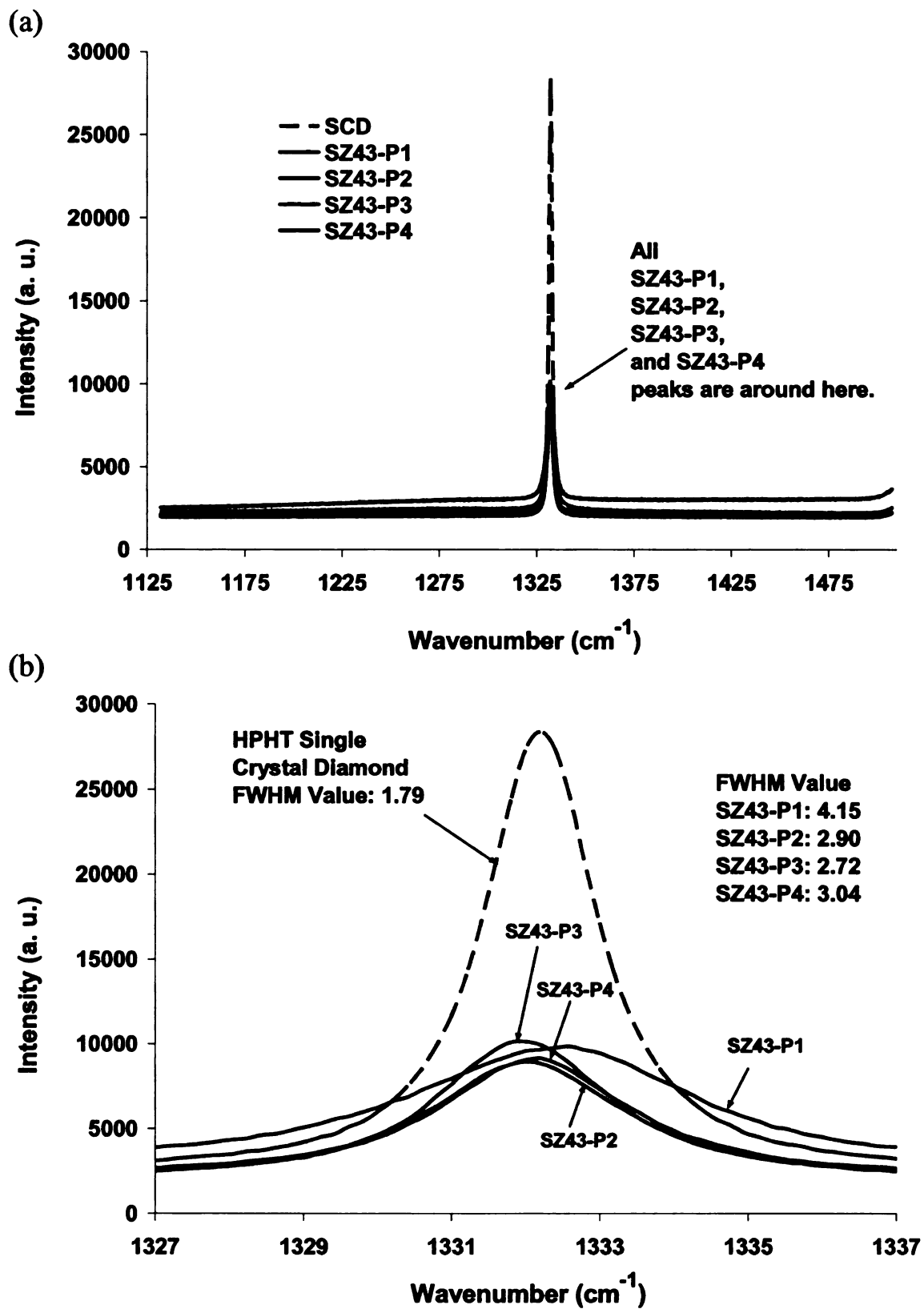


Figure 4-7: The Raman spectra of sample SZ-2inch-1mm-043 at points P1 through P4 in comparing with a HPHT Single Crystal Diamond (SCD). (a) Whole view. (b) Zoom-in view.

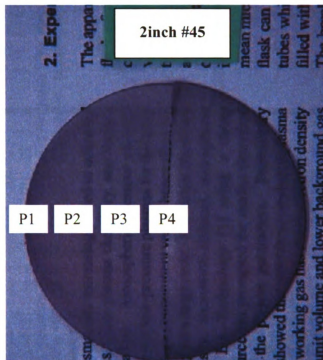


Figure 4-8: Sample SZ-2inch-1mm-45 with thickness of 75 micron is laid on a piece of print paper. The transparency of the film is shown from the print underneath. The average growth rate by weight gain was $1.57 \mu\text{m/h}$. The substrate temperature was 971°C at the beginning, then gradually decreased to 952°C at the end.

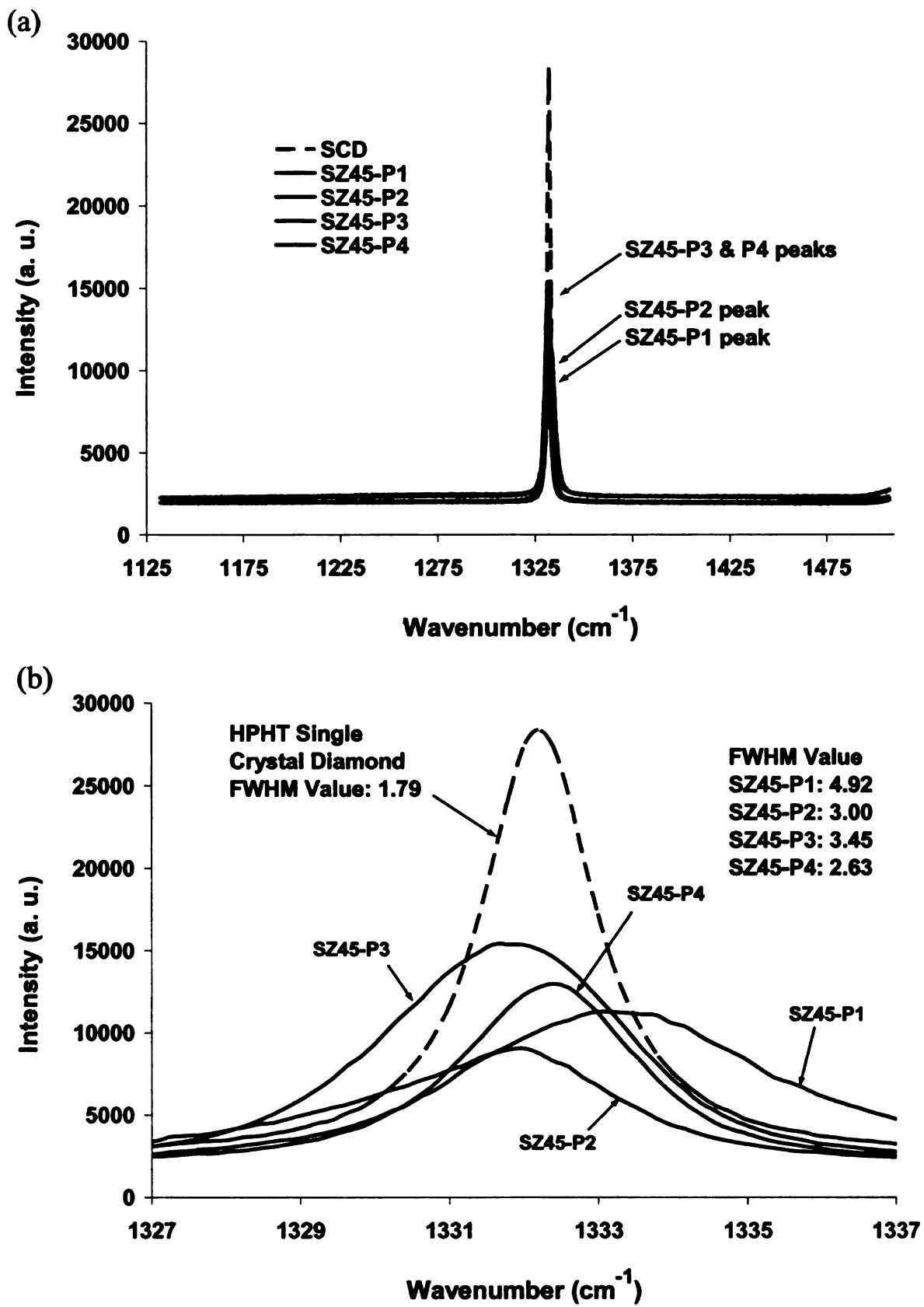
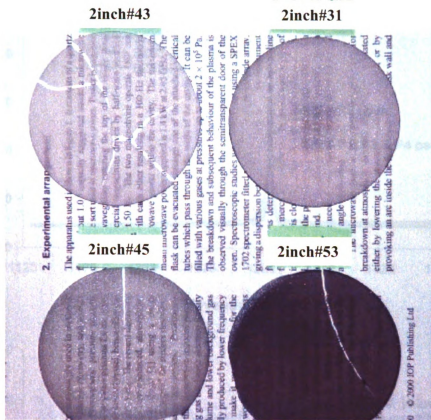


Figure 4-9: The Raman spectra of sample SZ-2inch-1mm-045 at points P1 through P4 in comparing with a HPHT Single Crystal Diamond. (a) Whole view. (b) Zoom-in view.



0% Gray (White)	25% Gray	40% Gray	50% Gray	80% Gray

Figure 4-10: Sample SZ-2inch-1mm-53 (lower-right photo) with thickness of 125 micron is laid on a piece of print paper together with other previous mentioned samples (SZ31, SZ43 and SZ45). The average growth rate by weight gain was $2.60 \mu\text{m/h}$. The substrate temperature was 977°C at the beginning, and then was gradually increased to 1017°C at the end. Their whiteness (or darkness) are significantly different and compared under the same lighting condition. The percentage gray scale below the photographs is a visual reference for the comparison of diamond film whiteness. However since the white paper in the photo looks like it contains 25% gray, we should shift the scale down by 25% when estimating the diamond film quality in the photo.

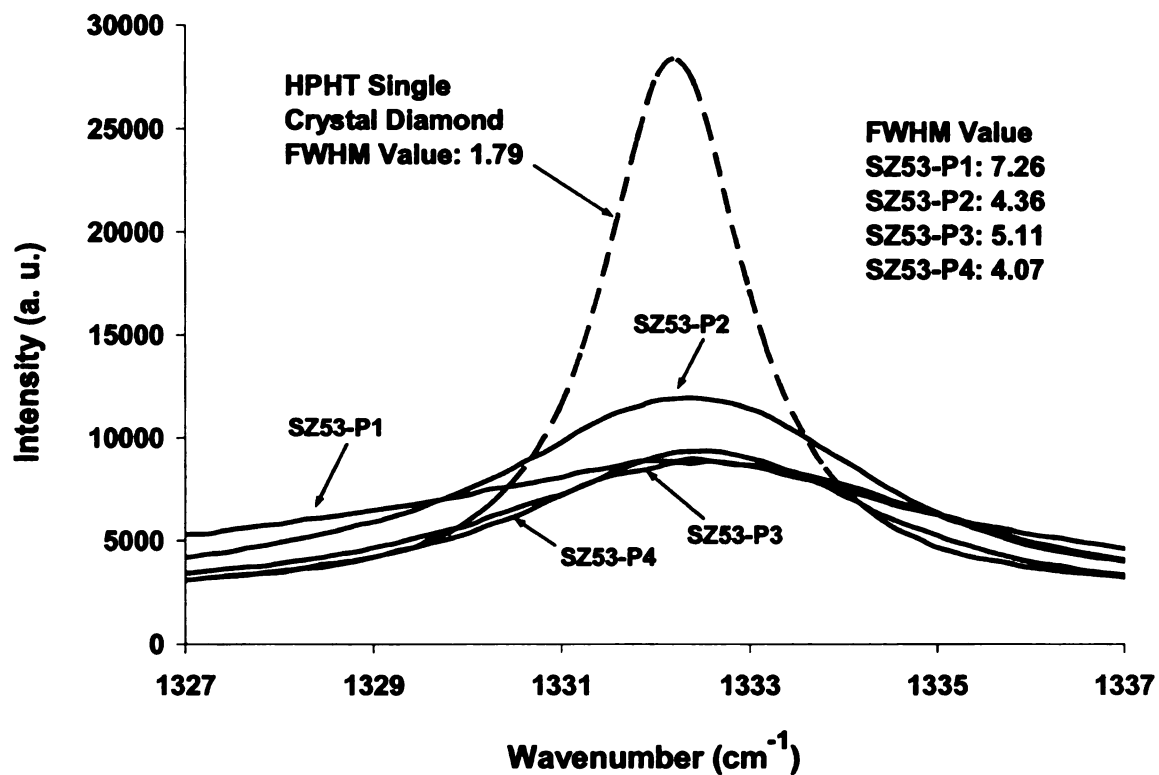
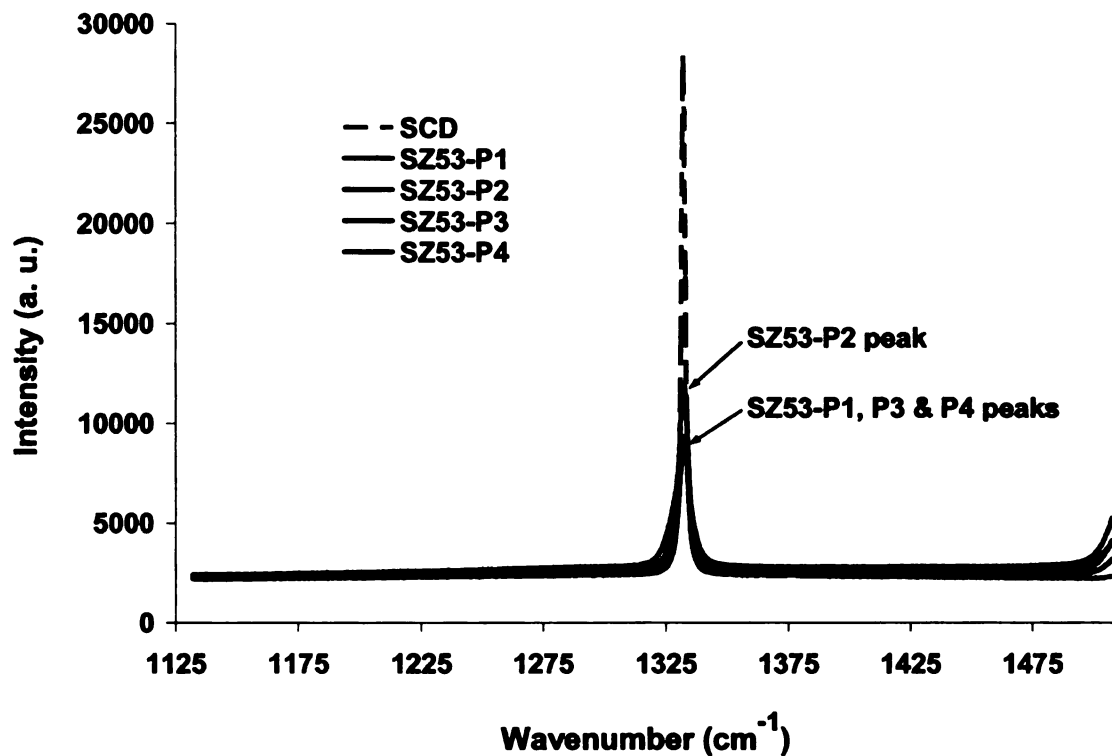


Figure 4-11: The Raman spectra of sample SZ-2inch-1mm-053 at points P1 through P4 in comparing with a HPHT single crystal diamond. (a) Whole view. (b) Zoom-in view.

Sample	Process duration (hrs)	Ave. thickness (μm)	CH ₄ /H ₂ (%)	Ar/H ₂ (%)	Pressure (Torr)	Power absorbed (kW)	T _S (°C)	Darkness (% Gray)	Peak Position (cm ⁻¹)	FWHM (cm ⁻¹)
HPHT SCD	NA	NA	NA	NA	NA	NA	NA	0	1332.20	1.87
2"-25-P1	25	19	1.25	0	140	3.6	NA	0	1333.19	4.02
P2							NA	0	1333.14	2.97
P3							NA	0	1332.83	3.91
P4							1080	0	1332.70	3.52
2"-31-P1	96	75	1.00	0	140	3.0	NA	0	1333.15	3.59
P2							NA	0	1332.45	2.54
P3							NA	0	1332.32	2.61
P4							995	0	1331.93	2.89
2"-43-P1	36	19	1.00	0	140	3.2	914	0	1332.33	4.15
P2							949	0	1332.02	2.90
P3							970	0	1331.97	2.72
P4							988	0	1332.12	3.04
2"-45-P1	48	75	1.50	0	140	3.1	940	10	1332.58	4.92
P2							957	5	1331.90	3.00
P3							965	5	1331.76	3.45
P4							967	5	1332.33	2.63
2"-53-P1	48	125	1.00	25	140	3.1	995	30-40	1331.84	7.26
P2							1008	30	1332.24	4.36
P3							997	30	1332.64	5.11
P4							989	30	1332.47	4.07

Table 4-1: Examples of diamond quality evaluated by Raman FWHM versus their growth conditions. The quality of these as grown diamond films range from near HPHT single crystal (by FWHM value) to close to acceptable (by visual estimation). T_S is the temperature of the substrate at each point averaged from the beginning to the end of the experiment.

As mentioned in section 3.10.2, the sp^2 carbon content, if there is sufficient quantity present in the film, can be observed from the Raman spectrum. An example of Raman spectrum showing a visible sp^2 graphite peak can be seen in Figure 4-12. To include the graphite peak, the scanning range of this Raman spectrum is from 1100 cm^{-1} to 1700 cm^{-1} . The valley on the plot around 1470 cm^{-1} is caused by combining multiple scans carried out by the software and the baseline drawn for the baseline correction is also shown in the figure. A relatively low quality sample with higher sp^2 carbon impurity is used for the purpose of showing the graphite peak. The FWHM value of this sample calculated from 1332 cm^{-1} , the diamond peak at the same measured point is about 11.0 cm^{-1} .

The Raman spectra for the range from 1100 cm^{-1} to 1700 cm^{-1} for the four samples SZ-2"-31, SZ-2"-43, SZ-2"-45, and SZ-2"-53, and all for a the point by the edge of the sample – P1, are shown in Figure 4-13. The spectra are shown from the top, the smallest FWHM value to largest FWHM value at the bottom and shifted apart from each other for the purpose of easy to compare those spectra. Therefore the vertical axis value shown in Figure 4-13 includes a different amount of intensities shifted for different spectrum. From the spectra provided in Figure 4-13, the graphite peaks can hardly be seen for all samples. This indicates very low sp^2 carbon impurities are deposited in the diamond film.

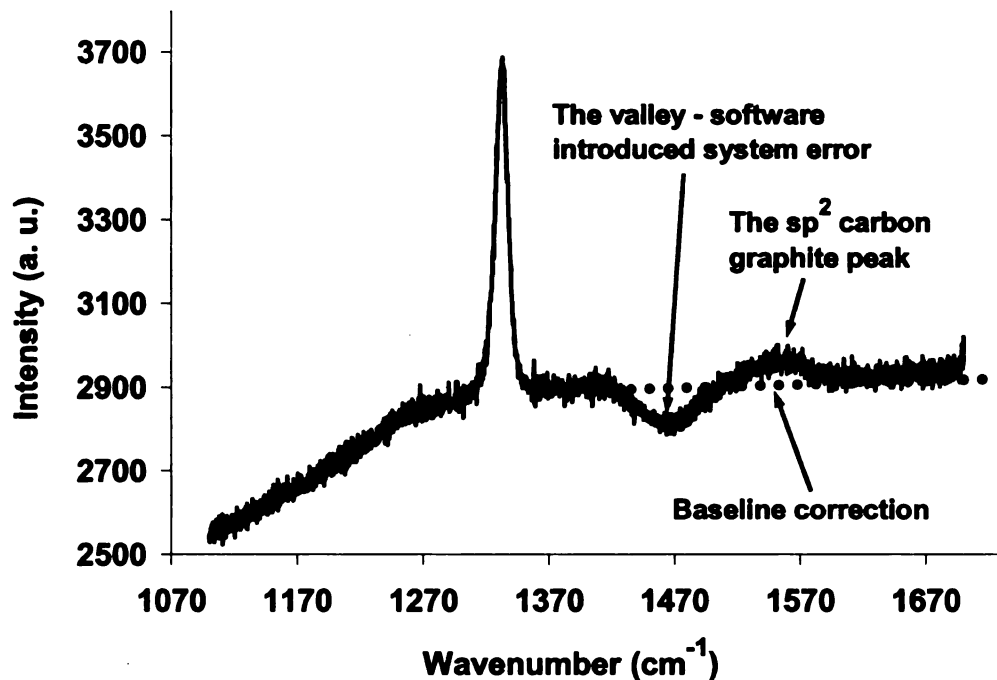


Figure 4-12: Raman spectrum for a low quality diamond sample. The sp^2 carbon peak at 1550 cm^{-1} is apparent. The FWHM value of the diamond film at the same measured point is about 11.0 cm^{-1} , much broader than single crystal.

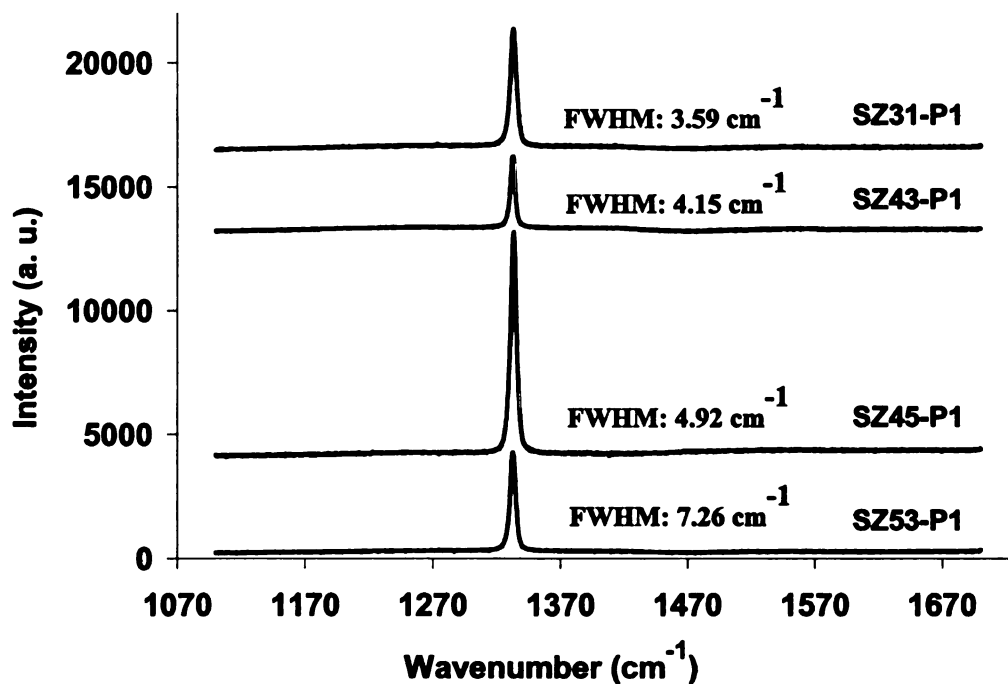


Figure 4-13: Raman spectra for the same four samples in Table 4-1. The graphite peaks centering around 1560 cm^{-1} are hardly seen for all samples.

4.5 Diamond film quality, the optical transmission analysis⁷

As we have explained in section 3.10.3, the diamond films required a series of post-processing steps before an optical transmission measurement can be made. Sample SZ-25-3P is first laser cut from sample SZ-2"-25 (Table 4-1) with a 35mm diameter circle then lapped for 16.3 hours. After that the sample is polished for 3.5 hours then a 9mm diameter circle is laser cut from that 35mm diameter circle. Finally the sample is back etched to remove the silicon from the 9mm diameter piece to form sample SZ-25-3P and it is visually transparent as shown in Figure 4-14. The optical transmission result for sample SZ-25-3P is plotted in Figure 4-15. Please note its thickness is measured to be 13.8 μm by the weight after the polishing and etching. The polished surface had an average roughness of $R_a = 6.2 \text{ nm}$.

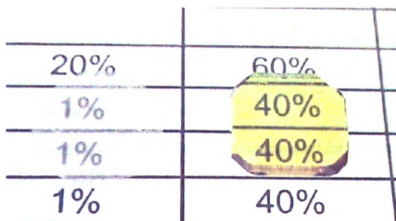


Figure 4-14: Sample SZ-25-3P (left) and a Sumitomo HPHT synthetic single seed crystal diamond (right, yellow) supported on a glass microscope slide above a printed white page. The vertical separation between the glass slide that holds the samples and the underlying page is 15 mm.

⁷ Dr. D. Reinhard is thanked for providing the backetching silicon wafer, lapping and polishing the diamond samples including the technical details and the optical transmission measurement results and analysis of sample SZ-25-3P used here as setting the standard guidelines of the overall diamond films post processing in the lab. Mr. Michael Becker is thanked for providing laser cutting of samples.

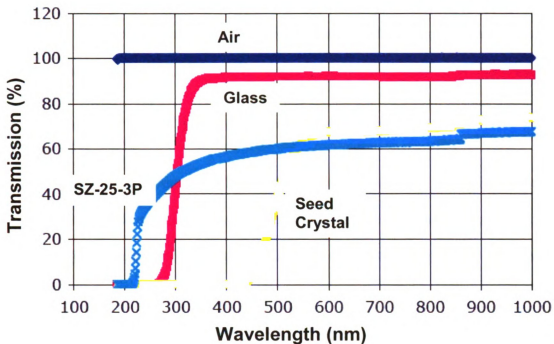


Figure 4-15: Optical transmission spectra for different materials measured with Perkin Elmer Lambda 900.

Figure 4-15 also shows scans of the air, glass, and a Sumitomo single crystal diamond. The results of the optical transmission spectra measurements are listed below:

Air: 100% transmission, as expected.

Glass microscope slide: 92% transmission, as expected for a refractive index of approximately 1.5. Transmission continues until the onset of ultraviolet absorption.

Sumitomo single crystal diamond: 67.7% transmission in the red portion of the spectra. There is a cut-off between 400 and 500 nm as expected from reports for yellow, high pressure, high temperature nitrogen doped diamond.

Sample SZ-25-3P: 62.2% transmission in the red portion of the spectra. The onset of strong absorption near 225 nm is consistent with band gap absorption in undoped diamond.

4.6 Growth rate and quality versus reactor pressure, methane concentration and substrate temperature

The selection of experiments that need to be done to complete objective 1 requires careful thought and planning. First the range of input variables to be studied is defined. For example, two variables could be selected and the values of each of these variables could consist of five levels. If all possible experiments are done for the possible values of the two variables, the number of experiments is already 25. With three or four variables this approach quickly becomes unmanageable given that each experiment may take days. To reduce the number of experiments, the values of the input variables are limited by first determining regions where the output variables meet a predetermined range of values. So the approach is to establish a range of possible input/reactor variables to study and establish a range of acceptable output variables, then to do experiments such that the output data obtained is used as a feedback to limit the number of input variables and hence experiments performed.

The proposed progression of experiments is detailed below. In order to understand how reactor pressure influences the growth rate, a series of pressures are selected as a sole variable while other conditions remaining as constants. The range of defined high pressures start at 100 Torr, then the pressure is raised 20 Torr each experiment till the upper limit pressure is reached for the current and improved reactor. The highest reactor pressure is set to 180 Torr. The conditions that remain as the constants are the feed gas

composition, the substrate temperature and the plasma size. The feed gas concentration is represented by the flow rate in terms of standard cubic centimeter per minute (sccm) of the reactant gases. Typically the hydrogen gas flows at 400 sccm and the methane gas flows at 4 sccm for the referenced lowest methane concentration point. The substrate temperature is controlled by the design of the substrate holder to be 900°C for the referenced lowest temperature point and not more than 1100°C for the highest temperature. When a single temperature is reported it usually refers to the temperature at the center of the substrate except when the temperature uniformity of the substrate is involved in the discussion. The temperature is measured by an Iacon one-color handheld pyrometer and the emissivity is set to 0.6 in order to approximate the substrate emissivity and the optical emission transmission and reflection losses of the substrate and the dome. The absorbed power is usually 2.6 kW for the lower microwave power limit such that the plasma covers the 2-inch diameter substrate. The highest absorbed microwave power used was over 3.6 kW for sample SZ-2"-42 when reactor pressure was as high as 180 Torr for this system. Though the plasma size appeared to be small on this substrate, the upper power limit is usually set by the plasma discharge approaching the dome size.

The methane concentration is the second independent parameter that varies the diamond growth rate significantly. Because it is independent of the changes of reactor pressure, the plasma size and the absorbed microwave power, it may be observed and measured together with other variables. Typical numerical values of the methane flow rate may be 4 sccm, 6 sccm, 8 sccm, 10 sccm, 12 sccm, and 14 sccm or higher depend on the targeted diamond film quality. Table 4-2 includes all conditions of pressure variations and methane concentrations of these experiments. At set of 25 experiments is too

exhaustive to be performed due to both expense and time. The set of experiments is reduced by removing regions of the experimental plan, which produces diamond of low quality or diamond at low deposition rates. Specifically, this project is looking for growth rates of greater than one micron per hour and diamond quality that is sufficient for window material. Table 4-2 is used only as a visual guideline for the experiments. Table 4-3 gives a set of diamond film samples that are actually grown and cover a range of typical experimental conditions include near good quality and acceptable growth rate.

At the end of each experiment, the growth rate of the diamond film is determined. The growth rate mostly refers to the linear growth rate of the thickness in micron per hour. However, the growth rate of the mass gain was also measured and recorded. The optical quality for transmission of the diamond film was measured as detailed earlier.

Table 4-2: Growth rate and quality versus reactor pressure and methane concentration.

		Pressure (Torr)				
		100	120	140	160	180
CH₄ Flow Rate (sccm)	2	<ol style="list-style-type: none"> 1. 25 possible experiments are needed; 2. Hydrogen is always set at 400 sccm; 3. For 2 inch diameter substrate, plasma discharge size is maintained to fully cover the substrate at all pressure; 4. Constant substrate temperature is maintained dependent on the substrate holder design. 				
	4					
	6					
	8					
	10					

Table 4-3: A set of samples that cover a range of typical experimental conditions without Ar addition. Substrate temperature is ending temperature if range is not given. The growth rates in parentheses are an average over multiple experiments at the same condition or an adjustment as indicated in the footnotes.

Sample	Pressure (Torr)	Absorbed power (kW)	Gases		Process duration (hrs)	T_S center (°C)	Ave. thickness (μm)	Growth rate (Ave.) (μm/hr)	FWHM range (cm ⁻¹)
			H ₂ (sccm)	CH ₄ (sccm)					
2"-55	100	2.6	400	4	24	883-867 ⁸	14	0.59(0.59)	3.21-4.99
3"-06	100	2.8	400	6	48	940 ⁹	52	1.08(0.92)	3.47-10.5
2"-12	120	3.0	400	4	72	900	40	0.55(0.55)	3.42-
3"-08	120	3.0	400	6	48	940	55	1.15(1.13)	4.67-9.83
3"-13	120	3.3	400	8	48	921	91	1.89(1.77)	6.90-7.79
2"-37	140	3.1	400	4	48	1028-955	29	0.60(0.60)	2.81-3.77
2"-45	140	3.1	400	6	48	1027-947	75	1.57(1.65)	2.63-8.70
2"-62	140	3.1	400	8	24	1065-1028	70	2.93(2.93)	5.77-8.97
2"-03	160	2.8	400	4	83	840	50.4	0.61(0.61)	2.66-3.08
2"-27	160	3.5	400	6	155	1205-1108	266	1.72(2.02)	3.51-
2"-65A	160	3.2	400	8	24	956-1021	78	3.27(3.27)	4.21-12.8
2"-58B	180	3.1	400	4	24	1140-1132	25.6	1.07 ¹⁰ (0.77)	2.53-6.41
2"-39	180	3.5	400	6	48	1028-986	39	0.81 ¹¹	2.62-4.79
2"-42	180	3.6	400	8	48	1093-1026	122	2.54 ¹² (3.33)	2.30-12.1

⁸ Value given is from a few hours after experiment was started to 1 hour before it was terminated.

⁹ Temperature is the final substrate temperature, usually one hour before experiment is terminated.

¹⁰ 2"-58B is grown on 2"-58A to avoid substrate overheat resulting in higher growth rate than when include the nucleation growth period; 2"-58B is also not uniform. The adjustment took a thickness value in the middle between the center and edge of the substrate based on the thickness distribution plot.

¹¹ Large scale non-uniform diamond deposition occurred and the growth rate is not used for plots.

¹² Thickness is adjusted for non-uniform sample by its thickness distribution plot.

The substrate temperature increases as the reactor gas pressure increases while the current substrate cooling stage doesn't give enough flexibility for precise temperature adjustment. The control of the substrate temperature is a tricky task due to the restriction of the devices working inside the microwave field region and the simplicity of the cooling stage design. However, the ideal temperature range should be set in between 900°C to 1100°C.

4.6.1 Growth rate and quality versus reactor pressure

This section discusses how growth rate changes with respect to reactor pressure inside the processing chamber. It was found that the higher the reactor pressure, the less the fraction of sp^2 carbon impurity in the film. Besides the visual inspection of the diamond film, it is also measured with Raman spectroscopy using its FWHM value. Considering the variations of the FWHM value from the film center to the edge, the film quality is considered to be excellent if the average FWHM value is around 5.0 cm^{-1} or less from film center to the edge. The sp^2 peaks in Raman spectra of these films are not noticeable as similarly seen for Raman examples given in Figure 4-13. It is also understood that substrate temperature is a non-negligible parameter and it is an issue controlling it, i.e. the substrate temperature is intended to be kept near 1000 °C as measured by the one-color pyrometer.

Figure 4-16 shows a set of experimental data that indicates the growth rate increases at higher reactor processing pressures while maintaining the same quality of the diamond film (measured by Raman FWHM value). One may immediately notice that the trend of the plot for 8 sccm doesn't quite share the same trend with the plot for 4 sccm

and 6 sccm and increase minimal versus pressure at pressures of 160 Torr and 180 Torr. The measured growth rate is lower than one would expect for sample SZ-2inch-1mm-#65A at 160 Torr reactor pressure and 8 sccm CH₄ concentration and for sample SZ-2inch-1mm-#42 at 180 Torr reactor pressure and 8 sccm CH₄ concentration. As it is showing in Figure 4-17, the uniformity of these diamond films was poor at higher reactor pressures for large area substrates. The lost growth rate came from shrinking plasma size.

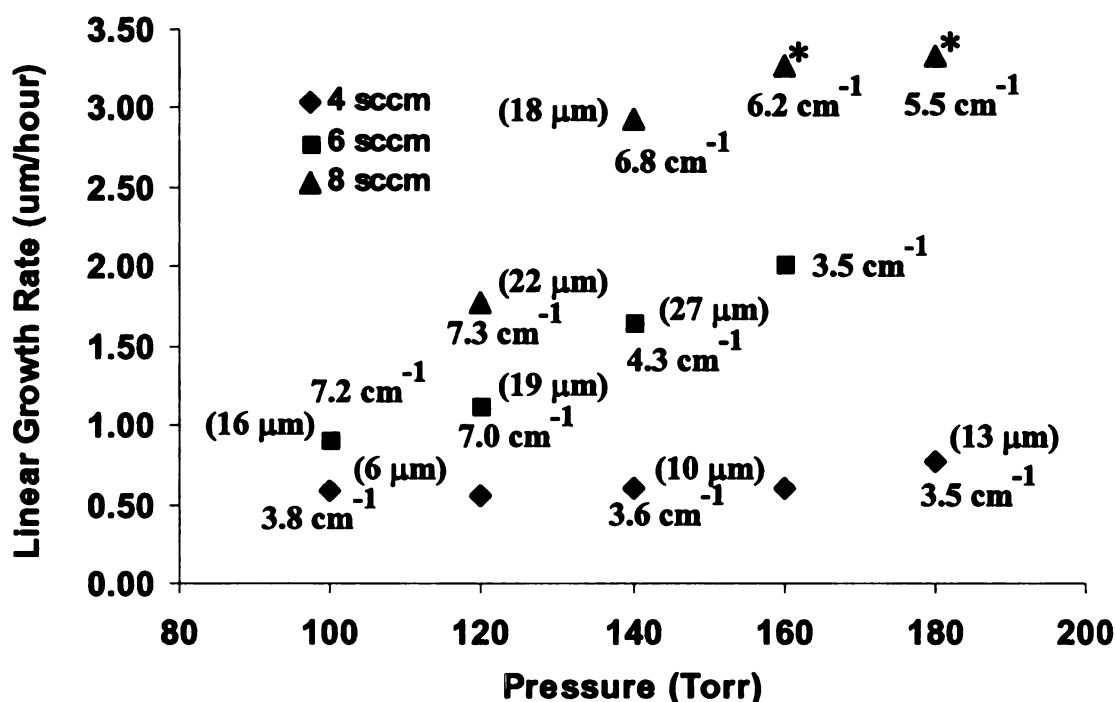


Figure 4-16: A plot of the growth rate versus reactor pressure for all samples included in Table 4-3. Growth rates are taken from the value in the parentheses, which are averaged from samples grown under the same condition, if there are more than one samples were grown. The numbers that are attached to the points are the average FWHM for Raman diamond peak of the sample and the other numbers in parentheses are the average grain size of that sample (same for the following figures). Please note the sample thickness uniformity is very low for the data marked with asterisk.

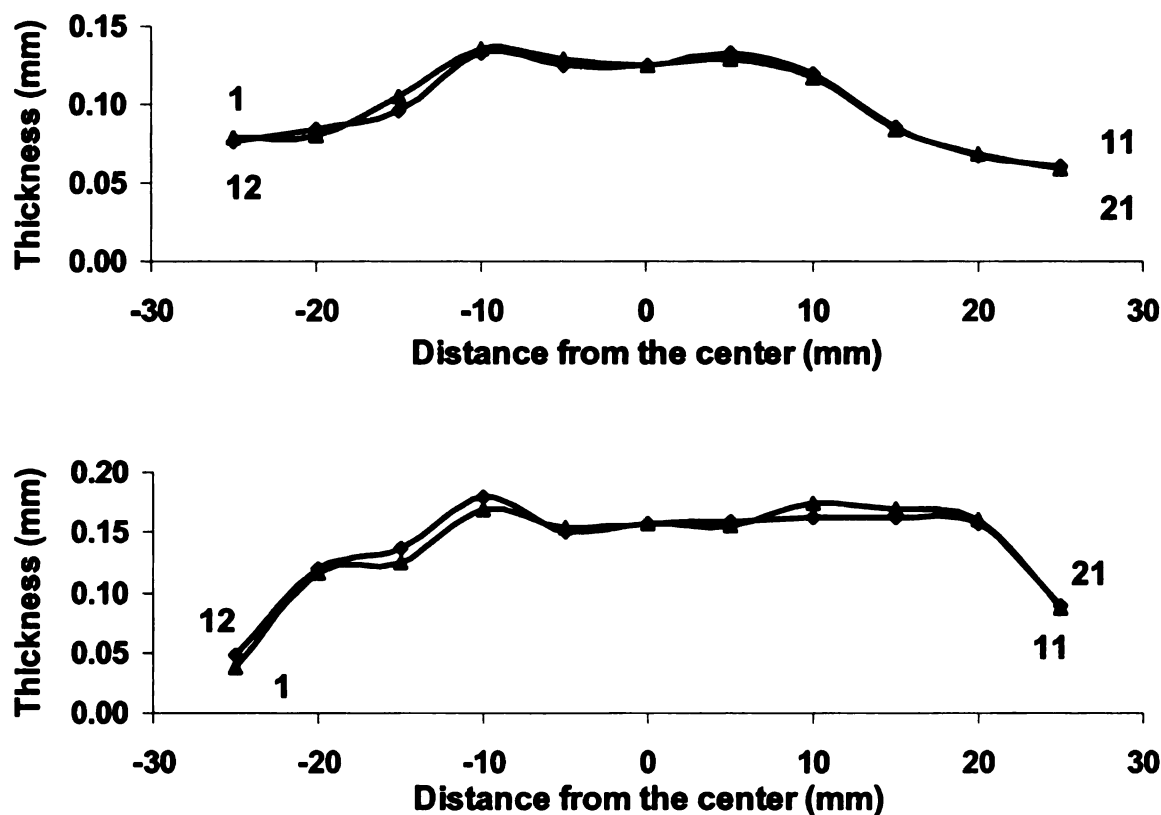


Figure 4-17: The diamond film thickness (in mm) distribution across the film diameter. The number 1-11 and 12-21 indicates the location where the thickness was measured as introduced in Figure 3-19. Above: SZ-2inch-1mm-#65A. Below: SZ-2inch-1mm-#42.

The film thickness was measured at the different locations across a film and the maximum thickness was plotted. The maximum film thickness occurs is seen at the center of all the samples. It is extracted from the thickness distribution plot, such as the one shown in Figure 4-17. The maximum growth rate and the average growth rate for a given growth condition are shown in Table 4-4 and the relationship of the diamond film growth rate versus the reactor pressure and methane concentration is depicted in Figure 4-18. The maximum value of growth rate is selected at the substrate temperature that is optimum for diamond film growth. All average growth rates calculated by weight gain

and the average of the average growth rates by weight gain over a number of samples that are grown under the same growth condition are also restated in Table 4-4 for comparison.

4.6.2 Growth rate and quality versus methane concentration

The relationship between growth rate, quality and methane concentration with respect to input gases can be described in two different ways. The first way is to look at the growth rate change versus methane concentrations in the input gases while keeping all other deposition conditions the same including the reactor pressure and the substrate temperature. From the literature and past experiences, the growth rate becomes higher when methane concentration increases in the feed gas. However, it is usually expected that the diamond film optical quality becomes lower due to the excessive carbon species in the plasma such that not all carbon atoms are deposited in the sp^3 diamond structure but some in the form of graphite and amorphous carbon. Also, more defects are prone to occur in the forming process of polycrystalline diamonds on the substrate. So this way of description misses one important parameter, the diamond film quality, and sometimes can be misleading if deposition conditions are not specified. By pointing this out nevertheless, a plot of growth rate versus methane concentration is still worthwhile to be presented. Similar to Figure 4-18, a set of data is extracted from Table 4-4 and plotted in Figure 4-19 that shows the maximum linear growth rates versus methane flow.

Table 4-4: Comparison of the average growth rate by weight gain and the maximum growth rate by linear encoder (LE*). Please note the average of the rows to the left is an average growth rate over a number of samples that were grown under the same growth condition.

Sample	Pressure (Torr)	CH ₄ (sccm)	Process duration (hrs)	Ave. thickness (μm)	Ave. G. rate by weightgain (μm/hr)	Ave. of the rows to the left (μm/hr)	Max growth rate by LE* (μm/hr)	Ave. of the Max growth rate to the left (μm/hr)
2"-55	100	4	24	14	0.59	0.59	1.05	1.05
2"-12	120	4	72	40	0.55	0.55	NA	NA
2"-29	140	4	48	24	0.50	0.60	NA	NA
2"-30A	140	4	48	24	0.50		NA	NA
2"-30B	140	4	65	38	0.59		NA	NA
2"-31	140	4	96	75	0.79		NA	NA
2"-32	140	4	70	48	0.69		NA	NA
2"-37	140	4	48	29	0.60		1.01	
2"-43	140	4	36	19	0.53		1.09	
2"-60	140	4	17.5	11	0.60		0.83	0.98
2"-03	160	4	83	50	0.61	0.61	NA	NA
2"-58B	180	4	24	26	(0.77)	0.77	1.83	1.83
3"-03	100	6	48	40	0.83	0.92	1.51(SEM)	1.38
3"-05	100	6	5	4	0.84		NA	
3"-06	100	6	48	52	1.08		1.25	
3"-08	120	6	48	55	1.15	1.13	1.59	1.53
3"-28	120	6	48	53	1.11		1.48	
2"-24	140	6	46	63	1.36	1.65	NA	NA
2"-26	140	6	31	39	1.25		NA	NA
2"-45	140	6	48	75	1.57		2.08	2.32
2"-50	140	6	12	26	2.15		2.33	
2"-52A	140	6	48	91	1.89		2.59	
2"-54A	140	6	37	63	1.70		2.29	
2"-27	160	6	155	266	1.72	2.02	NA	NA
2"-54B	160	6	60	140	2.33		2.95	2.95
2"-39	180	6	48	39	0.81			
3"-10	120	8	48	80	1.68	1.77	2.48	2.71
3"-13	120	8	48	91	1.89		2.83	
3"-26	120	8	48	83	1.73		2.80	
2"-62	140	8	24	70	2.93	2.93	4.18	4.18
2"-65A	160	8	24	78	3.27	3.27	5.65	5.65
2"-42	180	8	48	122	(3.33)	3.33	NA	NA

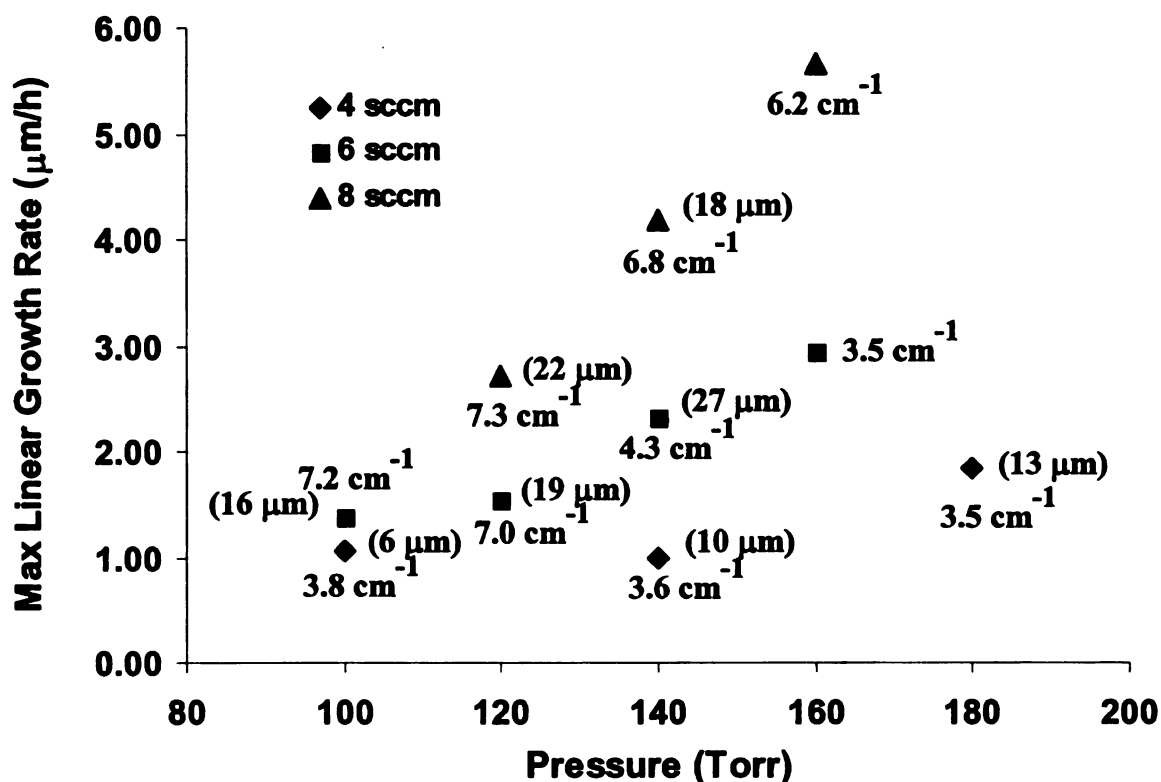


Figure 4-18: A plot of the maximum growth rates versus reactor pressure for samples included in Table 4-4. This plot trend indicates the growth rate achievable under different reactor pressure and methane flow conditions.

This plot confirms that the growth rate increases with respect to increases of the methane concentration in the feed gas at all reactor pressures included in the experiments. A set of photographs that shows the film optical quality (the darkness of the film) changes versus the methane concentration in the input gases is shown in Figure 4-20 for illustration. The pressure at which these samples are deposited is 140 Torr. All other growth conditions are listed in Table 4-3.

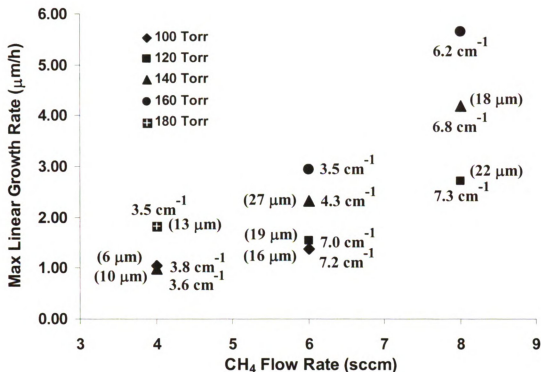


Figure 4-19: Variation of the growth rate with change in methane concentration in the feed gas at different reactor pressures. The hydrogen flow was fixed at 400 sccm. The growth rates were taken from Table 4-4.

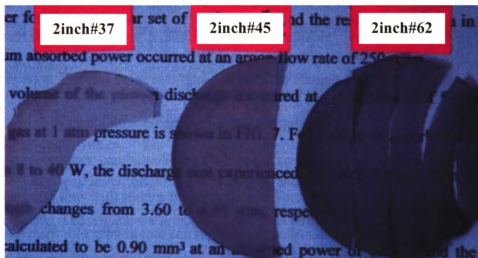


Figure 4-20: Photographs selected to show diamond film optical quality changes versus the methane concentration in the input gases for at pressure 140 Torr. The methane concentrations for samples #37, #45 and #62 were 4, 6 and 8 sccm, respectively.

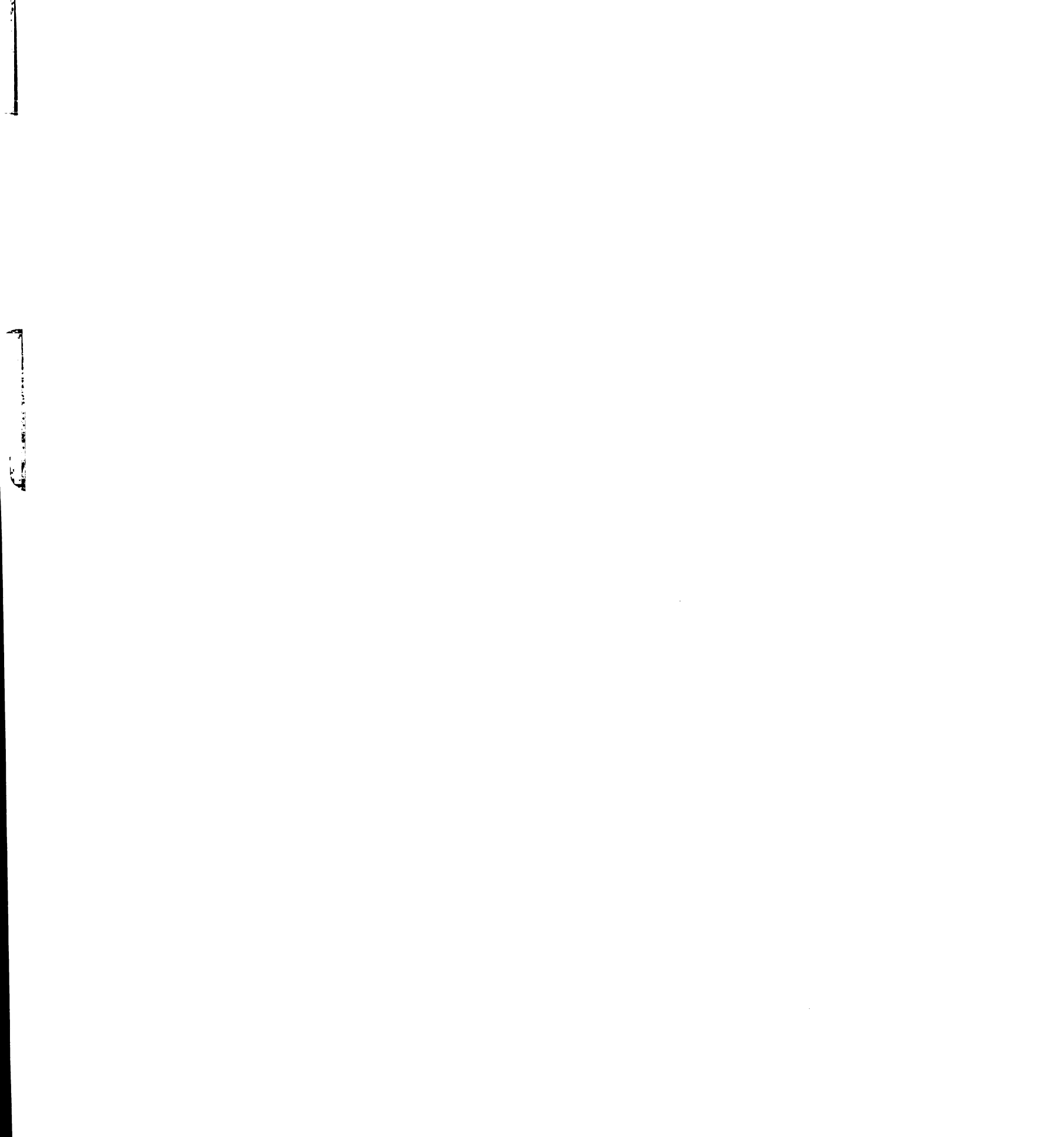


Figure 4-18 and Figure 4-19 can also be used to qualitatively show the good quality diamond film growth region. As it has been discussed in section 4.6.1, the increase of reactor pressure allows more methane flow in the feed gas without having to tradeoff the diamond film quality. An Example Quality Line is added into both figures that indicates this region and separates the better quality diamond growth region from the region that the films typically get darker. This line was constructed by reviewing the growth rate, reactor pressure, the methane concentration, and the quality of grown diamond film samples. Though this line was not made from the exact experimental data locations, they estimate the region of high quality and high growth rate diamond film. The plots shown in Figure 4-21 and Figure 4-22 are the two plots that illustrate this idea. As it has been mentioned before, the condition of using the maximum growth rate in the plot assumes that the substrate temperature is at its optimum value for diamond film growth. With the dashed arrow pointing to the better quality region, the line in Figure 4-21 roughly defines the maximum achievable growth rates for the acceptable film quality with the required growth conditions. The acceptable diamond film quality usually show an average FWHM value less than 5.0 cm^{-1} for Raman peak and the optical transmission above 60% after polishing for wavelength from 400 nm up to $3 \mu\text{m}$. The achievable growth rate can be as high as 4.0 micron per hour with acceptable optical quality diamond film with reactor pressure of 160 Torr and methane concentration of 6.5 sccm. The achievable growth rate can be over 6.0 micron per hour with the same optical quality diamond film with reactor pressure of 180 Torr and methane concentration of 8.0 sccm. Similar, the line in Figure 4-22 defines the maximum achievable growth rate with

the minimum reactor pressure at a given methane concentration that achieves acceptable quality polycrystalline diamond films.

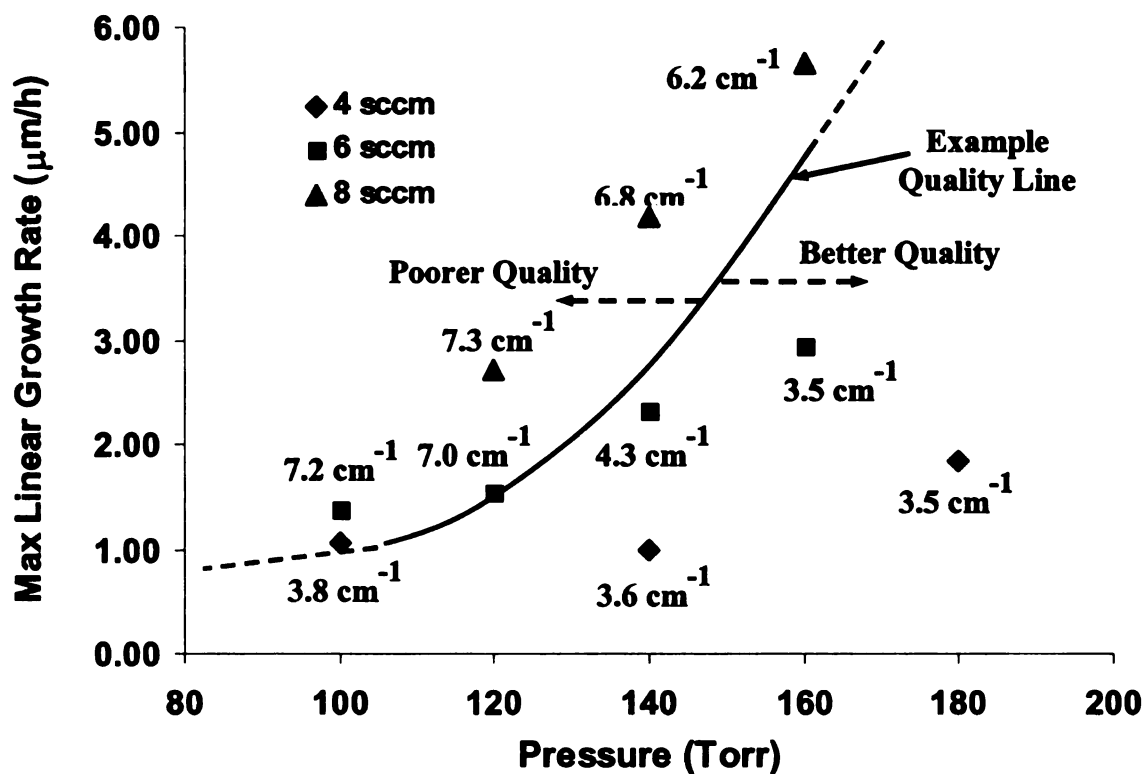


Figure 4-21: The Example Quality Line on the plot separates the region that the good optical quality diamond grows. This line roughly defines the maximum achievable growth rate for the acceptable film quality with the required growth conditions.

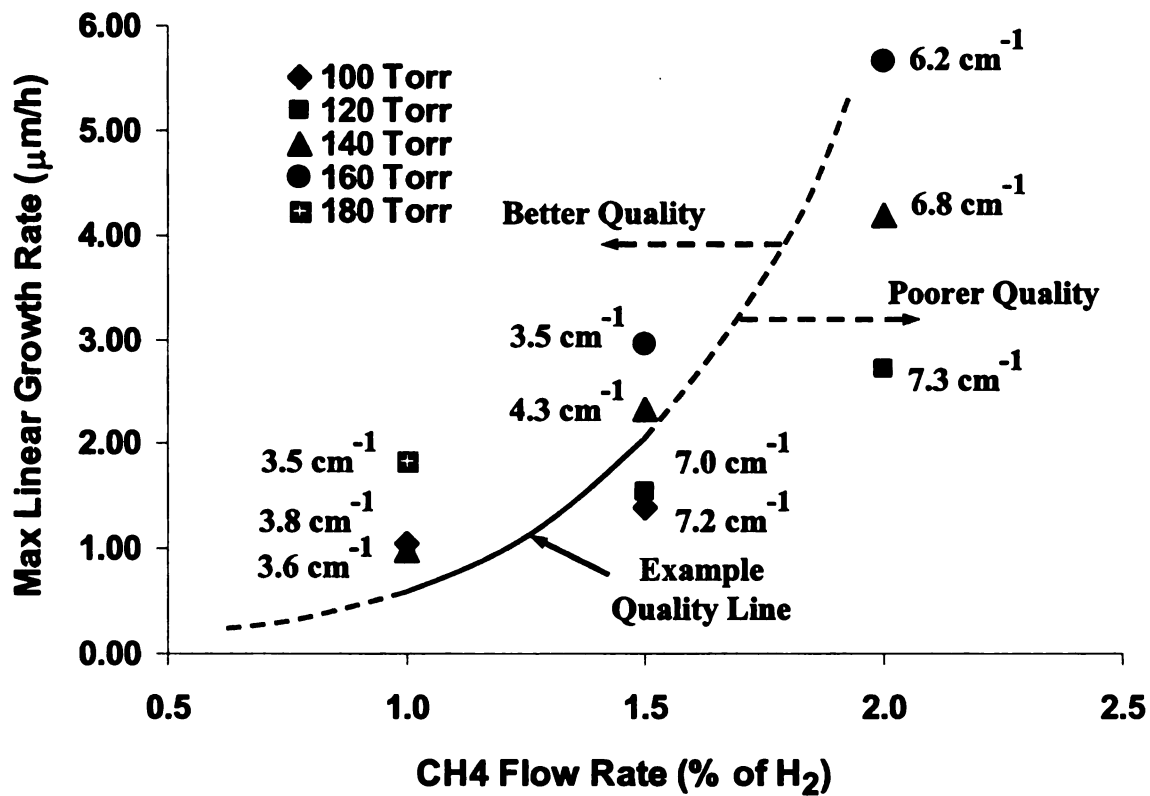
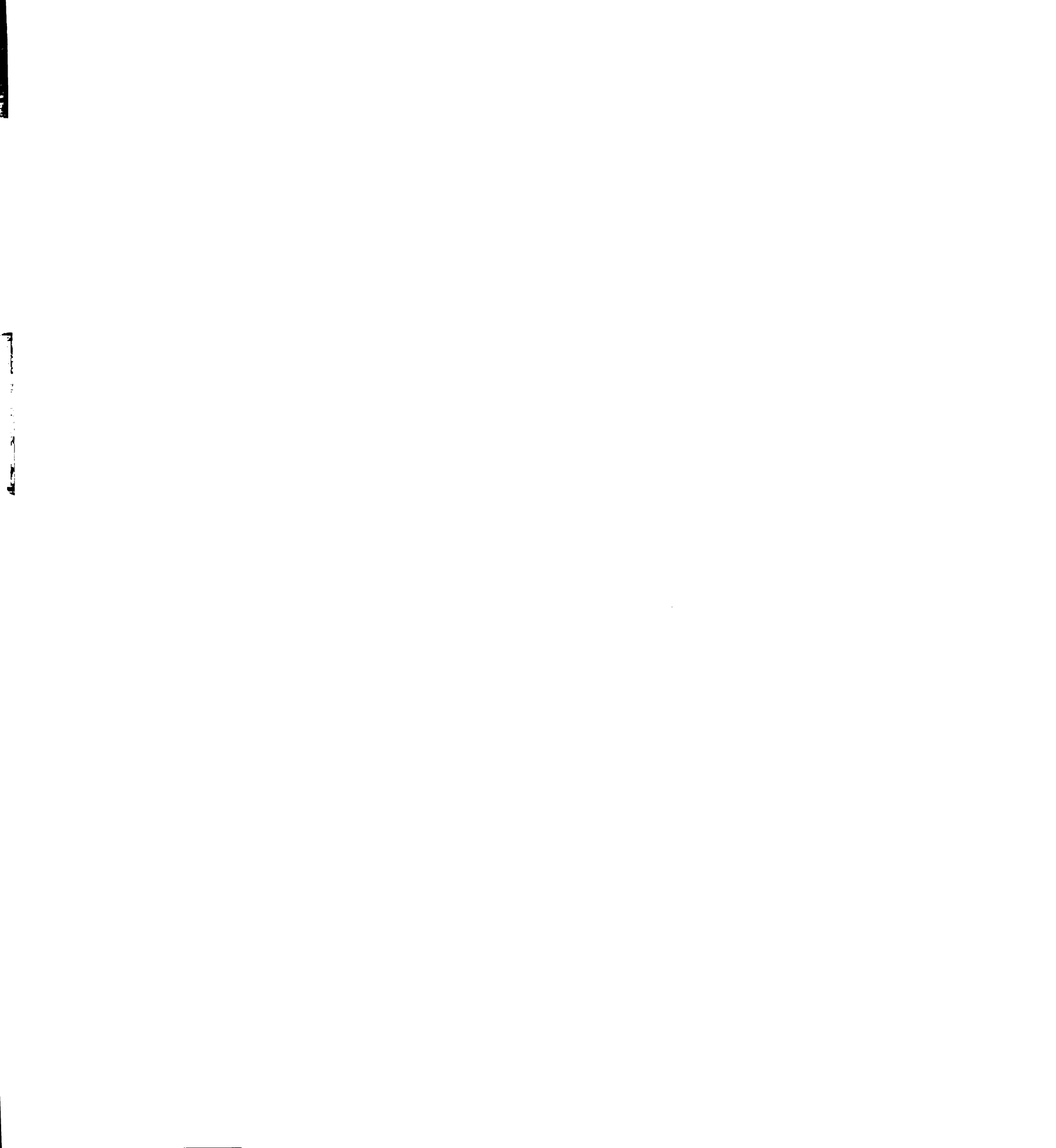


Figure 4-22: The Example Quality Line that indicates the growth condition region for which good optical quality diamond can grow on the plot of growth rate vs. the CH₄ concentration.



4.6.3 Growth rate and quality versus substrate temperature

Substrate temperature is the third most influential parameter that affects polycrystalline diamond film growth rate and quality in addition to reactor pressure and methane concentration. As it has been reviewed in Chapter 2, literature reported that the polycrystalline diamond film growth rate increases with the increase of substrate temperature in a range of temperature at a given power density or pressure (Figure 2-22, [34]). However, from observations and measurements, the film quality appears to decrease when substrate temperature becomes too high, such as more than 1100 °C. The graphite, instead of diamond, was deposited on the substrate. The growth rate of the diamond film deposition also appears to not increase significantly. There should be a range of temperature for the substrate that grows polycrystalline diamond film at its optimum rate near maximum with the good optical quality. This section is intended to find this optimum range.

An issue related to the substrate temperature measurement is the non-uniformity of the temperature across the substrate. The substrate temperature can not be represented by a single point temperature over a large surface area due to the non-uniformity of the substrate temperature measured during the growth process. Therefore the substrate temperature and diamond film thickness measurements are determined at specific points on the substrate in order to calculate the relationship between the growth rate and the substrate temperature. Seven points across the substrate are used for the temperature measuring points. The details are described in section 5.3.3 in Chapter 5 for the polycrystalline diamond film uniformity study and the relationship between points for measuring temperature and points for measuring thickness are given in Figure 5-9.

Figure 4-23, Figure 4-24 and Figure 4-25 depict seven sets of growth rate – substrate temperature data under the three different reactor pressures of 140 Torr, 160 Torr and 180 Torr. Each set of data are collected from diamond deposition processes run under the same pressure and same methane concentration. Therefore substrate temperature is considered the only variable that determines the growth rate in these data sets. The trend of how growth rate changes versus the substrate temperature can be determined by the location of the data and the shape form by those data dots from the same data set. Due to a relatively small span of the substrate temperature measured, some plots show the growth rate slightly increased while others show slightly decreased over the temperature range from about 900 °C to 1100 °C. All the substrate temperature data are selected from those samples whose optical quality is good. Therefore the optimum range of the substrate temperature that grows diamond films near its maximum rate can be determined by these data. Figure 4-26 is created for this purpose, which includes the entire growth rate – substrate temperature data sets from Figure 4-23, Figure 4-24 and Figure 4-25. From Figure 4-26, this optimum range of substrate temperature is roughly seen at from 950 °C to 1030 °C. To include errors from data and human, this estimated range is broadened and determined to be at from 930 °C to 1050 °C, over a 120 °C temperature range. The substrate temperature for obtaining maximum growth rate when other growth conditions are the same should be somewhere in between 930 °C to 1050 °C.

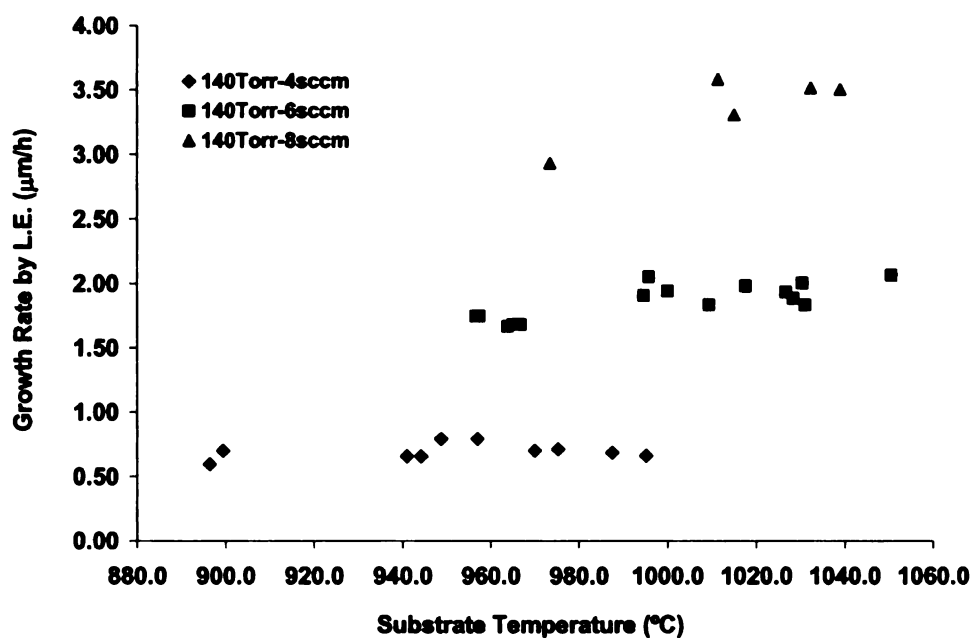


Figure 4-23: Diamond film linear growth rate relation with respect to the substrate temperature at the reactor pressure of 140 Torr. Thickness is measured by Solartron Linear Encoder (L. E.).

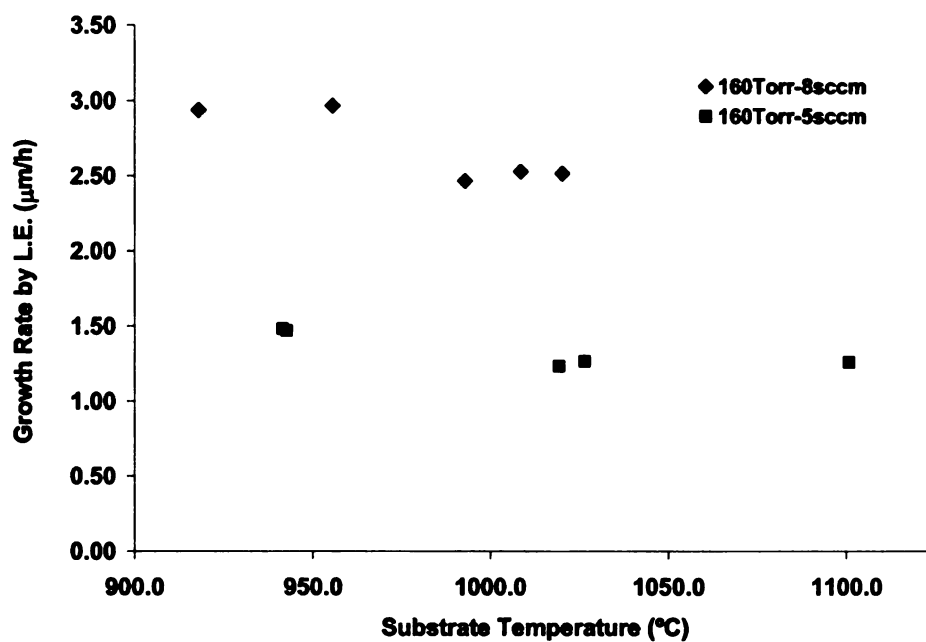


Figure 4-24: Diamond film linear growth rate relation with respect to the substrate temperature at the reactor pressure of 160 Torr.

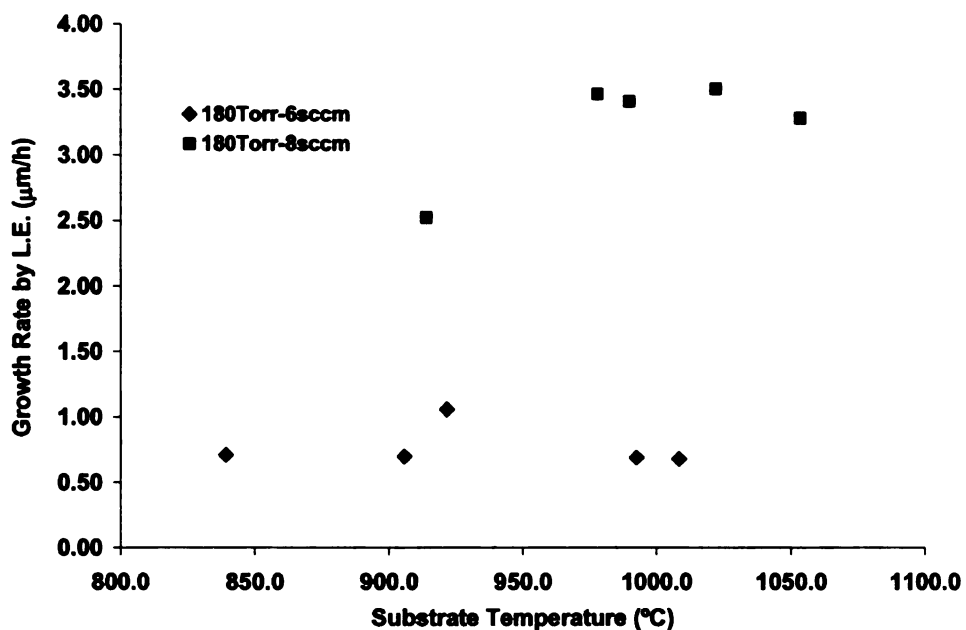


Figure 4-25: Diamond film linear growth rate relation with respect to the substrate temperature at the reactor pressure of 180 Torr.

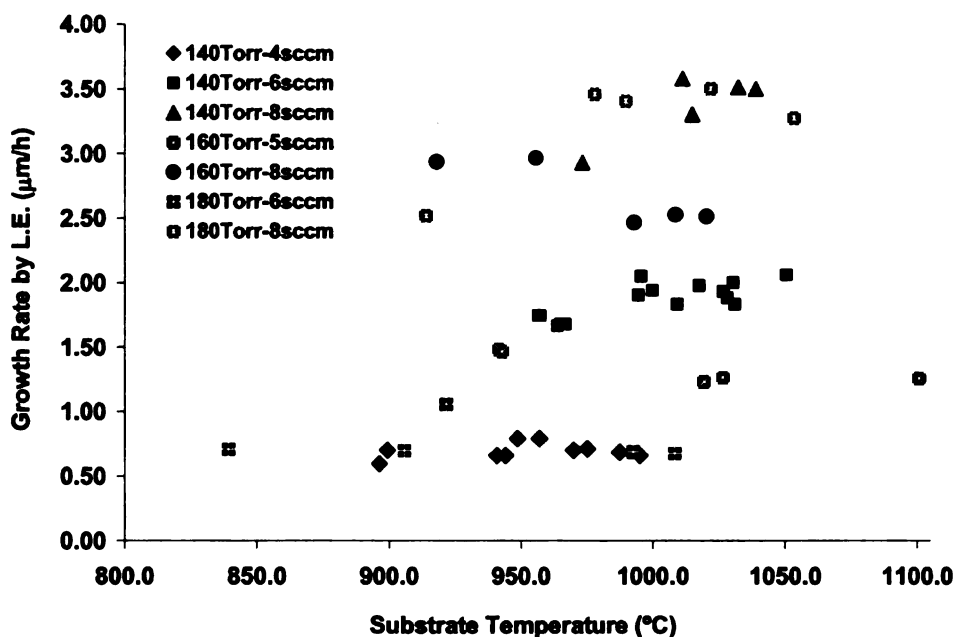


Figure 4-26: Diamond film linear growth rate relation with respect to the substrate temperature.

4.7 The argon effect on diamond film growth rate and quality

For the diamond film growth rate and optical quality studies with the addition of argon into the deposition plasma, a range of argon flow rates was investigated such that the argon percentage varied from 0% to 70% of the total feed gas flow rate. 70% argon is chosen because it was reported by R. Ramamurti that the optimum gas composition that gave the best quality diamond and the highest growth rate for microcrystalline diamond (MCD) film was 60% Ar/ 39% H₂/ 1% CH₄ [151, 52]. Zhu et al. [50] and Zhou et al. [51] groups also identified the drastic increase of C₂ emission intensity in the CVD plasma with the increase of argon concentration in the feed gas, especially when argon concentration reaches 80% and beyond. The large increase of C₂ concentration in plasma may cause too many impurities and defects in diamond films, therefore a decrease in the film quality. However, Ramamurti's result is based on experiments in a lower reactor pressure operating at 95 Torr. In addition, the optical transmission quality was not studied and diamond film quality was only evaluated by Raman spectroscopy. Therefore the study of argon addition in this section is focused on reactor pressures of 100 Torr and higher. The other plasma deposition conditions were selected using good diamond deposition conditions from experiments described earlier in the dissertation. The growth rate and the optical quality of the diamond films deposited with respect to argon flow rate in the feed gas are described in the next section.

4.7.1 The argon effect on diamond film growth rate and grain size

The growth rate of polycrystalline diamond films with the addition of argon to the feed gas is investigated under series typical reactor pressures of 100, 140, and 180 Torr.

Two sets of experiment are carried out with and without any argon addition, with argon experiments are done with argon flow 25% of hydrogen flow or 100 sccm. In considering the argon effect, the methane concentration is chosen to be low, 1% of hydrogen flow in the feed gas, which is 4 sccm. The hydrogen flow is set as constant at 400 sccm. The growth time for the comparing pair of experiments is the same. It is intended to keep the substrate temperature a constant, however the actual substrate temperature may vary a couple of hundred degrees Celsius from the lowest pressure (100 Torr) to the highest pressure (180 Torr). At a given pressure the substrate temperature is nearly the same for comparison purposes. The microwave power is also maintained in the same range. The absorbed microwave power is no more than a few hundred Watts different from the lowest pressure to the highest pressure. The difference of the microwave power occurs to keep the substrate fully covered by the microwave powered plasma. Figure 4-27 shows the argon influence on the average linear growth rate of the diamond film at the different pressures. Figure 4-28 shows the argon influence on linear growth rate at the film center for different pressures in order to compare Figure 4-27 for consistency. The film thickness at the film center was measured using linear encoder, a probing device for depth that was introduced in Chapter 3. The detailed growth conditions and the deposition results are also included in Table 4-5. One may conclude that the increase of the linear growth rate at higher pressure with argon addition is much greater than without the addition of argon. From the substrate temperatures given in Table 4-5, the large increase of the linear growth rate of the diamond film with argon addition is not because of the temperature. Previously this increase was not conclusively discovered due to the lower reactor pressure (100 to 120 Torr) was used for the polycrystalline diamond film

deposition [60]. Attention was more focused on the uniform deposition of the polycrystalline diamond film over a three inch diameter silicon wafer.

Table 4-5: A set of samples that shows the argon influences to diamond film growth rate and diamond grain size at different reactor pressure. The absorbed power is nearly controlled to be the same for the two comparing experiments at the same pressure. The film thickness and growth rate shows both the average value and the value at the center of the diamond film.

Sample	Pressure (Torr)	Gases			Process duration (hrs)	T_S center (°C)	Ave. thickness (μm)	Growth rate (μm/hr)	Grain sizes (μm)
		H ₂ (sccm)	CH ₄ (sccm)	Ar (sccm)					
2"-55	100	400	4	0	24	883-867	14	0.59	6.3
2"-56	100	400	4	100	24	878-878	18	0.75	8.8
2"-37	140	400	4	0	48	1028-955	29	0.60	9.5
2"-53	140	400	4	100	48	1015-990	125	2.60	31.1
2"-58B	180	400	4	0	24	1140-1132	26	1.07	12.8
2"-59B	180	400	4	100	24	1155-1140	70	2.92	29.7
2"-57	180	400	4	100	24	975-975	92	3.83	27.8

Sample	Pressure (Torr)	Gases			Process duration (hrs)	T_S center (°C)	Thickness at film center (μm)	Growth rate at film center (μm/hr)
		H ₂ (sccm)	CH ₄ (sccm)	Ar (sccm)				
2"-55	100	400	4	0	24	883-867	13	0.53
2"-56	100	400	4	100	24	878-878	17	0.73
2"-37	140	400	4	0	48	1028-955	32	0.66
2"-53	140	400	4	100	48	1015-990	144	2.99
2"-58B	180	400	4	0	24	1140-1132	9	0.39
2"-59B	180	400	4	100	24	1155-1140	54	2.24
2"-57	180	400	4	100	24	975-975	87	3.61

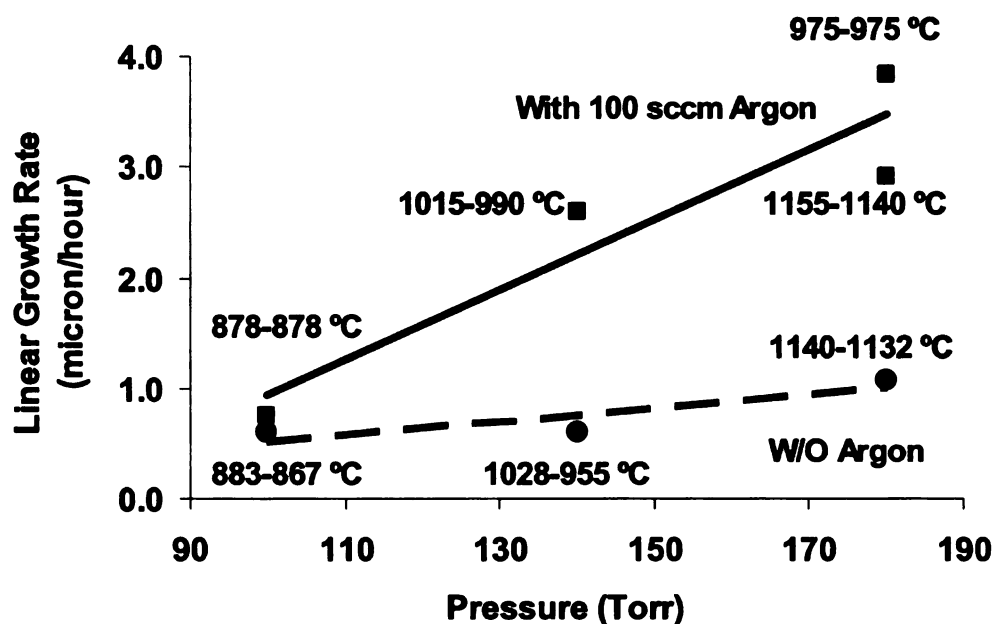


Figure 4-27: The argon gas influence on the linear growth rate of the diamond film at different reactor pressure. All diamond films are deposited on 2 inch Si substrate with 1% (or 4 sccm) CH₄ over 400 sccm H₂. Substrate temperatures range are also shown in the plot. Other data can be found in Table 4-5.

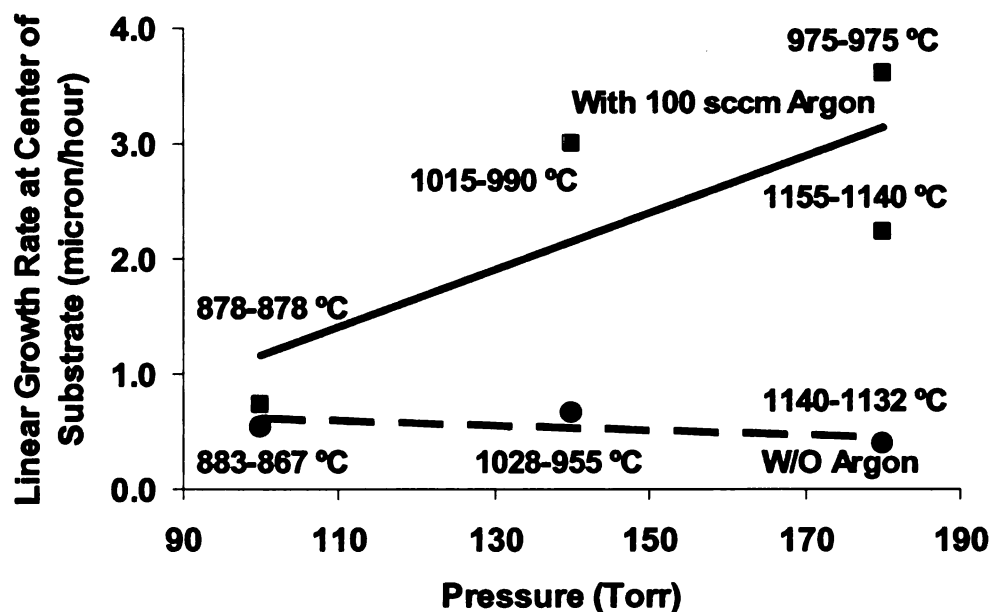


Figure 4-28: The argon gas influence on the linear growth rate of the diamond film at different reactor pressure. The film thickness used to calculate the growth rate is taken at the diamond film center using the linear encoder.

A plot of diamond film crystal size change at different reactor pressure with and without the addition of argon is also presented in Figure 4-29. The average crystal size is assessed by the method of linear intercepts (section 3.9) on the SEM photo of each diamond film surface. The greater increase at higher pressure with argon addition is also seen. This is consistent with growth rate change shown in Figure 4-27, however similar to the growth rate, the grain size doesn't show significant increase at the lower range of pressure.

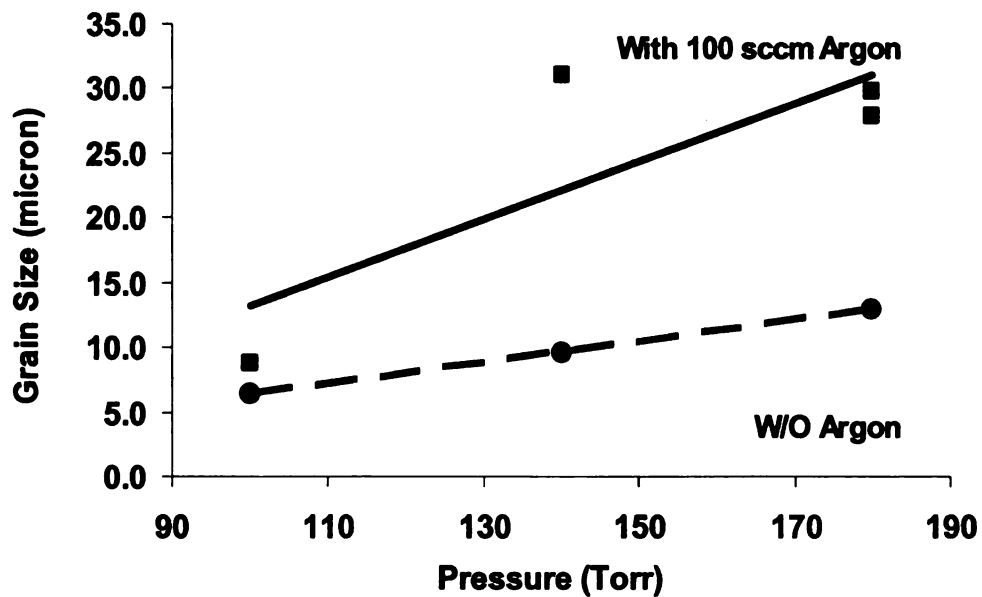


Figure 4-29: The argon gas influence on the diamond crystal grain size of the film at different reactor pressure. Data are from the same set of experiments shown in Table 4-5.

4.7.2 *The diamond film quality changes due to the argon addition*

The initial examination of diamond film quality changes due to the argon addition is done by visual inspection of samples that have been chemically back etched. Figure 4-30 includes photographs of the as-grown diamond samples that were used for growth rate study in section 4.7.1. The growth conditions of these samples are all listed in Table 4-5. These photographs indicate the diamond films (SZ-2inch-1mm-053 and SZ-2inch-1mm-059) become darker (compare SZ-2inch-1mm-037 and SZ-2inch-1mm-058B respectively) due to the addition of argon in the feed gas. Sample SZ-2inch-1mm-056 is an exception. This sample looks very white with excellent transparency. This most likely occurred because the diamond film was deposited on the substrate with its temperature lower than others. This indicates that the substrate temperature plays a very important role in diamond film optical quality. Also, sample SZ-2inch-1mm-059 looks whiter than SZ-2inch-1mm-053, which again shows the reactor pressure is critical to the diamond film optical quality. In assisting the visual inspection, the average of FWHM value of the diamond peak in Raman for each sample is also inserted in Figure 4-30 for comparison. The average value of FWHM for a sample is taken among the four points, P1 to P4 defined earlier in this chapter. The visual inspection shows the consistency of optical quality for samples compared with the FWHM value, i.e. samples deposited with argon addition have bigger number of FWHM values.

Figure 4-31 and Figure 4-32 are the Raman spectra of sample SZ-2inch-1mm-056 and SZ-2inch-1mm-059 respectively. The Raman spectrum of sample SZ-2inch-1mm-053 can be found in previous section 4.4, in Figure 4-11. Similar to the diamond film surface locations shown in Figure 4-4, the FWHM values at points P1 through P4 are

compared with the FWHM value of HPHT single crystal diamond and to the samples of those without the addition of argon gas in the feed gas. The result is consistent with the visual inspection. Please note though not provided, the Raman spectra and FWHM values for sample 2inch-055, 2inch-037 and 2inch-058B are nearly the same as those samples with no argon addition including 2inch-043 and 2inch-045 provided in section 4.4. A summary is provided in Table 4-6.

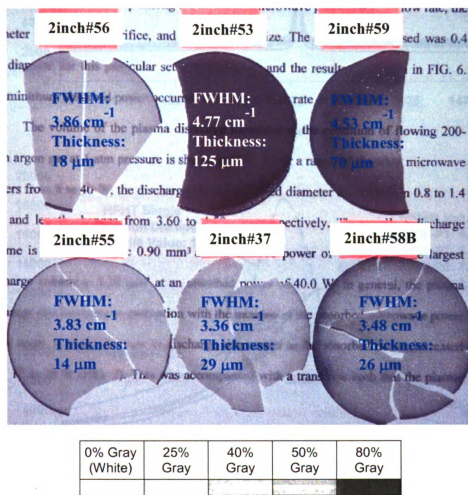


Figure 4-30: Samples that were used for growth rate study in last section, section 4.7.1 are laid on a piece of print paper for visual inspection of their grey scale and transparency quality. The growth conditions are listed in Table 4-5. Please note that thicker films may look darker with the same transparency.

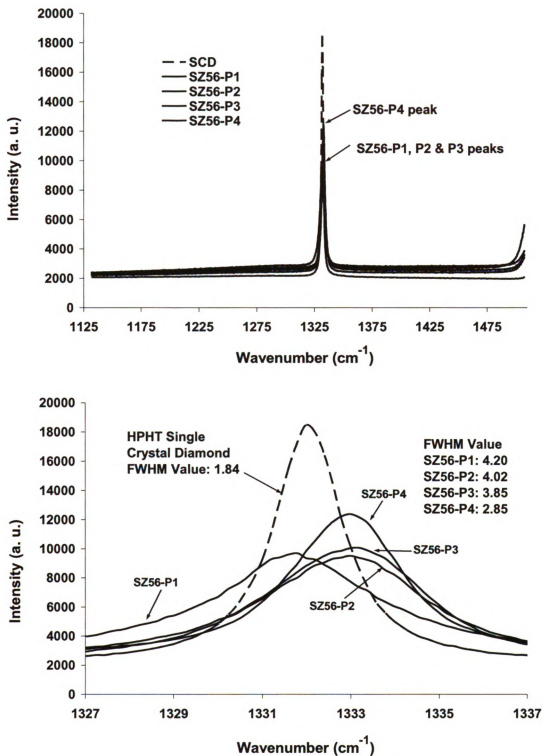


Figure 4-31: The Raman spectra of sample SZ-2inch-1mm-056 before the back etching of silicon at points P1 through P4 in comparing with a HPHT single crystal diamond (SCD). (a) Whole view. (b) Zoom-in view.

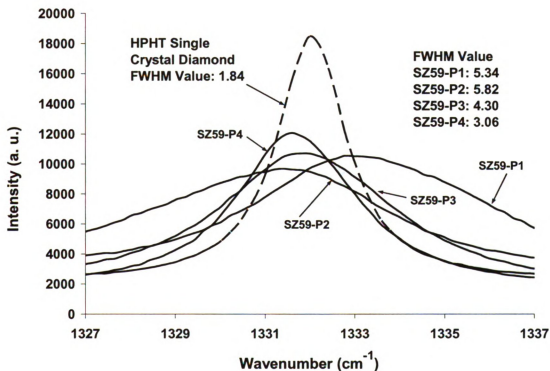
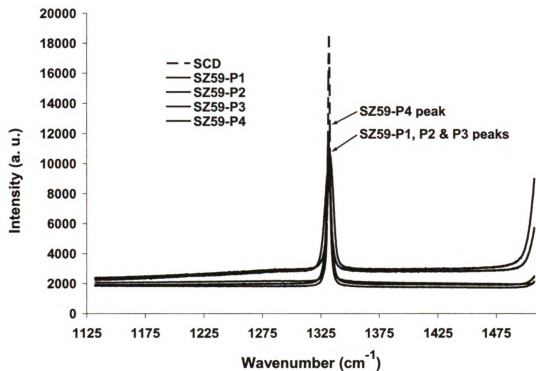
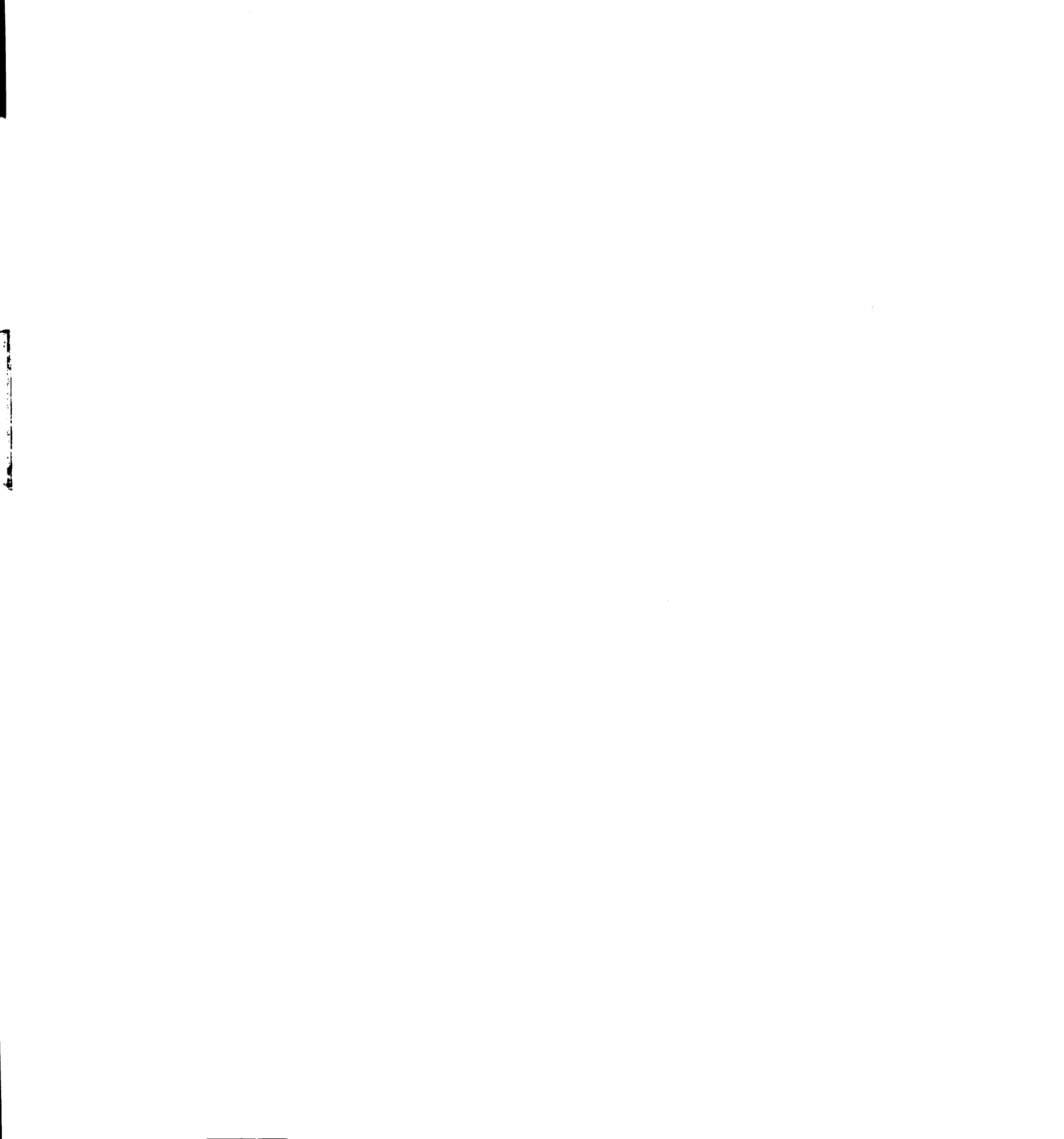


Figure 4-32: The Raman spectra of sample SZ-2inch-1mm-059 before the back etching of silicon at points P1 through P4 in comparing with a HPHT single crystal diamond (SCD). (a) Whole view. (b) Zoom-in view.

Table 4-6: The Raman FWHM comparison with growth conditions of diamond film samples deposited with argon gas addition to those without the argon addition. T_S is the temperature of the substrate at the point averaged from the beginning to the end of the experiment.

Sample	Process duration (hrs)	Ave. thickness (μm)	CH ₄ /H ₂ (%)	Ar/H ₂ (%)	Pressure (Torr)	T_S ($^{\circ}\text{C}$)	Darkness (% Gray)	Peak Position (cm^{-1})	FWHM (cm^{-1})
HPHT SCD	NA	NA	NA	NA	NA	NA	0	1332.04	1.87
2''-55-P1	24	14	1.00	0	100	909	0	1332.35	4.14
P2						899	0	1332.85	3.21
P3						884	0	1332.79	3.75
P4						876	0	1333.01	4.99
2''-56-P1	24	18	1.00	25	100	919	0	1331.73	4.20
P2						913	0	1332.84	4.02
P3						884	0	1332.89	3.85
P4						877	0	1332.90	2.85
2''-37-P1	48	29	1.00	0	140	860	0	1332.43	3.77
P2						896	0	1332.17	3.38
P3						941	0	1332.03	2.81
P4						995	0	1332.23	3.49
2''-53-P1	48	125	1.00	25	140	995	30-40	1331.84	7.26
P2						1008	30	1332.24	4.36
P3						997	30	1332.64	5.11
P4						989	30	1332.47	4.07
2''-58B-P1	24	26	1.00	0	180	937	20-25	1331.56	6.41
P2						990	5-10	1331.33	3.06
P3						1081	5-10	1331.84	2.67
P4						1137	5-10	1331.27	3.04
2''-59B-P1	24	70	1.00	25	180	1023	15-20	1333.28	5.34
P2						1072	15-20	1331.05	5.82
P3						1113	10	1331.90	4.30
P4						1144	10	1331.69	3.06



4.7.3 *The secondary nucleation and step bunching with argon addition*

One observation claimed by nanocrystalline diamond film researchers [52, 56, 68, 69, 109, 151] is that small diamond grains are found on the film surface for very high concentration argon addition. These small diamond grains are considered as the evidence of the secondary nucleation that benefits nanocrystalline and ultra-nanocrystalline diamond film growth. As described in some papers, these small diamond grains form on the surface of the bigger diamond crystals due to the twinning effect. If given the proper condition, some of these small grains grow bigger while some of them may be overgrown by big diamond crystals sooner or later. The growth of these small diamond grains from the secondary nucleation is quite dependent on how fast the new grains from the secondary nucleation are forming. It is controllable by the concentration of the argon addition. For this investigation, it is crucial for these small grains grow larger so that the diamond film contains large microcrystalline size diamond polycrystals, since larger diamond grain means better optical quality of the film. Figure 4-33 shows small diamond grains found on the surface of polycrystalline diamond films that were grown under the 200 sccm addition of argon gas in 400 sccm hydrogen and 6 sccm (SZ-2inch-1mm-028) methane and 4 sccm (SZ-2inch-1mm-034) methane. Sample SZ-2inch-1mm-038 was grown under the 230-sccm addition of argon gas in 150-sccm hydrogen and 4-sccm methane. All three samples are grown at a reactor pressure of 140 Torr.

It needs to be mentioned that the twinning effect is rarely found at on films grown with a low concentration addition of argon gas. Step bunching instead is often seen on the surface of relatively large diamond crystals. Figure 4-34 is a photograph of step bunching growth on microcrystalline diamond film surfaces under the condition of low

concentration of argon in the feed gas. Step bunching is also called step growth by some researchers.

SZ-2inch-1mm-028

**Secondary
Nucleation Sites**

SZ-2inch-1mm-034

**Secondary
Nucleation Sites**

SZ-2inch-1mm-038

**Secondary
Nucleation Sites**

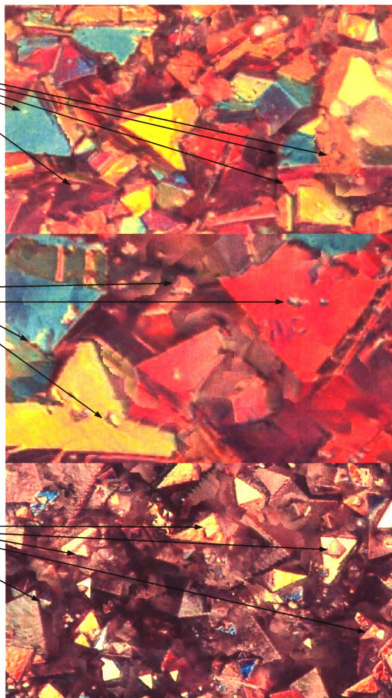


Figure 4-33: Diamond film with high concentration addition of argon causes the secondary nucleation of diamond grains on larger grain surface, which is often called as the twinning effect during the growth.

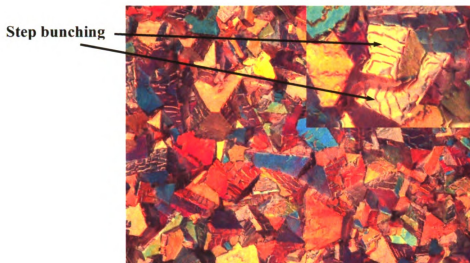


Figure 4-34: Sample SZ-2inch-053 showing typical step bunching on diamond crystal surfaces (upper right inset). The growth conditions list at pressure 140 Torr, 400 sccm hydrogen, 4 sccm CH_4 with addition of 100 sccm argon. The substrate temperature is measured between 990 to 1015 °C at the center of the substrate.

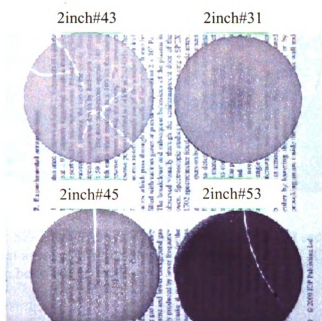


Figure 4-35: Sample SZ-2inch-053 is darker than films grown under the same condition except without argon (SZ-031 and SZ-043). It is even darker than sample SZ-045, which is grown under higher CH_4 (6 sccm) concentration. The substrate temperature is controlled at the same level.

Another finding is that both secondary nucleation and step bunching can be reduced by lowering the substrate temperature therefore improving the polycrystalline diamond film optical quality. Figure 4-36 shows the microstructure of sample SZ-2inch-1mm-056, which is deposited with 100 sccm argon addition in the feed gas at average substrate temperature below 900 °C. Though with some relatively smaller grains are found, the step bunching phenomenon can rarely be observed in the picture under 500× optical microscope. This is consistent with the quality we have seen of this sample in Figure 4-30.

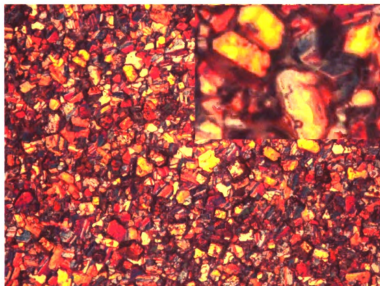


Figure 4-36: Sample SZ-2inch-1mm-056 was deposited with 100 sccm argon addition in the feed gas at average substrate temperature below 900 °C. Other growth condition can be found in Table 4-5.

Chapter 5 Uniformity of the Microcrystalline Diamond Film

Uniform growth of polycrystalline diamond film includes both uniform thickness and quality across the film. Chapter 3 discussed the development of a process methodology and associated reactor design/operation that synthesizes high-quality fast-growing polycrystalline diamond films uniformly over substrate areas. In this chapter it is discussed how actual substrate holders are designed, how well the input and output variables are controlled, and uniformity results are presented for substrates up to 2 – 3 inches in diameter.

5.1 Input and reactor parameters

The input variables and reactor variations studied to get uniform deposition include:

- 1) Variation of uniformity achievable through reactor short and substrate position tuning;
- 2) Improvement of the uniformity by redesign of the substrate holder;
- 3) Improvement of the uniformity by changing the feed gas composition, especially through the addition of argon gas.

The discussion of the reactor variations and tuning (items 1 and 2 above) are included in chapter 3 on general experimental equipments and methods. This chapter will display the results and observations obtained from each approach. The idea for item 3)

above is to add argon to increase the plasma discharge size at a given pressure and microwave power such that the uniformity of the diamond film deposition temperature and thickness across the substrate improves. In this study the focus is on lower percentage addition of argon into the microwave CVD plasma, i.e. less than 70%, for the purpose of increasing the plasma discharge size while maintaining good polycrystalline diamond film growth and quality.

5.2 Output variables

The temperature uniformity, the first output variable, is evaluated by the standard deviation of the temperatures measured across the substrate. Seven points measured on the substrate surface are taken across the substrate diameter with equal distance between points. The selection an odd number of points is for the purpose of locating one point at the center of the substrate.

The diamond film thickness uniformity is another output variable. The methods of film thickness measurement and how the thickness percentage deviation is evaluated were introduced earlier in section 3.7.

5.3 Substrate temperature, thickness and optical quality uniformity

Previously in Chapter 3, section 3.2.2 and section 3.4, was discussed the theory and two main approaches to help achieve the goal of uniform substrate temperature, specifically redesign of the inserts and tuning of the reactor. The inserts used in the past were holders with a flat top and bottom surface that sit on the main holder for the purpose of obtaining higher substrate temperature. However this approach did not compensate for the temperature difference from the center of the holder to the edge of the holder. In this

section, details are provided to show how these inserts were re-designed. The same cooling stage is still used however heat flow is modified due to the changes of the insert's conductive contact surface patterns. It is worth noting that one important factor that may cause a failure of the insert design is that the two contacting surfaces when they are stacked up on each other may be not in very good contact due to a poor machining surface finish. If one finds an uneven heating pattern, over heating of the substrate, or any odd heating behavior that is not what is expected, the surfaces of holders or inserts often need some re-work done.

5.3.1 Temperature uniformity by reactor short and substrate tuning

To find the optimal coax length, L_1 and L_2 , for a set of chosen holders and inserts, the shims are made with different thicknesses. Refer to Figure 3-1 or Figure 3-6 in Chapter 3. It is usually found better to start with the top surface of the substrate at about 2 ~ 3 mm below the cavity bottom. Then start the plasma discharge and increase to the designated working pressure with the proper mix of feed gases (such as 1 to 2% of methane in hydrogen for diamond growth). Tune the sliding short and the probe is done so that the reflected microwave power is minimal. The incident power is adjusted to make sure that the plasma is fully covering the substrate. Then the substrate temperature is measured at the center and at the edge of the substrate. The sliding short position and the substrate temperature data are recorded and it is designated as the middle value reference data. Then the sliding short is moved up by 1 mm and the temperatures are again measured from the center and the edge of the substrate. This process is continued by moving up the sliding short by another 1 mm twice then moving the sliding short three times down from the designated middle value reference position where the reflected

microwave power was minimal. There should be seven sets of data collected before the sliding short moved too high or too low and out of match of the microwave system.

Finally the data is plotted and called in this dissertation Test-1.

The second test is done by repeating the same procedure with the holder set moved up by 1 – 2 mm. The holder set can be moved up by reducing the thickness of the shims that are inserted in between of the baseplate and the flange of the cooling stage. Then tuning and moving the sliding short is done in the same way as done in Test-1 described above. Again, the sliding short position and the substrate temperature are recorded and plotted to give Test-2 data. Then the temperature difference between the center and edge of the substrate is compared to the previous test, Test 1. Next, if there still room for the plasma before it gets too close to the fused silica dome, reduce the shim thickness another 1 – 2 mm. Repeat this process until the smallest temperature difference is obtained between the center and edge of the substrate. It may take five or six tests (i.e. Test-5 or Test-6) in order to find the optimal position for the top surface of the substrate. Remember this setting and save it for the future. It also may happen that one finds the plasma is getting too close to the fused silica bell jar while it appears there is still room to push the substrate higher into the plasma and get more uniform temperature across the substrate. However, the plasma may get too close to the top of the fused silica bell jar and start to coat the bell jar and reduce the experimental run time or sometimes even overheat the bell jar. Always remember that it is not worth it to reduce the run time too much. Therefore it is best to keep some reasonable distance between the plasma and the bell jar.

Table 5-1 shows a set of temperature data recorded for the Test-5 substrate holder configuration and height versus sliding short tuning. The temperature difference between

the center and the edge of the substrate can be calculated by subtracting the temperature at the edge from the center. Figure 5-1 then shows the plot of the data collected from Table 5-1. The plot gives a visual sense for how different the temperature is between the center and the edge of the substrate when the system is tuned to minimum reflected power and when it is tuned away from the minimum reflected power.

Table 5-1: A set of data recorded on temperature variations for the Test-5 versus sliding short tuning where the minimum temperature difference between the center and the edge of the substrate is shown at 67 °C. UFL indicates under the low limit of the detectable range, which is 600 °C.

Sliding Short Position (cm)		19.2	19.4	19.6	19.8	20.0	20.2	20.4
Sliding Short Offset to Position of Min P_r (mm)		-6	-4	-2	0	2	4	6
T_{s-edge} (°C)	M1	UFL	758	866	892	860	784	630
	M2	UFL	759	865	892	861	784	630
	M3	UFL	758	865	892	859	784	630
	Average	UFL	758	865	892	860	784	630
$T_{s-center}$ (°C)	M1	645	885	943	959	941	890	745
	M2	645	884	943	959	941	889	747
	M3	645	884	943	960	941	890	746
	Average	645	884	943	959	941	890	746

**Test-5: Point-Temperature Variations Vs Short Tuning
Shims Thickness: 0.315 inch**

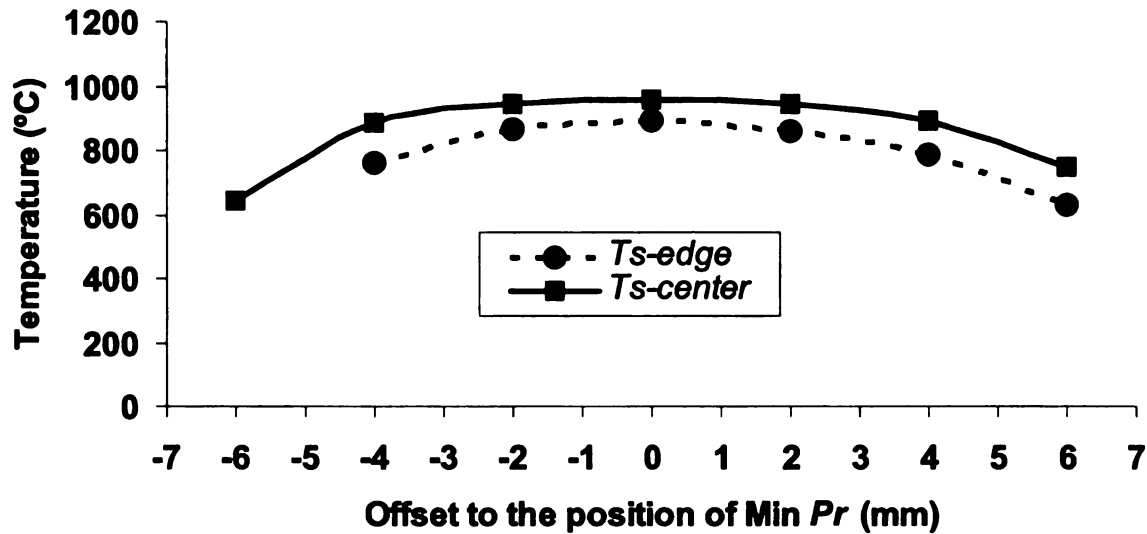


Figure 5-1: An example of plot of the temperature variations for both center and the edge of the substrate when the sliding short is shifted from the position of minimum reflected power. The shim thickness with this particular holder set is at 0.315 inch and the correlated $L_1 = 2.4946$ inch and $L_2 = 2.445$ inch are shown earlier in Figure 3-1.

Figure 5-2 shows the result of the optimization of the temperature uniformity with a silicon wafer as the substrate. As we gradually push the substrate holder set up into the plasma by reducing the thickness of the shims, the temperature difference between the center and the edge of the substrate gets smaller (shown by T_{s-diff} versus $L_1 - L_2$). It is noticed that the temperature difference does not get smaller after the Test-5 designated substrate holder position. For the Test-6 and Test-7 position, the top surface of the substrate is above the cavity bottom 2.1 mm and 2.84 mm, and the plasma is getting too close to the top inner surface of the bell jar. When running the Test-8 position with the top surface of the substrate 3.6 mm above the cavity bottom, which is not plotted in Figure 5-2, the fused silica bell jar was observed becoming red hot. As a result Test-8

was **not** continued. One interesting observation is that the center temperature of the substrate is decreasing and the edge temperature of the substrate is increasing till Test-5. One **speculation** is that the plasma is gradually squeezed into a flatter donut or pancake shape (though the plasma is not necessary empty in the center) during the process of **increasing** the position of the substrate and the holder set. The conclusion is that the best **setting** for this particular substrate holder set is taken as the setting used in Test-5. Test-3 and **Test-4** can also be taken if one prefers the plasma to stay further away from the top of the **bell jar**.

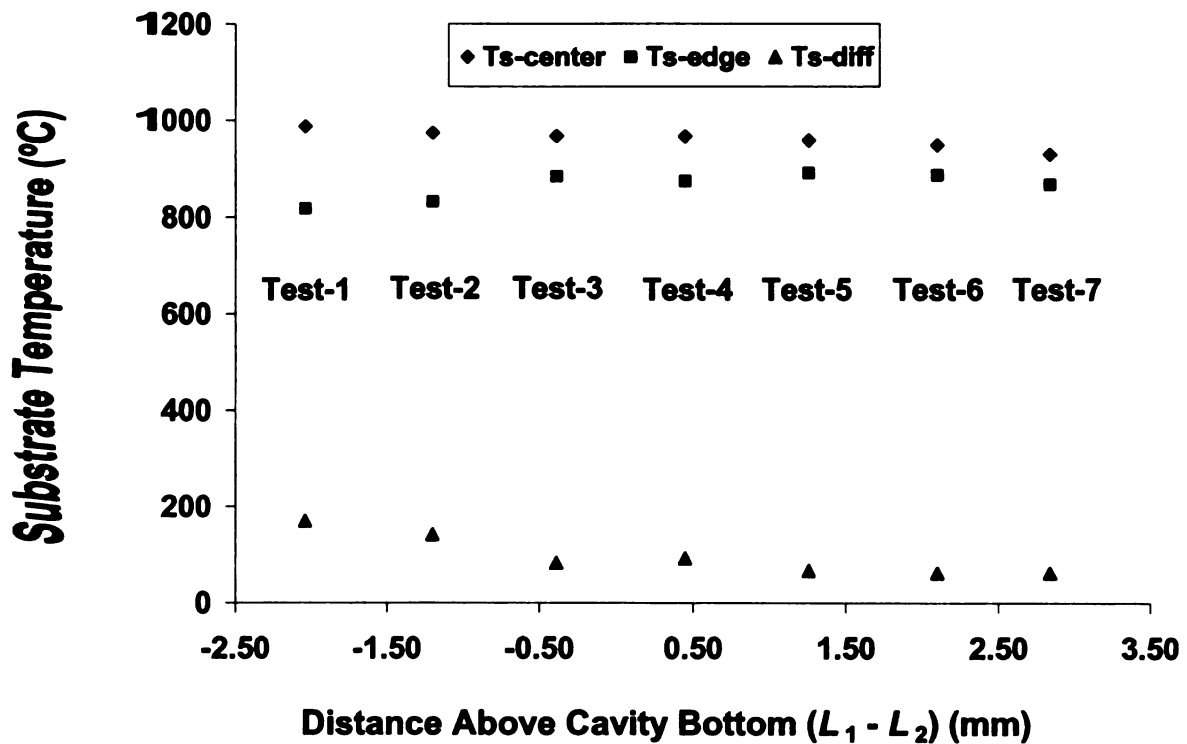


Figure 5-2: Result of the substrate temperature optimization. The temperature difference between the center and the edge of the substrate is getting smaller as $L_1 - L_2$ increases.

5.3.2 Temperature uniformity by substrate holder and insert design

Another technique investigated to improve temperature uniformity is to vary the **design** of the substrate holder inserts.

Figure 5-3 shows the first type of insert used to compensate the temperature **difference** from the center to the edge of the substrate. It has a relatively small area at the **center** of the insert that is in contact with the holder below. This is to compensate for a **situation** when the center temperature is much higher than the edge.

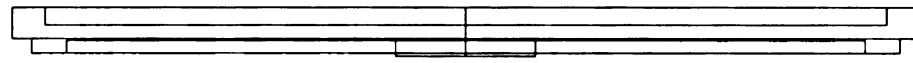
Figure 5-4 shows the second type of insert. At the bottom of the insert it has a **larger** central contact area tapered from the center to the edge. This design provides a **gradually** decreased cooling from the center to the edge to the substrate.

Figure 5-5 shows the third type of insert. A groove pattern is cut in the bottom of **the insert**. The groove width is cut bigger towards the edge of the insert. This design also **provides** a gradual change of the cooling from the center to the edge to the substrate.

Figure 5-6 shows the fourth type of insert. A single groove pattern is cut on the **top side** of the insert. This insert provides the possibility of combinations of inserts.

Figure 5-7 shows a photograph of the plasma heated substrate without using any **groove**-patterned insert. The center of the substrate is usually hotter than the edge.

Figure 5-8 shows a photograph of the plasma heated substrate using a type-4 **groove**-patterned insert as shown in Figure 5-6. The holder set with the type-4 insert **maintains** the same height, in terms of L_1 , as the flat holder set used in Figure 5-7 and the **same** plasma conditions such as the reactor pressure, gas composition and the absorbed **microwave** power. The temperature at the center of the substrate is compensated by the **insert** groove pattern and the center looks cooler than the edge.



Cross Section
A - A'

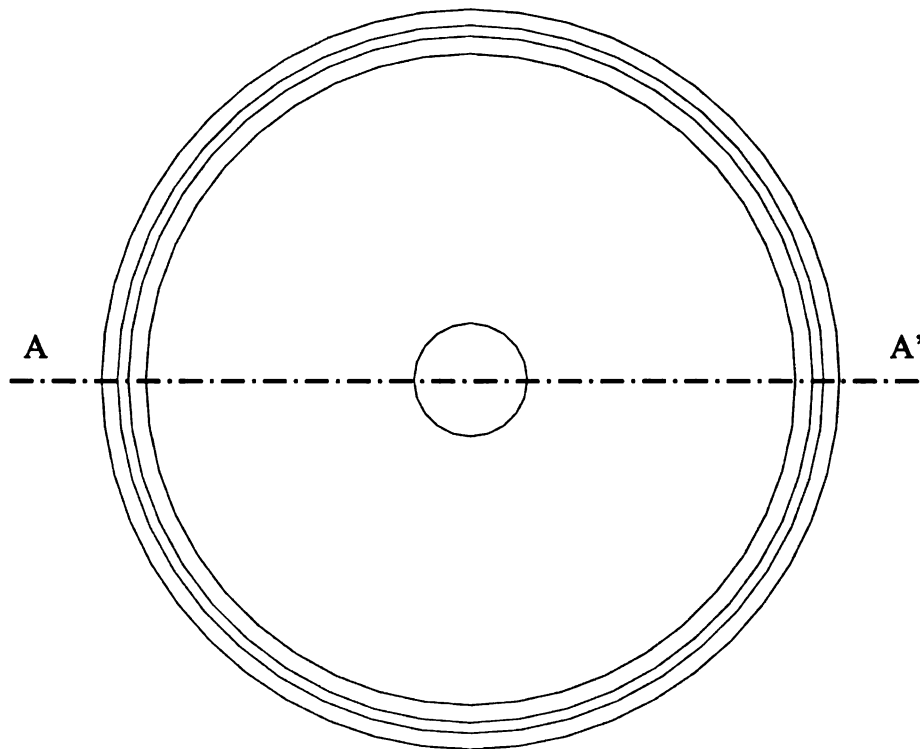
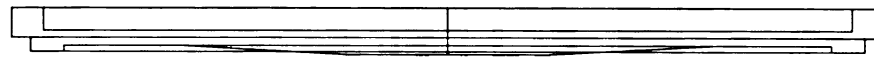


Figure 5-3: Insert type 1, a relatively small area at the center of the insert is in contact with the holder below. Above: cross-section view. Bottom: bottom view.



Cross Section
A - A'

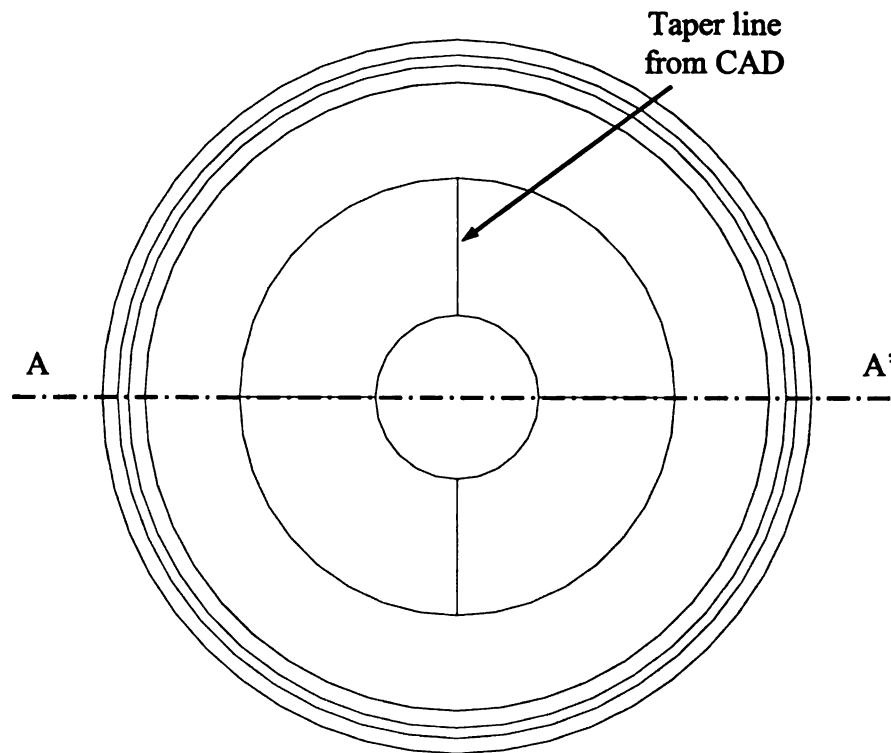


Figure 5-4: Insert type 2, a relatively large contact area is tapered from the center to the edge of the insert. Above: cross-section view. Bottom: bottom view.

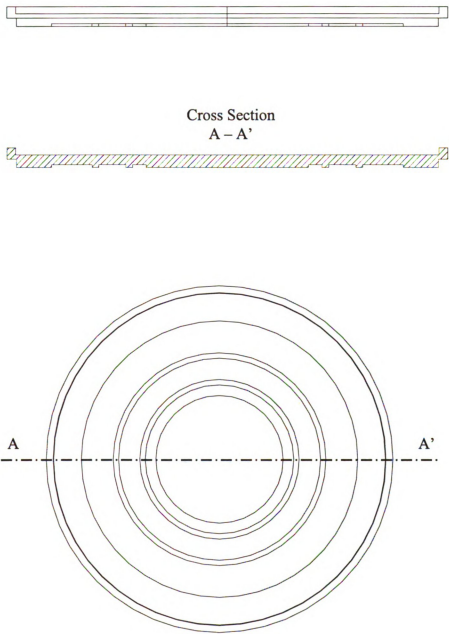
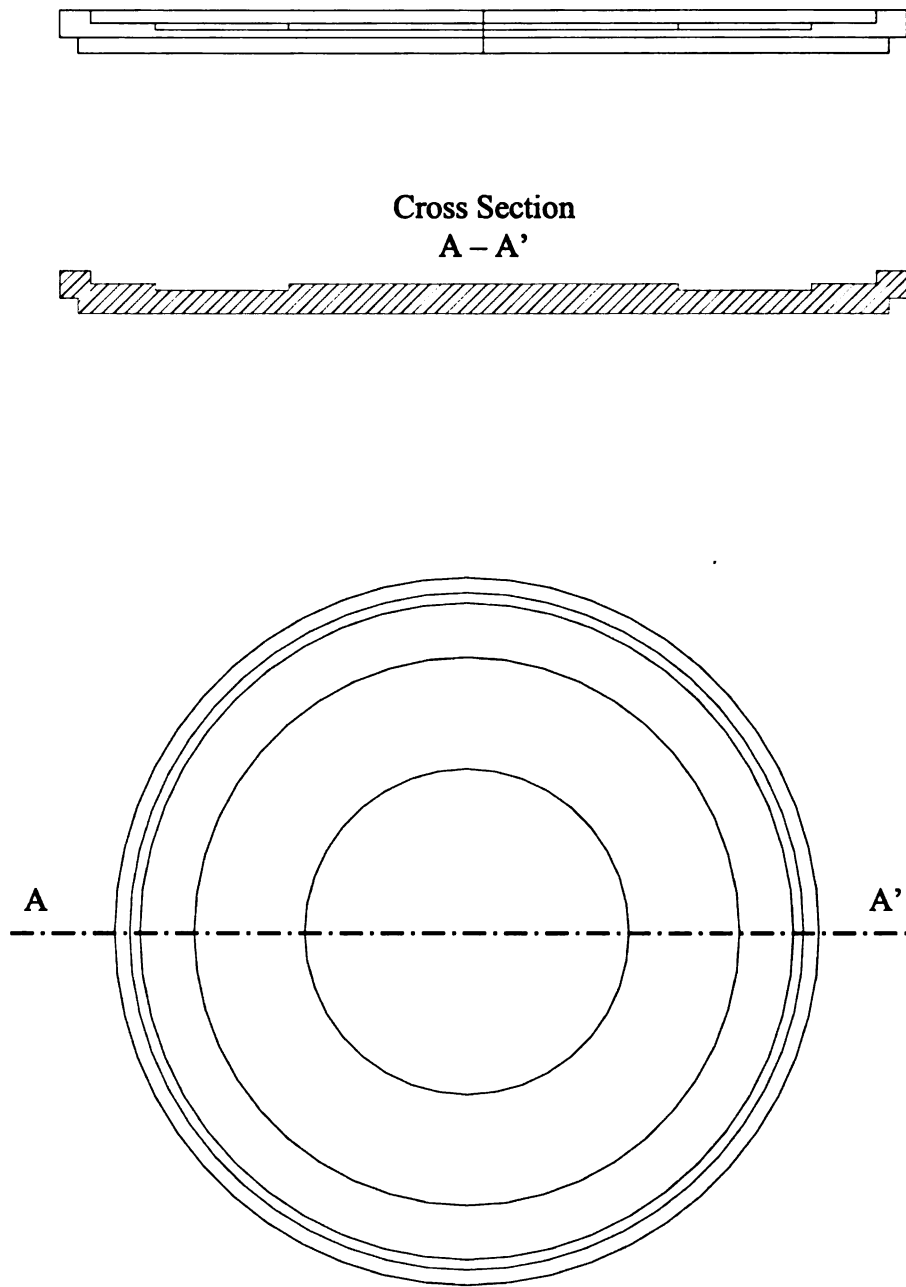


Figure 5-5: Insert type 3, a groove pattern is cut in the bottom of the insert. The groove width is cut bigger towards the edge of the insert. Above: cross-section view. Bottom: bottom view.



**Figure 5-6: Insert type 4, a single large groove pattern is cut at the top of the insert.
Above: cross-section view. Bottom: top view.**



Figure 5-7: A photograph of the heated substrate without using any groove-patterned inserts. Usually the center of the substrate is hotter than the edge.

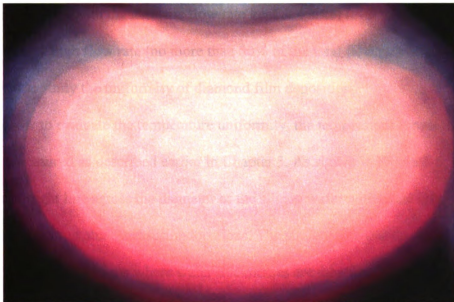


Figure 5-8: A photograph of the heated substrate with using type-4 groove-patterned inserts shown in Figure 5-6. The center of the substrate looks cooler than the edge. The holder set condition (L_1 and L_2) and the plasma condition such as reactor pressure, gas composition and the absorbed microwave power are the same as used in Figure 5-7.

5.3.3 The argon effect on film growth uniformity

The concept of argon increasing diamond film deposition uniformity is based on the observation that the H₂/CH₄ plasma size becomes larger when a flow of argon is added into the plasma. It is observed that the temperature uniformity can become better when argon is added into the plasma for polycrystalline diamond film deposition. This was described in Chapter 4, section 4.3, where the general operational field map for polycrystalline diamond film deposition was presented. The minimum/maximum temperature difference between the center and the edge of the substrate is about 40 °C less with the addition of argon than without the addition argon in the feed gases. In addition from the argon studies shown in Chapter 4, it is observed that to maintain high growth rate and high optical quality diamond film growth, the argon flow rate should be lower than 100 sccm with the methane flow rate kept at 4 sccm level. However, in this section relatively high flow rate (no more than 50% of the total flow rate or 200 sccm) argon is used to study the uniformity of diamond film deposition.

In order to evaluate the temperature uniformity, the temperature across the substrate is measured as described earlier in Chapter 3. As shown in Figure 5-9, seven points on a straight line across the diameter of the silicon wafer with equal spacing are selected for the temperature measuring locations. The straight line that these seven points are on is at the same locations where wafer thicknesses are measured for points from point-1 to point-11 (Figure 3-19). The wafer flat is always aligned with respected to the microwave cavity or view window as Figure 5-9 indicates. Because of this setup, the film thickness measured by the Solartron linear encoder for point-1 to point-11 can be related

to the substrate temperature measured and the relation can be extracted from the data for thickness-substrate temperature relationship.

Table 5-2 and Table 5-3 contain two sets of experimental data of substrate temperature, from experiment SZ-2inch-1mm-058B and experiment SZ-2inch-1mm-059B, for 24-hour runs. All the growth conditions are the same including the substrate holder configuration with the exception that one is without the addition of the argon and the other is with 100 sccm argon in the feed gas. The standard deviations of the temperature across the substrate are calculated in the table. The standard temperature deviations across the substrate and overtime are reduced due to the addition of the argon gas. It is need to mention that films SZ-2inch-1mm-058B and SZ-2inch-1mm-059B were intentionally grown on the diamond films SZ-2inch-1mm-058A and SZ-2inch-1mm-059A with silicon wafers still attached to the film. Both SZ-2inch-1mm-058A and SZ-2inch-1mm-059A were deposited at exactly the same microwave CVD chemistry and time length. The resulting films are considered nearly identical. The reason of doing this is to avoid the nucleation period when diamond grows slower. Additional, the silicon wafer can be susceptible to overheating at the start of diamond film growth. With the current substrate cooling and substrate holder set, either the center of the 2-inch silicon wafer gets overheated before even any diamonds could grow or a bull's eye forms in the center of the diamond film. Even with sufficient cooling, the non-uniform quality diamond film across large area silicon substrate is often obtained due to the large temperature non-uniformity during the nucleation period. To grow a diamond film on another diamond film usually obtains very uniform temperature overall whole film starts

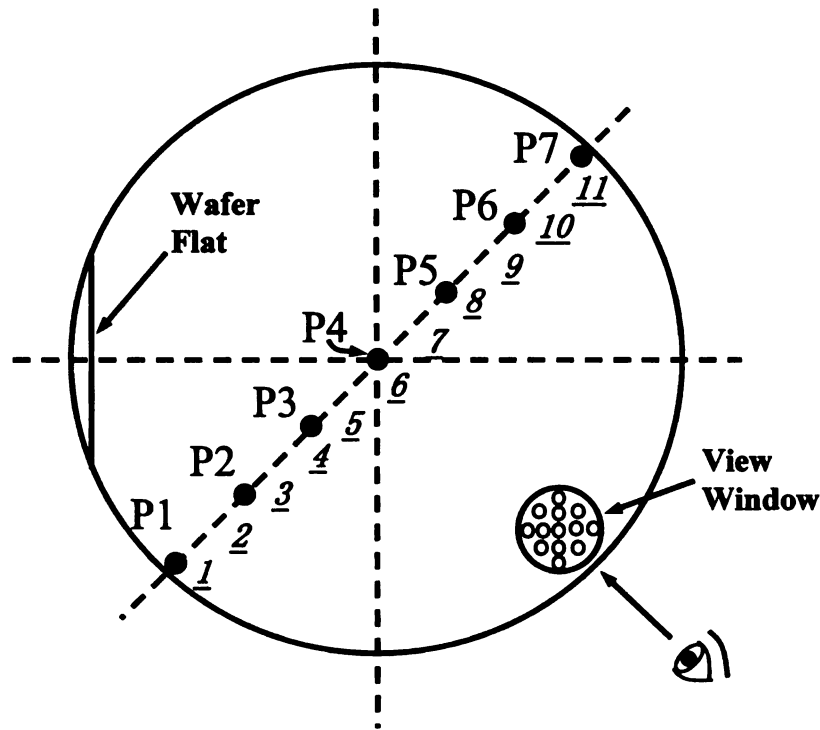


Figure 5-9: This figure shows how the silicon wafer is aligned with the orientation of the cavity and how and where the temperature on the wafer is measured. The underlined number from point-1 to point-11 are the places where thickness are measured and point P1 to point P7 are the temperature measurement locations.

Table 5-2: Sample SZ-2inch-1mm-058B temperature variation over time recorded within 24 hours. The growth conditions are 180 Torr, 400 sccm H₂, 4 sccm CH₄.

Time(h)	Pi(kW)	Pr(kW)	Pabs(kW)	P (T)	1	2	3	4	5	6	7	STD Dev.
1.5	3.120	0.065	3.055	180	921	973	1090	1140	1046	960	912	87.4
8	3.110	0.060	3.050	180	940	995	1095	1140	1054	973	924	81.2
22	3.070	0.060	3.010	180	950	1001	1059	1132	1050	981	931	70.1

Table 5-3: Sample SZ-2inch-1mm-059B temperature variation over time recorded within 24 hours. The growth conditions are 180 Torr, 400 sccm H₂, 4 sccm CH₄, and 100 sccm argon.

Time(h)	Pi(kW)	Pr(kW)	Pabs(kW)	P(T)	1	2	3	4	5	6	7	STD Dev.
1	3.105	0.130	2.975	180	1013	1067	1110	1155	1109	1063	1012	52.9
3	2.985	0.115	2.870	180	1010	1055	1099	1140	1105	1063	1014	48.3
15	2.945	0.105	2.840	180	1022	1070	1112	1142	1110	1070	1028	44.8
23	2.950	0.110	2.840	180	1048	1094	1129	1140	1124	1092	1041	39.1

at the beginning of the deposition due to its excellent thermal conductivity. Please note 58A and 59A are deposited at lower pressure.

Table 5-4 and Table 5-5 provide the thickness uniformity data for the two samples SZ-2inch-1mm-058B and SZ-2inch-1mm-059B. The uniformity is evaluated using the percentage deviation given in Eq. 3-12 in section 3.7.3. The diamond film thickness uniformity is improved significantly by argon addition with the percentage deviation being reduced from over 70 percent down to about 30 percent. This set of experiments shows the improvement made by adding argon gas. The absolute percentage deviation though is still high due to the insufficient compensation of cooling at the center of the substrate. The temperature at the center of the substrate is still too high, i.e. it reached the 1100 °C range. The diamond film growth rate at the center of the substrate becomes lower than at the edge. Both films were also carefully observed and photographed under the microscope. The grains sizes are also more uniform for the film deposited with addition of argon gas (Figure 5-10 and Figure 5-11).

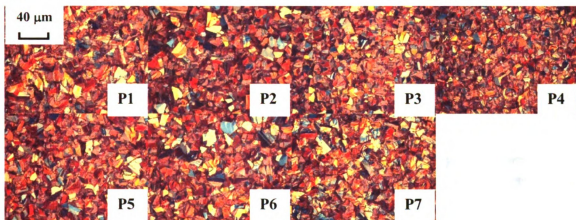
Table 5-4: Diamond film SZ-2inch-1mm-058B thickness measured by linear encoder and the film non-uniformity calculated using the percentage deviation formula, the Eq. 3-12 provided in section 3.7.3.

Point	1	2	3	4	5	6	7	8	9	10	11
Thickness (μm)	39.7	31.0	22.6	14.1	9.9	9.3	9.9	14.5	21.1	30.5	43.4
Point	12	13	14	15	16	6	17	18	19	20	21
Thickness (μm)	44.0	29.8	23.6	15.6	10.6	9.3	10.6	17.4	22.9	31.9	40.2
Percentage Deviation of Point 1-11 (%) ±					76.3	Percentage Deviation of Point 12-21 (%) ±					74.7

Table 5-5: Diamond film SZ-2inch-1mm-059B thickness measured by linear encoder and the film non-uniformity calculated using the percentage deviation formula, the Eq. 3-12 provided in section 3.7.3.

Point	1	2	3	4	5	6	7	8	9	10	11	
Thickness (μm)	64.8	89.7	93.6	76.8	56.3	53.8	54.2	75.8	92.7	84.6	64.8	
Point	12	13	14	15	16	6	17	18	19	20	21	
Thickness (μm)	61.0	86.8	94.7	75.7	49.2	53.8	55.5	74.8	90.0	79.6	58.6	
Percentage Deviation of Point 1-11 (%) \pm					27.2		Percentage Deviation of Point 12-21 (%) \pm					32.1

(a) SZ-2inch-1mm-058B



(b) SZ-2inch-1mm-059B

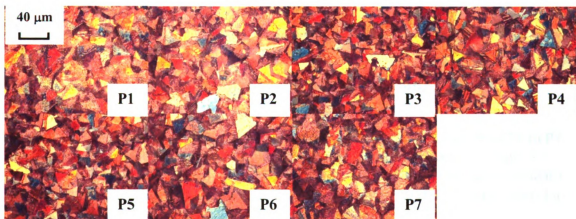
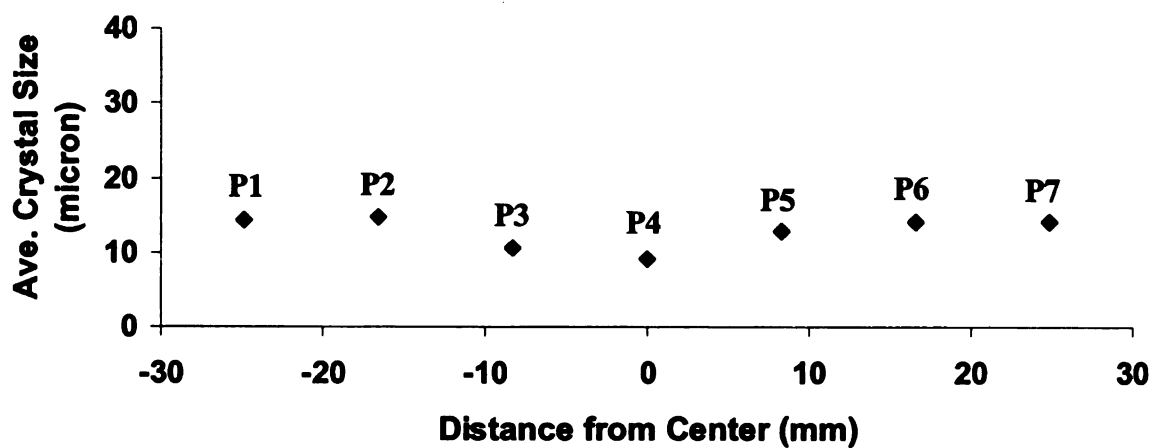


Figure 5-10: Microscopy photographs taken at seven selected points across the diamond film from, (a) sample SZ-2inch-1mm-058B and (b) sample SZ-2inch-1mm-059B, for the study of grains sizes and their size distribution. The seven points P1 to P7 are the same seven points as shown in Figure 5-9.

(a) SZ-2inch-1mm-058B



(b) SZ-2inch-1mm-059B

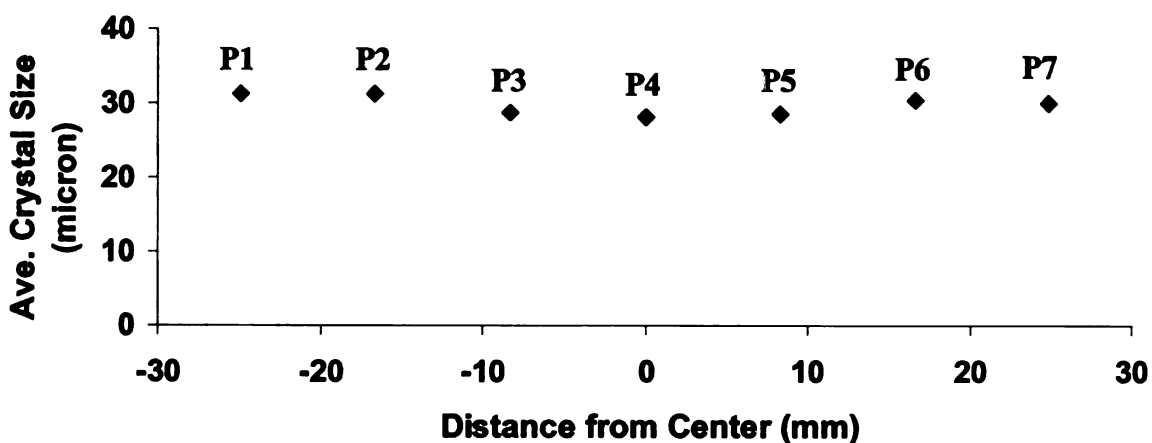


Figure 5-11: Calculated diamond grains sizes at the selected seven points from P1 to P7 using the method of the intercept and their size distributions of, (a) sample SZ-2inch-1mm-058B and (b) sample SZ-2inch-1mm-059B. The calculated standard deviation of the grains sizes for sample SZ-2inch-1mm-058B is 2.14 μm and for sample SZ-2inch-1mm-059B is 1.25 μm .

5.3.4 *Relation of substrate temperature and thickness uniformity to growth rate*

Figure 5-12 displays the relation between substrate temperature uniformity and film thickness uniformity. The data include almost all 2-inch diamond film samples except a few that show significant diamond film surface morphology changes. The substrate temperature uniformity is measured by the standard deviation and the thickness non-uniformity is measured by its percentage deviation as defined in Eq. 3-12. The trendline of the data points indicates that the substrate temperature uniformity has a large influence on thickness uniformity. The more uniform the substrate temperature, the more uniform the thickness of the diamond film. However, the uniformity of the substrate temperature may not be the only factor that affects the film thickness uniformity. The uniformity of the crystal sizes across the diamond film and the quality differences of the film observed from the center of the diamond film to the edge indicate other factors also contribute to the thickness and quality uniformity of the polycrystalline diamond films.

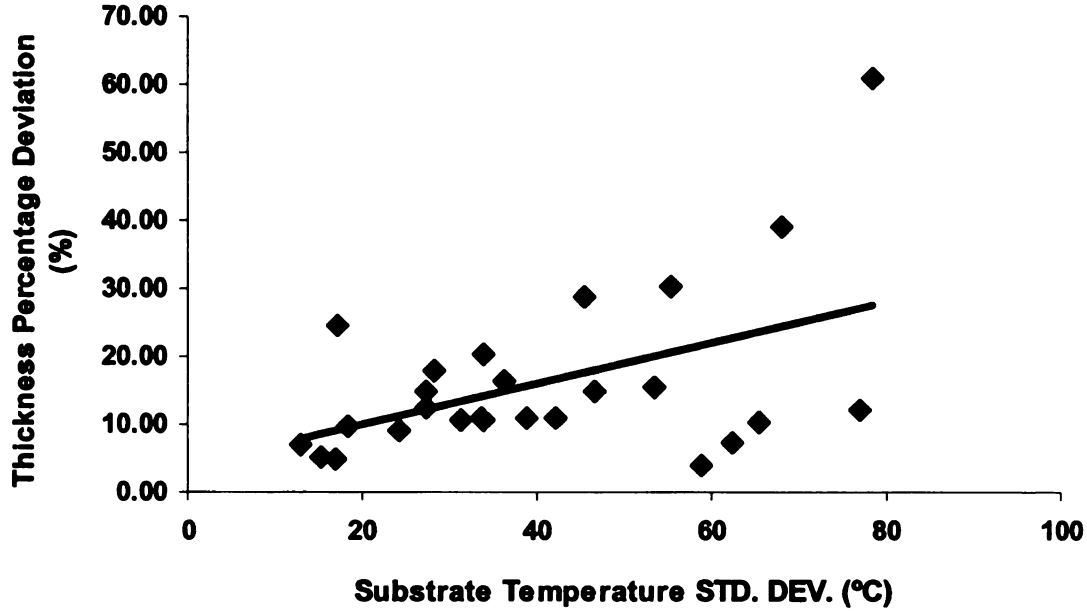


Figure 5-12: The uniformity relation between substrate temperature and film thickness of as grown diamond. The substrate temperature STD DEV stands for its standard deviation and the thickness non-uniformity is measured by its percentage deviation as defined in Eq. 3-12.

Figure 5-13 shows the relation between the average linear growth rate and the thickness percentage deviation. The data is from the same set of samples as used for Figure 5-12. The trendline of the data points indicate that the growth rate increases as the diamond film thickness is more uniform. This is understandable that the average diamond film growth rate reaches the maximum as more diamond is deposited on the substrate if the film thickness is more uniform.

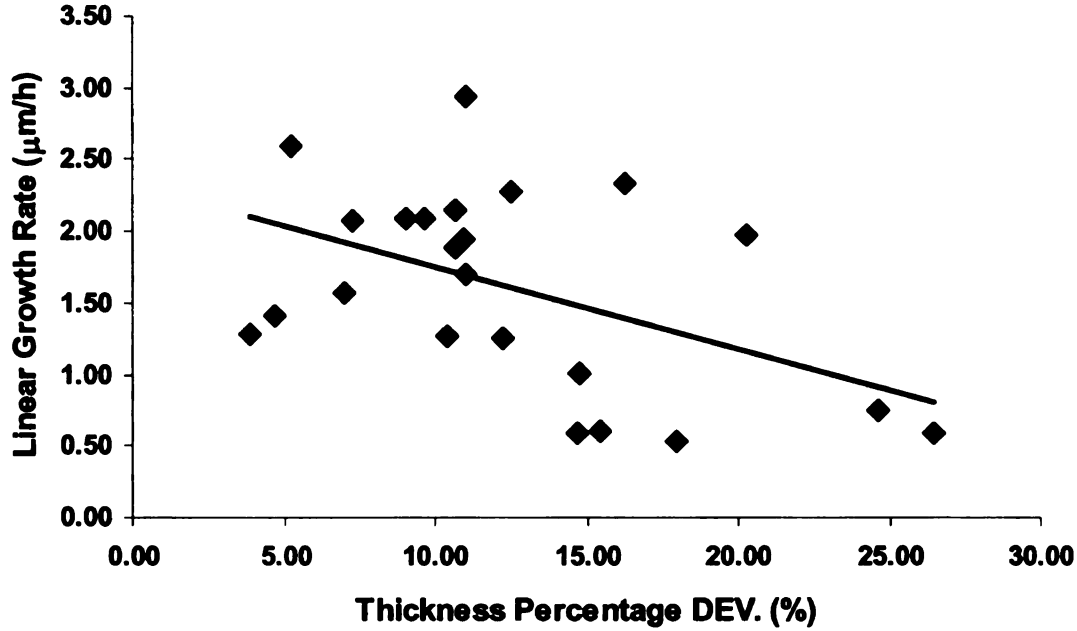


Figure 5-13: The relation between the average linear growth rate and the thickness percentage deviation. The more uniform the diamond film deposited, the higher the average growth rate.

Table 5-6 lists almost all the substrate temperature and diamond film thickness uniformity data for 2-inch diamond samples except those samples that failed (broke) before uniformity data could be collected and those samples with diamond film surface morphology that was significantly different from the rest. The average standard deviations of substrate temperature overtime are found to vary from 16 °C to 68 °C for these samples and the thickness non-uniformities are found to vary from 4.7% to 60.9%. Most of the data show that increased uniformity of substrate temperature improves the uniformity of the film thickness. The exceptions however, are highlighted in the table. Two very uniform substrate temperature samples turned out to have their thickness



uniformities not so good and the other two with the worse substrate temperature uniformity among these samples turned out to have very good thickness uniformity.

Table 5-6: Substrate temperature and diamond film thickness uniformity data overview. The substrate temperature uniformity is measured by its standard deviation and the thickness uniformity is measured by its percentage deviation as defined in Eq. 3-12.

Sample	2"-34	2"-36	2"-37	2"-39	2"-42	2"-43	2"-44	2"-45	2"-46	2"-49	2"-50	2"-51	2"-52A
Ave. Substrate Temperature STD. DEV. Overtime (°C)	17	77	47	68	55	28	27	13	34	27	31	18	34
Ave. Thickness non-uniformity (or % DEV.) (%)	4.7	12.3	14.7	39.2	30.5	18.0	14.8	7.0	11.0	12.6	10.7	9.7	10.7
Sample	2"-52	2"-53	2"-54A	2"-55	2"-56	2"-54B	2"-58A	2"-59A	2"-58B	2"-59B	2"-60	2"-61	2"-62
Ave. Substrate Temperature STD. DEV. Overtime (°C)	24	15	42	16	17	36	59	65	78	45	53	62	39
Ave. Thickness non-uniformity (or % DEV.) (%)	9.1	5.3	11.1	26.5	24.7	16.3	3.9	10.4	60.9	28.7	15.5	7.3	11.1

As a conclusion of this section, high diamond film thickness uniformity is best achieved if a high level uniformity of substrate temperature is achieved. A uniform substrate temperature is a necessary condition to grow uniform thickness polycrystalline diamond film due to the sensitivity of the growth rate to substrate temperature. However, the uniform substrate temperature does not guarantee uniform diamond film thickness

and optical quality across the diamond film due to the difference of the species density and their energy level from the center to the edge. This difference occurs because of how the excited species diffuse toward and naturalize at the wall of the fused silica bell jar or in the volume due to cooler gas temperature outside the plasma ball. This means the diamond film naturally grows faster at the film center than at the edge even if the substrate temperature is absolutely the same from the center to the edge. Therefore if the substrate temperature makes the edge to have a slightly faster growth rate than the center, this will compensate the slower growth rate at the edge resulting in the uniform growth. In addition, we have observed many samples with uniform substrate temperature and thickness that are only transparent in the center but gradually become darker toward the film edge. This problem may have to be left to future work.

5.4 Evaluation of diamond film growth uniformity – thickness, substrate temperature, grain size and surface morphology

Example 1:

The most uniform thickness polycrystalline diamond films are achieved with combining an optimum substrate holder design and the argon addition in the feed gas. An example is the average achieved growth non-uniformity or the percentage deviation for sample SZ-3inch-1mm-22D. The deviation was $\pm 4.74\%$ radially across a diameter of 2.5 inch (or 6.3 cm) and $\pm 4.0\%$ along the circumference at a radius of 1.25 inch (or 3.15 cm) for a 3-inch diameter deposition area. Table 5-7 shows the detailed thickness measurements. Refer to Figure 3-19 (b) for details regarding where the thickness is measured and how the percentage deviation is calculated. The plots of the radial and

circumferential thickness distributions are shown in Figure 5-14 and Figure 5-15, respectively.

The growth conditions for this particular 3-inch diameter diamond sample were at 100 Torr reactor pressure with a combination of hydrogen, methane, and argon gas in the feed at 400 sccm, 8 sccm, and 200 sccm and with average absorbed power of 2.5 kW. The total growth run time was 183 hours and the obtained polycrystalline diamond film average thickness was 311 μm calculated by weight gain. The average growth rate was 1.70 μm per hour. The temperature uniformity was also recorded for the first 48 hours of deposition. Usually in order to have reasonable film thickness uniformity of less than $\pm 10\%$ deviation, the standard deviation of the temperature of the seven points across the substrate should be less than 30 $^{\circ}\text{C}$ for the first 48 hours of diamond film deposition. For this example the standard deviation of these measured temperatures at the seven points across the 3-inch silicon wafer was within 20 $^{\circ}\text{C}$ (Table 5-8). The substrate holder configuration in terms of the parameters L_1 and L_2 in Figure 3-1 and Figure 3-6 are measured to be $L_1 = 2.2789$ inch and $L_2 = 2.2580$ inch. The minimum reflected power short position is tuned to be $L_S = 19.70$ cm + 1.19 cm. The probe position is tuned at $L_P = 3.50$ cm + 0 cm, where the calibration is zero centimeter.

Table 5-7: Diamond film SZ-3inch-1mm-022D thickness measured by linear encoder and the film non-uniformity calculated using the percentage deviation formula, the Eq. 3-12 provided in section 3.7.3.

Point	18	2	3	4	5	6	7	8	19
Thickness (μm)	340.6	343.8	361.1	357.2	356.1	349.6	353.7	344.1	328.2
Point	20	11	12	13	5	14	15	16	21
Thickness (μm)	328.2	338.8	348.3	353.1	356.1	356.7	357.1	341.2	329.4
Percentage Deviation of Point 18-19 (%) ±				4.7	Percentage Deviation of Point 20-21 (%) ±				4.2

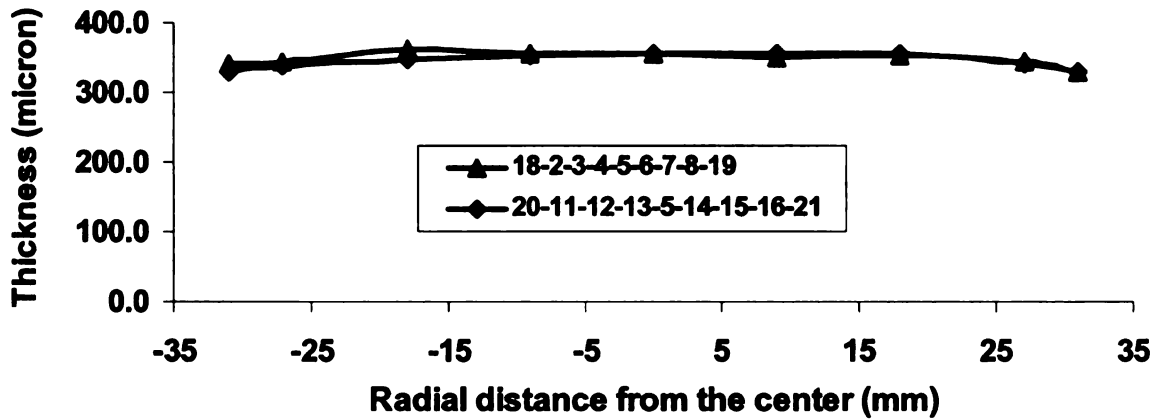


Figure 5-14: Diamond film thickness radial distribution and uniformity for sample SZ-3inch-1mm-22D.

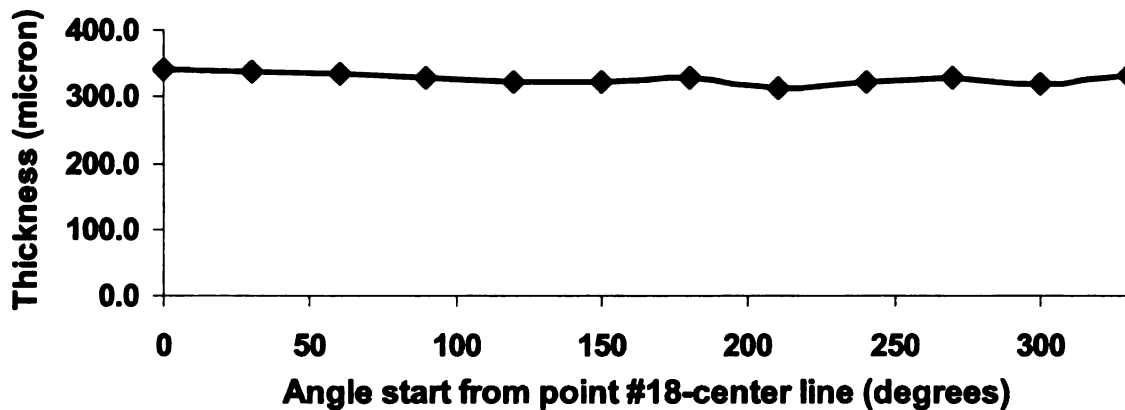


Figure 5-15: Diamond film thickness circumferential distribution and uniformity for sample SZ-3inch-1mm-22D.

Table 5-8: Sample SZ-3inch-1mm-022D temperature variation over time recorded for first 48 hours.

Time(h)	Pi(kW)	Pr(kW)	Pabs(kW)	P (T)	1	2	3	4	5	6	7	STD Dev.
6	3.225	0.840	2.385	100	980	1008	1016	1020	1010	1006	975	17.6
22	3.180	0.695	2.485	100	965	1011	1006	1002	1004	1009	960	21.7
45	3.105	0.475	2.630	100	960	1002	995	985	994	999	958	18.3

Example 2:

Another example that achieved uniform thickness polycrystalline diamond film deposition using the same technique with the addition of argon but without compensating the substrate temperature with a special holder design is selected from those grown on 2-inch diameter silicon substrates. The average achieved growth thickness non-uniformity or the percentage deviation for sample SZ-2inch-1mm-053 is $\pm 5.7\%$ radially across a diameter of 2 inch and $\pm 8.2\%$ along the circumference at a radius of 1-inch on the 2-inch diameter silicon substrate wafer. Table 5-9 shows the detailed thickness at the points (refer to Figure 3-19 (b)) where the thickness is measured and the percentage deviation is calculated. The plots of the radial and circumferential thickness distributions are shown in Figure 5-16 and Figure 5-17 respectively.

The growth conditions for this particular 2-inch diamond sample are at 140 Torr reactor pressure with a combination of hydrogen, methane, and argon gas in the feed at 400 sccm, 4 sccm, and 100 sccm respectively, with the average absorbed power at 3.0 kW. The total growth run time was 48 hours and the obtained polycrystalline diamond film average thickness is 125 μm calculated by weight gain. The average growth rate was 2.60 μm per hour. The temperature uniformity was also recorded during the 48 hour run. The standard deviation of the measured temperatures at the seven points crossing the 2-

inch silicon wafer was within 15 °C (Table 5-10). The uniformity of the grain sizes and the surface morphology are shown in Figure 5-18 (a) and (b). The substrate holder configuration in terms of the parameters L_1 and L_2 in Figure 3-1 and Figure 3-6 are measured to be $L_1 = 2.3441$ inch and $L_2 = 2.3150$ inch. The minimum reflected power short position is tuned to be $L_S = 20.30$ cm + 1.19 cm, where the first number is the reading obtained from the ruler and the second number is the calibration. The probe position is tuned at $L_P = 3.50$ cm + 0 cm, where the calibration is zero centimeter.

Table 5-9: Diamond film SZ-2inch-1mm-053 thickness measured by linear encoder and the film non-uniformity calculated using the percentage deviation formula, the Eq. 3-12 provided in section 3.7.3.

Point	1	2	3	4	5	6	7	8	9	10	11
Thickness (μm)	133.9	136.8	141.5	143.9	144.1	143.7	146.8	146.6	145.5	135.1	133.3
Point	12	13	14	15	16	6	17	18	19	20	21
Thickness (μm)	128.9	130.8	135.9	142.9	143.6	143.7	146.5	147.2	145.3	143.8	141.8
Percentage Deviation of Point 1-11 (%) \pm					4.8	Percentage Deviation of Point 12-21 (%) \pm					6.5

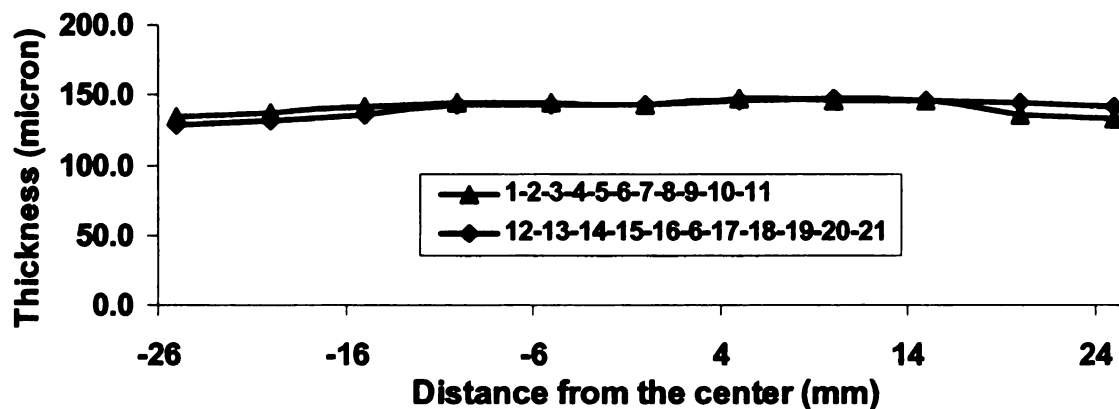


Figure 5-16: Diamond film thickness radial distribution and uniformity for sample SZ-2inch-1mm-053.

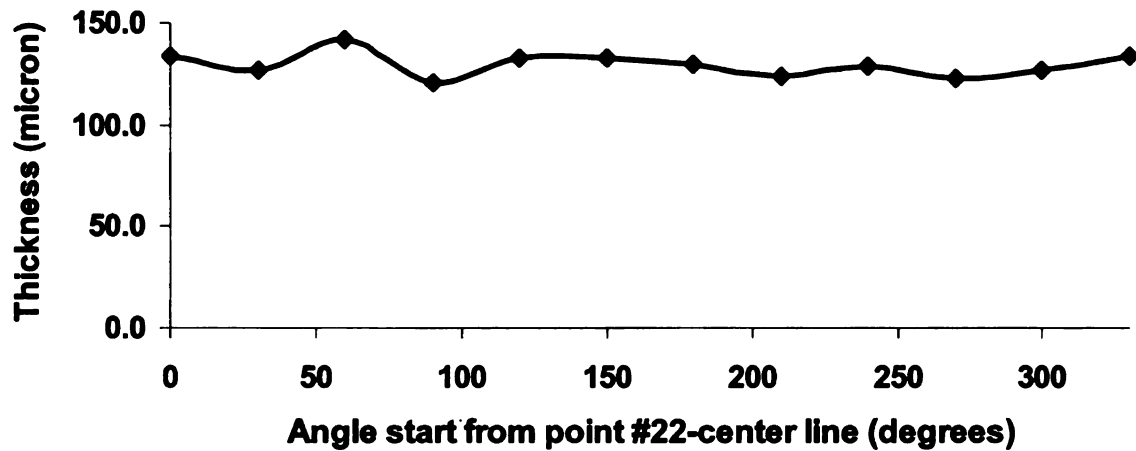


Figure 5-17: Diamond film thickness circumferential distribution and uniformity for sample SZ-2inch-1mm-053.

Table 5-10: Sample SZ-2inch-1mm-053 temperature variation over time.

Time(h)	Pi(kW)	Pr(kW)	Pabs(kW)	P(T)	1	2	3	4	5	6	7	STD Dev.
3	3.320	0.260	3.060	140	942	973	993	1015	995	976	945	26.7
18	3.285	0.265	3.020	140	992	1004	985	974	983	998	988	9.9
26	3.285	0.250	3.035	140	999	1014	1001	983	997	1012	992	10.8
40	3.270	0.235	3.035	140	1020	1022	1000	983	1010	1023	1013	14.4
47	3.320	0.258	3.062	140	1023	1028	1008	990	1012	1031	1026	14.5

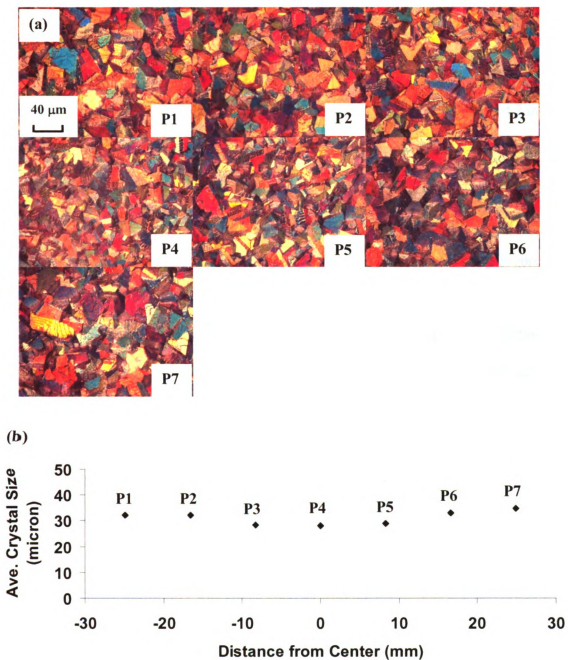


Figure 5-18: (a) Microscopy photographs from taken at points P1 to P7 across the diamond film of SZ-2inch-1mm-053. (b) Calculated diamond grains sizes at points from P1 to P7 and their size distributions. The calculated standard deviation of the grains sizes is 2.60 μm.

Example 3:

The following example that achieved a uniform thickness polycrystalline diamond film deposition is selected from those grown on 2-inch diameter silicon substrate without using argon gas. The average achieved growth non-uniformity or the percentage deviation for sample SZ-2inch-1mm-058A is $\pm 4.3\%$ radially across a diameter of 2 inch and $\pm 6.7\%$ along the circumference at a radius of 1-inch on the 2-inch diameter silicon wafer. Table 5-11 shows the detailed thickness data, (refer to Figure 3-19 (b)) where the thickness was measured and the percentage deviation was calculated. The plots of the radial and circumferential thickness distributions are shown in Figure 5-19 and Figure 5-20, respectively.

The growth conditions for this particular 2-inch diamond sample used a different technique to increase the growth rate and keep good film quality. During the first 12 hours of deposition the conditions were 140 Torr pressure and 4 sccm methane, then the pressure was increased to 160 Torr and methane flow was increased to 6 sccm while hydrogen was kept at 400 sccm for 12 hours. The absorbed power was increased from 3.0 kW to 3.25 kW. The total obtained polycrystalline diamond film average thickness is 30 μm calculated by weight gain. The average growth rate reached 1.28 μm per hour. Note that the temperature uniformity was not as good as with the addition of argon. However the standard deviation of the measured temperatures at the seven points crossing the 2-inch silicon wafer was stabled around 50 °C (Table 5-12). The uniformity of the grain sizes and the surface morphology are shown in Figure 5-21 (a) and (b). The substrate holder configuration in terms of the parameters L_1 and L_2 in Figure 3-1 and Figure 3-6 are measured to be $L_1 = 2.3441$ inch and $L_2 = 2.3150$ inch. The minimum reflected power

short position is tuned to be $L_S = 20.30 \text{ cm} + 1.19 \text{ cm}$, where the first number is the reading obtained from the ruler and the second number is the calibration. The probe position is tuned at $L_P = 3.50 \text{ cm} + 0 \text{ cm}$, where the calibration is zero centimeter.

Table 5-11: Diamond film SZ-2inch-1mm-058A thickness measured by linear encoder and the film non-uniformity calculated using the percentage deviation formula, the Eq. 3-12 provided in section 3.7.3.

Point	1	2	3	4	5	6	7	8	9	10	11
Thickness (μm)	34.9	34.5	34.1	32.7	32.6	32.7	33.5	34.3	34.3	33.5	33.3
Point	12	13	14	15	16	6	17	18	19	20	21
Thickness (μm)	35.3	34.9	34.4	33.7	32.9	32.7	32.4	32.0	31.9	32.4	33.3
Percentage Deviation of Point 1-11 (%) \pm					3.5	Percentage Deviation of Point 12-21 (%) \pm					5.0

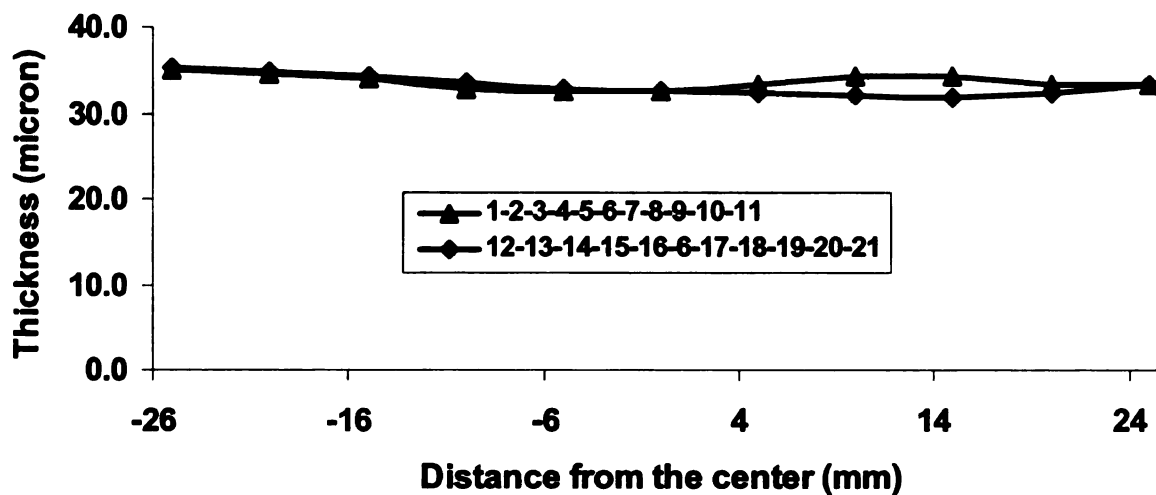


Figure 5-19: Diamond film thickness radial distribution and uniformity for sample SZ-2inch-1mm-058A.

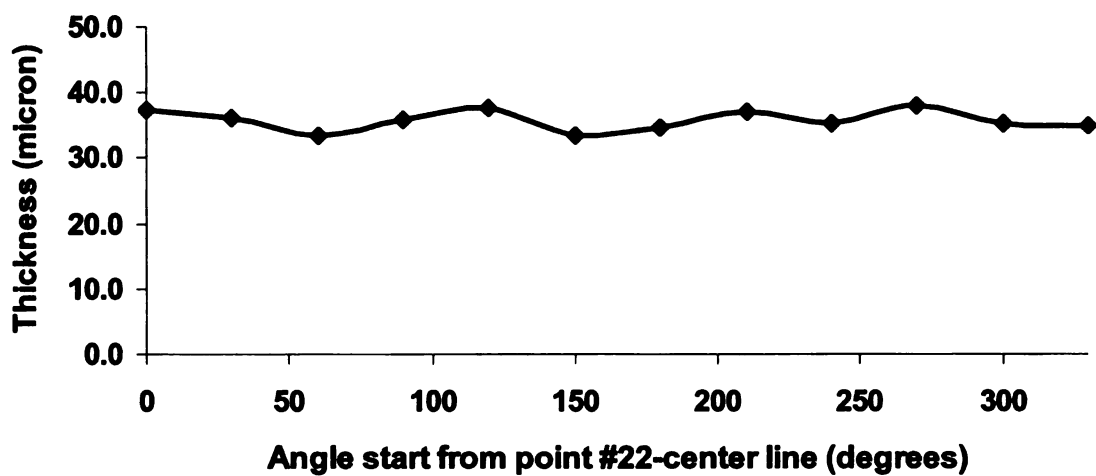


Figure 5-20: Diamond film thickness circumferential distribution and uniformity for sample SZ-2inch-1mm-058A.

Table 5-12: Sample SZ-2inch-1mm-058A temperature variation over time.

Time(h)	Pi(kW)	Pr(kW)	Pabs(kW)	P (T)	1	2	3	4	5	6	7	STD Dev.
2	3.200	0.170	3.030	140	898	942	1001	1030	975	914	870	57.8
12	3.180	0.160	3.020	140	876	911	955	983	943	894	868	43.0
20	3.385	0.132	3.253	160	938	1001	1045	1064	1036	971	913	57.0
23	3.322	0.100	3.222	160	945	1000	1029	1061	1025	970	920	50.3

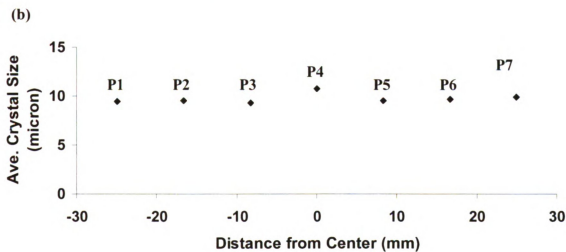
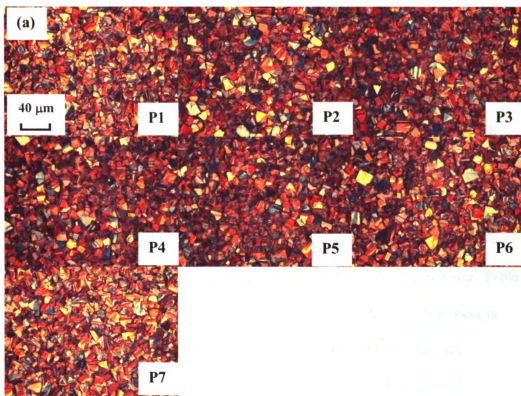


Figure 5-21: (a) Microscopy photographs from taken at points P1 to P7 across the diamond film of SZ-2inch-1mm-058A. (b) Calculated diamond grains sizes at points from P1 to P7 and their size distributions. The calculated standard deviation of the grains sizes is 0.50 μm .

Example 4:

The last example that achieved a uniform thickness polycrystalline diamond film is selected from those grown on 2-inch diameter silicon substrates. This example was selected to show that sometimes the edge effect may play a very important role in film thickness uniformity. The electromagnetic field can concentrate at the sharp pointing edges of objects forming stronger EM regions. A higher energy plasma can therefore result. The average achieved growth non-uniformity or the percentage deviation for sample SZ-2inch-1mm-045 is $\pm 11.5\%$ radially across a diameter of 2 inch and $\pm 4.6\%$ along the circumference at a radius of 1-inch on the 2-inch diameter silicon wafer. Table 5-13 shows the detailed thickness. Refer to Figure 3-19 (b) for where the thickness is measured and the percentage deviation is calculated. The plots of the radial and circumferential thickness distributions are shown in Figure 5-22 and Figure 5-23, respectively. A narrow ring of diamond film (less than 3 mm wide) near the film edge is abnormally thicker than the film near the diamond film center.

The growth conditions for this particular 2-inch diamond sample are a 140 Torr reactor pressure with a combination of hydrogen and methane gas in the feed gas at 400 sccm and 6 sccm, respectively, and with an average absorbed power of 3.15 kW. The total growth run time is 48 hours and the total obtained polycrystalline diamond film average thickness is 75 μm calculated by weight gain. The average growth rate reached 1.57 μm per hour. The temperature uniformity was exceptionally good. The standard deviation of the measured temperatures at the seven points crossing the 2-inch silicon wafer was less than 10 $^{\circ}\text{C}$ for more than $\frac{3}{4}$ of runtime to the end (Table 5-14). The uniformity of the grains sizes has a standard deviation of 1.57 μm and the surface

morphology is shown in Figure 5-24 (a) and (b). The substrate holder configuration in terms of the parameters L_1 and L_2 in Figure 3-1 and Figure 3-6 are measured to be $L_1 = 2.3441$ inch and $L_2 = 2.3150$ inch. The minimum reflected power short position is tuned to be $L_S = 20.30$ cm + 1.19 cm, where the first number is the reading obtained from the ruler and the second number is the calibration. The probe position is tuned at $L_P = 3.40$ cm + 0 cm, where the calibration is zero centimeter.

Table 5-13: Diamond film SZ-2inch-1mm-045 thickness measured by linear encoder and the film non-uniformity calculated using the percentage deviation formula, the Eq. 3-12 provided in section 3.7.3.

Point	1	2	3	4	5	6	7	8	9	10	11
Thickness (μm)	98.1	84.1	83.6	80.7	80.8	80.7	80.3	79.8	82.0	87.2	99.8
Point	12	13	14	15	16	6	17	18	19	20	21
Thickness (μm)	98.0	84.4	85.0	80.3	81.0	80.7	79.0	81.4	82.3	81.9	95.7
Percentage Deviation of Point 1-11 (%) \pm					11.8	Percentage Deviation of Point 12-21 (%) \pm					11.3

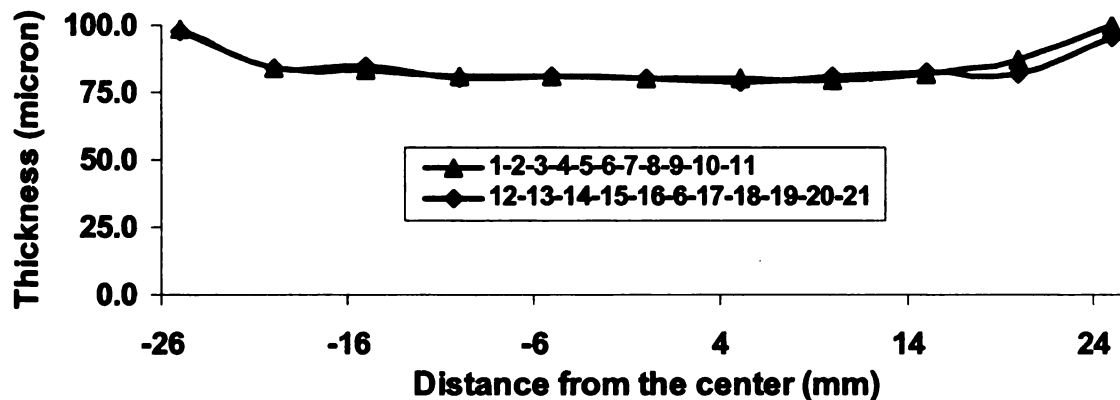


Figure 5-22: Diamond film thickness radial distribution and uniformity for sample SZ-2inch-1mm-045.

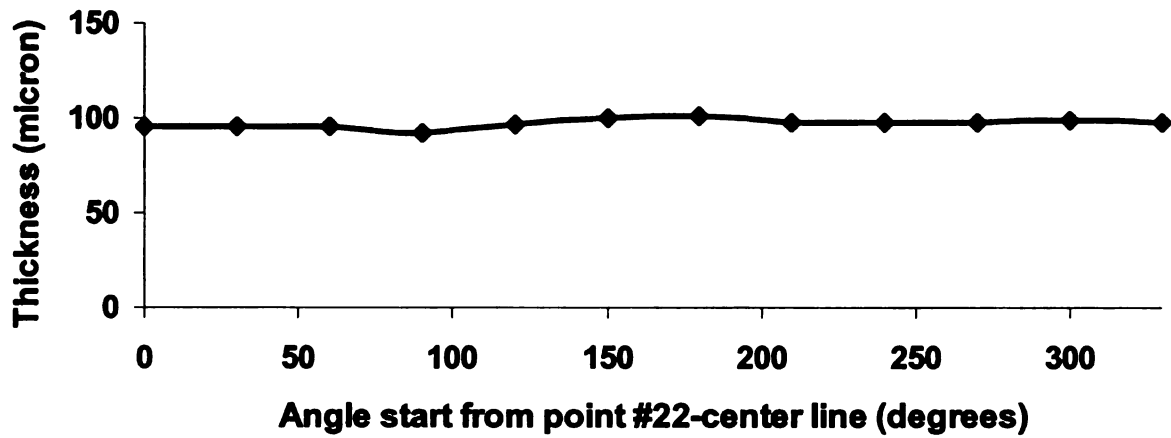


Figure 5-23: Diamond film thickness circumferential distribution and uniformity for sample SZ-2inch-1mm-045.

Table 5-14: Sample SZ-2inch-1mm-045 temperature variation over time.

Time(h)	PI(kW)	Pr(kW)	Pabs(kW)	P(T)	1	2	3	4	5	6	7	STD Dev.
1.5	3.280	0.200	3.080	140	925	957	1009	1027	1004	956	921	42.2
15	3.270	0.055	3.215	140	938	956	958	965	960	957	941	10.1
24	3.200	0.000	3.200	140	935	953	950	946	948	951	941	6.3
36	3.165	0.000	3.165	140	953	965	956	949	957	963	951	6.0
47	3.145	0.000	3.145	140	951	956	952	947	950	956	953	3.2

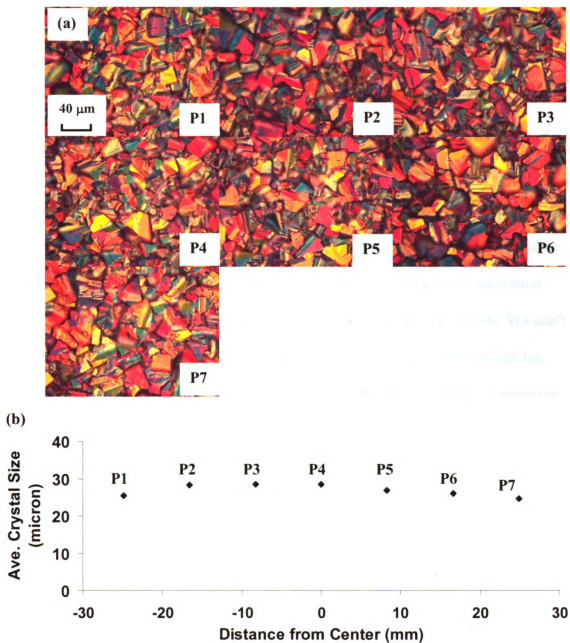


Figure 5-24: (a) Microscopy photographs from taken at points P1 to P7 across the diamond film of SZ-2inch-1mm-045. (b) Calculated diamond grains sizes at points from P1 to P7 and their size distributions. The calculated standard deviation of the grains sizes is 1.57 μm.

Chapter 6 Intrinsic Stresses of the Polycrystalline Diamond Film

This chapter describes work to understand and develop suitable mechanisms of controlling the intrinsic stress in the as grown polycrystalline diamond film. As mentioned in the Chapter 2, the intrinsic stress within a freestanding CVD diamond film is a complex issue with regard to its causes. However, this issue may be simplified if we look at the outcome of a film to which side it bends, the growth side or the nucleation side? It is like we watch two teams at tug of war and decide which team to win. We don't need to know who is in the team. If a gradient of the intrinsic stress exists through the thickness of the film, the film will bend towards the side that has the lower compressive stress or greater tensile stress. Similarly for the stress, we do not need to know the type of stress in the film. Rather, it is the variation in the stress across the thickness of the film that determines the final bowing of the film. Specifically, the side of the diamond film to which it bows (concave shape) is more tensile stress while on the other side the stress is less tensile (or more compressive).

In a general deposition process, the feed gas composition is usually kept constant during the growth for most of the plasma CVD diamond film deposition procedure. The substrate temperature, the area of the substrate covered, and the overall plasma conditions are also kept from changing during the experiment. However, the diamond crystal size naturally gets bigger along the growth direction, with the biggest increase in size

occurring early in the growth and then the size changing more slowly as columnar growth dominates. The increase in crystal size also naturally reduces the impurity and defect level due to the reduction in possible spaces for impurities and defects at the boundary between crystals. In another word, if the diamond crystal size doesn't change over the time and if we exclude the different formation mechanism of the nucleation layer, the statistical impurities and defects would be the same everywhere inside the film. Then we have reason to believe that the intrinsic stresses from every part of the film would also be the same and they would be completely canceled out. That means the film would not bend to either side of the film and it would be completely flat. So the first major way to reduce the bowing of the film is to keep the deposition conditions as uniform as possible both spatially across the substrate and temporally during the deposition process.

The literature on intrinsic stress in deposited CVD diamond contains useful information on ways to control the bowing of the deposited films. The stress in the films is generally found to be compressive on the nucleation side of the grown film [36, 41, 152]. The compressive region is in a thin layer of a few microns thick than consists of the region where the individual diamond crystals that started to grow coalesced into a continuous film [45]. The rest of the film grown above this coalescence layer is generally stressed in a tensile manner [41, 45, 152, 153]. The general trends for changing the tensile stress are that (1) reducing the methane concentration leads to increased tensile stress [41, 45] and (2) increasing the deposition temperature increases the tensile stress [41, 140, 154], though we may expect a reverse relation when the substrate temperature goes as high as 1200 °C and beyond. The films of diamond that are deposited and removed from the underlying silicon substrate often exhibit a bowing due to a gradient in

the intrinsic stress from the nucleation to the growth side. The bowing is such that the film is concave as viewed from the growth side. To produce this bowing there is a gradient in the stress with the top (or growth side) more tensile than the bottom (or nucleation side).

The research literature describes ways to minimize the intrinsic stress as the film grows such that the bowing is controlled. One technique is to reduce the probability of forming the major compressive stress in the thin coalescence layer of the film by stopping the deposition process at about the time the film coalesces. At this time the film is annealed at 900 °C for about 12 hours in a hydrogen/argon (7% hydrogen in argon) chamber atmosphere with the plasma off. This annealing has been shown to reduce the stress generation during subsequent growth [140]. A second technique is to vary the growth conditions such that the tensile stress is tailored as the film grows. A technique that is reported in the literature is to reduce the deposition temperature as the film grows such that the tensile stress is less on the growth side of the film than in the bulk of the film near the nucleation side [37]. A third important technique is to deposit the film with as uniform a temperature as possible [155]. This uniformity is both spatially and temporally. It is interesting to note that even if the spatial temperature is uniform, a time variation of the deposition temperature (increasing with time) would produce a film that is more tensile on the growth side and it would bend concave as viewed from the top (growth) side.

Another observation in some of the deposited films is a saddle shape formed by the diamond film after it is released from the silicon substrate. One possible explanation for this behavior is that the stress is not phi symmetric. It is speculated that one way to

get better phi symmetry, especially with respect to stress, is to rotate the substrate during the deposition.

6.1 Input and reactor parameters

The techniques to be employed to control the intrinsic stress include:

- 1) obtaining a uniform temperature profile across the substrate during deposition;
- 2) obtaining uniform temperature versus time during the deposition process;
- 3) varying the growth parameters (either substrate temperature, methane or argon gas composition) during the growth to reduce or eliminate bowing;

6.2 Output variables

A simple method of measuring the intrinsic stress is to measure the amount of film bending, or the curvature of a freestanding film. In considering that thin freestanding diamond film may be easily broken into smaller pieces during the wet etching and film handling, all diamond films are also measured for its curvature while they are still on the silicon wafer before the wet etching is carried out. This is why the current method of film stresses calculation is adapted as shown in Chapter 3. The curvature of the diamond film while it is still on the silicon wafer actually becomes the one used for film stress calculations. As has been mentioned in Chapter 3, it is the total stress that is extracted and calculated from the curvature of the diamond film while it is still attached to silicon wafer. The thicknesses of the diamond film and the silicon wafer are also needed for the calculation.

It has been noticed that different values of Young's moduli for CVD polycrystalline diamond films have been used by researchers in the past. In considering the high optical quality CVD diamond films that are deposited, the constant of the biaxial Young's moduli for CVD polycrystalline diamond films is taken as 1345 Gpa. A few comparisons of the values of Young's moduli among the researchers are made below showing the reasons why this value is picked for this study. The stiffness of the polycrystalline diamond films is found to decrease from 954 Gpa to 532 Gpa when a higher concentration of methane is used during the deposition [156]. Using the methane concentration as the sole condition may not be sufficient to establish a unique relation that produces desired polycrystalline diamond film properties including its Young's modulus. Still, Peng et al.'s [156] discovery indicated a reverse relationship between the Young's modulus of the polycrystalline diamond film and its impurities. Roy et al. [49] took a biaxial average of Peng et al.'s Young's moduli values with the result that a value of 667 Gpa was obtained for a relatively dark and thin diamond film. Noguchi et al. [157] and Rajamani et al. [45] also stated that the Young's modulus of CVD diamond films decreases with increasing nondiamond carbon content. The calculated biaxial Young's moduli values by Rajamani et al. are 971 Gpa and 800 Gpa for CH₄ content of 1% and 2% at a substrate temperature of 800 °C. The impurities, evaluated by Raman provided in their paper, are significantly higher than all of the samples provided in this research. The constant of the biaxial Young's modulus for single crystal silicon wafer is taken as 180 Gpa.

In order to obtain the quantitative measurement of intrinsic stress, the stress caused by thermal expansion difference between the diamond film and the silicon wafer

should be taken into account. It is believed that the different grains sizes along the radial direction may also contribute to the film stresses as discussed in the introduction of this chapter. Therefore the radial and circumferential distribution of the grains sizes are also recorded and studied similar to the way done in Chapter 5 for the grains sizes uniformity study. Other variable that is considered in this study is the diameter of the diamond film since larger diameter freestanding films curve more under the same stress. The temperature gradient across the diamond film during the deposition is also measured, recorded and studied.

6.3 The measurements of radius of curvature and other parameters for stress calculation

The curvature measurement or to be exact, the measurement of the radius of curvature introduced here is straight forward. The measurement is carried out by using the Solartron linear encoder. However, different from measuring the thickness of the silicon wafer or the composite piece of silicon wafer and diamond film, the point stage is replaced by its own smooth and flat base as the stage. First the probe is zeroed on the surface of the flat base as the reference of measuring the heights. Then the composite piece of wafer and film is laid on the flat base under the probe with the diamond film growth surface facing down on the base. The probe is then rested on the backside surface of the silicon wafer. Figure 6-1 illustrates how the diamond film specimen and probe are positioned. The measured quantity is δ (see Figure 6-1), the distance between a point on the top surface (the backside surface of the silicon wafer) and the base.

There are total 21 points on top of the surface that are to be measured for the distance δ . These points are chosen to be the same set of points as were used for film

thickness measurement as shown earlier in Figure 3-19. Each of these points is 5 mm apart. From point 1 to point 11, all 11 points are on a straight line that is across the center of the wafer at its diameter. The rest of the points form another diameter line perpendicular to the first line. Therefore two sets of curvature data that are perpendicular to each other. Each set of the curvature data then can be geometrically fit to a circle. The radius of this circle can be extracted from the geometrical equation of the circle.

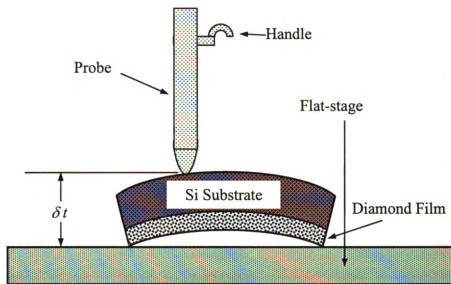


Figure 6-1: Illustration of measuring the distance from the back side surface (the top surface) of the silicon wafer to the top surface of the base. Please note the diamond film is on the bottom side of the measured piece.

Table 6-1 shows an example of two measured curvature data sets for sample SZ-2inch-1mm-065A. The curvature data are plotted in Figure 6-2 using MS Excel to illustrate the geometrical relationship between the point on the backside surface of silicon wafer and the distance from the center of silicon wafer. This Excel plot clearly shows that the surface curves of the backside of the silicon wafer and diamond film can be fitted to a

circle for the two perpendicular diameter on the wafer. The radius of the curvature for both directions are nearly the same.

Table 6-1: An example of 2-set measured curvature data on the backside surface of the silicon wafer by using Solartron linear encoder. These are real data from sample SZ-2inch-1mm-065A.

1 st Set Points	Distance From Center (mm)	Height From Base (mm)	2 nd Set Points	Height From Base (mm)
1	-25	1.11710	12	1.13020
2	-20	1.20730	13	1.22925
3	-15	1.29285	14	1.31395
4	-10	1.34250	15	1.35670
5	-5	1.37340	16	1.38070
6	0	1.38420	6	1.38420
7	5	1.37235	17	1.36910
8	10	1.34345	18	1.33910
9	15	1.28780	19	1.27570
10	20	1.22160	20	1.17430
11	25	1.11680	21	1.08035

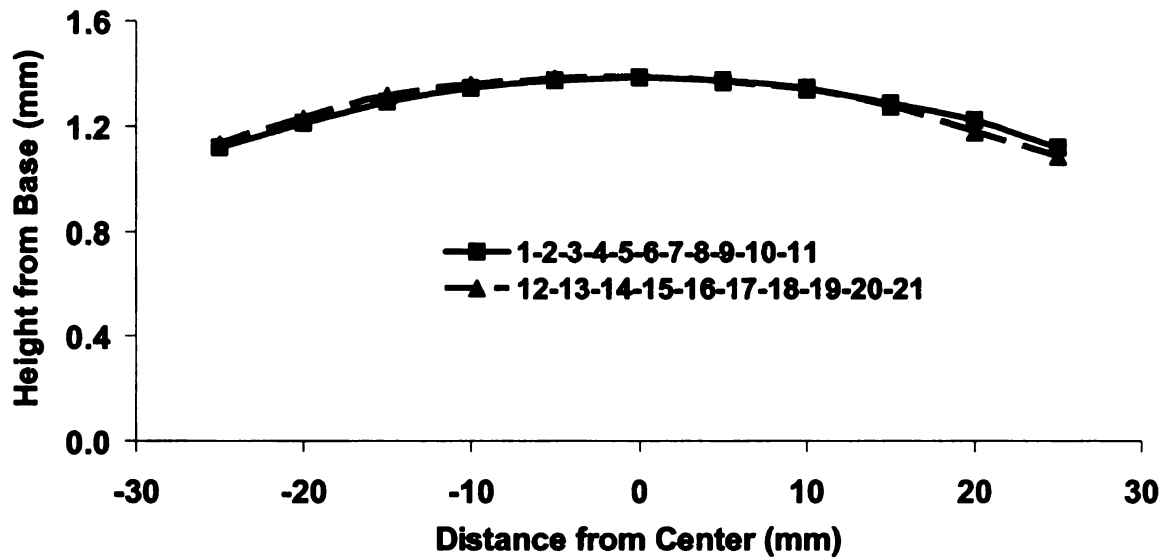


Figure 6-2: A simple plot to show geometrical relationship between the curvature data points and the distance from the center of the silicon wafer.

A m-file script run under Matlab 7.1 is used to fit each set of data into a circle that minimizes the geometric distance from the data points to the corresponding fit-points on the circle. This m-file script was written by Richard Brown and was submitted to MATHWORKS.COM on May 20th, 2007 [158]. The algorithm of this script is based on the paper “*Least-squares fitting of circles and ellipses*” published by W. Gander et al. on BIT Numerical Mathematics in 1994 [159]. The technique of nonlinear least squares is used to fit circles to 2D data. The major function that fits the circle is named [FITCIRCLE.M](#) and it is called by a main function, which inputs the data and plots the results. The main function, called [FITCIRCLE-DEMO.M](#), is also provided by Richard Brown and can be downloaded at MATHWORKS.COM. Though the original function does not provide the capability to calculate the radius of the fit circle, a simple line “*eval r*” can be inserted into the script after line “*plot*” for this purpose.

These two Matlab functions (Appendix A and Appendix C) including a modification of a set of typical input data (from sample SZ-2inch-1mm-065A, the 2nd set points) and the insertion of the m-file code that evaluates the radius of the curvature for this research (Appendix B) are duplicated. The Matlab plot (zoom-in view) of the 2nd set data points and part of the best geometric fit circle is shown in Figure 6-3 as an example of the results. For this set of data, the radius of the curvature was found to be $\underline{r = 1.0973e+003 \text{ mm}}$.

The last parameters needed for stress calculation are the thicknesses of the diamond film and silicon wafer. The thickness of the diamond film was taken from the average thickness calculated from weight gain, the Eq. 3-10. For the bare silicon wafer, the thickness was measured using the linear encoder. As it was shown in section 3.7.1, the thickness measurements using the linear encoder for silicon wafer were done at 21 points (Figure 3-19, a). Therefore the thickness of the silicon wafer before the diamond film deposition is simply the average thickness of these 21 points.

6.4 The intrinsic stress control with methane concentration and temperature variation versus time

The following relationships are investigated based on experiments in this section: (1) can the intrinsic stress be controlled with methane concentration variation versus time and, (2) can the intrinsic stress be controlled with substrate temperature variation versus time. Attempts will also be made to relate the methane concentration and substrate temperature variation to crystal grain size gradient versus thickness in the polycrystalline films. The gradient of the grain size is defined by the grain size changing per unit film thickness.

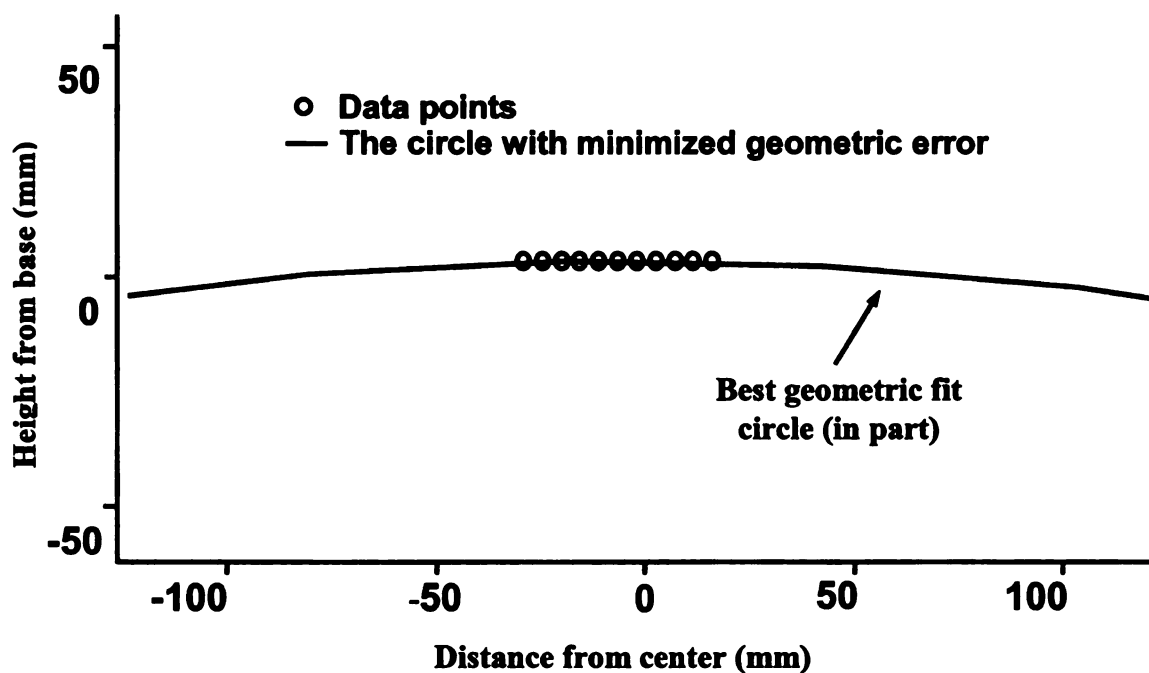


Figure 6-3: The Matlab plot of the data points (small circles represented dots) and the partial best geometric fit circle (the line).

For investigations of varying the input parameters such as the methane concentration, first a diamond film is deposited at a moderately high pressure and relatively low methane gases composition, such as 140 Torr and 4 or 6 sccm methane for 24 hours or 48hours. Then the crystal size is measured at the center of the wafer and around the edge of the wafer. Also the thickness of the diamond film and the bending of the wafer are measured. The substrate temperatures are managed to be in the same range of uniformity evaluated by their standard deviation following part 1) and part 2) in section 6.1. The impurity density is not precisely measured but only associated with methane concentration versus the total input gases as a preserved quantity to be discussed in the future. The next step is to grow another diamond film by increasing the methane flow rate gradually during the experiment starting from 4 sccm. It may be better to let the

film grow for about 12 hours before starting to increase the methane flow rate since we may want to wait until the crystal reaches a certain size for the reason of better quality. The final methane flow rate may be 6 or 8 sccm and it is to be determined by results and be modified from the experiments. Therefore if the experiment is to be 24 hours and the final methane flow rate is to be 6 sccm, the increase of methane flow rate can be set at 0.2 sccm per hour or 0.3 sccm per 2-hour or 1 sccm per 6-hour depends on the result. The procedure can also be used for the argon variation. For varying the substrate temperature, deposit a diamond film with substrate temperature lowered during the deposition. Measure the result to compare the film bending with the first film deposited at the common condition. A few experiments may be needed to complete the data set.

Table 6-2 includes experiments for intrinsic stress control with methane concentration variation versus time. Two different approaches are used to vary the methane concentrations in the feed gas. One is to increase the methane flow by a small amount every few hours while keeping the reactor pressure a constant. Experiment 2"-44, 2"-46 and 2"-51 belong to this approach. The other is to increase the methane flow rate by a larger amount, such as 2 sccm and staying much longer time for each increase while at the same time also increase the reactor pressure to match the methane increase. For example, we know that with 140 Torr reactor pressure and 4 sccm methane flow and that with 160 Torr pressure and 6 sccm methane good quality diamond film is obtained, so we can start with 140 Torr reactor pressure and 4 sccm methane flow for first 12 hours run then increase in the next step to 160 Torr reactor pressure and 6 sccm methane flow for a second 12 hour run and so on.



In order to properly simplify the substrate temperature to a single value instead of a series of values recorded during the diamond film growth, the recorded substrate temperatures at a certain spatial point are averaged over the runtime. Because of the time gap for each of the recorded data is not even, some are longer and some are shorter, and the substrate temperature may change over the deposition run time, the average temperature of the substrate is calculated based on the temperature distribution over the runtime. For example, if for the first 10-hour gap the temperature is measured once and is 900 °C and then for the next 30-hour gap the temperature is measured once and is 1100 °C, then the average temperature over time is,

$$T_{AVE.} = \frac{\sum_{i=1}^n t_i \cdot T_i}{\sum_{i=1}^n t_i} = \frac{10 \times 900 + 30 \times 1100}{40} = 1050^{\circ} C \quad \text{Eq. 6-1}$$

where n is the number of times the substrate temperature is recorded and the final average $T_{AVE.}$ reflects approximately the substrate temperature.

For the convenience of comparing the intrinsic stresses with regular runs, two groups of reference experiments ran under constant flow of CH₄ (4 and 6 sccm) are also included in Table 6-2. Even though efforts were made to control all other the deposition conditions to be the same in order to single out the methane influence on the film stress, not all of the experiments were successful. Both approaches ended up with samples with small intrinsic stresses and samples with medium and large intrinsic stresses. Two sets data were found with respect to growth conditions, especially substrate temperature. The first set of data is sample 2''-44 compared with the group reference sample 2''-43. The intrinsic diamond film stress is 565 Mpa by regular growth (sample 2''-43) with constant

methane concentration (4 sccm) in the feed gas. The stress is reduced to 441 Mpa for sample 2''-44 with methane concentration increasing from 4 sccm to 6.4 sccm during diamond growth. The second set of data is sample 2''-49 compared with the 2nd group reference sample 2''-50. The intrinsic diamond film stress calculated is 775 Mpa by regular growth (sample 2''-50) with constant methane concentration (6 sccm) in the feed gas. The stress is reduced to 517 Mpa for sample 2''-49 with methane concentration increasing from 6 sccm to 8.4 sccm during the diamond growth.

Sample name	Pressure (Torr)	CH4 (sccm)	Ave. Ts range over time (°C)	Time- Ave. of Ts over time (°C)	Ave. thickness (μm)	Ave. G. rate (μm/hr)	Ave. STD. DEV. of Ts over time (°C)	Ave. thickness non-uniformity (%)	Grain sizes P1-P7 STD. DEV. (μm)	Ave. Intrinsic stress (Mpa)
2"-44	140	4-6.4	969-947	953	36	1.01	27	14.8	NA	441
2"-46	140	6-8.4	965-972	960	93	1.94	34	11.0	4.52	344
2"-61	140, 160, 180	4,6,8	886-1051	980	149	2.07	62	7.3	9.77	418
2"-49	140	6-8.4	967-1045	1006	109	2.27	27	12.6	6.35	517
2"-51	140	6-7.6	995-1019	1020	85	2.09	18	9.7	0.94	586
2"-58A	140, 160	4, 6	947-993	960	31	1.28	59	3.9	0.48	616
2"-59A	140, 160	4, 6	952-1039	994	30	1.27	65	10.4	0.21	677
1st Group Ref.										
2"-37	140	4	920-894	914	29	0.60	47	14.7	2.57	433
2"-43	140	4	992-954	952	19	0.53	28	18.0	NA	565
2"-60	140	4	907-934	919	11	0.60	53	15.5	0.36	720
2nd Group Ref.										
2"-45	140	6	971-952	954	75	1.57	13	7.0	1.57	338
2"-50	140	6	1024-999	1004	26	2.15	31	10.7	0.42	775
2"-52A	140	6	1011-1023	1016	91	1.89	34	10.7	2.74	500
2"-52	140	6	1011-1030	1022	201	2.09	24	9.1	5.66	515
2"-54A	140	6	932-940	936	63	1.70	42	11.1	2.63	455
2"-62	140	8	991-1017	1001	70	2.93	39	11.1	3.52	645

Table 6-2: Experiments for intrinsic stress control with methane concentration variation versus time. Two groups of reference experiments ran under constant flow of CH₄ (4 and 6 sccm) are included in this table for comparison of their intrinsic stresses in the film. Other conditions that may be influential to the intrinsic stress are also included.

One may conclude the substrate temperature dependence of the diamond film intrinsic stress from Table 6-2. In Table 6-2, the 'Ave. T_s range over time' is the average substrate temperature (P1 to P7) from the beginning to the end of the experiment, the 'Time-Ave. of T_s over time' is the time-average of the spatial average (over P1 to P7) of substrate temperature mentioned in Eq. 6-1. The intrinsic stress appears to increase when substrate temperature increases. The plot in Figure 6-4 and Figure 6-5 agrees to this conclusion.

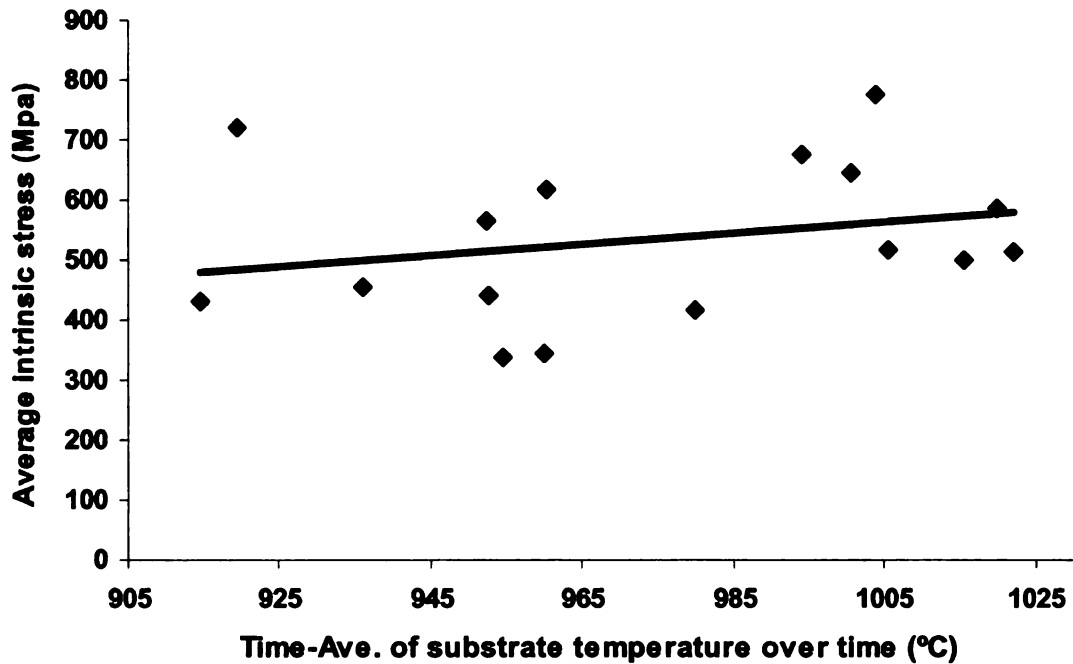


Figure 6-4: The relation of intrinsic stress versus the substrate temperature. All data are included in this plot from Table 6-2.

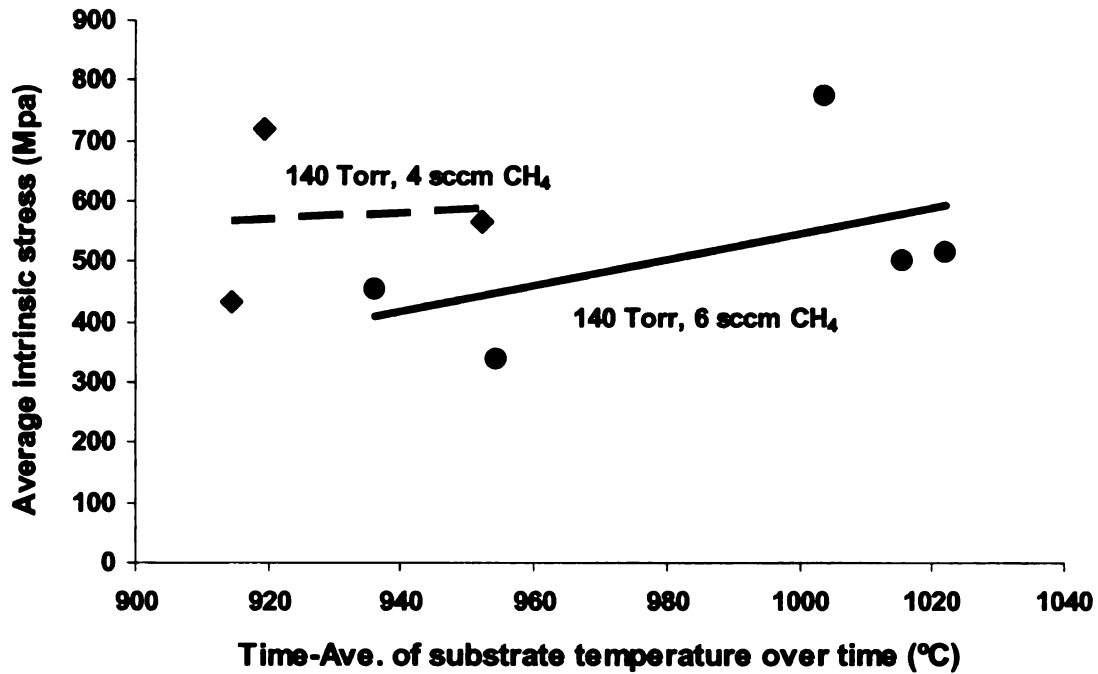
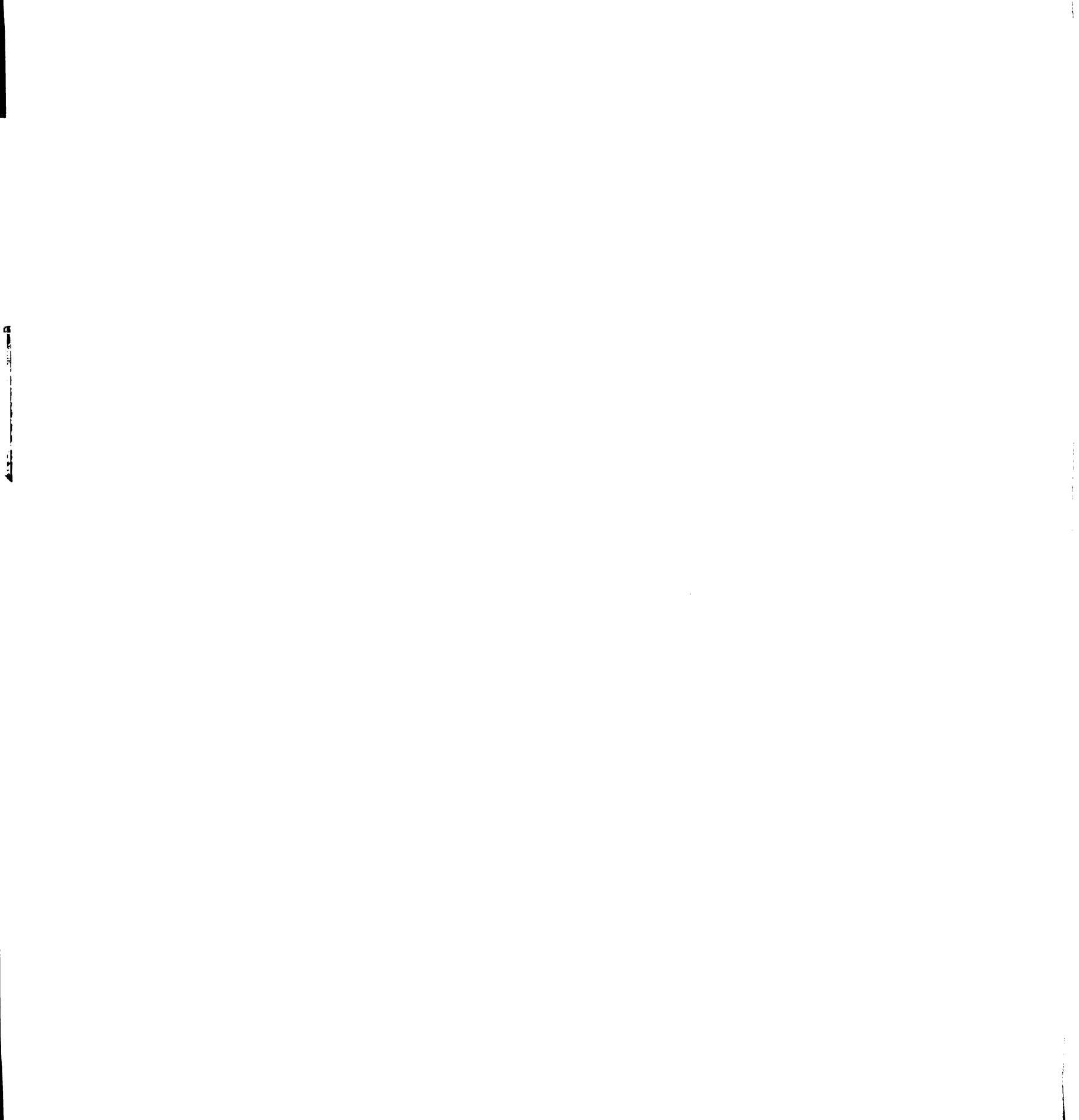


Figure 6-5: The relation of intrinsic stress vs. the substrate temperature. Reference data from Table 6-2 under the same experimental condition are classified as one plot.

Figure 6-4 includes all data from Table 6-2. The trendline indicates that the intrinsic stress increases when the substrate temperature increases. Figure 6-5 only includes the data in the same plot that the experiments are run under the same condition in order to avoid film stress influence come from other growth conditions. The trendlines from both 4 sccm and 6 sccm methane confirm that the intrinsic stress increases when substrate temperature increases despite the difference of the tilt angle of the trendline. It is understandable that the substrate temperature influence reduces when the methane concentration reduces due to less effect and impurities may involve in the diamond film growth. Initially we thought that the uniform substrate temperature and thickness, the grain size across the diamond film or even the thickness and the growth rate of the



diamond film may have influence to the film stress. The results from Table 6-2 show little of the relation between those conditions and the intrinsic stress.

Polycrystalline diamond films often break when the film stress reaches the limit or under some degrees of physical disturbances, such as back etching the silicon substrate in the chemical solution. However not all of these diamond films break easily. Table 6-3 shows all the samples that were not broken so the bowing of the diamond films were able to be measured after the silicon substrates were back etched. It may not be a coincidence that all calculated intrinsic stresses of these samples are very small as indicated in the caption. The intrinsic stresses are all smaller than 440 Mpa.

Sample name	Pressure (Torr)	CH4 (sccm)	Ar (sccm)	Ave. Ts range over time (°C)	Time-Ave. of Ts over time (°C)	Ave. thickness (μm)	Ave. G. rate (μm/hr)	Ave. STD. DEV. of Ts over time (°C)	Ave. thickness non-uniformity (%)	Ave. intrinsic stress (Mpa)
2"-35	140	4	0	932-931	927	95	1.98	34	20.25	336
2"-36	160	5	0	993-966	972	60	1.25	77	12.25	319
2"-37	140	4	0	920-894	914	29	0.60	47	14.7	433
2"-39	180	6	0	935-933	930	39	0.81	68	39.15	356
2"-42	180	8	0	963-974	971	122	2.54	55	30.45	354
2"-45	140	6	0	971-952	954	75	1.57	13	7.0	338
2"-46	140	6-8.4	0	965-972	960	93	1.94	34	11.0	344
2"-53	140	4	100	977-1017	996	125	2.60	15	5.25	394
2"-54	140, 160	6	0	932-1059	986	203	2.09	39	16.25	425
2"-58	140, 160, 180	4, 6	0	947-1015	987	56	1.17	69	60.9	423
2"-59	140, 160, 180	4, 6	100	952-1095	1037	100	2.09	55	28.65	401
2"-61	140, 160, 180	4, 6, 8	0	886-1051	980	149	2.07	62	7.3	418

Table 6-3: Samples were not broken during the chemical back etch process. It appears that samples tend to break during the chemical back etch process when the intrinsic stress is greater than 440 Mpa.

6.5 Evaluation of diamond film stress using Raman diamond peak shift and interpretation of stress data

In this section, we will evaluate the diamond film stress using the Raman diamond peak shift technique by simply following what was discussed in section 3.11.3. First the Raman diamond peak position for both the selected point of the as grown diamond film and the reference HPHT single crystal diamond are obtained from their spectra. Then the X-ray diffraction pattern of the film was measured and the intensity data of the X-ray diffraction pattern for each crystal plane was calibrated by dividing by the multiplicity (Table 3-4) of that plane. Next a normalization of the calibrated intensities to a total of 100% was done. Eq. 3-59, Eq. 3-61 and Eq. 3-63 were then used to calculate the biaxial stresses associated with each crystal plane. Finally the average of the stresses among the crystal planes was determined by using Eq. 3-67. It should be noted that the stress formula for singlet phonon is used due to the observation of the only single peaks of the spectra from these samples. The Raman spectrum can actually be separated into singlet and doublet spectra using polarized laser source and analyzing device with the Raman machine [147], however, the technique of using polarized Raman spectroscopy was not carried out here. In addition, the stress calculated is an average of the location due to the 30 μm spot size of the laser beam (most of the diamond grain sizes were less than 30 μm).

Table 6-4 shows the detailed data of calculations for every step mentioned above. The silicon substrates were back etched from the diamond film for all these three samples. The original X-ray diffraction patterns with intensities labeled for each peak (plane) of each diamond film sample are also given in Figure 6-6, Figure 6-7 and Figure

6-8. To fit the sample holder, the diamond film sample was broken into smaller piece about finger nail size. Therefore the texture of the diamond film was assumed to be the same everywhere for the same sample.

Based on the results in Table 6-4, local stresses in diamond film sometimes show compressive and sometimes show tensile. It appears that near the center of the diamond film tends to show tensile stress whereas near the edge of the diamond film tends to show compressive stress.

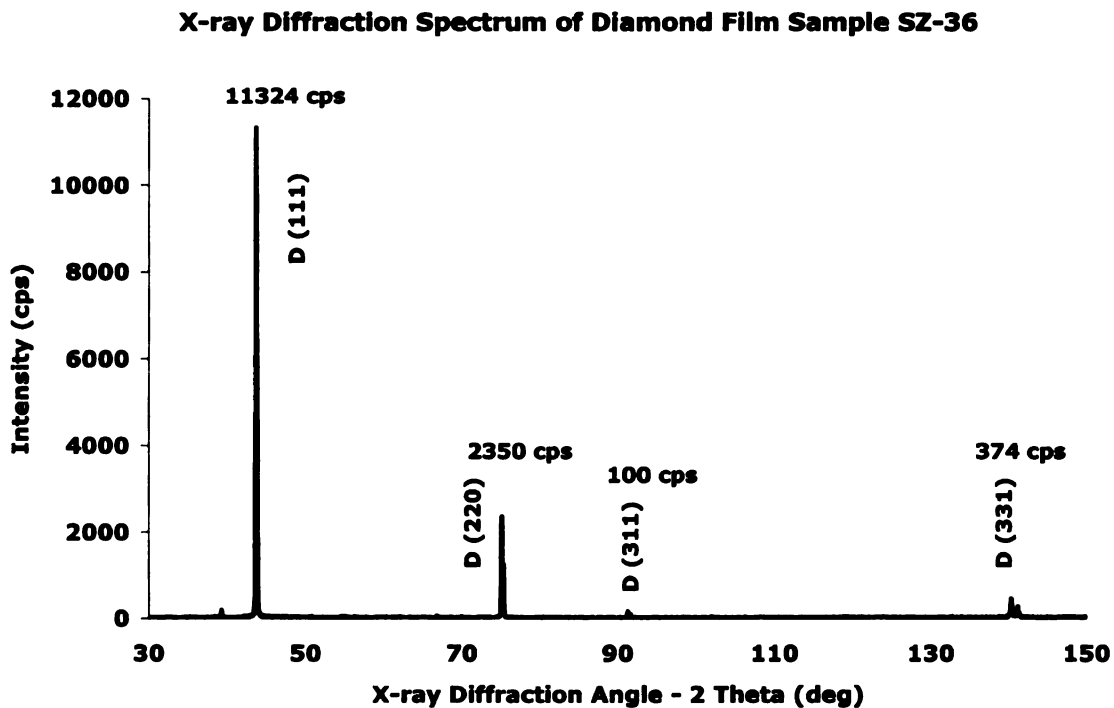


Figure 6-6: The X-ray diffraction spectrum of diamond film sample SZ-2inch-1mm-36. The intensities of each type diffraction plane are indicated in the figure.

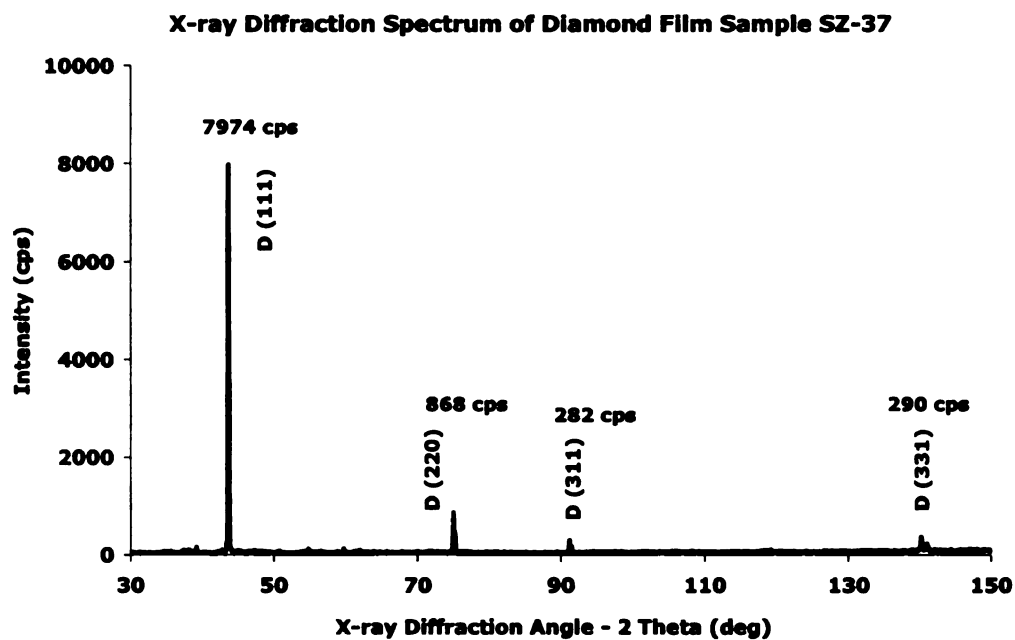


Figure 6-7: The X-ray diffraction spectrum of diamond film sample SZ-2inch-1mm-37. The intensities of each type diffraction plane are indicated in the figure.

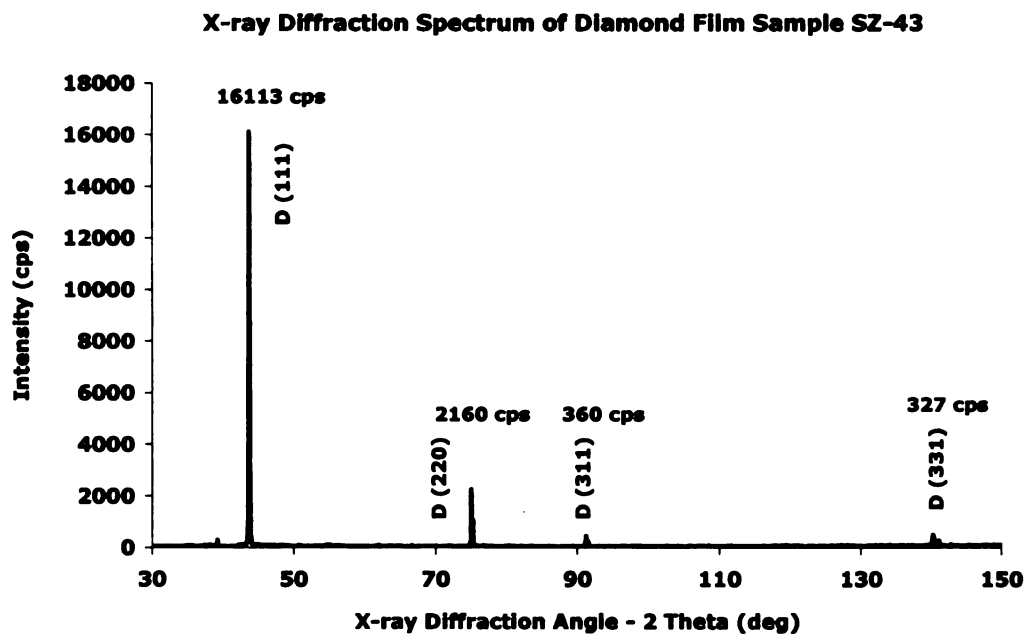


Figure 6-8: The X-ray diffraction spectrum of diamond film sample SZ-2inch-1mm-43. The intensities of each type diffraction plane are indicated in the figure.

Sample name	Pressure (Torr)	HPHT SCD Peak Ref. (cm ⁻¹)	Measured Diamond Peak (cm ⁻¹)	Raman Peak Shift ($\nu_s - \nu_0$) (cm ⁻¹)	Normalized Relative Intensities of X-ray Diffraction			Biaxial Stress Associated with the Crystal Plane (Mpa)			Local Ave. Intrinsic stress (Mpa)		
					(111)	(220)	(311)	(331)	(111)	(220)		(311)	(331)
2 ⁺ -36-P1 (edge)	160	1332.20	1332.49	0.29	0.87	0.12	0.00	0.01	-432	-316	-296	0.0	-414
P2		1332.20	1332.42	0.22	0.87	0.12	0.00	0.01	-328	-240	-224	0.0	-314
P3		1332.20	1331.79	-0.41	0.87	0.12	0.00	0.01	611	447	418	0.0	585
P4 (center)		1332.20	1331.90	-0.30	0.87	0.12	0.00	0.01	447	327	306	0.0	428
2 ⁺ -37-P1 (edge)	140	1332.20	1332.43	0.23	0.91	0.07	0.01	0.01	-343	-251	-235	0.0	-332
P2		1332.20	1332.17	-0.03	0.91	0.07	0.01	0.01	44.7	32.7	30.6	0.0	43
P3		1332.20	1332.03	-0.17	0.91	0.07	0.01	0.01	253	185	173	0.0	245
P4 (center)		1332.20	1332.23	0.03	0.91	0.07	0.01	0.01	-44.7	-32.7	-30.6	0.0	-43
2 ⁺ -43-P1 (edge)	140	1332.20	1332.33	0.13	0.91	0.08	0.01	0.01	-194	-142	-133	0.0	-188
P2		1332.20	1332.02	-0.18	0.91	0.08	0.01	0.01	268	196	184	0.0	260
P3		1332.20	1331.97	-0.23	0.91	0.08	0.01	0.01	343	251	235	0.0	332
P4 (center)		1332.20	1332.12	-0.08	0.91	0.08	0.01	0.01	119	87.2	81.6	0.0	116

Table 6-4: This table shows how diamond film stress is calculated for a local point. The growth conditions for these samples can be found in Table 6-2 and Table 6-3 in this chapter. Please note the coefficients of equations for calculating the stress associated with crystal planes are included in Eq. 3-59, Eq. 3-61 and Eq. 3-63.

Chapter 7 Conclusions and Future Work

In this research, investigations were devoted to increase the growth rate of polycrystalline diamond films on large area silicon substrates without trading off optical quality. For synthesizing colorless diamond films, the option of using an additive gas such as nitrogen is not an option. Higher pressure appears to be the only accessible approach for this purpose. Due to the nature of the plasma however, the shrinking size of the coverage of the substrate because of the pressure increasing produces a reduced uniformity when depositing diamond films. Fast growing diamond films at higher pressures with higher substrate temperatures brings about greater stress in the films that needs to be dealt with. As a result of this research, 1) the deposition parameter space for sufficient quality was defined in terms of the growth conditions including the reactor pressure and the methane concentration. A quality boundary was defined for the maximum rate that diamond films can be grown with acceptable optical quality. This identifies the operating window where high quality and high growth rate diamond film may grow in terms of variations in pressure and the methane concentration; 2) the diamond film thickness uniformity was significantly improved by controlling the substrate temperature uniformity and the addition of the argon gas in the feedgas; 3) the operating conditions were identified for uniform deposition of the polycrystalline diamond films at higher pressure above 100 Torr; 4) the reactor operating time was

prolonged by enhancing the fused silica bell jar cooling, reactor air cooling and substrate cooling; 5) a methodology of measuring and calculating the intrinsic stress was developed and a stress value for predicting film breaking was identified and additional major factors that influence the diamond film stress were identified.

7.1 Conclusion of this research

7.1.1 Conditions of high quality, fast growing polycrystalline CVD diamond films

This research successfully deposited large-area high-quality, uniform polycrystalline diamond films at higher pressures from 100 Torr to 180 Torr. A higher growth rate was obtained in this higher pressure regime. The deposition conditions for high growth rate, high quality polycrystalline diamond films are primary defined by the quality-acceptable line in Figure 4-21. Though it may not be the fastest growth conditions, the higher quality, whiter diamond film can be obtained with reasonable fast growth rates by increasing the reactor pressure. The quality-acceptable line is a boundary of where the near maximum speed diamond film can grow with acceptable optical quality. The acceptable diamond film quality usually shows an average FWHM value of less than 5.0 cm^{-1} for the diamond peak in the Raman spectrum and the optical transmission is above 60% in the visible light region after the diamond film is polished. The growth rate can be in excess $6.0 \text{ }\mu\text{m/hr}$ at 180 Torr and a methane concentration of about 2%. This is assuming that the substrate temperature is uniform across the substrate and at about $990 \text{ }^\circ\text{C}$ (or in between $950 \text{ }^\circ\text{C}$ and $1030 \text{ }^\circ\text{C}$) as indicated in Chapter 4 and Chapter 5. However under a lower reactor pressure of 140 Torr and methane concentration maximum of about 1.25% must be used to the achievable maximum

growth rate with good quality. The maximum growth rate at 140 Torr is less than 2.0 micron per hour with the same level of optical quality.

7.1.2 Improved diamond film uniformity

The key findings in this research regarding diamond film uniformity included the uniformity improvement of the substrate temperature and film thickness while maintaining a certain level of uniformity of film quality. The uniformity at the most basic level refers to the thickness of films, discs or plates. The uniformity of the diamond film also implies uniform quality across the film area, which also indicates that uniform diamond grain size and film texture is desired across the film area. If conditions are controlled correctly, samples with uniform thickness, uniform grain size distribution and uniform film texture can be obtained. Though substrate temperature doesn't determine uniform growth of the polycrystalline diamond film solely, it is used as a primary indicator for adjustments to achieve uniform deposition in the radial direction. In this research, the substrate holder design and the tuning of substrate holder position as illustrated earlier in Chapter 5 brought down the substrate temperature non-uniformity (depicted by the standard deviation of the substrate temperature across the diameter) to about 30 °C. Argon addition in the feed gas was determined to further bring down this value to about 15 °C or less. The thickness non-uniformity can be as small as 5% across the whole diamond film if all the techniques are applied. However the uniformity of the diamond film in every aspect including the thickness, grain sizes and optical quality became difficult to obtain when the reactor pressure reached 180 Torr in the 2.45 GHz microwave plasma reactor that was used for this study for deposition across 2 – 3 inch diameter substrates. One of the problems at the higher pressure of 180 Torr is that the

substrate temperature is higher due to the higher heat load and the temperature gradient also becomes much greater in radial direction. This occurs because of the substrate by the cooling stage becomes ineffective with the current substrate holder design of compensating the radial temperature gradients. The contacts between each substrate holder inserts in the set need to be improved if a similar design approach is kept.

7.1.3 Measuring and ways of reducing diamond film intrinsic stress

This research is the first to adapted Chu and Chuang's [132, 133] extended mechanical stress model for diamond film/silicon substrate stress calculation, which was initially studied by Stoney [122]. This extended stress model distinguishes the difference of internal stress from the external stress of Stoney's original model by treating the substrate/film as two welded rigid beams or plates. The biaxial stress model with the bending caused by the internal stress between two flexible beams is considered suitable for the bending study of diamond films grown on silicon wafers. The actual measurement is quite simple involving the measurement of the radius of curvature of the diamond film and silicon wafer and the measurement of the thickness of the diamond film and the silicon wafer. This was our primary quantitative method of measuring the diamond film stresses and the intrinsic stress calculated is the average of the diamond film on the silicon substrate.

A few approaches were tried as planned to reduce the diamond film intrinsic stress and intrinsic stress gradient. Some experiments provided indications that increasing the methane flow during the deposition may help to control the intrinsic stress from getting too high. Another finding was that the intrinsic stress evaluated by the curvature can be used for determining if a film will break during the chemical etch removal of the

silicon substrate. Specifically all the diamond films with calculated intrinsic stresses less than 440 Mpa while on the silicon substrate did not break during the wet chemical etching process to remove silicon wafer.

7.2 Suggestions for future work

A major improvement that is suggested for the future is improved cooling when the reactor pressure reaches 180 Torr and beyond. The deficiency of system cooling includes cooling of the substrate and the top of the fused silica bell jar. A fine control of the substrate temperature is also needed. All these became a bottle neck for the system to grow high optical quality, uniform and low stress polycrystalline diamond films at high deposition rates.

7.2.1 *Alternatives of microwave power supply*

It has been mentioned before that the plasma size became much smaller when reactor pressure reaches 180 Torr and higher than it is at 140 Torr. The plasma does not cover the two inch diameter substrate with sufficient uniformity even with the full microwave power provided by the power supply and the best tuning of the microwave plasma reactor. One suggestion is that a higher output microwave power supply is needed for the current reactor if it is used for two and three inch diameter substrates at high pressures. An output power of 10 kW should be enough.

A pulsed microwave power supply may be a plus over the CW microwave power supply. Studies from many researchers [13, 160, 161, 162, 163, 164, 165] indicate that pulsed microwave power may provide advantages at the same level of average power input for the same reactor. A larger size of the plasma was observed for pulsed

microwave power operation for the same level of average power as compared to an equal output power from a CW power supply. The heat deposited on the substrate per unit area can also be reduced by utilizing pulsed microwave power which is just what is needed for high pressure operation in CVD diamond deposition process.

7.2.2 Improving cooling deficiency and temperature control of the system at higher pressure

High reactor pressure microwave plasma operation produces tremendous heating of the substrate and that is initially why the active cooling process (cooled substrate holder) was introduced. Though this worked for a range of high pressure operations, the current cooling stage design appeared to become insufficient to remove the heat from the substrate when reactor pressure reaches beyond 180 Torr. There are actually two aspects to this problem. First, it is necessary to remove enough heat so that the substrate temperature falls into the desired temperature range. The second is to remove more heat from the center than from the edge of the substrate to compensate for the radial plasma heating gradient. Future designs of the cooling stage and the substrate holders or inserts should focus more on better contact in between the substrate holder pieces. In addition to that, a capability of finer control of substrate temperature would be a plus to solve this problem. As it has been known from the conclusion of Chapter 4, the substrate temperature is best to be controlled to 990 °C or a narrow range from 950 °C to 1030 °C for the highest growth rate and this range of substrate temperature is also good for best optical quality and for lower intrinsic stress.

Appendices

Appendix A Original source code for the `fitcircle_demo.m` file

```
%% Fitcircle Demonstration
% This publishable m-file demonstrates |fitcircle|, a function for finding
% the best fit circle by least squares. The implementation is based on
% *Least-Squares Fitting of Circles and Ellipses*, W. Gander, G.H. Golub,
% R. Strebler, BIT Numerical Mathematics, Springer, 1994

%% Fitting circles by minimising algebraic distance (linear least squares)
% Consider an algebraic representation of a circle in the plane:
%%
%
% 
$$F(\mathbf{x}) = a\mathbf{x}^T \mathbf{x} + \mathbf{b}^T \mathbf{x} + c = 0$$

%
% where
%
% 
$$a \neq 0, \quad \mathbf{b}, \mathbf{x} \in \mathbf{R}^2$$

%
% This equation can be minimised by linear least squares. The drawback to
% this approach is that geometrically, it's not clear what exactly is being
% minimised. In the following example it's clear that this does not always
% yield optimal results. |fitcircle| can be used to obtain this solution as
% follows:

% Set of points
x = [1 2 5 7 9 3; 7 6 8 7 5 7];

% Find the linear least squares fit
[zl, rl] = fitcircle(x, 'linear');

% And plot the results
t = linspace(0, 2*pi, 100);
plot(x(1,:), x(2,:), 'ro', ...
      zl(1) + rl * cos(t), zl(2) + rl * sin(t), 'b')
axis equal
axis([0 10 4 12])
title('Minimising the algebraic error')
legend('Data points', 'best fit minimising algebraic error')

%% Best Fit - minimising geometric distance
% The true best fit of a circle minimises the geometric error, i.e. the sum
% of the squares of distances
```

```

%
% 
$$\sum d_i^2 = \sum (\|\mathbf{z} - \mathbf{x}_i\| - r)^2$$

%
% where *z* is the centre of the circle, and r the radius. This is a
% nonlinear least squares problem and can be solved using fitcircle as
% follows (c.f. the algebraic fit):

% Set of points
x = [1 2 5 7 9 3; 7 6 8 7 5 7];

% Find the linear least squares fit
[zl, rl] = fitcircle(x, 'linear');

% Find the best geometric fit
[z, r] = fitcircle(x);

% And plot the results
t = linspace(0, 2*pi, 100);
plot(x(1,:), x(2,:), 'ro', ...
     zl(1) + rl * cos(t), zl(2) + rl * sin(t), 'b--', ...
     z(1) + r * cos(t), z(2) + r * sin(t), 'k')

axis equal
axis([-2 20 -2 14])
title('Minimising the geometric error')
legend('Data points', 'best fit minimising algebraic error', ...
      'Best fit minimising geometric error')

```

Appendix B Modified source code for the fitcircle_demo.m file

```
% Preface is not included to save space

% Set of points
% x = [1 2 5 7 9 3; 7 6 8 7 5 7];
x = [-25 -20 -15 -10 -5 0 5 10 15 20 25; 1.13020 1.22925 1.31395 1.35670 1.38070
1.38420 1.36910 1.33910 1.27570 1.17430 1.08035];

% Find the linear least squares fit
[zl, rl] = fitcircle(x, 'linear');

% Find the best geometric fit
[z, r] = fitcircle(x);

% And plot the results
t = linspace(0, 2*pi, 100);
% plot(x(1,:), x(2,:), 'ro', ...
% zl(1) + rl * cos(t), zl(2) + rl * sin(t), 'b--', ...
% z(1) + r * cos(t), z(2) + r * sin(t), 'k')
plot(x(1,:), x(2,:), 'ro', ...
      z(1) + r*cos(t), z(2)+ r*sin(t), 'k')

eval r

axis equal
axis([-3500 3500 -6000 10])
title('Best Geometric Fit Circle')
legend('Data points', ...
       'The circle with minimized geometric error')
```

Appendix C Original source code for the fitcircle.m file

```
function [z, r, residual] = fitcircle(x, varargin)
%FITCIRCLE least squares circle fit
%
% [Z, R] = FITCIRCLE(X) fits a circle to the N points in X minimising
% geometric error (sum of squared distances from the points to the fitted
% circle) using nonlinear least squares (Gauss Newton)
% Input
% X : 2xN array of N 2D points, with N >= 3
% Output
% Z : center of the fitted circle
% R : radius of the fitted circle
%
% [Z, R] = FITCIRCLE(X, 'linear') fits a circle using linear least
% squares minimising the algebraic error (residual from fitting system
% of the form  $ax^2 + b'x + c = 0$ )
%
% [Z, R] = FITCIRCLE(X, Property, Value, ...) allows parameters to be
% passed to the internal Gauss Newton method. Property names can be
% supplied as any unambiguous contraction of the property name and are
% case insensitive, e.g. FITCIRCLE(X, 't', 1e-4) is equivalent to
% FITCIRCLE(X, 'tol', 1e-4). Valid properties are:
%
% Property:          Value:
% -----
% maxits             positive integer, default 100
% Sets the maximum number of iterations of the Gauss Newton
% method
%
% tol                positive constant, default 1e-5
% Gauss Newton converges when the relative change in the solution
% is less than tol
%
% [X, R, RES] = fitcircle(...) returns the 2 norm of the residual from
% the least squares fit
%
% Example:
% x = [1 2 5 7 9 3; 7 6 8 7 5 7];
% % Get linear least squares fit
% [zl, rl] = fitcircle(x, 'linear')
% % Get true best fit
% [z, r] = fitcircle(x)
%
% Reference: "Least-squares fitting of circles and ellipses", W. Gander,
```

```

% G. Golub, R. Strebler - BIT Numerical Mathematics, 1994, Springer

% This implementation copyright Richard Brown, 2007, but is freely
% available to copy, use, or modify as long as this line is maintained

error(nargchk(1, 5, nargin, 'struct'))

% Default parameters for Gauss Newton minimisation
params.maxits = 100;
params.tol = 1e-5;

% Check x and get user supplied parameters
[x, fNonlinear, params] = parseinputs(x, params, varargin{:});

% Convenience variables
m = size(x, 2);
x1 = x(1, :);
x2 = x(2, :);

% 1) Compute best fit w.r.t. algebraic error using linear least squares
%
% Circle is represented as a matrix quadratic form
%  $ax^2 + b^2x + c = 0$ 
% Linear least squares estimate found by minimising  $Bu = 0$  s.t.  $\text{norm}(u) = 1$ 
% where  $u = [a; b; c]$ 

% Form the coefficient matrix
B = [x1.^2 + x2.^2, x1, x2, ones(m, 1)];

% Least squares estimate is right singular vector corresp. to smallest
% singular value of B
[U, S, V] = svd(B);
u = V(:, 4);

% For clarity, set the quadratic form variables
a = u(1);
b = u(2:3);
c = u(4);

% Convert to centre/radius
z = -b / (2*a);
r = sqrt((norm(b)/(2*a))^2 - c/a);

% 2) Nonlinear refinement to minimise geometric error, and compute residual
if fNonlinear

```

```

    [z, r, residual] = fitcircle_geometric(x, z, r);
else
    residual = norm(B * u);
end

% END MAIN FUNCTION BODY

% NESTED FUNCTIONS
function [z, r, residual] = fitcircle_geometric(x, z0, r0)
    % Use a simple Gauss Newton method to minimize the geometric error
    fConverged = false;

    % Set initial u
    u = [z0; r0];

    % Delta is the norm of current step, scaled by the norm of u
    delta = inf;
    nIts = 0;

    for nIts = 1:params.maxits
        % Find the function and Jacobian
        [f, J] = sys(u);

        % Solve for the step and update u
        h = -J \ f;
        u = u + h;

        % Check for convergence
        delta = norm(h, inf) / norm(u, inf);
        if delta < params.tol
            fConverged = true;
            break
        end
    end

    if ~fConverged
        warning('fitcircle:FailureToConverge', ...
            'Gauss Newton iteration failed to converge');
    end

    z = u(1:2);
    r = u(3);
    f = sys(u);
    residual = norm(f);

function [f, J] = sys(u)

```

```

%SYS Nonlinear system to be minimised - the objective
%function is the distance to each point from the fitted circle
%contained in u

% Objective function
f = (sqrt(sum((repmat(u(1:2), 1, m) - x).^2)) - u(3))';

% Jacobian
denom = sqrt( (u(1) - x1).^2 + (u(2) - x2).^2 );
J = [(u(1) - x1) ./ denom, (u(2) - x2) ./ denom, repmat(-1, m, 1)];
end % sys

end % fitcircle_geometric

% END NESTED FUNCTIONS

end % fitcircle

function [x, fNonlinear, params] = parseinputs(x, params, varargin)
% Make sure x is 2xN where N > 3
if size(x, 2) == 2
    x = x';
end

if size(x, 1) ~= 2
    error('fitcircle:InvalidDimension', ...
        'Input matrix must be two dimensional')
end

if size(x, 2) < 3
    error('fitcircle:InsufficientPoints', ...
        'At least 3 points required to compute fit')
end

% determine whether we are measuring geometric error (nonlinear), or
% algebraic error (linear)
fNonlinear = true;
switch length(varargin)
    % No arguments means a nonlinear least squares with default parameters
    case 0
        return

    % One argument can only be 'linear', specifying linear least squares
    case 1
        if strcmpi(varargin{1}, 'linear', length(varargin{1}))

```

```

    fNonlinear = false;
    return
else
    error('fitcircle:UnknownOption', 'Unknown Option')
end

% Otherwise we're left with user supplied parameters for Gauss Newton
otherwise
    if rem(length(varargin), 2) ~= 0
        error('fitcircle:propertyValueNotPair', ...
            'Additional arguments must take the form of Property/Value pairs');
    end

    % Cell array of valid property names
    properties = {'maxits', 'tol'};

    while length(varargin) ~= 0
        property = varargin{1};
        value = varargin{2};

        % If the property has been supplied in a shortened form, lengthen it
        iProperty = find(strcmpi(property, properties, length(property)));
        if isempty(iProperty)
            error('fitcircle:UnkownProperty', 'Unknown Property');
        elseif length(iProperty) > 1
            error('fitcircle:AmbiguousProperty', ...
                'Supplied shortened property name is ambiguous');
        end

        % Expand property to its full name
        property = properties{iProperty};

        switch property
            case 'maxits'
                if value <= 0
                    error('fitcircle:InvalidMaxits', ...
                        'maxits must be an integer greater than 0')
                end
                params.maxits = value;
            case 'tol'
                if value <= 0
                    error('fitcircle:InvalidTol', ...
                        'tol must be a positive real number')
                end
                params.tol = value;
        end % switch property
    end
end

```

```
    varargin(1:2) = [];  
end % while  
  
end % switch length(varargin)  
  
end %parseinputs
```

References

- [1] D. G. Goodwin, *Scaling Laws for Diamond Chemical-vapor Deposition. I. Diamond Surface Chemistry*, J. Appl. Phys. **74**, 6888 (1993).
- [2] J. E. Butler, R. L. Woodin, L. M. Brown, P. Fallon, *Thin Film Diamond Growth Mechanisms [and Comment]*, Phil. Trans.: Phys. Sci. & Eng. **342**, 209 (1993).
- [3] M. A. Cappelli, M. H. Loh, *In-situ Mass Sampling During Supersonic Arcjet Synthesis of Diamond*, Diam. Relat. Mat. **3**, 417 (1994).
- [4] J. C. Angus, E. A. Evans, *Nucleation and Growth Processes During the Chemical Vapor Deposition of Diamond*, Proceedings of Materials Research Society Symposium, Boston, 1994, pp. 385.
- [5] D. S. Dandy, M. E. Coltrin, *A Simplified Analytical Model of Diamond Growth in Direct Current Arcjet Reactors*, J. Mater. Res. **10**, 1993 (1995).
- [6] P. W. May, *Diamond Thin Films: A 21st-Century Material*, Phil. Trans. R. Soc. Lond. A **358**, 473 (2000).
- [7] P. K. Bachmann, D. Leers, H. Lydtin, *Towards a General Concept of Diamond Chemical Vapor Deposition*, Diam. Relat. Mat. **1**, 1 (1991).
- [8] P. K. Bachmann, H. J. Hagemann, H. Lade, D. Leers, F. Picht, D. U. Wiechert. In: C. H. Carter, G. Gildenblatt, S. Nakamura, R. J. Nemanich, eds. *Diamond, SiC, and Nitride Wide Band Gas Semiconductors*. MRS Symp. Proc. Vol 339. Pittsburgh: Materials Research Society, 1994, p 267
- [9] T. A. Grotjohn and J. Asmussen, Chapter 7: *Microwave Plasma-Assisted Diamond Film Deposition*, in: J. Asmussen and D. K. Reinhard (Eds.), *Diamond Films Handbook* Marcell Dekker, New York, 2001.
- [10] T. Mitomo, T. Ohta, E. Kondoh, K. Ohtsuka, *An Investigation of Product Distributions in Microwave Plasma for Diamond Growth*, J. Appl. Phys. **70**, 4532 (1991).
- [11] W. L. Hsu, *Gas-phase Kinetics during Microwave Plasma-assisted Diamond Deposition: Is the Hydrocarbon Product Distribution Dictated by Neutral-neutral Interactions?*, J. Appl. Phys. **72**, 3102 (1992).
- [12] W. A. Weimer, R. F. Cario, C. E. Johnson, *Examination of the Chemistry Involved in Microwave Plasma Assisted Chemical Vapor Deposition of Diamonds*, J. Mater. Res. **6**, 2134 (1991).

-
- [13] H. Chatei, J. Bougdira, M. Remy, P. Alnot, C. Bruch, J. K. Krüger, *Combined Effect of Nitrogen and Pulsed Microwave Plasma on Diamond Growth*, *Diam. Relat. Mat.* **6**, 505 (1997).
- [14] N. Setaka, *Diamond Synthesis from Vapor Phase and Its Growth Process*, *J. Mater. Res.* **4**, 664 (1989).
- [15] T. Lamara, M. Belmahi, G. Henrion, R. Hugon, J. Bougdira, M. Fabry, M. Rémy, *Correlation Between the Characteristics of a Pulsed Microwave Plasma Used for Diamond Growth and the Properties of the Produced Films*, *Surf. Coat. Technol.* **200**, 1110 (2005).
- [16] E. Vietzke, V. Philipps, K. Flaskamp, J. Winter, S. Vepereck, *Proceeding of the 10th International Symposium on Plasma Chemistry, ISPC'10, Bochum (Germany)*, 1991.
- [17] M. J. Wouters, J. Khachan, I. S. Falconer, B. W. James, *Production and Loss of H Atoms in a Microwave Discharge in H₂*, *J. Phys. D: Appl. Phys.* **31**, 2004 (1998).
- [18] S. Farhat, C. Findeling, F. Silva, K. Hassouni, A. Gicquel, *Role of the Plasma Composition at the surface on Diamond Growth*, *J. Phys. IV Fr.* **8** (Pr-7), 391 (1998).
- [19] A. Gicquel, M. Chenevier, K. H. Hassouni, A. Tserepi, M. Dubus, *Validation of Actinometry for Estimating Relative Hydrogen Atom Densities and Electron Energy Evolution in Plasma Assisted Diamond Deposition Reactors*, *J. Appl. Phys.* **83**, 7504 (1998).
- [20] A. C. Metaxas and R. J. Meredith, *Industrial Microwave Heating*, IEE Power Engineering Series 4, Peter Peregrinus LTD, London, 1983, pp. 192.
- [21] R. A. Akhmedzhanov, A. L. Vikharev, A. M. Gorbachev, V. A. Koldanov, D. B. Radishchev, *Studies of Pulse Operation Regime of Microwave Plasma CVD Reactor*, *Diam. Relat. Mat.* **11**, 579 (2002).
- [22] C. V. Raman, *On the Molecular Scattering of Light in Water and Color of the Sea*, *R. Soc. Lond. A* **101**, 64 (1922).
- [23] A. Gicquel, M. Chenevier, Y. Breton, M. Petiau, J. P. Booth, K. Hassouoni, *Ground State and Excited State H-atom temperatures in a Microwave Plasma Diamond Deposition Reactor*, *J. Phys. III Fr.* **6**, 1167 (1996).

-
- [24] A. Gicquel, K. Hassouni, Y. Breton, M. Chenevier, J. C. Cubertafon, *Gas Temperature Measurements by Laser Spectroscopic Techniques and by Optical Emission Spectroscopy*, *Diam. Relat. Mat.* **5**, 366 (1996).
- [25] T. A. Grotjohn, J. Asmussen, J. Sivagnaname, D. Story, A. L. Vikharev, A. Gorbachev, A. Kolysko, *Electron Density in Moderate Pressure Diamond Deposition Discharges*, *Diam. Relat. Mat.* **9**, 322 (2000).
- [26] K. P. Kuo and J. Asmussen, *An Experimental Study of High Pressure Synthesis of Diamond Films Using a Microwave Cavity Plasma Reactor*, *Diam. Relat. Mat.* **6**, 1097 (1997).
- [27] K. P. Kuo, *Microwave Assisted Plasma CVD of Diamond Films Using Thermal-like Plasma Discharge*, Ph.D. thesis at Michigan State University, Department of Electrical and Computer Engineering (1997).
- [28] A. Tallaire, J. Achard, F. Silva, R. S. Sussmann, A. Gicquel, *Homoepitaxial Deposition of High-quality Thick Diamond Films: Effect of Growth Parameters*, *Diam. Relat. Mat.* **14**, 249 (2005).
- [29] V. Mortet, A. Kromka, R. Kravets, J. Rosa, V. Vorlicek, J. Zemek, and M. Vanecek, *Investigation of Diamond Growth at High Pressure by Microwave Plasma Chemical Vapor Deposition*, *Diam. Relat. Mat.* **13**, 604 (2004).
- [30] T. Teraji, S. Mitani, and T. Ito, *High Rate Growth and Luminescence Properties of High-quality Homoepitaxial Diamond (100) Films*, *Phys. Stat. Sol.* **198**, 395 (2003).
- [31] C. S. Yan, Y. K. Vohra, H. Mao, and R. J. Hemley, *Very High Growth Rate Chemical Vapor Deposition of Single-crystal Diamond*, *P.N.A.S.* **99**, 12523 (2002).
- [32] J. Wei and Y. Tzeng, *Critical Process Parameters for High-Rate Deposition of Diamond by Hot-Filament CVD Technique*, *Diam. Films and Tech.* **5**, 79 (1995).
- [33] O. A. Williams and R. B. Jackman, *High Growth Rate MWPECVD of Single Crystal Diamond*, *Diam. Relat. Mat.* **13**, 557 (2004).
- [34] T. H. Chein, J. Wei, and Y. Tzeng, *Synthesis of Diamond in High Power-density Microwave Methane/Hydrogen/Oxygen Plasma at Elevated Substrate Temperatures*, *Diam. Relat. Mat.* **8**, 1686 (1999).
- [35] F. M. d'Heurle and J. M. E. Harper, *Note On the Origin of Intrinsic Stresses in Films Deposited via Evaporation and Sputtering*, *Thin Solid Films* **171**, 81 (1989).

-
- [36] S. Kamiya, M. Sato, M. Saka, and H. Abe, *Residual Stress Distribution in the Direction of the Film Normal in Thin Diamond Films*, J. Appl. Phys. **86**, 224 (1999).
- [37] J. K. Lee, Y. J. Park, K. Y. Eun, Y. J. Baik, and J. W. Park, *Synthesis of Crack-free Thick Diamond Wafer by Step-down Control of Deposition Temperature*, J. Mater. Res. **15**, 29 (2000).
- [38] *Thermophysical Properties of Matter: Vol. 13: Thermal Expansion of Nonmetallic Solids*, edited by Y. S. Touloukian, R. K. Kirby, R. E. Taylor, and T. Y. Lee (Plenum, New York, 1977).
- [39] D. J. Pickrell, K. A. Kline, and R. E. Taylor, *Thermal Expansion of Polycrystalline Diamond Produced by Chemical Vapor Deposition*, Appl. Phys. Lett. **64**, 2353 (1994).
- [40] D. Rats, L. Bimbault, L. Vandenbulcke, R. Herbin, K. F. Badawi, *Crystalline Quality and Residual Stresses in Diamond Layers by Raman and X-ray Diffraction Analyses*, J. Appl. Phys. **78**, 4994 (1995).
- [41] H. Windischmann, G. F. Epps, Y. Cong, and R. W. Collins, *Intrinsic Stress in Diamond Films Prepared by Microwave Plasma CVD*, J. Appl. Phys. **69**, 2231 (1991).
- [42] Q. H. Fan, J. Grácio and E. Pereira, *Evaluation of Residual Stresses in Chemical-vapor-deposited Diamond Films*, J. Appl. Phys. **87**, 2880 (2000).
- [43] G. A. Slack and S. F. Bartram, *Thermal Expansion of Some Diamondlike Crystals*, J. Appl. Phys. **46**, 89 (1975).
- [44] L. Maissel, *Thermal Expansion of Silicon*, J. Appl. Phys. **31**, 211 (1960).
- [45] A. Rajamani, B. W. Sheldon, S. Nijhawan, A. Schwartzman, J. Rankin, B. L. Walden, and L. Riester, *Chemistry-induced Intrinsic Stress Variations during the Chemical Vapor Deposition of Polycrystalline Diamond*, J. Appl. Phys. **96**, 3531 (2004).
- [46] M. Hempel and M. Härting, *Characterization of CVD Grown Diamond and Its Residual Stress State*, Diam. Relat. Mat. **8**, 1555 (1999).
- [47] N. G. Ferreira, E. Abramof, N. F. Leite, E. J. Corat, and V. J. Trava-Airoldi, *Analysis of Residual Stress in Diamond Films by X-ray Diffraction and Micro-Raman Spectroscopy*, J. Appl. Phys. **91**, 2466 (2002).

-
- [48] L. Wang, P. Pirouz, A. Argoitia, J. S. Ma, and J. C. Angus, *Heteroepitaxially Grown Diamond on a c-BN {111} Surface*, *Appl. Phys. Lett.* **63**, 1336 (1993).
- [49] D. Roy, Z. H. Barber and T. W. Clyne, *Strain Gradients Along the Growth Direction in Thin Diamond Film Deposited on Silicon Wafer*, *J. Appl. Phys.* **94**, 136 (2003).
- [50] W. Zhu, A. Inspektor, A. R. Badzian, T. McKenna, and R. Messier, *Effects of Noble Gases on Diamond Deposition from Methane-hydrogen Microwave Plasma*, *J. Appl. Phys.* **68**, 1489 (1990).
- [51] D. Zhou, D. M. Gruen, L. C. Qin, T. G. McCauley, and A. R. Krauss, *Control of Diamond Film Microstructure by Ar Additions to CH₄/H₂ Microwave Plasmas*, *J. Appl. Phys.* **84**, 1981 (1998).
- [52] R. Ramamurti, V. Shanov, R. N. Singh, S. Mamedov, and P. Boolchand, *Raman Spectroscopy study of the Influence of Processing Conditions on the Structure of Polycrystalline Diamond Films*, *J. Vac. Sci. Technol. A* **24**, 179 (2006).
- [53] A. N. Goyette, J. E. Lawler, L. W. Anderson, D. M. Gruen, T. G. McCauley, D. Zhou, and A. R. Krauss, *C₂ Swan Band Emission Intensity As A Function of C₂ Density*, *Plasma Sources Sci. Technol.* **7**, 149 (1998).
- [54] V. Shogun, A. Tyablikov, St. Schreiter, W. Scharff, T. Wallendorf, S. Marke, *Emission Actinometric Investigations of Atomic Hydrogen and CH Radicals in Plasma-enhanced Chemical Vapor Deposition Processes of Hexamethyldisiloxane*, *Surface and Coatings Technology* **98**, 1382 (1998).
- [55] J. Zhang, *Experimental Development of Microwave Cavity Plasma Reactors for Large Area and High Rate Diamond Film Deposition*, Ph.D. thesis at Michigan State University, Department of Electrical and Computer Engineering (1993).
- [56] W. S. Huang, D. T. Tran, J. Asmussen, T. A. Grotjohn, D. Reinhard, *Synthesis of Thick, Uniform, Smooth Ultrananocrystalline Diamond Films by Microwave Plasma-assisted Chemical Vapor Deposition*, *Diam. Relat. Mat.* **15**, 341 (2006).
- [57] D. M. Gruen, *Ultrananocrystalline Diamond in The Laboratory and in The Cosmos*, *Mat. Res. Soc. Bulletin* **26**, 771 (2001).
- [58] D. M. Gruen, X. Pan, A. R. Krauss, S. Liu, J. Luo, and C. M. Foster, *Deposition and Characterization of Nanocrystalline Diamond Films*, *J. Vac. Sci. Technol. A* **12**, 1491 (1994).
- [59] P. C. Redfern, D. A. Horner, L. A. Curtiss, and D. M. Gruen, *Theoretical Studies of Growth of Diamond (110) from Dicarbon*, *J. Phys. Chem.* **100**, 11654 (1996).

-
- [60] S. S. Zuo, M. K. Yaran, T. A. Grotjohn, D. K. Reinhard, J. Asmussen, *Investigation of Diamond Deposition Uniformity and Quality for Freestanding Film and Substrate Applications*, *Diam. Relat. Mat.* **17**, 300 (2008).
- [61] L. J. Mahoney, *The Design and Testing of A Compact Electron Cyclotron Resonant Microwave-Cavity Ion Source*, Ph.D. thesis at Michigan State University, Department of Electrical and Computer Engineering (1989).
- [62] J. A. Hopwood, *Macroscopic Properties of A Multipolar Electron Cyclotron Resonance Microwave-Cavity Plasma Source for Anisotropic Silicon Etching*, Ph.D. thesis at Michigan State University, Department of Electrical and Computer Engineering (1990).
- [63] F. C. Sze, *Design and Experimental Investigation of A Large Diameter Electron Cyclotron Resonant Plasma Source*, Ph.D. thesis at Michigan State University, Department of Electrical and Computer Engineering (1993).
- [64] M. A. Perrin, *The Electromagnetic Evaluation of A Compact ECR Microwave Plasma Source*, M.S. thesis at Michigan State University, Department of Electrical and Computer Engineering (1996).
- [65] P. U. Mak, *An Experimental Evaluation of A 12.5-cm Diameter Multipolar Microwave Electron Cyclotron Resonance Plasma Source*, Ph.D. thesis at Michigan State University, Department of Electrical and Computer Engineering (1997).
- [66] A. H. Khan, *Experimental Characterization of A Compact MPDR Plasma Source Employing Three Different Coupling Geometries*, M.S. thesis at Michigan State University, Department of Electrical and Computer Engineering (1999).
- [67] M. A. Perrin, *Investigation of A 17.8 cm Diameter End Feed Microwave Cavity Plasma Source With and Without A static Magnetic Field*, Ph.D. thesis at Michigan State University, Department of Electrical and Computer Engineering (2002).
- [68] W. S. Huang, *Microwave Plasma Assisted Chemical Vapor Deposition of Ultra-Nanocrystalline Diamond Films*, Ph.D. thesis at Michigan State University, Department of Electrical and Computer Engineering (2004).
- [69] D. T. Tran, *Synthesis of Thin and Thick Ultra-nanocrystalline Diamond Films by Microwave Plasma CVD System*, M. S. thesis at Michigan State University, Department of Electrical and Computer Engineering (2005).
- [70] H-H Lin, *Theoretical Formulation and Experimental Investigation of a Cylindrical Cavity Loaded with Lossy Dielectric Materials*, Ph.D. thesis at Michigan State University, Department of Electrical and Computer Engineering (1989).

-
- [71] <http://mathworld.wolfram.com/BesselFunctionZeros.html>, last updated: April 15, 2008/
- [72] M. Abramowitz and I. A. Stegun (Eds.), "Zeros." §9.5 in *Handbook of Mathematical Functions with Formulas, Graphs, and Mathematical Tables*, 9th printing. New York: Dover, pp. 370-374, 1972.
- [73] D. K. Cheng, §10-5 "Circular Waveguides" in *Field and Wave Electromagnetics*, 2nd Edition, Addison-Wesley Publishing Company, Inc., pp. 565, 1992
- [74] K. W. Hemawan, T. A. Grotjohn, D. K Reinhard, and J. Asmussen, *High Pressure Microwave Plasma Assisted CVD Synthesis of Diamond*, IEEE Conference on Plasma Science, 2008, Abstract 3E2
- [75] Ircon, Inc. 7300 N. Natchez Avenue, Niles, IL 60714, USA.
- [76] J. Hopwood, D. K. Reinhard and J. Asmussen, *Charged Particle Densities and Energy Distributions in A Multipolar Electron Cyclotron Resonant Plasma Etching Source*, J. Vac. Sci. Technol. A **8**, 3103 (1990).
- [77] J. Root and J. Asmussen, *Experimental Performance of A Microwave Cavity Plasma Disk Ion Source*, Rev. Sci. Instrum. **56**, 1511 (1985).
- [78] J. Asmussen and M. Dahimene, *The Experimental Test of A Microwave Ion Beam Source in Oxygen*, J. Vac. Sci. Technol. B **5**, 328 (1987).
- [79] X. Jiang, K. Schifffmann and C.-P. Klages, *Nucleation and Initial Growth Phase of Diamond Thin films on (100) Silicon*, Phys. Rev. B **50**, 8402 (1994).
- [80] C. L. Jia, K. Urban and X. Jiang, *Heteroepitaxial Diamond Films on Silicon (001): Interface Structure and Crystallographic Relations Between Film and Substrate*, Phys. Rev. B **52**, 5164 (1995).
- [81] J. Yang, Z. Lin, L. Wang, S. Jin, and Z. Zhang, *Local Hetero-epitaxial Diamond Formed Directly on Silicon Wafers and Observed by High-resolution Electron Microscopy*, J. Phys. D: Appl. Phys. **28**, 1153 (1995).
- [82] J. Yun and D. S. Dandy, *A Kinetic Model of Diamond Nucleation and Silicon Carbide Interlayer Formation During Chemical Vapor Deposition*, Diam. Relat. Mat. **14**, 1377 (2005).
- [83] B. R. Stoner and J. T. Glass, *Textured Diamond Growth on (100) β -SiC via Microwave Plasma Chemical Vapor Deposition*, Appl. Phys. Lett. **60**, 698 (1992).

-
- [84] U. F. Kocks, C. N. Tome, and H. R. Wenk, "*Texture and Anisotropy*", Cambridge University Press, Cambridge, 1998.
- [85] C. Detavernier and C. Lavoie, "*Influence of Pt Addition on the Texture of NiSi on Si (001)*", Appl. Phys. Lett. **84**, 3549 (2004).
- [86] W. L. Bragg, *The Specular Reflection of X-rays*, Nature **90**, 410 (1912).
- [87] W. L. Bragg, *The Diffraction Of Short Electromagnetic Waves By A Crystal*, Proc. Camb. Phil. Soc. **17**, part 1, 43 (1913).
- [88] <http://www.esfm.ipn.mx/~fcruz/ADR/Otros/INTRODUCTION-TO-XRD.PPT>
- [89] H. P. Klug and L. E. Alexander, *X-ray Diffraction Procedures*, John Wiley & Sons, New York, 1974, pp. 37, pp. 163.
- [90] K. J. Roe, J. Kolodzey, C. P. Swann, M. W. Tsao, J. F. Rabolt, J. Chen, and G. R. Brandes, *The Electrical and Optical Properties of Thin Film Diamond Implanted with Silicon*, Appl. Surf. Sci., **175-176**, 468 (2001).
- [91] H. Takashima and Y. Kanno, *Evaluation by Extended Huckel Method On the Hardness of the B-C-N Materials*, Sci. and Technol. of Advanced Materials **6**, 910 (2005).
- [92] V. M. Davidenko, S. V. Kidalov, F. M. Shakhov, M. A. Yagovkina, V. A. Yashin, and A. Ya. Vul, *Fullerenes As A Co-catalyst For High Pressure – High Temperature Synthesis of Diamonds*, Diam. Relat. Mat. **13**, 2203 (2004).
- [93] H. P. Klug and L. E. Alexander, *X-ray Diffraction Procedures*, John Wiley & Sons, New York, 1974, pp. 164
- [94] H. P. Klug and L. E. Alexander, *X-ray Diffraction Procedures*, John Wiley & Sons, New York, 1974, pp. 135 – pp. 166
- [95] H. P. Klug and L. E. Alexander, *X-ray Diffraction Procedures*, John Wiley & Sons, New York, 1974, pp. 162 and pp. 167 equations (3 – 75) to (3 – 78).
- [96] H. P. Klug and L. E. Alexander, *X-ray Diffraction Procedures*, John Wiley & Sons, New York, 1974, pp. 164.
- [97] http://en.wikipedia.org/wiki/Pole_figure
- [98] H. P. Klug and L. E. Alexander, *X-ray Diffraction Procedures*, John Wiley & Sons, New York, 1974, pp. 726.

-
- [99] H. P. Klug and L. E. Alexander, *X-ray Diffraction Procedures*, John Wiley & Sons, New York, 1974, pp. 726.
- [100] H. Feng, H. Zhu, W. Mao, L. Chen, and F. Lu, *Microstructure and Texture in Free-standing CVD Diamond Films*, Mater. Sci. Forum **495-497**, 1365 (2005).
- [101] C. Detavernier, A. S. Ozcan, J. Jordan-Sweet, E. A. Stach, J. Tersoff, F. M. Ross, and C. Lavoie, *An Off-normal Fibre-like Texture in Thin Films on Single-Crystal Substrates*, Nature **426**, 641 (2003).
- [102] T. F. Chang and L. Chang, *Diamond Deposition on Si (111) and Carbon Face 6H-Si-C (0001) Substrate by Positively Biased Pretreatment*, Diam. Relat. Mat. **11**, 509 (2002).
- [103] Chang Q. Sun, H. Xie, W. Zhang, H. Ye, and P. Hing, *Preferential Oxidation of Diamond {111}*, J. Phys. D: Appl. Phys. **33**, 2196 (2000).
- [104] T. F. Chang and L. Chang, *Highly Oriented Diamond Growth on Positively Biased Si Substrates*, J. Mater. Res. **16**, 3351 (2001).
- [105] A. L. Yee, H. C. Ong, L. M. Stewart, and R. P. H. Chang, *Development of Flat, Smooth (100) Faceted Diamond Thin Films Using Microwave Plasma Chemical Vapor Deposition*, J. Mater. Res. **12** 1796 (1997).
- [106] J. J. Schermer, W. J. P. van Enckevort, L. J. Giling, *Orientation Dependent Surface Stabilization on Flame Deposited Diamond Single Crystals*, J. of Crystal Growth **148**, 248 (1995).
- [107] <http://www.vcbio.science.ru.nl/en/fesem/applets/diamond/>, Source from John Schermer.
- [108] M. I. Mendelson, *Average Grain Size in Polycrystalline Ceramics*, J. Am. Ceram. Soc. **52**, 443 (1969).
- [109] D. K. Reinhard, T. A. Grotjohn, M. Becker, M. K. Yaran, T. Schuelke, and J. Asmussen, *Fabrication and Properties of Ultranan, Nano, and Microcrystalline Diamond Membranes and Sheets*, J. Vac. Sci. Technol. B **22**, 2811 (2004).
- [110] H. P. Klug and L. E. Alexander, *X-ray Diffraction Procedures*, John Wiley & Sons, New York, 1974, pp. 643.
- [111] H. G. Jiang, M. Ruhle, and E. J. Lavernia, *On the Applicability of the X-ray Diffraction Line Profile Analysis in Extracting Grain Size and Microstrain in Nanocrystalline Materials*, J. Mater. Res. **14**, 549 (1999).

-
- [112] Th. H. de Keijser, J. I. Langfor, E. J. Mittemeijer, and A. B. P. Vogels, *Use of the Voigt Function in a Single-line Method for the Analysis of X-ray Diffraction Line Broadening*, J. Appl. Crystallogr. **15**, 308 (1982).
- [113] G. S. Ristic, Z. D. Bogdanov, S. Zec, N. Romcevic, Z. D. Mitrovic, and S. S. Miljanic, *Effect of The Substrate Material on Diamond CVD Coating Properties*, Materials Chemistry and Physics **80** 529 (2003).
- [114] S. Marinkovic and S. Zec, *Characterization of Diamond Coatings by X-ray Diffraction, Raman Spectroscopy and Scanning Electron Microscopy*, J. Serb. Chem. Soc. **58**, 679 (1993).
- [115] M. Grus, A. J. Frydel, J. Bohdanowicz, and K. Zawada, *Chemical Vapor Deposition of Diamond Films in Hot Filament Reactor*, Cryst. Res. Technol. **36**, 961 (2001).
- [116] R. N. Chakraborty, D. K. Reinhard and P. D. Goldman, *Etching of Diamond Wafers with Electron Cyclotron Resonance Plasmas*, Extended Abstracts, Vol. 95-1, The Electrochemical Society, 396 (1995).
- [117] R. N. Chakraborty, *Post-Depositional Processing of Diamond Film Using Electron Cyclotron Resonance Plasmas*, Ph.D. thesis at Michigan State University, Department of Electrical and Computer Engineering (1995).
- [118] Logitech Ltd, Erskine Ferry Road, Old Kilpatrick, G60 5EU, Scotland.
- [119] I. Filinski, *The Effects of Sample Imperfections on Optical Spectra*, Physica Status Solidi (b) **49**, 577 (1972).
- [120] M. Thomas, W. J. Tropsf, *Optical Properties of Diamond*, Johns Hopkins APL Technical Digest **14**, 16 (1993).
- [121] M. Born, E. Wolf, *Principles of Optics*, 7th ed., Cambridge University Press, Cambridge, 1999.
- [122] G. G. Stoney, *The Tension of Metallic Films Deposited by Electrolysis*, Proc. R. Soc., London **82**, 172 (1909).
- [123] S. Timoshenko, *Analysis of Bi-Metal Thermostats*, J. Opt. Soc. Am. **11**, 233 (1925).
- [124] A. Brenner and S. Senderoff, *Calculation of Stress in Electrodeposits from the Curvature of a Plated Strip*, J. Res. Natl. Bur. Stand. **42**, 105 (1949).
- [125] N. N. Davidenkov, *Measurement of Residual Stress in Electrolytic Deposits*, Sov. Phys. – Solid State **2**, 2595 (1961).

-
- [126] R. W. Hoffman, *Physics of Thin Films – Advances in Research and Development*, Eds. G. Hass and R. E. Thun, Academic Press, New York, Vol. 3, 211 (1966).
- [127] K. Röhl, *Analysis of Stress and Strain Distribution in Thin Films and Substrates*, J. Appl. Phys. **47**, 3224 (1976).
- [128] G. E. Henein and W. R. Wagner, *Stresses Induced in GaAs by TiPt Ohmic Contacts*, J. Appl. Phys. **54**, 6395 (1983).
- [129] P. A. Flinn, D. S. Gardner, and W. D. Nix, *Measurement and Interpretation of Stress in Aluminum-Based Metallization as a Function of Thermal History*, IEEE Trans. Electron Devices ED-34, 689 (1987).
- [130] P. H. Townsend, D. M. Barnett, and T. A. Brunner, *Elastic Relationships in Layered Composite Media with Approximation for the Case of Thin Films on a Thick substrate*, J. Appl. Phys. **62**, 4438 (1987).
- [131] S. N. G. Chu, A. T. Macrander, K. E. Strage, and W. D. Johnston, Jr., *Misfit Stress in InGaAs/InP Heteroepitaxial Structures Grown by Vapor-phase Epitaxy*, J. Appl. Phys. **57**, 249 (1985).
- [132] S. N. G. Chu, *Elastic Bending of Semiconductor Wafer Revisited and Comments on Stoney's Equation*, J. Electrochem. Soc. **145**, 3621 (1998).
- [133] T. J. Chuang and S. Lee, *Elastic Flexure of Bilayered Beams Subject to Strain Differentials*, J. Mater. Res. **15**, 2780 (2000).
- [134] C. H. Hsueh, *Modeling of Elastic Deformation of Multilayers Due to Residual Stresses and External bending*, J. Appl. Phys. **91**, 9652 (2002).
- [135] I.C. Noyan and J.B. Cohen, *Residual Stress: Chapter 5 "Measurement by Diffraction and Interpretation"*, Springer-Verlag, New York, 1987.
- [136] J. W. Ager III and M. D. Drory, *Quantitative Measurement of Residual Biaxial Stress by Raman Spectroscopy in Diamond Grown on a Ti Alloy by Chemical Vapor Deposition*, Phys. Rev. B **48**, 2601 (1993).
- [137] I. A. Blech, I. Blech and M. Finot, *Determination of Thin-film Stresses on Round Substrates*, J. Appl. Phys. **97**, 113525 (2005).
- [138] Y. Zhang and Y. Zhao, *Applicability Range of Stoney's Formula and Modified Formulas for a Film/Substrate Bilayer*, J. Appl. Phys. **99**, 053513 (2006).

-
- [139] H. Windischmann and K. J. Gray, *Stress Measurement of CVD Diamond Films*, *Diam. Relat. Mat.* **4**, 837 (1995).
- [140] S. Nijhawan, S. M. Jankovsky, B. W. Sheldon, and B. L. Walden, *Reduction of Intrinsic Stresses During the Chemical Vapor Deposition of Diamond*, *J. Mater. Res.* **14**, 1046 (1999).
- [141] H. Li, B. W. Sheldon, A. Kothari, Z. Ban, and B. L. Walden, *Stress Evolution in Nanocrystalline Diamond Films Produced by Chemical Vapor Deposition*, *J. Appl. Phys.* **100**, 094309 (2006).
- [142] C. A. Klein, *How Accurate are Stoney's Equation and Recent Modifications*, *J. Appl. Phys.* **88**, 5487 (2000).
- [143] N. H. Zhang and J. J. Xing, *An Alternative Model for Elastic Bending Deformation of Multilayered Beams*, *J. Appl. Phys.* **100**, 103519 (2006).
- [144] C. A. Klein, R. P. Miller, *Strains and Stresses in Multilayered Elastic Structures: The Case of Chemically Vapor-deposited ZnS/ZnSe Laminates*, *J. Appl. Phys.* **87**, 2265 (2000).
- [145] http://en.wikipedia.org/wiki/Neutral_axis, last updated: June 20, 2008
- [146] E. Anastassakis and M. Cardona, Chapter 3: *Phonons, Strains, and Pressure in Semiconductors*, in: T. Suski, W. Paul, R. K. Willardson, and E. R. Weber (Eds.), *High Pressure in Semiconductor Physics II*, Volume **55**, Academic Press, USA, pp. 167, 1998.
- [147] J. Mossbrucker and T. A. Grotjohn, *Determination of the Components of Stress in a Polycrystalline Diamond Film Using Polarized Raman Spectroscopy*, *J. Vac. Sci. Technol. A* **15**, 1206 (1997).
- [148] Z. Fang, Y. Xia, L. Wang, and Z. Wang, *A New Quantitative Determination of Stress by Raman Spectroscopy in Diamond Grown on Alumina*, *J. Phys.: Condens. Matter* **14**, 5271 (2002).
- [149] T. Grotjohn, R. Liske, K. Hassouni, J. Asmussen, *Scaling Behavior of Microwave Reactors and Discharge Size for Diamond Deposition*, *Diam. Relat. Mat.* **14**, 288 (2005).
- [150] F. Silva, A. Gicquel, A. Tardieu, P. Cledat, Th. Chauveau, *Control of an MPACVD Reactor for Polycrystalline Textured Diamond Films Synthesis: Role of Microwave Power Density*, *Diam. Relat. Mat.* **5**, 338 (1996).

-
- [151] R. Ramamurti, *Synthesis of Diamond Thin Films for Applications in High Temperature Electronics*, Ph.D. thesis at University of Cincinnati, Department of Chemical and Materials Engineering (2005).
- [152] N. C. Burton, J. W. Steeds, G. M. Meaden, Y. G. Shreter, and J. E. Butler, *Strain and Microstructure Variation in Grains of CVD Diamond Film*, *Diam. Relat. Mat.* **4**, 1222 (1995).
- [153] B. W. Sheldon, K. H. A. Lau, and Ashok Rajamani, *Intrinsic Stress, Island Coalescence, and Surface Roughness During the Growth of Polycrystalline Films*, *J. Appl. Phys.* **90**, 5097 (2001).
- [154] H. Windischmann, R. W. Collins and J. M. Cavese, *Effect of Hydrogen on The Intrinsic Stress in Ion Beam Sputtered Amorphous Silicon Films*, *J. Non-cryst. Solids* **85**, 261 (1986).
- [155] J. Zimmer and K. V. Ravi, *Aspects of Scaling CVD Diamond Reactors*, *Diam. Relat. Mat.* **15**, 229 (2006).
- [156] X. L. Peng, Y. C. Tsui, T. W. Clyne, *Stiffness, Residual Stresses and Interfacial Fracture Energy of Diamond Films on Titanium*, *Diam. Relat. Mat.* **6**, 1612 (1997).
- [157] H. Noguchi, Y. Kubota and I. Okada, *Fabrication of X-ray Mask from a Diamond Membrane and Its Evaluation*, *J. Vac. Sci. Technol. B* **16**, 2772 (1998).
- [158] <http://www.mathworks.com/matlabcentral/fileexchange/15060>
- [159] W. Gander, G. H. Golub, and R. Strelbel, *Least Squares Fitting of Circles and Ellipses*, *BIT Numerical Mathematics* **34**, 556 (1994)
- [160] A. L. Vikharev, A. M. Gorbachev, V. A. Koldanov, R. A. Akhmedzhanov, D. B. Radishchev, T. A. Grotjohn, S. Zuo, J. Asmussen, *Comparison of Pulsed and CW Regimes of MPACVD Reactor Operation*, *Diam. Relat. Mat.* **12**, 272 (2003).
- [161] Z. Ring, T. D. Mantei, S. Tlali, and H. E. Jackson, *Low-temperature Diamond Growth in a Pulsed Microwave Plasma*, *J. Vac. Sci. Technol. A* **13**, 1617 (1995).
- [162] Z. Ring, T. D. Mantei, S. Tlali, and H. E. Jackson, *Plasma Synthesis of Diamond at Low Temperature with a Pulse Modulated Magnetoactive Discharge*, *Appl. Phys. Lett.* **66**, 3380 (1995).
- [163] H. Chatei, J. Bougdira, M. Remy, and P. Alnot, *Optical Emission Diagnostics of Permanent and Pulsed Microwave Discharges in H₂-CH₄-N₂ for Diamond Deposition*, *Surf. Coat. Technol.* **116-119**, 1233 (1999).

-
- [164] T. Lamara, M. Belmahi, J. Bougdira, F. Benedic, G. Henrion, M. Remy, *Diamond Thin Film Growth by Pulsed Microwave Plasma at High Power Density in a CH₄-H₂ Gas Mixture*, Surf. Coat. Technol. **174-175**, 784 (2003).
- [165] P. Bruno, F. Benedic, A. Tallaire, F. Silva, F. J. Oliveira, M. Amaral, A. J. S. Fernandes, G. Cicala, R. F. Silva, *Deposition of Nanocrystalline Diamond Films on Silicon Nitride Ceramic Substrates Using Pulsed Microwave Discharges in Ar/H₂/CH₄ Gas Mixture*, Diam. Relat. Mat. **14**, 432 (2005).

MICHIGAN STATE UNIVERSITY LIBRARIES



3 1293 03063 1471